

**PARAGENESIS OF URANIUM MINERALS IN THE GRANTS
MINERAL BELT, NEW MÉXICO: APPLIED GEOCHEMISTRY
AND THE DEVELOPMENT OF OXIDIZED URANIUM
MINERALIZATION**

Samantha Caldwell

Submitted in Partial Fulfillment of the Requirements for the Degree:

Master of Science
in
Mineral Engineering,
with
Specialization in Mineral Exploration

New Mexico Institute of Mining and Technology
Department of Mineral Engineering

Socorro, New Mexico
June, 2018

ABSTRACT

The Grants Mineral Belt of northwestern New Mexico was mined from the 1940s to the late 1980s, with more than 340 million pounds of U_3O_8 extracted during that time (McLemore et al., 2013). Currently, the Grants Mineral Belt contains over 400 million pounds of U_3O_8 (McLemore et al., 2013), once again bringing the region under consideration for inexpensive in-situ recovery (ISR) of uranium.

This study focuses on providing a preliminary mineral profile for portions of the Ambrosia Lake and Laguna sub-districts in order to aid leaching tests directed at assessing the feasibility of ISR for recovery of Grants-style mineralization. X-ray diffraction (XRD) analysis was employed as the primary means of identifying reduced and oxidized uranium-bearing phases and other minerals associated with sandstone-hosted uranium. Thin section and polished-block petrography, and electron microprobe analyses were employed to evaluate and confirm XRD results.

Host-rock constituents identified in thin section and XRD analysis include quartz, microcline, and orthoclase, with albite, kaolinite, and illite as the volumetrically-dominant alteration products of magmatic feldspars (Austin, 1980). Calcite was identified in barren sandstone as cement.

Analysis of reduced mineralization from the Jackpile-Paguate and St. Anthony mines identify coffinite [generally $U(SiO_4)_{1-x}(OH)_{4x}$] as the dominant crystalline phase in these mines. Very fine-grained uraninite (UO_2) overgrowths on coffinite were identified via polished petrographic analysis in reduced samples containing abundant carbonaceous matter in the Mt. Taylor and Section 31 mines. Fine-grained pyrite is observed with carbonaceous matter from numerous uranium occurrences via polished petrography, including the Mt. Taylor, St. Anthony, and Section 31 mines. Microprobe analysis of black ore from the Mt. Taylor Mine identified the mineraloid ilsemanite [$Mo_3O_8 \cdot n(H_2O)$] in the carbonaceous material, associated with weakly crystalline coffinite.

Oxidized uranium species are mineralogically diverse, reflecting availability of oxyanions and other metals in oxidizing groundwaters; this diversity is reflected in the abundance of sulfate, carbonate, and phosphate minerals identified in this study. The St. Anthony mine hosts abundant uranyl-sulfate and -phosphate minerals, with lesser carbonates. Dominant uranyl-sulfate phases occurring in the St. Anthony mine are zippeite

[$\text{K}_3(\text{UO}_2)_4(\text{SO}_4)_2\text{O}_3(\text{OH}) \cdot 3\text{H}_2\text{O}$] and jachymovite [$(\text{UO}_2)_8(\text{SO}_4)(\text{OH})_{14} \cdot 13(\text{H}_2\text{O})$], with ubiquitous gypsum ($\text{CaSO}_4 \cdot 2\text{H}_2\text{O}$). Several phosphates are identified, with (meta-) autunite [$\text{Ca}(\text{UO}_2)_2(\text{PO}_4)_2 \cdot 10\text{-}12\text{H}_2\text{O}$] the dominant phosphate, with trace meta-ankoleite [$\text{K}_2(\text{UO}_2)_2(\text{PO}_4)_2 \cdot 6(\text{H}_2\text{O})$] and phurcalite [$\text{Ca}_2(\text{UO}_2)_3\text{O}_2(\text{PO}_4)_2 \cdot 7(\text{H}_2\text{O})$]. The uranyl-vanadates carnotite [$\text{K}_2(\text{UO}_2)_2(\text{VO}_4)_2 \cdot 3\text{H}_2\text{O}$] and meta-tyuyamunite [$\text{Ca}(\text{UO}_2)_2(\text{VO}_4)_2 \cdot (3\text{-}5)\text{H}_2\text{O}$] are dominant where vanadium is present, such as at the Piedra Triste mine in the Laguna District (Fig. 3). Samples from the St. Anthony and Section 31 mines contain phases with multiple oxyanions, such as zippeite + autunite (St. Anthony), and andersonite + gypsum. These minerals reflect the composition of post-deposition oxidizing groundwaters and, in some cases, post-mine and meteoric waters.

Consideration for uranium recovery at the St. Anthony Mine should focus on employing oxidizing, carbonate-bearing solutions with a weakly-acidic to neutral pH to treat reduced mineralization; this would allow mobilization and transport of uranium as uranyl-carbonate complexes so as prevent uranium precipitation as uranyl-phosphates.

Vanadium, molybdenum, and selenium are geochemically scant at the majority of locations for this study, but should be considered as potential products during recovery in the reduced mineralized horizons being explored for uranium potential. Importantly, vanadium greatly restricts uranium mobility when uranium is oxidized and, similar to uranyl-phosphates, is stable under acidic conditions. During in-situ leaching, the use of alkaline, carbonate-bearing solutions increases the solubility of uranyl-phosphates and uranyl-vanadates (see Garrells and Christ, 1990) reducing their ability to precipitate. Although pyrite is present in trace quantities at the St. Anthony Mine, quantification of pyrite in the reduced mineralization horizons should be considered, as pyrite would be expected to react with oxidizing leach solutions, consequently reducing the pH of the leaching environment, possibly decreasing uranium solubility, and allowing for precipitation of uranyl-phosphates. Attention must also be given to the abundant calcite in the barren sandstones of the St. Anthony Mine and in the Grants Mineral Belt, as calcite will prevent oxidizing solutions from reaching reduced uranium mineralization. Although detailed geochemical evaluation of Mt. Taylor and Section 31 ores with respect to ISR requires a larger sample size in order to obtain a more complete and quantitative profile of the reduced and oxidized mineralization, this study suggests that carbonate-bearing leach solutions would oxidize and transport uranium effectively and without development of competing uranium species.

Keywords: Grants Mineral Belt, Uranium, X-Ray Diffraction, McKinley County, Valencia County, Oxyanions, Groundwater, Leaching, Sandstone-hosted

ACKNOWLEDGMENTS

I would like to express my gratitude to Dr. William X. Chávez, Jr. for taking me as his student, and providing me with instruction through the Mineral Engineering program, as well as the thesis presented below. Thank you, Bonnie Frey and New Mexico EPSCoR, “Energize New Mexico” for providing funding for this project through the National Science Foundation, award number IIA-1301346. Dr. Virgil Lueth for his availability and extensive knowledge of X-ray diffraction analyses. I am very grateful for the encouragement of Dr. Navid Mojtabai. Thank you, Alexandra Pearce, for samples from the Jackpile Mine. Ted Wilton and Westwater Resources Inc. are sincerely thanked for their financial support and encouragement of this project.

TABLE OF CONTENTS

List of Figures	iii
List of Tables	ix
List of Abbreviations	xiii
1. Introduction	1
1.1 Summary: Geology of Sandstone-Hosted Uranium-Vanadium Deposits	2
1.2 Geochemistry of Uranium in Sandstone-Hosted Deposits	3
1.3 Role of Organic/Carbonaceous Matter in Primary (Tabular) Deposits: Mobilization	4
1.4 Note on Uranium and its Supergene and Post-Mine Behavior	5
2. Study Areas	6
2.1 Stratigraphy: Laguna to Ambrosia Lake	6
2.2 Laguna District	8
2.3 Ambrosia Lake District	10
2.4 Midnite Mine (Washington State)	10
3. Methods of Analysis	11
3.1 Field Collection	11
3.2 Laboratory Methods	11
i. Petrographic Analysis	11
ii. X-Ray Diffraction Analysis	12
iii. Electron Microprobe Analysis	12
iv. Detection Limits	12

4. This Study: Minerals Identified from the Grants Mineral Belt	13
4.1 Reduced Uranium-Vanadium Minerals	15
4.2 Oxidized Uranium-Vanadium Minerals	26
4.3 St. Anthony Mine: Analysis Focus	32
5. Host-rock Characterization and Other Prominent Minerals	38
6. Discussion: Geochemical Environment of Precipitation	43
7. Conclusions and Implications	56
References	60
Appendix 1: Sample Photos and Descriptions (Includes Thin/Polished Sections)	64
Appendix 2: X-Ray Diffractometer Parameters and Data	79
Appendix 3: Microprobe Parameters and Data	169
Appendix 4: Sample and Mineral Locations in the St. Anthony Mine	176

LIST OF FIGURES

Figure 1: Stratigraphy Column, Laguna and Ambrosia Lake Districts	6
Figure 2: Cross Section, Ambrosia Lake to Laguna District	7
Figure 3: Grants Mineral Belt Map	8
Figure 4: Photo, St. Anthony South Pit Highwall	9
Figure 5: Sample JP1	16
Figure 6: Diffractogram, Sample JP1, Coffinite	16
Figure 7: Core from Mt. Taylor Mine	17
Figure 8: Diffractogram, Sample MT1, Coffinite	17
Figure 9: Hand Sample MT3	18
Figure 10: Hand Sample MT3 with Ilsemaninite	18
Figure 11: Sample STA3	19
Figure 12: Polished Probe Mount of Sample STA5, Coffinite	20
Figure 13: Samples STA13A and STA13B	21
Figure 14: Diffractogram, Sample STA13A, Coffinite	21
Figure 15: Sample STA18	22
Figure 16: Diffractogram, Sample STA18, Coffinite, Uraninite	22
Figure 17: Polished Probe Mount of Sample STA18, Coffinite	23
Figure 18: Sample KM2	24
Figure 19: Diffractogram, Sample KM2, Hydronium-Jarosite	25
Figure 20: Sample WWCM	27
Figure 21: Diffractogram, Sample WWCM, Carnotite	27
Figure 22: Sample PT1	28

Figure 23: Diffractogram, Sample PT3, Meta-Tyuyamunitite	28
Figure 24: Sample KM1	29
Figure 25: Diffractogram, Sample KM1, Andersonite, Gypsum	29
Figure 26: Sample MT2	30
Figure 27: Diffractogram, Sample MT2, Zippeite	30
Figure 28: Sample MT5	31
Figure 29: Diffractogram, Sample MT5, Jachymovite	31
Figure 30: Sample STA1	33
Figure 31: Diffractogram, Sample STA1, Magnesiopascoite	33
Figure 32: Sample STA9	34
Figure 33: Diffractogram, Sample STA9, Cejkaite	34
Figure 34: Sample STA11	35
Figure 35: Diffractogram, STA11, Autunite and Sabugalite	35
Figure 36: Sample STA19	36
Figure 37: Diffractogram, Sample STA19, Jachymovite	36
Figure 38: Sample STA21	37
Figure 39: Diffractogram, Sample STA21	37
Figure 40: Thin Section Photo, Sample STA18B	40
Figure 41: Eh-pH Diagram, Aqueous Uranyl-Sulfate and -Carbonate	49
Figure 42: Eh-pH Diagram, Uranyl-Carbonate Species	51
Figure 43: Eh-pH Diagram, Uranyl-Vanadate Species	54
Figure 44: Eh-pH Diagram, Aqueous Vanadate	55
Figure 45: Sample JP2 and JP3	64
Figure 46: Sample PT2	65
Figure 47: Sample PT3	65
Figure 48: Samples MD1 and MD2	66
Figure 49: Sample STA2	66
Figure 50: Sample STA4	67

Figure 51: Sample Horizon for STA5, STA6, and STA21	67
Figure 52: Sample STA5	68
Figure 53: Sample STA8	68
Figure 54: Sample STA10	69
Figure 55: Sample STA12	69
Figure 56: Sample Horizons of STA13A and STA13B	70
Figure 57: Sample STA14, STA16, and STA20	70
Figure 58: Sample STA15	71
Figure 59: Sample STA17	71
Figure 60: Sample STA18 Collection	72
Figure 61: Thin Section Photo, Sample MT1	73
Figure 62: Thin Section Photo, Sample STA3	74
Figure 63: Thin Section Photo, Sample STA18A	74
Figure 64: Polished Probe Mount Photo, Sample MT1, Coffinite	75
Figure 65: Polished Probe Mount Photo, Sample MT1, Pyrite	75
Figure 66: Polished Probe Mount Photo, Sample MT3, Coffinite	76
Figure 67: Polished Probe Mount Photo, Sample MT5	76
Figure 68: Polished Probe Mount Photo, Sample KM2, Coffinite, Pyrite	77
Figure 69: Polished Probe Mount Photo, Sample STA3, Coffinite	78
Figure 70: Polished Probe Mount Photo, Sample STA7, Fossil Trash	78
Figure 71: Diffractogram, Sample JP1	80
Figure 72: Pattern List, Sample JP1	80
Figure 73: Diffractogram, Sample JP2	82
Figure 74: Pattern List, Sample JP2	82
Figure 75: Pattern List, Sample JP3	84
Figure 76: Pattern List, Sample MT1	86
Figure 77: Diffractogram, Sample MT2, Jachymovite, Schoepite	88
Figure 78: Pattern List, Sample MT2	88
Figure 79: Diffractogram, Sample MT3, Coffinite	90
Figure 80: Pattern List, Sample MT3	91

Figure 81: Pattern List, Sample MT5	93
Figure 82: Pattern List, Sample KM1	95
Figure 83: Pattern List, Sample KM2	97
Figure 84: Diffractogram, Sample KM3, Pyrite, Gypsum	99
Figure 85: Pattern List, Sample KM3	100
Figure 86: Diffractogram, Sample MD1	102
Figure 87: Pattern List, Sample MD1	102
Figure 88: Diffractogram, Sample MD2	103
Figure 89: Pattern List, Sample MD2	104
Figure 90: Diffractogram, Sample PT1, Meta-Tyuyamunite	105
Figure 91: Pattern List, Sample PT1	105
Figure 92: Diffractogram, Sample PT2, Meta-Tyuyamunite	107
Figure 93: Pattern List, Sample PT2	107
Figure 94: Pattern List, Sample PT3	109
Figure 95: Pattern List, Sample WWCM	111
Figure 96: Diffractogram, Sample STA1, Meta-Schoepite	113
Figure 97: Diffractogram, Sample STA1, Studtite	113
Figure 98: Diffractogram, Sample STA1, Oswaldpeetersite	114
Figure 99: Pattern List, STA1	114
Figure 100: Diffractogram, Sample STA2, Meta-Ankoleite	117
Figure 101: Pattern List, Sample STA2	117
Figure 102: Diffractogram, Sample STA3, Coffinite	119
Figure 103: Pattern List, Sample STA3	120
Figure 104: Diffractogram, Sample STA4, Natrozippeite	122
Figure 105: Diffractogram, Sample STA4, Schoepite, Meta-Schoepite	122
Figure 106: Pattern List, Sample STA4	123
Figure 107: Diffractogram, Sample STA5, Meta-Autunite	124
Figure 108: Pattern List, Sample STA5	125
Figure 109: Diffractogram, Sample STA6, Phurcalite, Carnotite	126
Figure 110: Pattern List, Sample STA6	127

Figure 111: Diffractogram, Sample STA7, Schoepite, Hydronium-Jarosite	129
Figure 112: Pattern List, Sample STA7	129
Figure 113: Diffractogram, Sample STA8, Zippeite, Jachymovite, Natrojarosite	131
Figure 114: Pattern List, Sample STA8	132
Figure 115: Pattern List, Sample STA9	133
Figure 116: Diffractogram, Sample STA10, Natrozippeite, Gypsum	135
Figure 117: Pattern List, Sample STA10	136
Figure 118: Diffractogram, Sample STA11, Hexahydrite, Minasragrite	138
Figure 119: Diffractogram, Sample STA11, Zippeite	138
Figure 120: Pattern List, Sample STA11	139
Figure 121: Diffractogram, Sample STA12, Coffinite	141
Figure 122: Pattern List, Sample STA12	142
Figure 123: Diffractogram, Sample STA13A, Coffinite	144
Figure 124: Pattern List, Sample STA13A	144
Figure 125: Diffractogram, Sample STA13B, Calcite, Hematite	146
Figure 126: Pattern List, Sample STA13B	146
Figure 127: Diffractogram, Sample STA14, Kaolinite, Calcite	148
Figure 128: Pattern List, Sample STA14	148
Figure 129: Diffractogram, Sample STA15, Zippeite, Gypsum	150
Figure 130: Pattern List, Sample STA15	151
Figure 131: Diffractogram, Sample STA16	153
Figure 132: Pattern List, Sample STA16	153
Figure 133: Diffractogram, Sample STA17, Carnotite	155
Figure 134: Pattern List, Sample STA17	156
Figure 135: Pattern List, Sample STA18, Coffinite	157
Figure 136: Diffractogram, Sample STA18A (Host-rock), Calcite	159
Figure 137: Pattern List, Sample STA18A (Host-rock)	159
Figure 138: Diffractogram, Sample STA18B (Host-rock), Calcite	161
Figure 139: Pattern List, Sample STA18B (Host-rock)	161
Figure 140: Diffractogram, Sample STA19, Zippeite, Oswaldpeetersite	163

Figure 141: Pattern List, Sample STA19	163
Figure 142: Diffractogram, Sample STA20	165
Figure 143: Pattern List, Sample STA20	166
Figure 144: Pattern List, Sample STA21	167
Figure 145: BSE Image, Sample MT3	170
Figure 146: Uranium Map, Sample MT3	170
Figure 147: BSE Image, Sample MT5	171
Figure 148: Uranium Element Map, Sample MT5	171
Figure 149: Uranium Element Map, Sample KM2	172
Figure 150: BSE Image, Sample KM3	172
Figure 151: Uranium Element Map, Sample KM3	173
Figure 152: BSE Image, Sample STA7	173
Figure 153: Mineral Map, St. Anthony North Pit	176
Figure 154: Mineral Map, St. Anthony South Pit	177
Figure 155: Sample Number Map, St. Anthony North Pit	177
Figure 156: Sample Number Map, St. Anthony South Pit	178

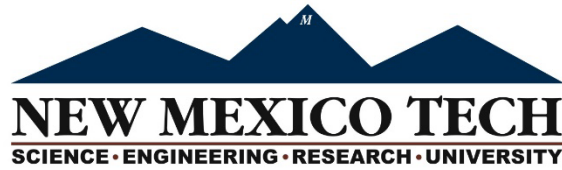
LIST OF TABLES

Table 1: Uranium Minerals Identified in this Study	14
Table 2: Reduced Uranium Identified in this Study	15
Table 3: Oxidized Uranium Minerals Identified in this Study	26
Table 4: Oxidized Uranium Minerals identified within the St. Anthony Mine	32
Table 5: Host-rock Minerals Identified in this Study	40
Table 6: X-Ray Diffractometer Scan Parameters	79
Table 7: Peak List, Sample JP1	81
Table 8: Peak List, Sample JP2	83
Table 9: Peak List, Sample JP3	84
Table 10: Peak List, Sample MT1	86
Table 11: Peak List, Sample MT2	89
Table 12: Peak List, Sample MT3	91
Table 13: Peak List, Sample MT5	93
Table 14: Peak List, Sample KM1	95
Table 15: Peak List, Sample KM2	98
Table 16: Peak List, Sample KM3	100
Table 17: Peak List, Sample MD1	103
Table 18: Peak List, Sample MD2	104
Table 19: Peak List, Sample PT1	106
Table 20: Peak List, Sample PT2	108
Table 21: Peak List, Sample PT3	109

Table 22: Peak List, Sample WWCM	111
Table 23: Peak List, Sample STA1	115
Table 24: Peak List, Sample STA2	118
Table 25: Peak List, Sample STA3	120
Table 26: Peak List, Sample STA4	123
Table 27: Peak List, Sample STA5	125
Table 28: Peak List, Sample STA6	127
Table 29: Peak List, Sample STA7	130
Table 30: Peak List, Sample STA8	132
Table 31: Peak List, Sample STA9	134
Table 32: Peak List, Sample STA10	136
Table 33: Peak List, Sample STA11	139
Table 34: Peak List, Sample STA12	142
Table 35: Peak List, Sample STA13A	145
Table 36: Peak List, Sample STA13B	147
Table 37: Peak List, Sample STA14	149
Table 38: Peak List, Sample STA15	151
Table 39: Peak List, Sample STA16	154
Table 40: Peak List, Sample STA17	156
Table 41: Peak List, Sample STA18	158
Table 42: Peak List, Sample STA18A (Host-rock)	160
Table 43: Peak List, Sample STA18B (Host-rock)	162
Table 44: Peak List, Sample STA19	164
Table 45: Peak List, Sample STA20	166
Table 46: Peak List, Sample STA21	168
Table 47: Microprobe Scan Parameters	169
Table 48: Sample MT3 Microprobe Data	174
Table 49: Sample MT5 Microprobe Data	174
Table 50: Sample KM2 and KM3 Microprobe Data	175
Table 51: Sample STA7 Microprobe Data	175

LIST OF ABBREVIATIONS

XRD	X-Ray Diffraction
ISR	In-Situ Recovery
ppm	Parts Per Million
Wt%	Weight Percent
Ma	Million Years Ago
Cof	Coffinite
Epx	Epoxy
Fsp	Feldspar
Mc	Microcline
OM	Organic Matter
Py	Pyrite
Si	Silicate
VF	Volcanic Fragment



This thesis is accepted on behalf of the faculty
of the Institute by the following committee:

Dr. Navid Mojtabai

Academic Advisor

Dr. William X. Chávez, Jr.

Research Advisor

Bonnie Frey

Committee Member

Dr. Virgil Lueth

Committee Member

Dr. Navid Mojtabai

Committee Member

I release this document to New Mexico Institute of Mining and Technology

Samantha Caldwell

Student Signature

4 June, 2018

Date

CHAPTER 1

INTRODUCTION

Sandstone-hosted uranium-vanadium deposits represent the earliest and most productive types of uranium +/- vanadium ore deposits in the United States, having been mined from the mid-1940s to the late 1980s, when the price of uranium rapidly declined. Exploration for these deposits was undertaken because of their size and distribution, with prominent localities in the Colorado Plateau region of northwest New Mexico and adjacent Colorado, Utah, and Arizona, as well as Wyoming. The Grants Mineral Belt produced 340 million pounds of U_3O_8 , and greater than 400 million pounds of uranium as yet remain (McLemore et al., 2013). With the development of new mining technology, particularly in-situ recovery, the Grants Mineral Belt represents increased potential for economically-viable uranium recovery.

The goal of this study is to determine the mineralogy and paragenesis of ore samples from several localities within the Grants Mineral Belt, including the Laguna (St. Anthony mine) and Ambrosia Lake sub-districts. Hand-specimen examination, X-Ray diffraction (XRD) and microprobe analyses, and thin and polished section petrography are used to produce geochemical profiles for select areas of the Grants Mineral Belt. This information is expected to contribute to the understanding of the in-situ leach-recovery characteristics of reduced and oxidized uranium minerals and associated minerals.

1.1 Summary: Geology of Sandstone-Hosted Uranium-Vanadium Deposits

The sandstone-hosted uranium+/-vanadium deposits of the Colorado Plateau are comprised of reduced and oxidized minerals occurring as pore-space fillings and grain coatings in fluvial, continental sandstones (Finch, 1980); to a much lesser extent, uranium is found as oxide minerals filling fractures within continental limestones (Hilpert, 1969). For this study, the Jurassic-Age Jackpile and Westwater Canyon Members of the Morrison Formation were sampled, as they are the dominant units hosting uranium mineralization (Wilton, 2017). These sandstones are comprised of arkosic- to quartz-arenites (Austin, 1980; see Fig. 1 for stratigraphic column), commonly with granitic and volcanic clasts. Although the source of uranium in these sandstones is yet debated, the background values for uranium are observed to be elevated in felsic volcanic material (7-10 ppm) when compared to other igneous rock types, such as granite (Larson and Gottfried, 1960). The Datil-Mogollon Highlands to the south is a potential metal source for the Grants Mineral Belt. The sedimentary host-rocks for uranium mineralization in the Grants Mineral Belt contain igneous contributions that reflect regional felsic volcanic activity (Gruner, 1956; Austin, 1980). Devitrification of this volcanic material is surmised to have liberated uranium and other metals into regional groundwaters (Gruner, 1956), to be transported and precipitated as reduced uranium minerals, including uraninite or coffinite.

The greatest uranium +/- vanadium grades (0.20% U_3O_8) comprise primary “tabular/pene-concordant” deposit types (Adler, 1974; McLemore, 2010). These elongate deposits are sub-parallel to parallel, trend west-northwest (Turner-Peterson and Fishman, 1986), and are intimately associated with humic material or “fossil trash” deposited along the braided-stream environment of the Morrison Formation (McLemore, 2010). The Jackpile and St. Anthony mines in the Laguna sub-district are present as primary deposits (Wilton, 2017). Redistributed deposits result from the transport and precipitation of primary deposit types and are produced as a result of multiple cycles of uranium (vanadium, molybdenum, selenium) mobility and precipitation, termed “Multiple-Migration Accretion” (MMA) by Gruner (1956). These deposits are asymmetrical and have slightly lower grade (0.16% U_3O_8) than primary deposits (McLemore, 2010). Primary uranium minerals precipitate in reducing environments characterized by carbonaceous matter and pyrite, +/- “fossil trash,” with the carbonaceous matter itself or possibly hydrocarbon gases as a reductant; similarly, the uranium deposits of Texas are interpreted to have been formed as a result of uranium precipitation induced by groundwater reacting with H_2S gas (Gruner, 1956; Dahlkamp, 2010). Some authors speculate that mixing of oxidized and reduced groundwaters in areas devoid of carbonaceous matter may also create the reducing environment needed for uranium minerals to precipitate (McLemore et al., 2013).

In order to remobilize uranium and associated metals and semi-metals, studies have suggested that weakly acidic, carbonate-, sulfate- or phosphate-bearing groundwater passing through uraninite and coffinite-bearing sandstones oxidizes these minerals,

creating an aqueous uranium phase in the form of UO_2^{2+} , uranyl di- and tri-carbonates, or phosphates under acidic conditions (Hostetler and Garrels, 1962; Runnells et al., 1980). These solutions are transported “short distances” to a reducing environment to be precipitated again as uraninite or coffinite. Redistributed deposits located far from their source do not always have indigenous plant material (fossil trash) as the reducing agent. Adler (1974) theorizes instead that humic and fulvic acids originating from bogs overlying the host sandstones are the source of redistributed humic material. These multiple migratory and accretionary processes produce displacement of an oxidation-reduction (redox) zone, comprising the down-flow hydraulic front of roll-type deposits as groundwaters travel down-dip from an initial redox environment. The sandstone surrounding this roll front generally has a gray, “reduced” color, while the oxidation zone up-dip of the roll is commonly red in color, due to the presence of oxidized hematite (Saucier, 1980). One of the objectives of this study is to identify some of the reduced uranium species and their oxidized products representing this redox environment and subsequent, continued oxidation of uranium minerals.

1.2 Geochemistry of Uranium in Sandstone-Hosted Deposits

Mobilization and Transportation

Uranium can occur in five valence states. U (+6) is the preferred valence state in solution, followed by +4 in crystalline form, and rarely as +2, +3, or +5 (Lide, 2008). In the minerals uraninite and coffinite, uranium exists in the U (+4) valence state (Gruner, 1956). Once uranium has been subjected to an oxidizing solution, the valence state will readily oxidize to UO_2^{2+} (+6), allowing the metal to be easily complexed and transported (Adler, 1974; Gruner, 1956). This ion is very soluble and can complex and form minerals with the various oxyanions (sulfate, carbonate, etc.). Alkali, and alkaline earth metals, such as Na^+ or Mg^{2+} will also increase the solubility of uranium minerals in water and were studied as a method of extraction by mining companies (Gruner, 1956).

The chemistry of the groundwater transporting uranium plays a vital role in mobilization and precipitation. Jennings and Leventhal (1978) experimented with differing groundwater systems using distilled water. For systems lacking significant dissolved carbonate, the solutions need to have significant acidic or alkaline properties to solubilize uranium-bearing minerals. Uraninite and schoepite are both stable within this system, and therefore are immobile under these conditions. Stable uranium ions within a pure groundwater system are UO_2^{2+} , $\text{UO}_2(\text{OH})^+$, and H_2UO_4^- (Jennings and Leventhal, 1978). Groundwater is rarely this pure, and its chemistry depends upon rock and atmospheric inputs.

Once bicarbonate is contributed to the system, uranium solubility increases greatly. Uranium complexes with carbonate to form uranyl-di- $[\text{UO}_2(\text{CO}_3)_2]^{2-}$ and tri-carbonates

$[\text{UO}_2(\text{CO}_3)_3]^{4-}$ (Jennings and Leventhal, 1978; Breger, 1974). These carbonate complexes are sensitive to pressure and temperature. A decrease in either condition will cause destabilization and precipitation of uranium minerals. Solid phases in this system are uraninite, schoepite, and rutherfordine (Jennings and Leventhal, 1978).

In natural systems with pH values lower than 6, bisphosphate $[(\text{HPO}_4)^{2-}]$ aids in the transport of uranium, when carbonate becomes unavailable (Runnells et al., 1980). Uranyl-phosphate minerals are stable in acidic conditions when uranyl-phosphates are saturated in groundwater (Singh, 2010), removing uranium from groundwater in low pH conditions (Arey, et al., 1999). Phosphate works so well restricting uranium mobility, previous researchers have experimented with it as means to prevent mobility in areas contaminated by uranium (Catalano 2016; Singh, 2010). This will need to be considered when examining ISR of the St. Anthony deposit, as many of the identified oxidized uranium minerals present are uranyl-phosphates.

In U-O₂-H₂O-CO₂ systems with a pH lower than 3.5 and depleted in either -carbonate or -phosphate, uranium will complex with SO_4^{2-} to produce $\text{UO}_2(\text{SO}_4)_4^{6-}$ or $\text{UO}_2(\text{SO}_4)_3^{4-}$ (Hostetler and Garrels, 1962). Sulfate complexation with uranium does not form any solid phases (Jennings and Leventhal, 1978). This complexation may occur locally within the San Juan Basin; uranyl-sulfates are abundant, yet conspicuous carbonate is noted in the Grants region (Rautman, 1980), along with multiple uranyl-phosphate minerals identified in this study.

These systems are further complicated by the presence of metals commonly associate with sandstone-hosted uranium. Vanadium, molybdenum, selenium, iron, cobalt, arsenic, and copper are frequently associated with sandstone-hosted uranium (Adler, 1974; Harshman, 1974). This study identifies vanadium, molybdenum, selenium, and abundant iron intimately associated with uranium mineralization. As with phosphate, when vanadium and uranium minerals precipitate, the phase is very stable (Adler, 1974), and requires significant change in pH or Eh to re-mobilize the elements. Iron is very common as pyrite or marcasite in reduced uranium beds (Gruner, 1956), and molybdenum can occur as sulfides or oxides (Harshman, 1974). Selenium is observed as its native element in reduced mineral horizons (Harshman, 1974).

1.3 Role of Organic/Carbonaceous Matter in Primary (Tabular) Deposits: Mobilization

Early geologists studying sandstone-hosted uranium were quick to note the intimate association uranium and metals with transitional valence states (Adler, 1974) have with carbonaceous matter (Gruner, 1956). Organic matter can play two roles in the mobilization/immobilization of uranium. In the first, uranium may be mobilized by soluble humic and fulvic acid, generated from decomposing plant material contained within the uranium-host sandstone units (Jennings and Leventhal, 1978). These soluble organic compounds represent the near-surface oxidative decomposition of contained carbonaceous

matter; in acidic conditions, fulvic acids mobilize significant amounts of metals, and can reach a pH of 2 (Jennings and Leventhal, 1978); decomposition of pyrite may also contribute to pH decrease in these open systems. Where carbonaceous matter has accreted, it is an excellent reductant of metals (Gruner, 1956). Adsorption and chelation of uranium onto the carbonaceous matter is effective in uranium's reduction in these deposits (Jennings and Leventhal, 1978; Krauskopf and Bird, 1995), and are dominant as organo-uranium complexes in the Grants Mineral Belt (McLemore, 2002).

For the purposes of this study, organic matter, humate, and carbonaceous matter have the same meaning to prevent repetitive reading. Also, of note is the use of organo-uranium complexes. This term is historical and refers to the adsorption or chelation of metals onto carbonaceous matter. These complexes consist of carbon, hydrogen, nitrogen, oxygen, as well as sulfur (Krauskopf and Bird, 1995). No testing was executed to determine the composition of these organic molecules and are henceforth referred to as the general "organo-uranium complexes."

1.4 Note on Uranium and its Supergene and Post-Mine Behavior

The action of multiple migration-accretion events on uranium ore bodies, as well as post-mine weathering, has produced complex mineral associations in the ores of the Grants Mineral Belt, starting with oxidative destruction of uraninite, coffinite and organo-uranium complexes (Gruner, 1956; Kelley et al., 1967). Once uranium minerals are subjected to low-temperature or related supergene processes, the uranium minerals produced reflect the interaction of groundwaters, host-rock components, and local redox environments. Sulfate, carbonate, and phosphate oxyanions within ground- and surface waters react with soluble uranium species to produce complex hydrated uranium-vanadium mineral assemblages, discussed in Chapter 4, Section 4.2. The presence of alkali, and alkaline earth metal cations, especially Na^+ , Mg^{2+} , K^+ , and Ca^{2+} , results in the formation of metastable uranium-(vanadium) hydroxy-oxides (Gruner, 1956). As such, there are over 250 known uranium mineral species, most of which are oxidized (e.g., see Hazen et al., 2009).

CHAPTER 2

STUDY AREA

2.1 Stratigraphy of Study Area

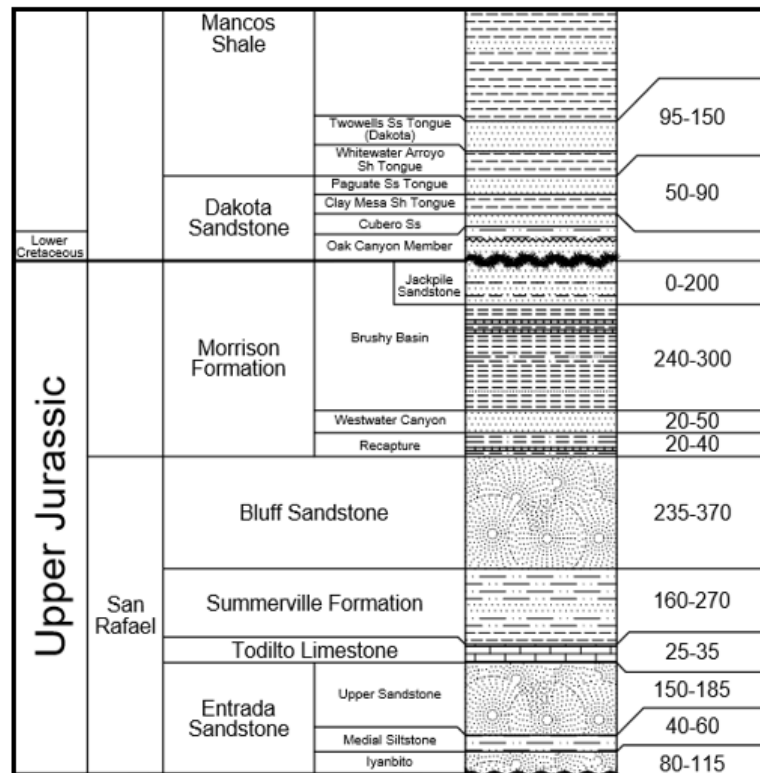


Figure 1: Stratigraphic column of the Cebolleta (Laguna-Paguete) Area, Valencia County, New Mexico. The lithology of the Laguna area is nearly identical to the Ambrosia Lake District. The difference in Laguna is the presence of the Jackpile Member of the Morrison Formation. The Jackpile Member shown here is a prominent host for U +/- V deposits in the Laguna District. Thickness of units in feet (right hand side). Modified from Wilton (2018).

The oldest stratigraphic unit in the Grants Mineral Belt is the late Permian San Andreas Limestone, with the youngest unit the Point Lookout Sandstone of the upper Cretaceous (Fig. 1). The majority of uranium mineralization in the Grants region is hosted in Morrison Formation sandstones, with less mineralization in the limestone of the Todilto Formation and the Dakota and Entrada Sandstones (McLemore, 2010). The Jackpile Member of the Morrison is the dominant host unit for mineralization in the Laguna District, it has limited lateral distribution though, which does not extend into the Ambrosia Lake sub-district (Fig. 2; Kelley et al., 1967). The Westwater Canyon Member is the dominant host in the Ambrosia Lake sub-district, with some mineralization in the Poison Canyon Tongue (Wilton, 2017). Figure 2 illustrates the stratigraphic relationships within the two sub-districts.

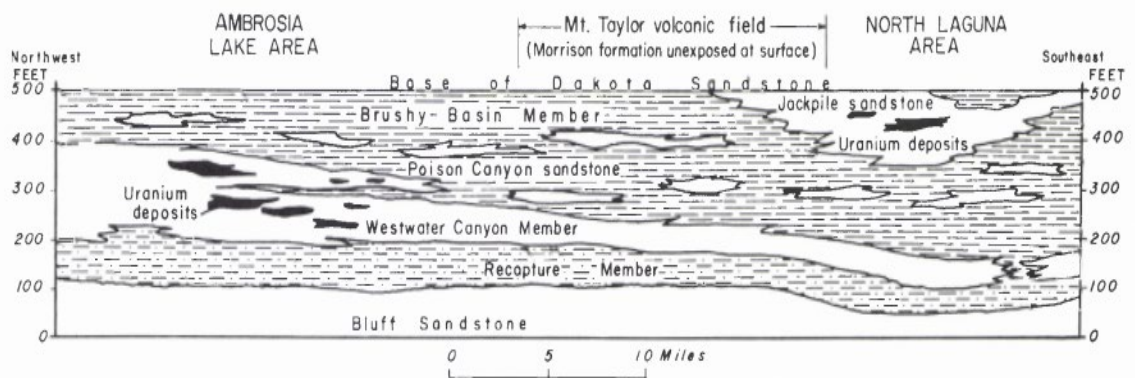


Figure 2: Cross section for study area displaying the major units hosting uranium mineralization in the Morrison Formation, from Ambrosia Lake to the northern portion of the Laguna District. From Kelley et al., 1967. Unmodified.

Of note in Figure 2 is the absence of the Todilto Formation in the cross-section area. The Bluff Sandstone and the Summerville Formation separate the Todilto limestone from the Morrison Formation (Fig. 1). The mineralization in the Todilto is distinguished not only in age but style of mineralization. The Todilto hosts mineralization that is approximately 150-155 Ma in age and is predominantly oxidized uranium-vanadium mineralization (McLemore, 2010).

2.2 Laguna Sub-District

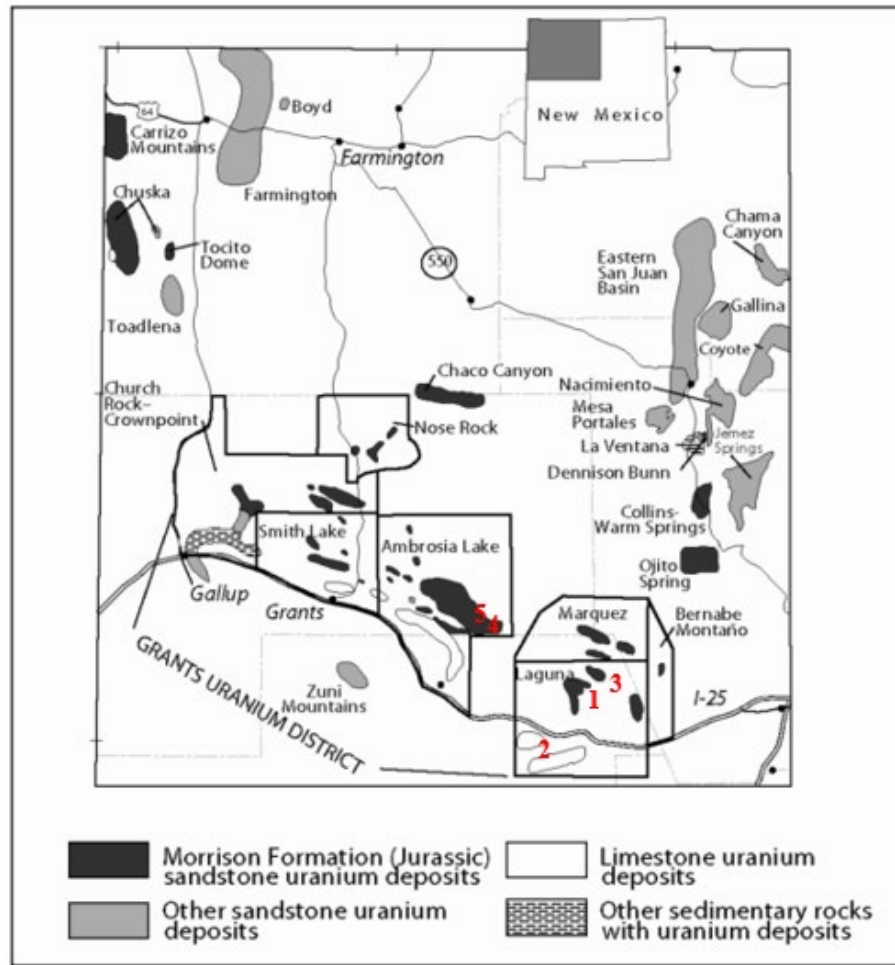


Figure 3: Sample locations for this study. Laguna sub-district: 1-Jackpile mine. 2-Piedra Triste mine. 3-St. Anthony mine. Ambrosia Lake sub-district: 4- Mt. Taylor mine. 5-Section 31 mine. Modified from McLemore (2010).

Jackpile Mine (Jackpile Member, Morrison Formation)

The Jackpile mine operated from 1953 to 1982, moving over 25 million tons of uranium ore (EPA, 2018) consisting dominantly of the minerals coffinite and lesser uraninite (McLemore, 1982). The Jackpile is the uppermost member of the Morrison formation within the Grants region (Fig. 1), which Moench and Schlee (1967) separate into upper and lower units. The upper unit is quartz dominated and bleached in appearance due to kaolinite alteration of feldspars and lacks any appreciable mudstone; the lower unit is more arkosic, contains green interbedded mudstone lenses, and has an orange/yellow cast due to iron-oxides within the sandstone. Both units consist of a friable, fine- to medium-grained sandstone, with quartz, minor feldspar, clay rip-up clasts, and igneous fragments. Variable amounts of clay, calcite, and silica cement the clasts together (Moench & Schlee, 1967; Wilton, 2017).

Piedra Triste Mine (Todilto Formation)

The Piedra Triste Mine differs from the well-known sandstone deposits in the Grants Mineral Belt, as the host-rock is a fractured, laminated continental limestone within the organic-rich Todilto Formation (Hilbert, 1969). The southwestern deposits in the Grants region are exclusively hosted in the Todilto Formation (Fig. 3). Deposition of the Entrada Sandstone deformed the limestone, creating intraformational folds favorable for the precipitation of uranium (McLemore, 2010). The limestone is relatively thin, and uranium-vanadium mineralization occurs along the elongate portion of folds. The limestone grades from thinly laminated to massive, is described as light to medium grey, and contains some sulfur, evidenced by the fetid odor given off when freshly broken. The rock is dominantly micritic, with coarser calcite filling fractures and vugs. The deposits of the Todilto were originally mined for their oxidized yellow ores, which progress into primary black ores with depth (Berglof & McLemore, 2003). There is also a difference in age for the limestone-hosted deposits of the Todilto; U-Pb isotopic dating places the Todilto Formation at 150-155 Ma, 25 million years older than the mineralization in the Morrison Formation (McLemore, 2010).



Figure 4: South wall of the St. Anthony south pit. Note the large channel scours in the Jackpile Member of the Morrison Formation (arrows). This area is capped by the Cretaceous Mancos Shale (grey unit).

St. Anthony Mine (Jackpile Member, Morrison Formation)

The ore within the St. Anthony mine occurs within the Jackpile Member of the Morrison Formation and is capped by the Mancos Shale and the Dakota Sandstone (Moench & Schlee, 1967). The host-rock within the pits consist dominantly of quartz arenite, and patches of arkosic arenite can be observed on the highwalls. Wilton (2017) notes that kaolinite cements individual lenses of sandstone, while calcite cement is widespread and observed in the north pit (observed in thin sections produced of host-rock). There are large channel scours within the Jackpile member of the St. Anthony mine (Fig. 4), which are frequently mineralized along the bottom contact. These scours frequently cut through deeper units and are deposited in the braided-stream environment common to the Morrison Formation (Wilton, 2017).

2.3 Ambrosia Lake District

Mt. Taylor Mine (Westwater Canyon Member, Morrison Formation)

The mineralization at the Mt. Taylor mine occurs within the Westwater Canyon Member of the Morrison Formation. This member of the Morrison consists of fine- to coarse-grained arkosic sandstone deposited in a braided-stream environment (Moench & Schlee, 1937; Alief & Kern, 1989). McLemore et al. (2002) describes the mineralization of Mt. Taylor as organo-uranium complexes with no defined uranium-bearing minerals.

Section 31 Mine, McKinley County

As with many of the mines in the Grants Mineral Belt, literature defining the mineralization and geology at the Section 31 mine is limited. McLemore (2002) describes the ore as primary tabular deposits consisting of organo-uranium complexes in the Westwater Canyon Member of the Morrison Formation.

2.4 Other Sample Areas

Midnite Mine (Washington State)

This area was selected for a comparison analysis of the mineraloid pitchblende (amorphous UO_2) to the uranium mineralization in this study. Due to its amorphous nature, pitchblende produces a unique diffractogram. The Midnite Mine differs substantially from the sandstone-hosted deposits in the Grants Mineral Belt. The mineralization is hydrothermal in origin and is hosted in a brecciated schistose phyllite on a contact with an intrusive quartz monzonite porphyry (Boudette & Weis, 1956). Comparison of the unique pitchblende pattern to the Grants samples concluded no pitchblende present in this study.

CHAPTER 3

METHODS OF ANALYSIS

3.1 Field Methods – St. Anthony Mine

Sample collection of St. Anthony mineralization occurred in June and October of 2017. Prior to this study, Westwater Resources Inc. made a series of cuts into the highwalls of the north and south pits in 2010, with 4-inch x 3-foot vertical channel samples analyzed for U_3O_8 grade but not mineralogy. Sample collection during 2017 sampled these channels to analyze reduced and oxidized mineralization. A map of sample and mineral locations is available in Appendix 4 (Figs. 155 and 156, p. 177). A field-portable scintillometer was used to detect mineralization.

3.2 Laboratory Methods

i. X-Ray Diffraction (XRD) Analysis

The dominant method of analysis for this study is powder X-ray diffraction, using a PANalytical X'Pert Pro³ X-Ray Diffractometer, made available through the New Mexico Bureau of Mines and Geology. Scan parameters and reports are available in Appendix 2. All samples were analyzed via this method; several of these samples are complemented by optical petrographic and microprobe analysis of thin and polished sections.

Sieving:

149, 105, and 75-micron sized sieves were utilized to remove the large quartz and feldspar grains as well as concentrate the finer material for XRD analysis in order to increase detection of the lesser and trace uranium minerals. This method was employed for both reduced and oxidized sample suites.

Note on Graphic XRD Scans:

To display the low intensity of the uranium phases identified in this study, feldspar and clays peaks are excluded from the presented scans due to their abundance, which imparts numerous, intense peaks on the diffractogram, obscuring the uranium minerals that occur in much lower concentrations.

ii. Optical Petrography: Thin and Polished Section Analysis

An Olympus CX31 microscope was used for thin section analysis, and an Infinity 1 by Luminera camera used for photographs at 4, 10, and 20x magnification. A Nikon OPTIPHOT-POL microscope was used for polished-block petrographic analysis of reduced mineralization, with samples photographed with a Luminera 2 camera. Photos of thin sections and polished probe mounts are located in Appendix 1.

iii. Electron Microprobe Analysis

Due to the fine-grained nature of sandstone-hosted uranium, several samples were analyzed via microprobe for mineral identification. A Wavelength-Dispersive Spectrometer Cameca SX 100 Electron Microprobe was used courtesy of the New Mexico Bureau of Mines and Geology. The detection limit of uranium for this probe is 150 parts per million (ppm) and 300 ppm for molybdenum, and a 5 micron-diameter beam was used for analysis. Scan parameters and data are located in Appendix 3.

iv. Detection Limits

The detection limit for the diffractometer used in this study is a practical limit; for analysis times at 40 minutes or greater, the diffractometer can reliably detect the presence of a mineral at approximately two weight-percent. The true detection limit can reliably be calculated, provided mineral standards are analyzed prior to sample analysis. For this study, no standards were used, and the detection limit of minerals in the unknown samples is undefined.

The electron microprobe detection limits for uranium, vanadium, molybdenum, and selenium are approximately 150 ppm, 120 ppm, 300ppm, and 175 ppm, respectively. The detection limit variation in microprobe analyses is partly determined by background interference. The greater the interference, the greater the detection limit for the target element becomes. In this study, molybdenum consistently caused elevated background interference during analysis for the other selected elements.

CHAPTER 4

RESULTS: MINERALS IDENTIFIED FROM THE GRANTS MINERAL BELT

Mine Areas Sampled

This study presents a limited list of uranium +/- vanadium minerals encountered in local uranium occurrences of the Grants Mineral Belt; although only a minor total of the minerals described from the sandstone-hosted ores of the Grants region, the mineral assemblages have been used to interpret the various geochemical conditions that engendered the observed complex mineral associations. Table 1 defines the uranium and associated minerals identified in this study, with their chemical formulas for reference.

High-grade ore from Jackpile and St. Anthony mines hosted in the Jackpile Member of the Morrison Formation consist of coffinite and uraninite, with numerous oxidized uranium species identified at the Jackpile mine (Kelley et al., 1967). The majority of the samples analyzed for this study were collected from the St. Anthony mine, as Westwater Resources permitted sampling of the reduced black ore and yellow, oxidized, and post-mining uranium minerals.

The coarse grain arkosic-arenites of the Mt. Taylor mine and quartz-arenite of the Section 31 mine, hosted in the Westwater Canyon Member of the Morrison Formation, were analyzed via XRD, electron microprobe, thin and polished section petrography to determine the presence of reduced uranium minerals and other metals associated with this deposit type. XRD methods were utilized to determine the oxidized uranium phases associated with reduced uranium mineralization.

Samples from the Piedra Triste Mine were taken from the “crinkly” zone (McLaughlin, 1963) within limestone of the Luciano Mesa Member of the Todilto Formation; oxidized uranium-vanadium minerals occurring as fracture coatings in Piedra Triste ores were analyzed by XRD methods.

Table 1: Minerals identified in this study, with their respective chemical formulas.

Group	Mineral Name	Formula
Silicate	Coffinite	$U(SiO_4)_{1-x}(OH)_{4x}$
Oxide	Uraninite	UO_2
Hydroxy-Oxide	Schoepite	$(UO_2)_8O_2(OH)_{12} \cdot 12H_2O$
	Meta-Schoepite	$UO_3 \cdot 1-2H_2O$
	Studtite	$[(UO_2)O_2(H_2O)_2](H_2O)_2$
Uranyl-Sulfate	Zippeite	$K_4(UO_2)_6(SO_4)_3(OH)_{10} \cdot 4H_2O$
	Natrozippeite	$Na_4(UO_2)_6(SO_4)_3(OH)_{10} \cdot 4H_2O$
	Jachymovite	$(UO_2)_8SO_4(OH)_{14} \cdot 13H_2O$
Uranyl-Phosphate	Autunite	$Ca(UO_2)_2(PO_4)_2 \cdot 10H_2O$
	Meta-Autunite	$Ca(UO_2)_2(PO_4)_2 \cdot 2-6H_2O$
	Meta-Ankoleite	$K_2(UO_2)_2(PO_4)_2 \cdot 6(H_2O)$
	Chernikovite	$(H_3O)_2(UO_2)_2(PO_4)_2 \cdot 6(H_2O)$
	Phurcalite	$Ca_2(UO_2)_3O_2(PO_4)_2 \cdot 7(H_2O)$
	Sabugalite	$HA(UO_2)_6(PO_4)_4 \cdot 16H_2O$
Uranyl-Carbonate	Andersonite	$Na_2Ca(UO_2)(CO_3)_3 \cdot 6H_2O$
	Cejkaite	$Na_4(UO_2)(CO_3)_3$
	Oswaldpeetersite	$(UO_2)_2CO_3(OH)_2 \cdot 4(H_2O)$
Uranyl-Vanadate	Carnotite	$K_2(UO_2)_2(VO_4)_2 \cdot 3H_2O$
	Meta-Tyuyamunite	$Ca(UO_2)_2(VO_4)_2 \cdot (3-5)H_2O$
Sulfate	Gypsum	$CaSO_4 \cdot 2H_2O$
	Hexahydrate	$MgSO_4$
	Hydronium-Jarosite	$(H_3O)Fe_3(SO_4)_2(OH)_6$
	Natrojarosite	$NaFe_3(SO_4)_2(OH)_6$
	Minasragrite	$(VO)SO_4 \cdot 5H_2O$
Vanadate	Magnesiopascoite	$Ca_2MgV_{10}O_{28} \cdot 16H_2O$
Carbontate	Calcite	$CaCO_3$
Sulfide	Pyrite	FeS_2
Molybdate	Ilsemanite	$Mo_3O_8 \cdot n(H_2O)$
Native Metal	Selenium	Se

4.1 Reduced Uranium-Vanadium Minerals

Reduced mineralization occurring in the Grants Mineral Belt has been defined by various authors as predominantly organo-uranium complexes (McLemore, et al., 2002); higher grade zones contain fine-grained coffinite with lesser uraninite (Kelley et al., 1967; Squyers, 1979). The following samples selected for this study were analyzed to confirm the presence of uranium-bearing minerals identified, and to describe minerals not previously observed in the selected deposits. Table 2 outlines the reduced uranium minerals identified by XRD and polished petrographic analysis encountered in this study. Host-rock constituents and alteration products were also identified in this analysis and are listed in Table 5 (Page 40).

Table 2. Summary table of the identified reduced uranium mineralization and associated metals through XRD, polished section petrography, and microprobe analyses. The mineraloid pitchblende from the Midnight Mine in Washington state was analyzed for comparison analysis to determine the presence of pitchblende however, no pitchblende was identified in this study.

Sample Location	Number	Uranium Minerals	Mo, Se, V, Fe
Jackpile Mine	JP1	Coffinite [■]	-
	JP2	Coffinite [■]	Pyrite [■]
	JP3	Coffinite [■]	Pyrite [■]
Mount Taylor Mine	MT1	Coffinite ^{*■} , Uraninite [*]	Pyrite [*]
	MT3	Coffinite ^{*■}	Ilsemanite [^] , Native Se [^] , V [^]
St. Anthony Mine	STA3	Coffinite [*]	-
	STA5	Coffinite [*]	Pyrite [*]
	STA12	Coffinite [■]	-
	STA13A	Coffinite [■]	-
	STA18	Coffinite ^{*■} , Uraninite ^{*■}	Pyrite [*]
Section 31 Mine	KM2	Coffinite [*] , Uraninite [^]	Pyrite [*] , Jarosite [■]
	KM3	-	Pyrite ^{*■}
Midnight Mine (WA)	MD1	Pitchblende [■] , Uraninite [■]	-
	MD2	Pitchblende [■] , Uraninite [■]	-

■ -Indicates XRD Analysis

* -Indicates polished section petrography

^- Indicates microprobe analysis

Jackpile Mine

Samples JP1, JP2, and JP3

Kelley et al., (1967) describes the ore from the Jackpile mine as 80% black oxidized uranium complexes, and “coffinite and uraninite [are] relatively more abundant in the higher-grade zones.” Analysis of the carbonaceous matter in the JP samples (Fig. 5) suggests the presence of coffinite within the sandstone, consistent with the observations from Kelley et al., (1967). See also Adams et al., 1978 and Adams and Saucier, 1981 for detailed description of Jackpile Mine host-rocks and alteration assemblages. Because uranium mineral concentrations in samples collected for this study were uniformly scant, pre-concentration of uranium minerals through sieving was necessary to improve the presence of minerals other than coffinite, especially in high-grade core samples of JP2 and JP3. Coffinite in these samples is poorly crystallized (Fig. 6). Samples JP2 and 3 also contain lesser amounts of pyrite, not observed in JP1. The presence of pyrite is consistent with the observations of Adams et al. (1978).



Figure 5: Hand sample of JP1. Black carbonaceous matter cementing the sandstone was analyzed by XRD and confirms the presence of the mineral coffinite.

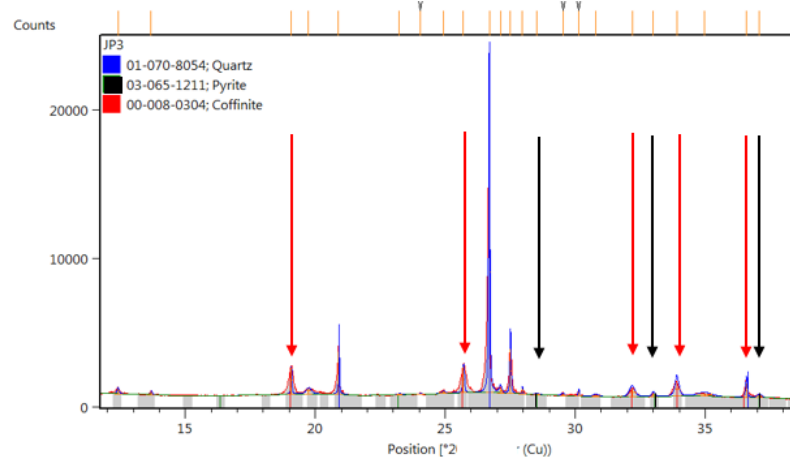


Figure 6: Diffractogram of sample JP3. Of the reduced mineralization analyzed in this study, the Jackpile samples present some of the most intense coffinite (red arrows) peaks. The mineral is poorly crystallized, evidenced by the peak broadening. Pyrite (black arrows) is present in lesser quantities.

Mt. Taylor

Sample MT1

Visual observations of the hand sample indicate the mineralization is hosted in the carbonaceous matter filling the pore space of the host-rock (Fig. 7). Core sample MT1 was analyzed via XRD, which indicated poorly crystalline coffinite (Fig. 8). A polished-block microprobe mount of the core examined using standard reflected-light microscopy identified uranium-bearing minerals as coffinite with poorly-crystallized, atoll-like uraninite (“pitchblende”) overgrowths (Fig. 64; Ono, 2001), complementing the XRD analysis. Initial microprobe results also confirm coffinite, as microprobe analyses show as U and Si have a ratio of approximately 1:1, generally consistent with coffinite $[\text{U}(\text{SiO}_4)_{1-x}(\text{OH})_{4x}]$. Pyrite is also present as euhedral, 10-20 micron-scale grains (Appx. 1, Fig. 65).

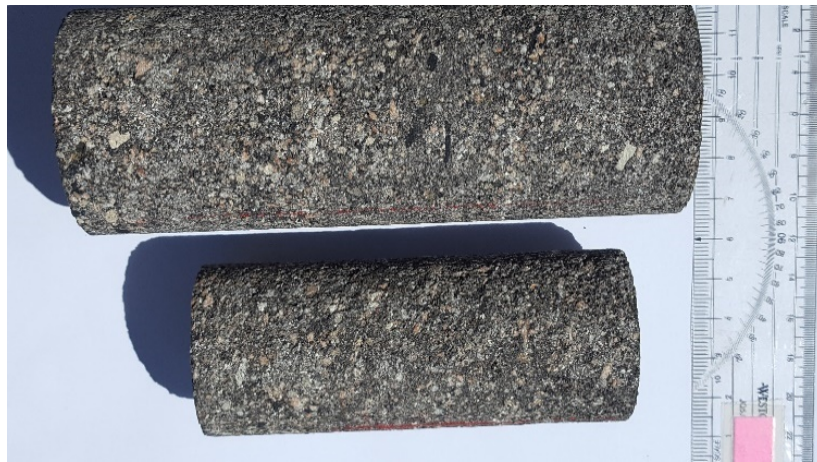


Figure 7: Host-rock of MT1 is a coarse-grained, arkosic sandstone. Note abundant pink microcline grains and white, chalky former plagioclase grains altered to kaolinite.

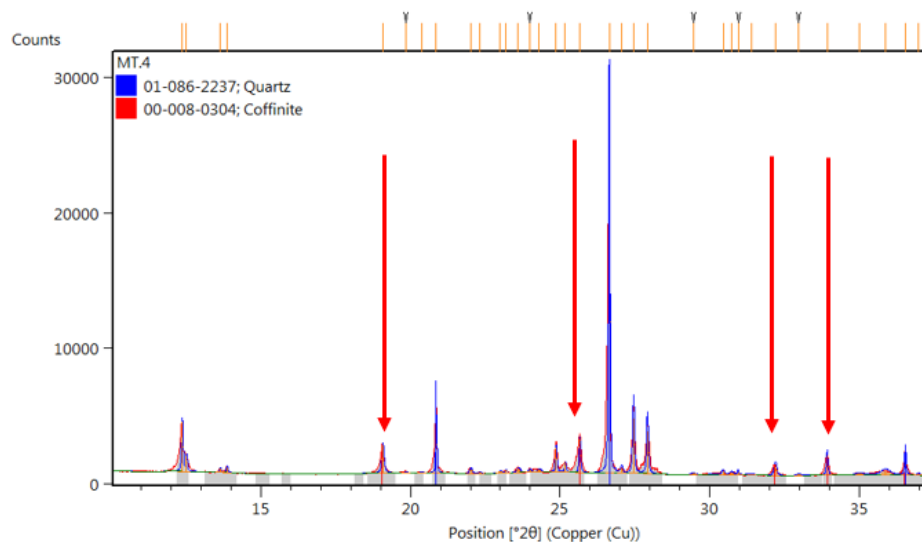


Figure 8: Diffractogram pattern of core sample MT1. In contrast to the Jackpile samples, pyrite was not identified by XRD, but was observed during polished-block petrographic analysis.

Sample MT3

This hand sample (Fig. 9) comprises carbonaceous matter filling pore space of an arkosic sandstone host-rock. McLemore et al. (2002) categorized the ore as organo-uranium complexes. XRD analysis identifies weakly crystallized coffinite; during preparation of a polished probe mount, a dark blue, waxy precipitate was observed on the sample (Fig. 10). Initial XRD analysis indicated iriginite as the molybdenum phase present, but microprobe analysis is consistent with the mineraloid ilsemaninite ($\text{Mo}_3\text{O}_8 \cdot n\text{H}_2\text{O}$) (Appx. 3, Table 48). In addition, microprobe analysis also identifies scant uranium, vanadium, and selenium; notably, uranium and vanadium have an inverse relationship such that greater uranium content is inversely related to vanadium. This relationship is not observed with uranium and selenium.



Figure 9: Sample MT3 consisting of dark, carbonaceous material impregnating arkosic sandstone. XRD analysis shows the presence of poorly crystallized coffinite, displayed through broad peaks in Figure 79.



Figure 10: Precipitation of ilsemaninite occurred on sample MT3 after preparation of polished probe mount for microprobe analysis. Blue arrow is cut surface for polished probe mount.

St. Anthony Mine

Samples from the St. Anthony mine collected for this study comprise lower-grade patches or pods surrounded by barren sandstone or sandstone-mudstone contacts that host irregular black to locally-oxidized uranium minerals within the Jackpile Member of the Morrison Formation. Exact collection locations can be found in Appendix 4 (Figs. 155 and 156).

Kelley et al. (1967) describe coffinite with lesser uraninite in the high-grade zones of the St. Anthony mine; organo-uranium complexes are the dominant form of uranium mineralization (Wilton, 2017). In this study, coffinite was identified in all reduced St. Anthony Mine samples, with uraninite overgrowths on some coffinite observed in polished sections. Other prominent minerals identified in the reduced mineralization study include pyrite, kaolinite, illite, and other clay minerals (Chapter 5).

Sample STA 3

This sample was collected at a sandstone and mudstone lens contact, as shown in Figure 11. A uranium phase was identified as coffinite, with quartz and microcline as host-rock constituents. A polished probe mount was made from the same material; petrographic study shows very fine-grained coffinite with uraninite overgrowths mixed in with the carbonaceous material (Appx. 1, Fig. 69).

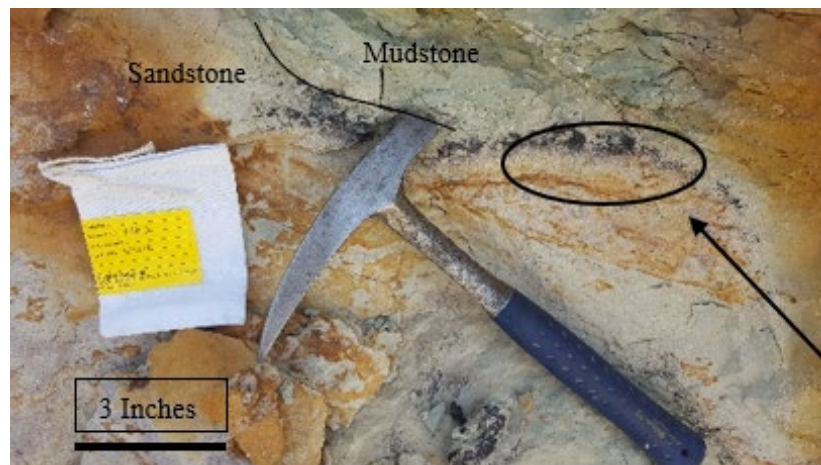


Figure 11: Sample STA3 location. The majority of reduced samples from St. Anthony were collected in horizons similar to Figure 11. With the exception of sample STA3 and 18, horizons are between 1 and 6 inches in thickness.

Sample STA5 (reduced)

The arkosic sandstone consists of large, sub-rounded quartz grains, with lesser feldspar. The mineral identified from this sample is coffinite, and occurs within the carbonaceous material coating grains and filling available pore space. Figure 12 below shows coffinite that appears to be fractures, likely caused during collection of the sample.

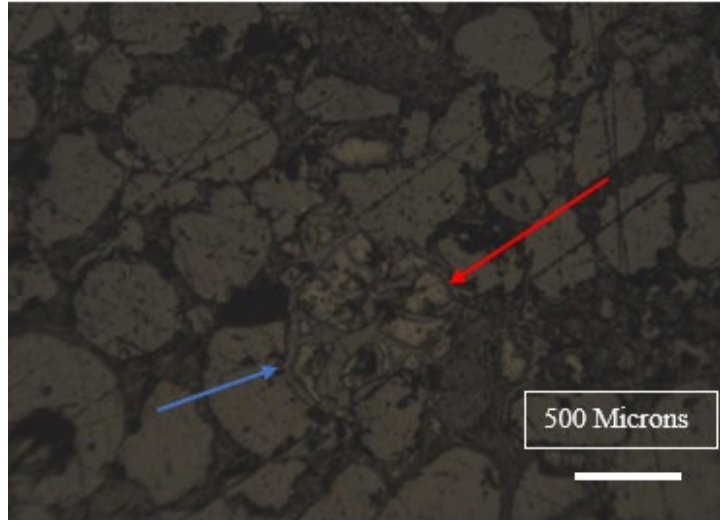


Figure 12: Polished probe mount showing the mineral coffinite (red arrow), with epoxy (blue arrow) preserving the fractured coffinite. Photo at 4x magnification.

Sample STA13A

Samples from this location are such that sample STA 13B is located directly above STA 13A, separated by six inches of barren sandstone (Appx. 1, Fig. 56); the lower sample comprises a one-inch band of reduced mineralization, while the upper unit contains a cement of calcite and trace hematite.

XRD analysis of sample STA 13A (Fig. 13, left) contains weakly crystalline coffinite (Fig. 14). The arrows in the XRD scan point to the broad, low intensity peaks of coffinite. Diffractogram for sample STA13B is located in Appendix 2 (Fig. 125).



Figure 13: Sample STA 13A and B. The reduced sandstone-hosted mineralization of STA13A (left) occurs beneath sample STA13B (right). Note the completely oxidized nature of STA13B, comprised primarily of quartz, kaolinite, and calcite, with hematite-staining.

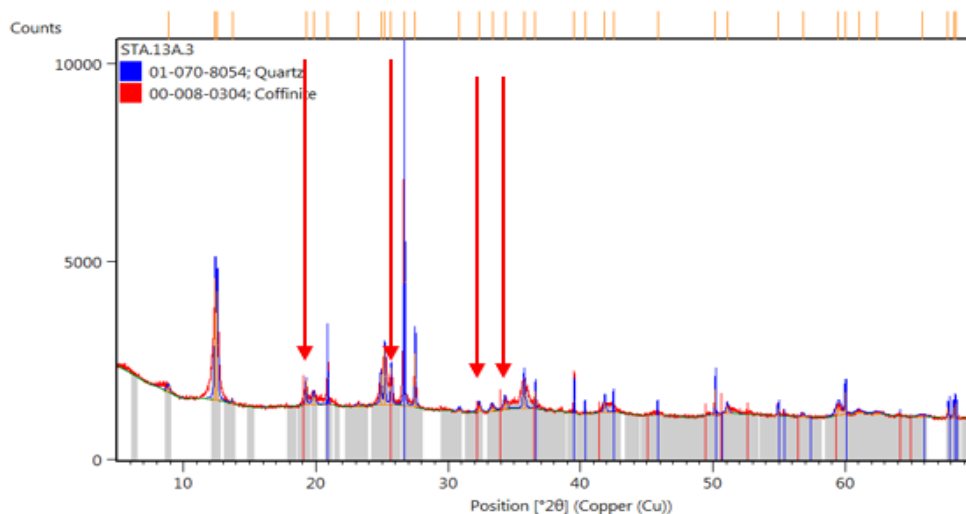


Figure 14: Diffractogram of sample STA13A. Red arrows point out the highest intensity coffinite peaks.

Sample STA18

Sample STA 18 was collected from a small pod in the north pit (Appx. 1, Fig. 60). This reduced-mineral pod was found to display substantial radiometric counts using a field-portable scintillometer; the hard, compact mineralization (Fig. 15) displays high intensity coffinite peaks with lesser uraninite peaks in its diffractogram (Fig. 16). Optical petrography of the sample identified very fine-grained, euhedral pyrite present within this coarsely-crystalline mineralization (Fig. 17). In contrast to the Section 31 and Jackpile samples, the pyrite present in St. Anthony is scarce and very fine-grained. Figure 16 illustrates the abundant coffinite observed in optical petrography of sample STA18. This sample is the only one collected for this study from St. Anthony containing uraninite, which is very poorly crystallized; this mineral occurs in lesser quantities than coffinite.



Figure 15: Sample STA18 – note durable, compact nature of this sample, which was identified via scintillometer. Uraninite and coffinite were both identified by XRD and optical petrographic analysis.

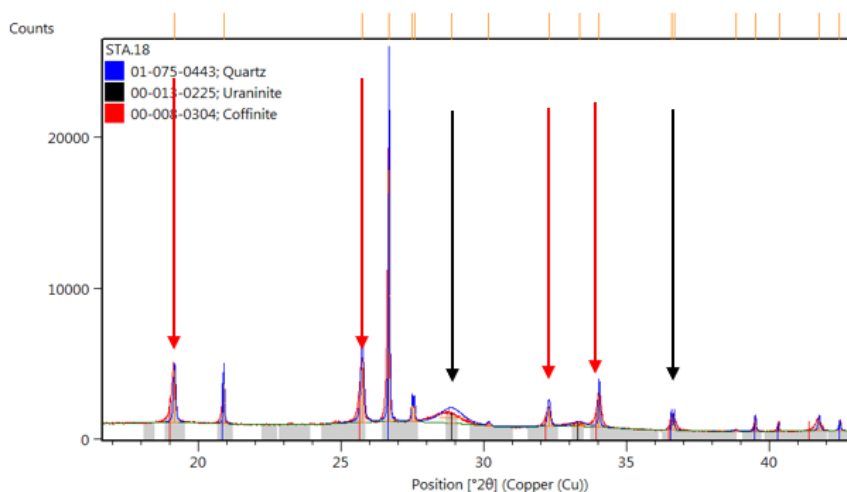


Figure 16: Diffractogram of sample STA18. The abundant coffinite produces high intensity peaks, approximately 5000 counts, though are poorly crystalline similar to the remaining STA samples.

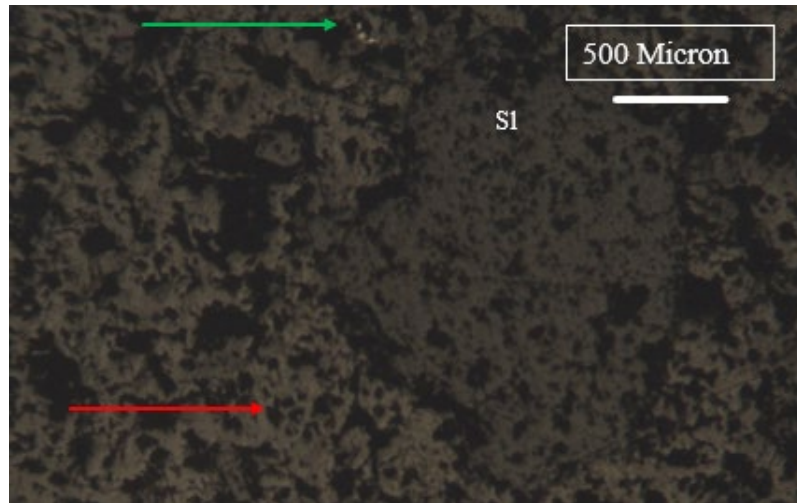


Figure 17: High-grade sample of coffinite, identified in sample STA18. Note the coarse-grained nature of the coffinite, compared to STA3 in Appendix 1, Figure 69. The silicate in the right-hand corner is quartz. 10x magnification. S1-Silicate.

Section 31

One sample of quartz arenite (Fig. 18) from the Section 31 mine was analyzed for reduced uranium mineral content in the carbonaceous cement and for uranium minerals in clay galls. Optical petrography and microprobe analysis of KM2 identify an erratic distribution of a mixed phase of coffinite with minor uraninite (Appx. 1, Fig. 68; Appx. 3, Fig. 149), with very well-crystallized, large (>100 micron), abundant, euhedral pyrite (Appx. 1, Fig. 68). XRD analysis of the carbonaceous matter (Fig. 19) displays weakly-crystallized gypsum and hydronium-jarosite. The abundant pyrite in this sample produced the low pH needed for the precipitation of hydronium-jarosite.

Clay galls were also analyzed via XRD and microprobe to determine the presence of reduced uranium minerals (Fig. 18, circle). XRD and optical petrography analysis identify pyrite and gypsum within the clay gall, finer in grain size than KM2 (Appx. 3, Fig. 150). Comparison of the weight percent of silicon to uranium from microprobe analyses reveals silicon values approximately four times that of uranium for two of three analysis points (Appx. 3, Table 50). This suggests that uranium is not present as coffinite or uraninite, but rather may comprise uranium ions adsorbed onto clay minerals. Molybdenum was also identified in trace quantities.

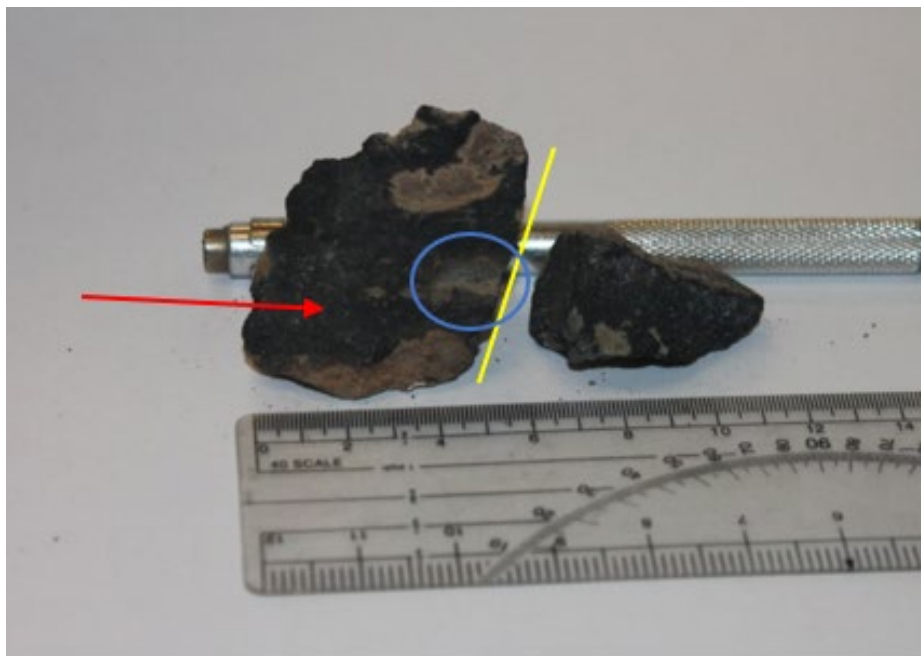


Figure 18: Carbonaceous material filling pore space hosts weakly crystalline coffinite with uraninite overgrowths (Appx. 1, Fig. 68). Abundant, well-crystallized pyrite is present in the sample, and is illustrated in Figure 68 of Appendix. 1. Red arrow is sample KM2. Yellow line is the cut from probe mount preparation. Blue circle is clay gall selected as sample KM3.

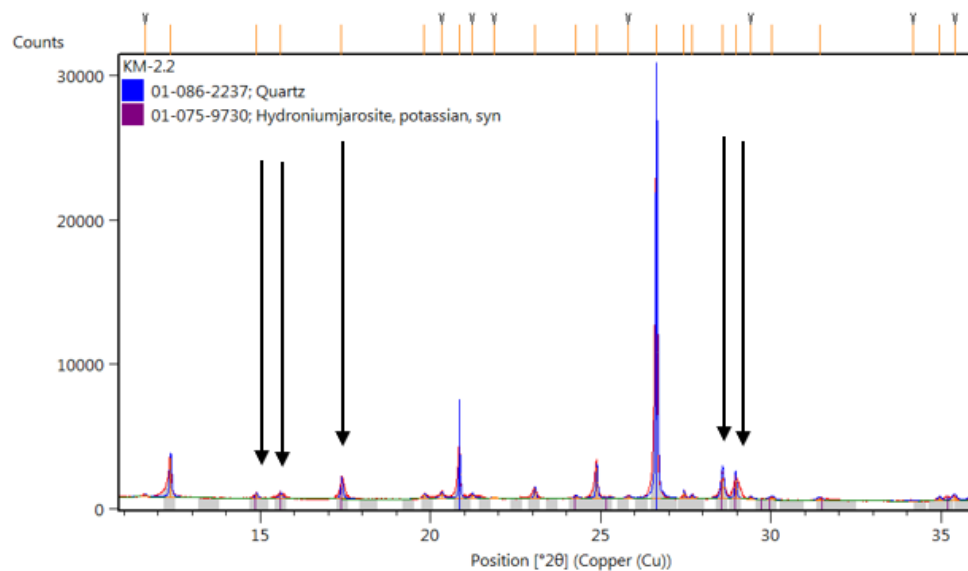


Figure 19: Diffractogram of sample KM2 showing recognizable, low intensity peaks of hydronium-jarosite. This sample also contains abundant pyrite (Appx. 1, Fig. 68) which would aid the organic matter in lowering the pH enough to produce jarosite (Jennings and Leventhal, 1987).

4.2 Oxidized Uranium - Vanadium Minerals

Oxidized uranium +/- vanadium minerals are complex associations comprising a series of oxyanion-associated mineral assemblages. Tables 3 and 4 summarize the oxidized uranium phases identified in this study, with Table 4 focusing on the St. Anthony mine occurrences. All minerals shown in Table 3 consist of fracture coatings and crusts, except Westwater Canyon 1, which comprises grain coatings within the host quartz arenite.

Table 3: Oxidized uranium minerals identified in this study via XRD. Sample MT2 contains the most diverse uranium mineralogy, comprising sulfates and hydroxyl-oxide uranium minerals. However, other minerals (excluding host-rock minerals) have been identified, including gypsum occurring with the carbonate andersonite in sample KM1.

Sample Location	Number	Uranyl-Sulfate	Uranyl-Carbonate	Uranyl-Vanadate	Hydroxy-Oxide
Westwater Canyon Member	1			Carnotite*	
Piedra Triste Mine	PT1			Meta-Tyuyamunite*	
	PT2			Meta-Tyuyamunite*	
	PT3			Meta-Tyuyamunite*	
Section 31 Mine	KM1		Andersonite*		
Mt. Taylor Mine	MT2	Natrozippeite*, Jachymovite			Schoepite
	MT5	Jachymovite* ^T			

* -Indicates dominant uranium mineral in sample

^T -Indicates uranium mineral present in trace quantities

Westwater Canyon Member

A sample of fine-grained quartz arenite from the Westwater Canyon Member of the Morrison Formation was analyzed using XRD to determine the oxidized yellow mineral coating the quartz grains (Fig. 20). XRD analysis identifies the uranyl-vanadate carnotite $[K_2(UO_2)_2V_2O_8 \cdot 3H_2O]$ (Fig. 21), with other minerals including quartz and clays; these attendant minerals are discussed in Chapter 4.



Figure 20: Observe the fine-grained nature of the carnotite (yellow) coating grains of the fine-grained quartz arenite host-rock.

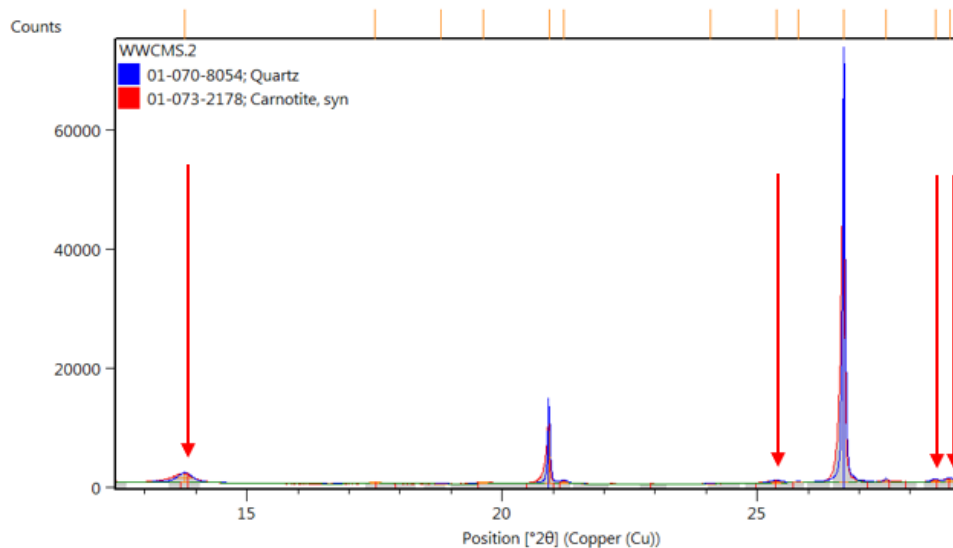


Figure 21: Diffractogram of a sample from the Westwater Canyon Member of the Morrison Formation. Notice the very low intensity, broad carnotite peaks. This poorly crystalline carnotite occurs as grains coatings in the sandstone, which is volumetrically much less abundant than quartz in the host-rock.

Piedra Triste Mine

Samples PT1, PT2, and PT30

These samples comprise limestone-hosted, straw-yellow oxide coatings hosted by the Jurassic-age Todilto Formation. McLemore (2002) describes the ore minerals present at Piedra Triste, with no mention of meta-tyuyamunite. Fracture coatings on limestone hand-specimens from the Piedra Triste mine were analyzed by XRD, with samples PT1 (Fig. 22) and PT2 (Appx. 1, Fig. 46) occurring on the sample; the mineralization on either side of the sample appeared to consist of differing minerals. XRD analysis (Fig. 23) for all samples indicate that the yellow coatings are meta-tyuyamunite $[\text{Ca}(\text{UO}_2)_2(\text{VO}_4)_2 \cdot 3(\text{H}_2\text{O})]$. Although analysis of these samples also indicates the presence of calcite, no uranyl carbonate minerals were detected from this suite.

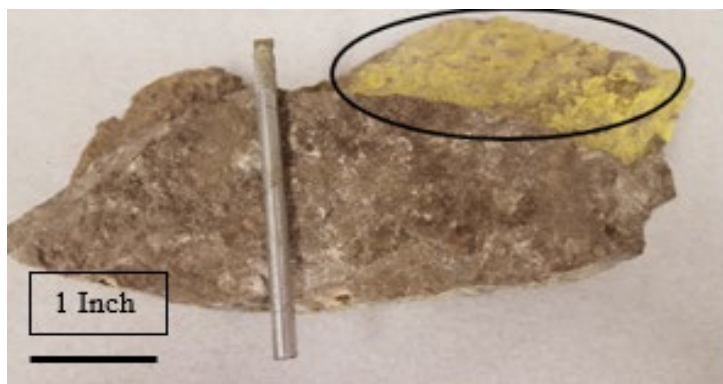


Figure 22: Jurassic-age Todilto Limestone host-rock with meta-tyuyamunite coating fractures. Sample PT2 was collected from the back side, and is pictured in Appendix 1, Section 1. The host-rock comes from the “crinkly” member (McLaughlin, 1963) of the Todilto Formation, is micritic, and possesses a fetid odor.

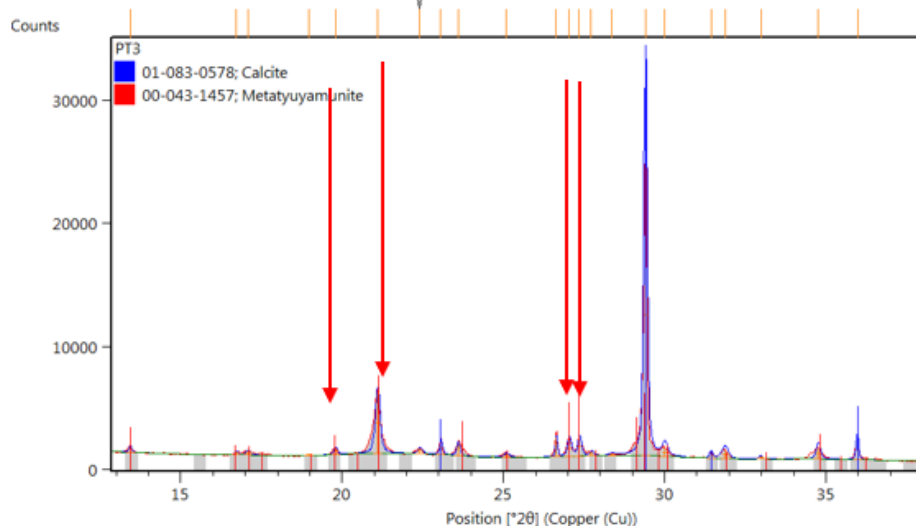


Figure 23: Diffractogram of sample PT3, pictured in Appendix 1 (Fig. 47). Meta-tyuyamunite is greater in abundance than most oxidized uranium minerals analyzed in this study, though still poorly crystallized, evidenced by the broad peak shapes. Red arrows point to highest intensity peaks for meta-tyuyamunite. Diffractograms for samples PT1 and PT2 are located in Appendix 2.

Section 31 Mine

Sample KM1 reflects a distinctly different mineralogy (uranyl-carbonate) from the other samples in this study (Fig. 24). XRD analysis identifies well-crystallized andersonite as the dominant mineral, with lesser gypsum (Fig. 25). Visual observation of the hand sample identifies the gypsum occurs only on the surface of andersonite.

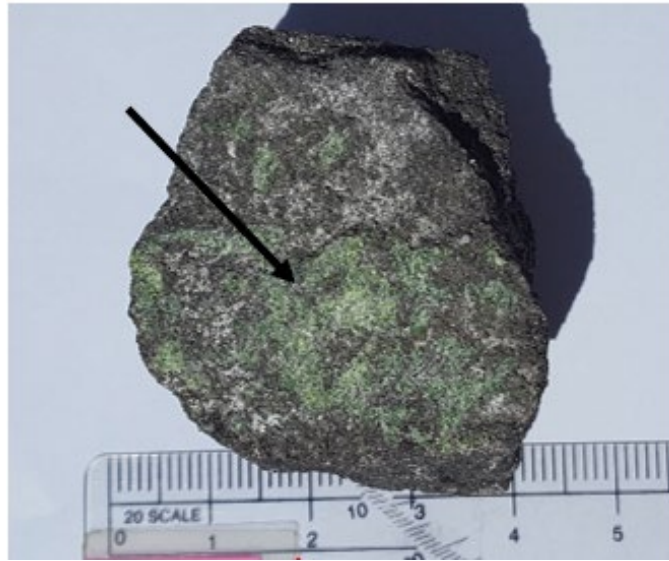


Figure 24: Green coating of andersonite and gypsum from the Section 31 mine. The white mineral present is the alteration of feldspar to kaolinite, not gypsum.

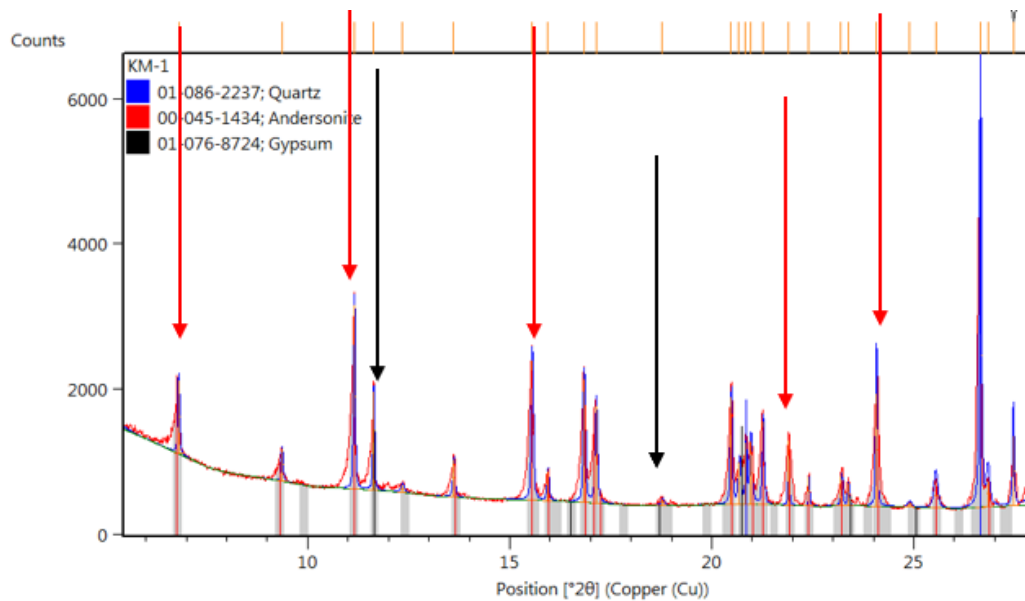


Figure 25: Diffractogram of Sample KM1, displaying abundant, well-crystallized andersonite with lesser gypsum.

Mt. Taylor

Sample MT2

Samples collected from underground exposures in the Mt. Taylor mine were analyzed to compare both reduced and oxidized uranium species with others identified from this study. Sample MT2 was analyzed for the yellow mineral coating the hand sample shown in Figure 26. XRD analysis indicates poorly-crystalline natrozippeite $[\text{Na}_4(\text{UO}_2)_6(\text{SO}_4)_3(\text{OH})_{10} \cdot 4(\text{H}_2\text{O})]$ as the dominant phase, with lesser schoepite $[(\text{UO}_2)_8\text{O}_2(\text{OH})_{12} \cdot 12(\text{H}_2\text{O})]$ and jachymovite $[(\text{UO}_2)_8(\text{SO}_4)(\text{OH})_{14} \cdot 13(\text{H}_2\text{O})]$ (Fig. 27).



Figure 26: Hand sample from the Mt. Taylor mine. Observe the vibrant yellow mineral coatings on the arkosic arenite. Scrapings were taken from the entirety of the sample to ensure even collection.

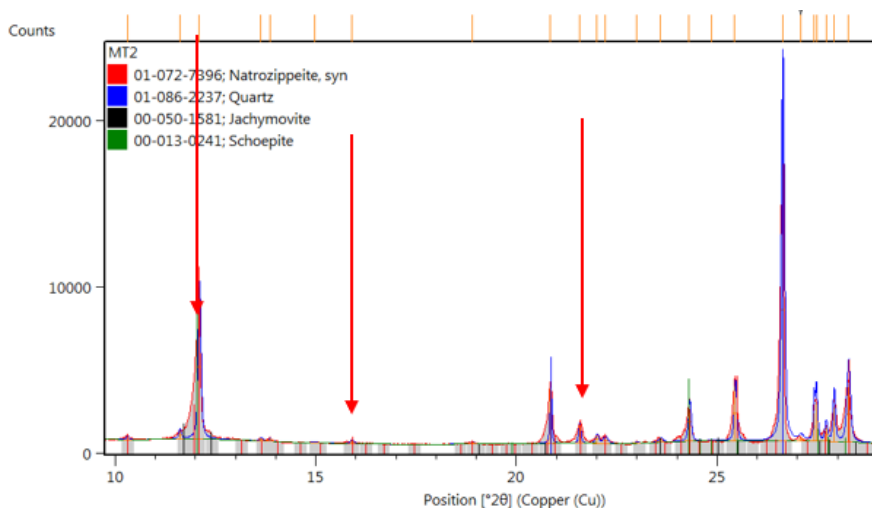


Figure 27: Graphic XRD scan of sample MT2 highlighting the dominant uranium phase, natrozippeite. Arrows point to top intensity peaks for natrozippeite. Diffractograms including schoepite and jachymovite are shown in Appendix 2 (Fig. 77).

Sample MT5

This sample differs greatly from others in the Mt. Taylor suite. Visual observation indicates a smaller amount of carbonaceous matter filling pore space than the others from Mt. Taylor, while scintillometer counts are much lower as well, close to the levels observed in the barren sandstone of St. Anthony. There is a very thin, dark-yellow, oxidized uranium mineral occurring as small patches on the hand sample (Fig. 28). XRD analysis indicates trace quantities of poorly-crystallized jachymovite $[(\text{UO}_2)_8(\text{SO}_4)(\text{OH})_{14} \cdot 13(\text{H}_2\text{O})]$, shown in Figure 29. Qualitative analysis of uranium using a microprobe for sample MT5 displays very low concentrations of uranium (Appx. 3, Table 49), as 0.23 Wt% UO_2 was measured. Comparatively, the element map of uranium in sample MT5 is lower in intensity than for MT3. Molybdenum is also present in this sample as ilsemanite (Appx. 3, Table 49), again in much lower concentrations than MT3.



Figure 28: Hand sample from the Mt. Taylor mine. Oxidized mineralization is extremely fine-grained as a yellow-green crust limited only to surficial patches. To determine reduced uranium mineralogy, a sample was prepared as a polished mount for microprobe analysis.

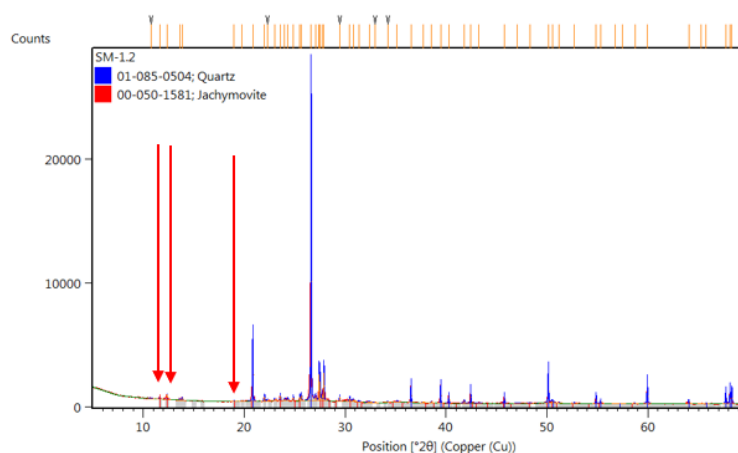


Figure 29: Graphic XRD scan showing the trace amount of jachymovite compared to quartz in intensity. Red arrows show most intense jachymovite peaks.

4.3 St. Anthony Mine Focus

The samples collected from the St. Anthony mine occur in the Jackpile Sandstone Member of the Morrison Formation (Owen et al., 1984). Previous studies do not report the oxidized uranium mineral phases present within the St. Anthony mine deposit, although oxidized uranium minerals have been described in the Jackpile deposit, two miles southwest of St. Anthony, in which Kittel and others (1967) describe hydrated uranium oxides, vanadates, and phosphates; including schoepite and autunite. Table 4 summarizes the oxidized uranium minerals identified during this study for the St. Anthony mine, with samples representing the north and south open pit mine areas. Of note are the abundance of sulfates in each of the mine areas, with zippeite-series minerals and jachymovite identified in both pits, along with gypsum. Phosphates are volumetrically minor but widespread, along with scant carbonates.

Table 4: Summary of minerals identified from the St. Anthony mine in this study.

Number	Sulfate	Carbonate	Phosphate	Hydroxy-Oxide	Mo, V, Se, Fe, Other
STA1	-	Oswaldpeetersite	-	Meta-Schoepite, Studtite	Magnesiopascoite*
STA2	-	-	Meta-Ankoleite* ^T	-	-
STA4	Natrozippeite*	-	-	Meta-Schoepite, Schoepite	-
STA5	-	-	Meta-Autunite*	-	-
STA6	-	-	Phurcalite*	-	Carnotite ^T
STA7	-	-	-	Schoepite* ^T	Pyrite, Hydronium-Jarosite
STA8	Jachymovite*, Zippeite	-	-	-	Gypsum, Natrojarosite
STA9	-	Cejkaite*	-	-	Calcite
STA10	Natrozippeite*	-	-	-	Gypsum
STA11	Zippeite	-	Autunite, Sabugalite	-	Hexahydrite*, Minasragrite
STA15	Zippeite*	-	-	-	Gypsum
STA17	-	-	-	-	Carnotite ^{T*}
STA19	Jachymovite*, Zippeite	Oswaldpeetersite	-	-	Gypsum
STA21	-	-	Meta-Autunite*, Chernikovite	-	-

* -Indicates dominant mineral in sample

^T -Indicates mineral is present in trace quantities

Sample STA1

STA 1 is the only sample not personally collected by the author from the St. Anthony mine and contains mineralogy observed in only one other sample. The vibrant orange and yellow oxide minerals are a fracture coating on coarse-grained sandstone shown in Figure 30. XRD analysis of STA1 produced a complex diffractogram, with magnesiopascoite $[\text{Ca}_2\text{Mg}(\text{V}_{10}\text{O}_{28})\cdot 16\text{H}_2\text{O}]$ the dominant phase (Fig. 31). Oswaldpeetersite $[(\text{UO}_2)_2\text{CO}_3(\text{OH})_2\cdot 4(\text{H}_2\text{O})]$ is also indicated, in minor quantities and much less abundant than magnesiopascoite. Trace amounts of the uranium oxides meta-schoepite $[\text{UO}_3\cdot 1-2(\text{H}_2\text{O})]$ and studtite $[(\text{UO}_2)_2\text{O}_2(\text{H}_2\text{O})_2](\text{H}_2\text{O})_2$ are also present (Appx. 2, Figs. 96, 97, and 98).



Figure 30: Hand sample of the vibrant minerals characteristic of oxidized uranium and vanadium. Black circles indicate sample areas. The bright orange magnesiopascoite dominates the sample, coating and therefore occurred paragenetically later than the uranium phases. The meta-schoepite beneath magnesiopascoite are also observed in other samples from the St. Anthony mine.

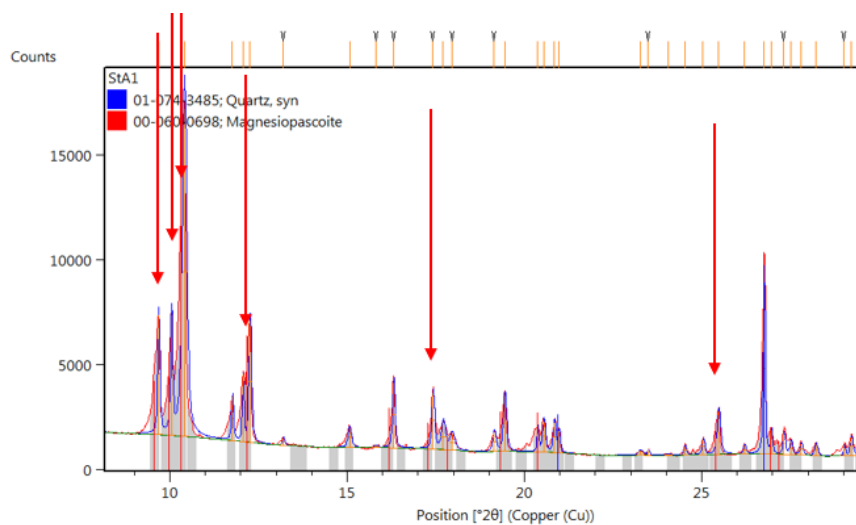


Figure 31: Diffractogram reflecting the abundance of magnesiopascoite within this sample. Arrows highlight the top intensity peaks for magnesiopascoite. Diffractograms showing the other minerals present in sample STA1 are located in Appendix 2 (Figs. 96, 97, and 98).

Sample STA 9

Sample STA 9 was collected from the highwall with no visible reduced uranium mineralization in the vicinity. The sample consists of coatings on the sandstone, preserved in an overhang of the South Pit highwall (Fig. 32). XRD analysis shows that the pale yellow mineral is the uranyl-carbonate cejkaite [$\text{Na}_4(\text{UO}_2)(\text{CO}_3)_3$], occurring with minor calcite (Fig. 33).

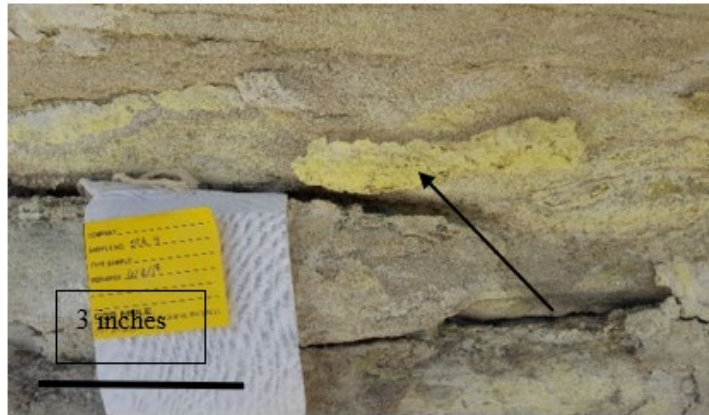


Figure 32: Overhang on South Pit highwall where sample STA9 was collected. Observe the “crusty” appearance of the sample, showing the surficial nature of the cejkaite. Sample was disaggregated during transport. The black arrow indicates the sample location.

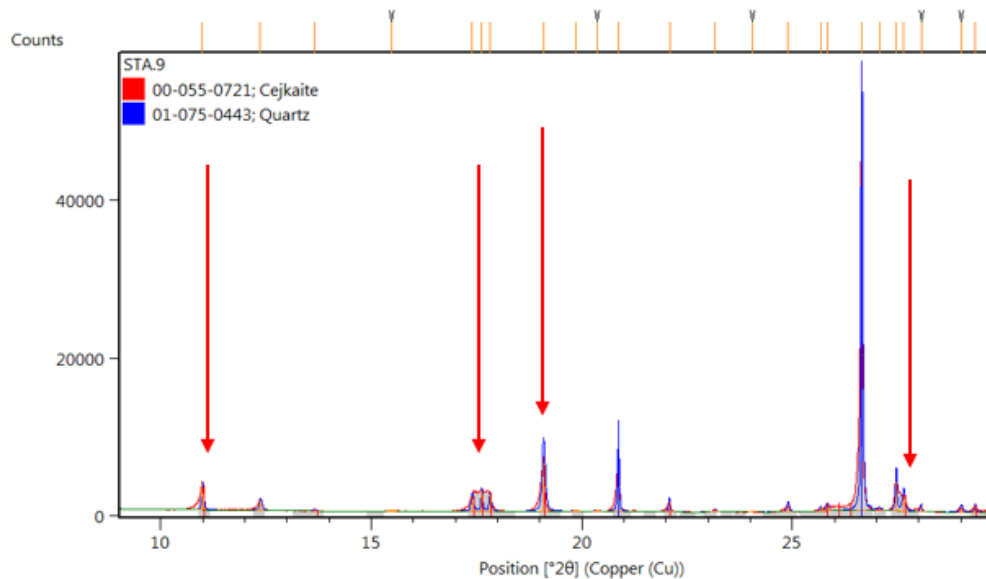


Figure 33: Diffractogram of sample STA9. The cejkaite displays recognizable peaks, however the mineral is not well-crystallized, as indicated by peak broadening.

Sample STA 11

This sample was collected from a talus slope of fine-grained sand, with no visible reduced uranium mineralization observed in the vicinity (Fig. 34). XRD analyses show that hexahydrate $[\text{MgSO}_4 \cdot 6(\text{H}_2\text{O})]$ is the volumetrically-dominant mineral in STA11, along with subordinate sabugalite $[\text{HAl}(\text{UO}_2)_4(\text{PO}_4)_4 \cdot 16(\text{H}_2\text{O})]$, autunite $[\text{Ca}(\text{UO}_2)_2(\text{PO}_4)_2 \cdot 10\text{H}_2\text{O}]$, scant zippeite $[\text{K}_4(\text{UO}_2)_6(\text{SO}_4)_3(\text{OH})_{10} \cdot 4(\text{H}_2\text{O})]$, and minor minasragrite $[\text{VO}(\text{SO}_4) \cdot 5(\text{H}_2\text{O})]$, with autunite and sabugalite highlighted in the diffractogram of Figure 35. Figures 118 and 119 in Appendix 2 display the Graphic scans of hexahydrate, zippeite, and minasragrite.

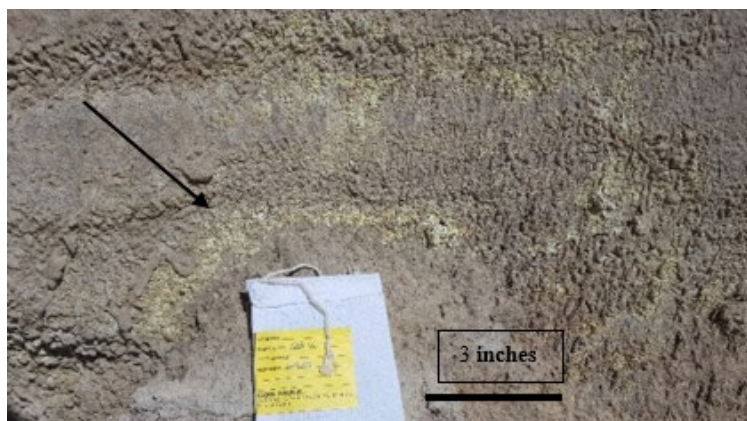


Figure 34: Sample STA11 represents minerals formed as a thin crust on the surface of the mine wall. Arrow points to collection area.

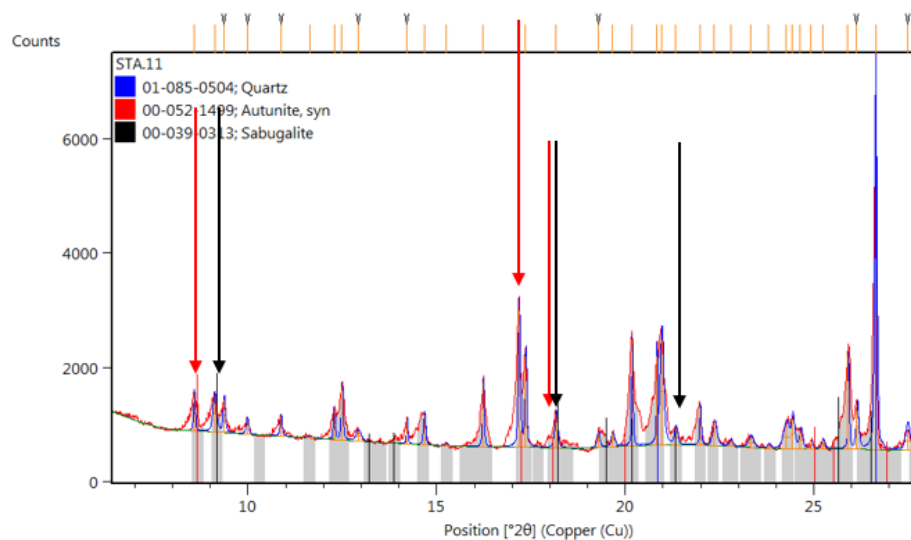


Figure 35: Diffractogram of autunite and sabugalite from STA11. Note how peaks for the uranium minerals are very broad, indicating very poor crystallinity of these minerals.

Sample STA 19

During the second round of St. Anthony mine sampling in October 2017, water was observed to be seeping down the western side of the highwall in the North Pit, with the upper part of the seeps showing yellow and white mineral precipitates. Sample STA19 was taken from the middle of the seep, shown in Figure 36. XRD analysis identifies jachymovite, zippeite, and gypsum as the dominant precipitates, with trace oswaldpeetersite, observed previously only in sample STA1 (Fig. 37).



Figure 36: Area on highwall where sample STA 19 was collected. The precipitate coats the ledge in what was identified as gypsum, with lesser jachymovite, zippeite, and trace oswaldpeetersite. Circle indicates sample location.

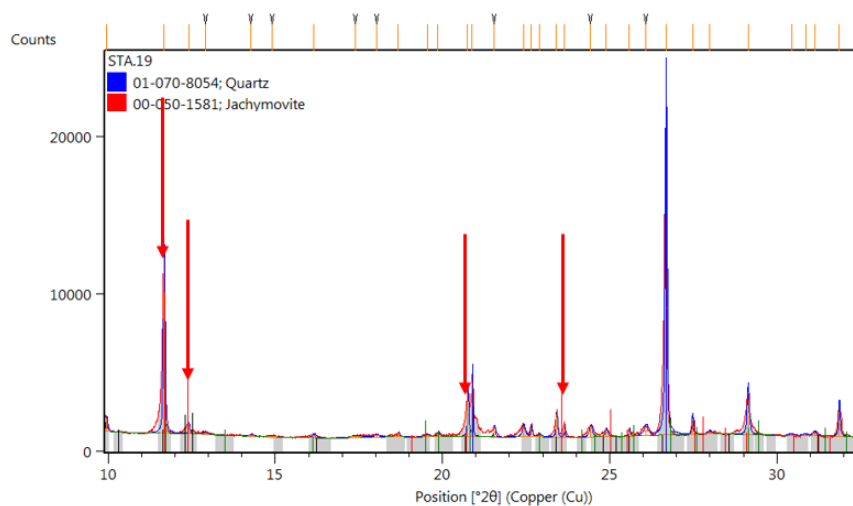


Figure 37: Diffractogram of STA19 showing jachymovite (red) as the dominant uranyl-sulfate. Zippeite and oswaldpeetersite included in Appendix 2, Figure 140.

Sample STA21

Sample STA 21, shown below in Figure 38, features a bright yellow mineral collected from a lens of reduced uranium mineralization. The mineral occurred as a very thin (2-3mm) lens approximately one foot along the reduced horizon (Appx. 1, Fig. 51). XRD analysis of the yellow mineral is consistent with the calcium uranyl-phosphate meta-autunite $[\text{Ca}(\text{UO}_2)_2(\text{PO}_4)_2 \cdot 2-6(\text{H}_2\text{O})]$ and trace chernikovite $[(\text{H}_3\text{O})_2(\text{UO}_2)_2(\text{PO}_4)_2 \cdot 6(\text{H}_2\text{O})]$ (Fig. 39).

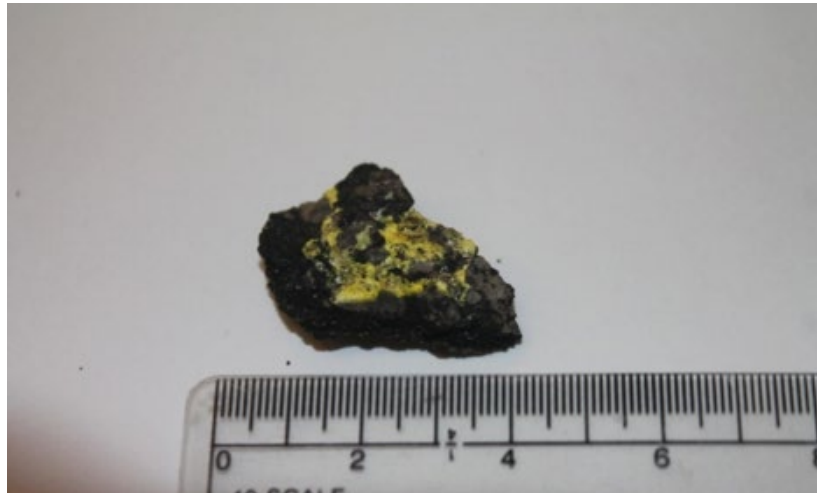


Figure 38: Note the thickness of STA21 mineralization compared to the other St. Anthony samples. The yellow minerals in STA21 are much more abundant and thicker; this indicates an oxidizing groundwater was sustained for a longer period than the majority of St. Anthony.

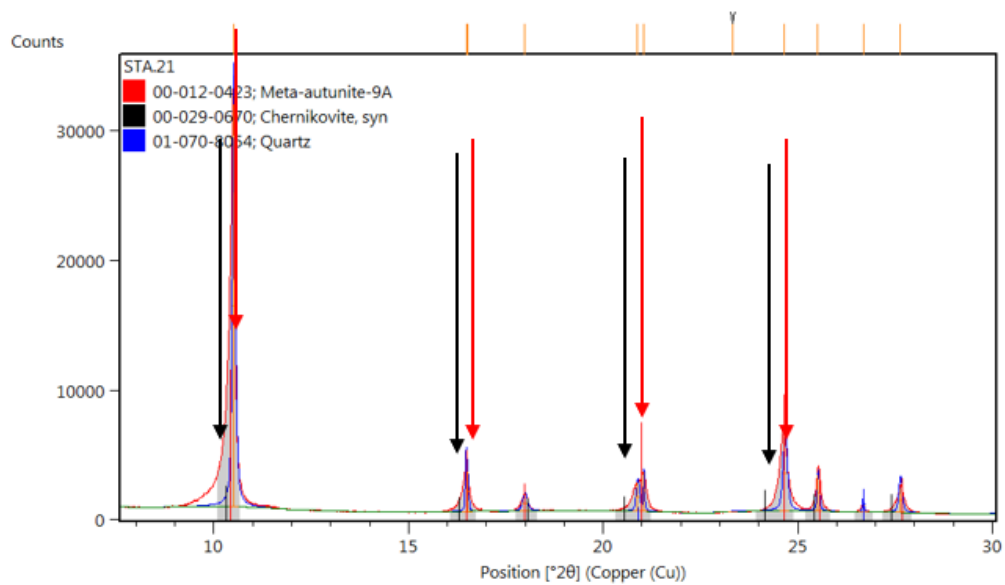


Figure 39: Diffractogram of sample STA 21 displaying the well-defined peaks of meta-autunite (red), and left-skewed peaks suggesting the presence of a trace amount of chernikovite (black).

CHAPTER 5

HOST-ROCK AND ASSOCIATED MINERALS

Sandstone-hosted uranium mineralization within the Grants region occurs dominantly in quartz- to arkosic-arenites (Austin, 1980). Within the St. Anthony sample suite, microcline and orthoclase are consistently identified, as well as their alteration products kaolinite and illite (Table 5). In areas devoid of reduced mineralization, calcite is commonly identified as the cement for the host-rock, observed in other deposits within the Grants region (Moench & Schlee, 1967). Gypsum is a prominent accessory mineral, although minasragrite and hexahydrite are identified in small quantities within the St. Anthony North Pit (Appx. 4, Fig. 153).

Table 5: Summary table of host-rock constituents and other common associated minerals identified in this study. The dominant clays identified in this study consist of kaolinite and illite. Unless noted, all minerals were identified via XRD analysis.

Sample Location	Number	Primary Host-rock Constituents	Clays	Other Minerals
Jackpile Mine	JP1	Quartz, Microcline	Illite	-
	JP2	Quartz, Microcline, Albite	Illite, Kaolinite	Pyrite
	JP3	Quartz, Microcline	Illite, Kaolinite	Pyrite
Mt. Taylor Mine	MT1	Quartz, Microcline, Albite	Kaolinite	Pyrite*
	MT2	Quartz, Albite	-	-
	MT3	Quartz, Microcline, Albite	Kaolinite	Ilsemanite^
	MT5	Quartz, Orthoclase, Albite	Kaolinite	Ilsemanite^
Section 31 Mine	KM1	Quartz	Kaolinite	-
	KM2	Quartz	Illite, Kaolinite	Pyrite*, Jarosite
	KM3	Quartz, Orthoclase	Illite	Pyrite*, Gypsum

* -Indicates optical petrography

^- Indicates microprobe analysis

Table 5 continued

St. Anthony Mine	STA1	Quartz	-	-
	STA2	Quartz, Albite, Orthoclase	Illite, Kaolinite	-
	STA3	Quartz, Microcline, Albite	Illite	-
	STA4	Quartz, Microcline, Albite	-	-
	STA5	Quartz, Orthoclase, Albite	Kaolinite	Pyrite *
	STA6	Quartz, Microcline	Kaolinite	-
	STA7	Quartz	Illite, Kaolinite	Pyrite [*] , Hydronium-Jarosite
	STA8	Quartz	Kaolinite	Gypsum, Hydronium-Jarosite
	STA9	Quartz, Microcline	Illite, Kaolinite	Calcite
	STA10	Quartz, Microcline	Na-Illite, Kaolinite	Gypsum
	STA11	Quartz	Illite	Hexahydrite, Minasragrite
	STA12	Quartz, Microcline	Illite, Kaolinite	-
	STA13A	Quartz, Microcline	Illite, Kaolinite	-
	STA13B	Quartz	Illite, Kaolinite	Calcite, Hematite
	STA14	Quartz, Orthoclase	Illite, Kaolinite	Calcite
	STA16	Quartz, Microcline	Illite, Kaolinite	Gypsum
	STA17	Quartz, Microcline	Kaolinite	-
	STA18	Quartz, Microcline	Kaolinite	Pyrite*
	STA18A	Quartz, Microcline	Illite, Kaolinite	Calcite
	STA18B	Quartz, Microcline	Kaolinite	Calcite
	STA19	Quartz, Orthoclase	Illite, Kaolinite	Gypsum
	STA20	Quartz, Microcline, Albite	Kaolinite	-

* -Indicates optical petrography

[^]- Indicates microprobe analysis

Sample STA13B

Adams et al. (1978) describe zones of iron-oxidation adjacent to the reduced mineralization in the Jackpile deposit that consist of hematite cement with lesser siderite or other iron-carbonates. This type of oxidation has been observed throughout the Jackpile mine, even occurring above the reduced horizons. Sample STA 13B consists of a dark red horizon (Appx. 1, Fig. 56), hematite-stained quartz arenite, with kaolinite alteration of feldspars. This style of oxidation has been described by Saucier (1980), who concluded that iron-oxide staining of host-rock sandstones was the result of the oxidation of pyrite, as pyrite is more abundant in reduced uranium horizons. XRD analysis of this oxidized sample showed the presence of quartz, well-crystallized kaolinite, calcite, and trace hematite. A scintillometer analyzed the counts per minute of this sample, and returned very low counts, similar to that of barren sandstone from other areas of the St. Anthony deposits.

Carbonates and Sulfates

X-Ray Diffraction analysis also identified carbonates and sulfates within the St. Anthony sample suite that do not contain uranium (calcite and gypsum dominant, Table 5). This is further aided by thin-section analysis, where significant carbonate cement is identified in sample STA18B (Fig. 40). This occurrence of carbonate cement is common throughout the Grants region (Moench & Schlee, 1967). No carbonate was identified in areas containing reduced mineralization.

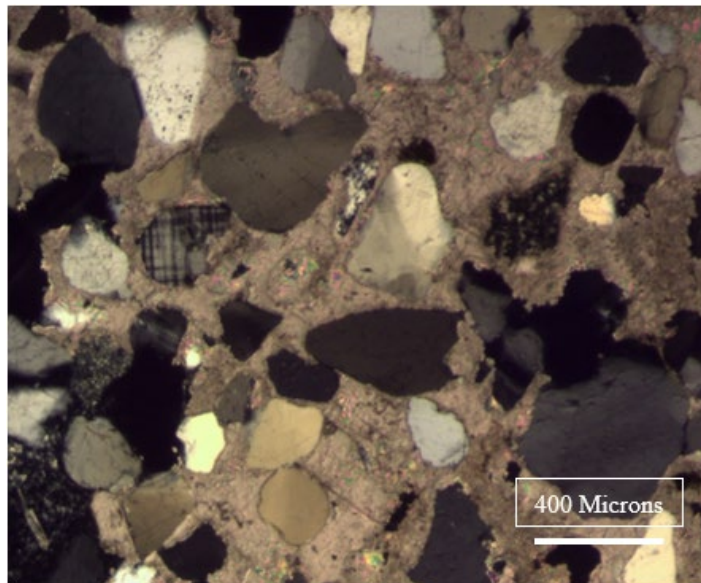


Figure 40: Thin section of STA18B, barren sandstone collected from the St. Anthony mine, North Pit. Significant carbonate cements the sandstone. Sample consists dominantly of quartz, with lesser microcline and volcanic grains. Of note is the abundance of carbonate mineral when reduced uranium mineralization is not present. 4x magnification.

Gypsum and hexahydrate were also identified by XRD analysis. Gypsum is common to the St. Anthony sample suite, as selenite, and was observed littering the bottom of the mine in both pits during sample collection. Gypsum occurrence differs greatly from calcite. It is observed with oxidized uranium minerals in the vicinity of reduced mineralization horizons, generally as a fracture coating. Calcite is not observed in reduced mineral horizons. Hexahydrate ($\text{MgSO}_4 \cdot 6\text{H}_2\text{O}$) was indicated in one XRD analysis with a variety of other uranyl-sulfates and -phosphates (Appx. 2, Fig. 118).

Clays

The clay minerals identified in this study show excellent consistency, comprised of kaolinite $[\text{Al}_2\text{Si}_2\text{O}_5(\text{OH})_4]$ and illite $[(\text{K},\text{H}_3\text{O})(\text{Al},\text{Mg},\text{Fe})_2(\text{Si},\text{Al})_4\text{O}_{10}[(\text{OH})_2 \cdot (\text{H}_2\text{O})]]$ (Table 4). These clays have been identified by multiple authors in the Grants Mineral Belt (Sachdev, 1980; Squyres, 1980) as alteration of feldspars or cementing of barren sandstone. No clay cement was observed in this study. Kaolinite generally possesses more intense diffractogram peaks than that of illite, indicating the kaolinite is greater in abundance. Thin sections from Mt. Taylor core and hand samples from the St. Anthony North Pit have weak alteration of feldspars to clay. Some clay-altered feldspars in Mt. Taylor core have a blue tint in cross-polarized light, indicating kaolinization.

Thin Section Petrography and Host-rock Characterization

Mt Taylor Core

Core samples from the Mt. Taylor orebody are medium- to coarse-grained arkosic arenites comprising fragments of quartz, rose-pink microcline, plagioclase, and volcanic shards (similar to the descriptions provided by Squyres, 1980) that possess the same radial extinction as volcanic glass. Grains are angular to sub-rounded. Importantly, the cement for this sample is dark carbonaceous matter of organo-uranium complexes (McLemore, 2002) and fine-grained coffinite (this study).

St. Anthony Mine, STA 3

This sample consists of fine to medium grains of dominant quartz, with lesser volcanic fragments, and scant K-feldspars (Appx. 1, Fig. 62), classifying the sample as a quartz arenite. Cement consists of black carbonaceous material containing weakly-crystalline coffinite.

St. Anthony STA18A

Sample consists an arkosic arenite comprising quartz (dominant), plagioclase, K-feldspar, and lesser volcanic fragments (Appx. 1, Fig. 63). Larger grains are angular to sub-rounded; smaller grains are sub-angular to well-rounded. Calcite is present as matrix cement. (Appx. 2, Fig. 136).

St. Anthony 18B

This arkosic arenite sample was taken approximately two feet from sample STA18A in the same stratigraphic unit. Grains in 18B are uniform in size and are sub-angular to rounded comprising predominant quartz, with volcanic fragments, and approximately equal parts K-feldspar and plagioclase (Fig. 40). These two distinct sandstones indicate sample STA18A scoured through the STA18B sandstones.

CHAPTER 6

DISCUSSION: GEOCHEMICAL ENVIRONMENT OF URANIUM PRECIPITATION

Many of the uranium minerals identified in this study may display multiple metals in their mineral structure in addition to uranium. Before producing possible reactions as an explanation for the presence of uranium minerals, the sources for the mineral constituents need to be explored. Alkali metal cations potassium, sodium, and magnesium are present in numerous samples as the principal cations in most of the oxidized uranium minerals encountered. Oxyanions such as phosphate and sulfate are also prominent constituents in oxidized uranium minerals, particularly at the St. Anthony Mine. As with uranium, the sources for many of these elements are debated and likely have multiple sources.

Mg, K, and Fe Sources

Regarding the possible metal sources for oxidized uranium, the following host-rock components are suggested as likely cation sources for oxidized U-V minerals. Biotite is considered in this study to be the likely source for Mg^{2+} , as well as K^+ . Riese and Popp (1980) indicate biotite alteration to chlorite is the primary source for potassium and magnesium in groundwater within the Mariano Lake deposit. Optical microscopy of thin sections from the Mt. Taylor and St. Anthony mines shows weak, inconsistent, weathering-derived alteration of microcline and orthoclase to white phyllosilicate and kaolinite (Appx. 1, Fig. 61). This kaolinization of K-feldspar releases K^+ into groundwater, providing another source for the cation. The presence of chlorite in host-rocks of the Grants region has been cited by several researchers (Squyres, 1980; Sachdev, 1980) as another source for Mg^{2+} and especially Fe^{2+} within the ore zones.

Regarding the fate of Fe^{2+} , Sachdev (1980) points out that Fe-Ti (e.g., ilmenite) minerals have been observed by multiple researchers studying the Grants region, with Fe-Ti oxides and their alteration products (e.g., anatase) the dominant heavy-mineral species within the host sandstone. Reduction and leaching of Fe^{2+} occurs in a reducing environment and can be facilitated by organic matter (Sachdev, 1980; Adams et al., 1974). In addition, Squyres (1980) notes that ferric iron was present during deposition of the Westwater Canyon and Brushy Basin Members of the Morrison Formation, which later underwent large-scale reduction to Fe^{2+} as pyrite. Iron precipitates as pyrite with uranium in reduced mineralization horizons (Gruner, 1956; Kelley et al., 1976).

Na, Ca, and Al Sources

Sodium and calcium components occurring in uranium minerals are identified in several samples, and both elements may have come from the same mineralogic source. Austin (1980) states plagioclase is the most common feldspar to be altered to white phyllosilicate, suggesting that this feldspar may be a logical source for Na^+ and Ca^{2+} ions. Most of the feldspars within the Grants region show evidence of albitization (Austin, 1980), and this study also describes kaolinization of feldspars. The release of calcium during albitization of plagioclase would not be enough to produce the extensive calcite cementing occurring in the uranium host-rock units. Sachdev (1980) suggests high-calcium bentonites, derived from volcanic ash components of parent tuffaceous material in the Poison Canyon Tongue of the Brushy Basin Member of the Morrison Formation, would liberate Ca^{2+} during devitrification, along with many of the other metals and constituent ions necessary for mineralization-alteration.

Regarding aluminum mobility in the low-temperature environment, Jennings and Leventhal (1978) state that decomposing organic matter produces humic and fulvic acids capable of lowering the local $\text{pH} \approx 2$. In rock units that host significant organic matter, the genesis of organic acids may produce conditions that engender alteration of aluminosilicates, releasing Al^{3+} . In addition, pyrite observed in Section 31 and Mt. Taylor samples suggest another source of low-pH solutions capable of liberating Al^{3+} . Although devitrification of volcanic material releases some Al^{3+} into groundwater, essentially all Al^{3+} at low temperatures will form either soluble hydroxides or clay minerals (Sachdev, 1980). In the analysis of oxidized St. Anthony uranium minerals, only the phosphate sabugalite is identified as an aluminum-bearing mineral; although sabugalite is impoverished in Al^{3+} , containing only 1.52%-wt Al^{3+} . (Fron del and Fleischer, 1955, p. 188), the presence of sabugalite suggests that aluminum was available locally during oxidation of St. Anthony reduced uranium ores, capable of mobilizing Al^{3+} .

Carbonate Source

Leventhal (1980) indicates that organic material can release CO₂ gas if it is buried deeply and heated under anaerobic conditions; however, under aerobic conditions carbonate is easily produced from decomposing organic matter (Krauskopf and Bird, 1995). Oxygenated groundwater passing through organic matter will oxidize organic matter and metals to an extent that is a function of the amount of available O₂(g); metals and carbonate ions may then be transported from the source region (or rocks), dependent on solution pH, temperature, and oxidation state. While there is abundant organic matter occurring in the Grants Mineral Belt, the majority of dissolved carbonate comes from surface waters (Tessendorf, 1980); the presence of carbonate in groundwaters serves multiple purposes in the Grants region, as it has the capability to transport uranium as a uranyl-carbonate complex ([UO₂(CO₃)₃]⁴⁻) and can precipitate uranium to form multiple minerals including uranium-carbonates, and calcite.

Phosphate Source

There are several uranyl-phosphates observed within the St. Anthony mine; with phosphate likely derived from the decomposition of apatite within the host arkosic sandstone. Moench & Schlee (1967) discuss fluorapatite, which can hold to 1% U, as a source for uranium and phosphate. Detrital apatite was observed during thin-section analysis of the Monument Project, McKinley Co. (Crook, 1979). Local acidity produced by organic material can lower pH enough to dissolve apatite and liberate phosphate into solution, where phosphate ions may comprise several components in sandstone-hosted uranium deposits: 1) phosphate can precipitate with uranium to form phosphate minerals, and complex with uranium in groundwater; and 2) biphosphate [(HPO₄)²⁻] can complex with, and therefore transport, uranium in neutral to acidic conditions (Runnells et al., 1980). However, if di- or tri-carbonate complexes are also present with the biphosphate ion, the carbonate ion is preferred by uranium as a complexing oxyanion.

Sulfate Source

Sulfur is abundant in the carbonaceous matter that hosts much of the uranium in the Grants Mineral Belt (Alder, 1963). During decomposition of organic matter, sulfur is liberated to form pyrite via bacterial mediation in the reduction of sulfate sulfur to sulfide; this process occurs during reduction of primary “tabular” deposits (Gruner, 1956). In an oxidizing environment, pyrite can decompose to produce hydrogen sulfide gas (H₂S). In deposits where organic matter is unavailable or not present, H₂S gas may provide the reduced component necessary to precipitate reduced U-minerals (Gruner, 1956; Dahlkamp, 2010). Sulfate, similar to carbonate and phosphate, can serve multiple purposes in sandstone-hosted deposits; in conditions where the pH is lower than 3, sulfate and uranium can complex and be transported as uranyl sulfate complexes (Jennings and

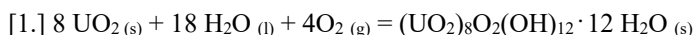
Leventhal, 1967). Uranyl-sulfate minerals would precipitate when the pH of the solution environment increases above the pH 3 that is sulfate stability.

Discussion: Reactions that Interpret the Geochemical Environment of Uranium Deposition

Because the mechanisms for precipitating uranium-bearing minerals differ for reduced/primary and redox-controlled redistributed deposits, the geochemical reactions that are proposed for the mineralogy and mineral paragenesis determined from this XRD-based study must consider field observations of occurrence of reduced and oxidized uranium minerals. The reactions below offer a possible explanation of the geochemical conditions present during uranium and associated metals precipitation. Conditions that existed during uranium ore deposit formation were more complicated than the simple reactions below, but these geochemical relationships suggest the general scope of conditions that existed as uranium mineralization developed in host arkosic sandstones.

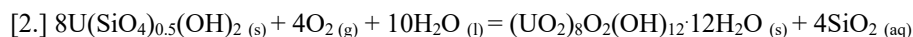
Oxidation of Uraninite, Coffinite, and Organo-Uranium Complexes

This study and many other researchers have documented the diversity of oxidized uranium minerals present in the Grants Mineral Belt. In order to produce these complex phases, the reduced minerals coffinite and uraninite, and organo-uranium complexes, are initially oxidized and hydrated to form schoepite. Because many of the uranium phases identified in this study occur as post-mining oxidation and re-precipitation, the likely cause for this re-precipitation is the evaporation of water during post-mine weathering. In this study, schoepite is identified in volumetrically minor to trace quantities and is interpreted to be the result of rapid oxidation of reduced uranium minerals (Finch et al., 1998). Uraninite is identified at the St. Anthony mine, and although in minor amounts, would be available for oxidation to produce schoepite:

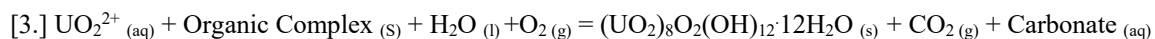


This reaction produces one mole of schoepite from 8 moles uraninite and would result in a decrease in overall rock density (uraninite=10.63g/cm³; schoepite=4.8g/cm³), meaning more space in the form of fractures or pore space would be required for the precipitation of schoepite from (replacement) uraninite. Many of the oxidized minerals identified were adjacent to a reduced uranium mineralization horizon, suggesting that the adjacent reduced mineralization supplied the uranium needed to develop schoepite and related secondary and tertiary oxide minerals. Notably, coffinite is observed as being more abundant than uraninite in the Grants District (Kelley et al., 1967) as noted in the ore deposits comprising this study; as such, coffinite will be a greater contributor of uranium to subsequent oxide minerals than uraninite, though may contribute less than the abundant organic matter observed in the region.

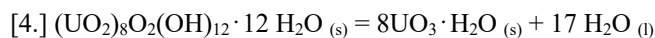
As coffinite is the dominant ore mineral in many of the mines within the Grants region, this mineral must be scrutinized for its potential to produce oxidized uranium species. Reaction 2 is a simple hydration reaction, producing schoepite and aqueous silica (SiO₂) from coffinite. Aqueous silica is produced in this reaction in preference over quartz (overgrowths on host arkosic-sandstone grains); while documented in the Grants region as banding on grains with radial extinction, (Falkowski, 1980; Squyres, 1980), there were no quartz overgrowths observed in this study, so the reaction considers silica as soluble component, potentially transported from the deposits in this study. Sachdev (1980) describes aqueous silica transported from the Poison Canyon Tongue after devitrification of volcanic ash, in alkaline groundwater. The observation of uranyl phosphates at the St. Anthony Mine suggests the involvement of very weakly alkaline to acidic groundwater (Reactions 11-15; See Jerden and Sinha (2002)) in post-deposition oxidation-alteration of St. Anthony ores (Reaction 8). Because coffinite is present in minor quantities, and because no quartz overgrowths on mineral grains were observed in sandstones associated with coffinite destruction, this mineral apparently provided limited amounts of uranium for oxidized minerals.



Coffinite and uraninite are minor, but likely, sources for oxidized uranium minerals; nonetheless carbonaceous matter is the main contributor producing oxidized uranium minerals. Organo-uranium complexes have been identified as the predominant source of uranium in the Grants region (McLemore, 2002, Wilton, 2017). Organic molecules will adsorb uranium onto its reactive surface; uranium may also be chelated by these organic molecules (Jennings and Leventhal, 1987; Krauskopf and Bird, 1995), from which the uranium can be oxidized. Reaction 3 is a generalized reaction producing schoepite from organo-uranium complexes, producing schoepite, CO_{2(g)}, and carbonate from UO₂²⁺_(aq). Because a carbonate ion is produced in this reaction from organo-uranium complexes, this reaction represents another potential source of carbonate for the transportation of uranium.



Schoepite and meta-schoepite apparently were the initial minerals from which were produced many of the diverse minerals observed in this study; this is because dehydration of schoepite is rapid following initial precipitation (Finch et al., 1998). As most of the samples were collected post-mining, these minerals apparently dehydrated to their meta(-) components, with the dehydration of schoepite to meta-schoepite is suggested in Reaction 4.



Sulfates

Uranyl-sulfates are very common in the Grants region, particularly in the St. Anthony deposit. Zippeite is among the most common uranyl-sulfate mineral identified from this study. To precipitate zippeite $[\text{K}_4(\text{UO}_2)_6(\text{SO}_4)_3(\text{OH})_{10} \cdot 4 \text{H}_2\text{O}]$, potassium, sulfate, protons and water are needed. When present, zippeite represents the removal of sulfate and potassium from groundwater although depletion of sulfate in mineralizing-oxidizing groundwaters was likely quite variable and not geochemically complete; nonetheless, if zippeite were to be re-oxidized, K^+ and SO_4^{2-} would have been made available for other minerals to precipitate, such as jachymovite $[(\text{UO}_2)_8\text{SO}_4(\text{OH})_{14} \cdot 13 \text{H}_2\text{O}]$. Under acidic conditions, uranyl-sulfate is stable and may produce uranium sulfate minerals if subjected to dehydration (Fig. 41). For the following reactions involving zippeite, a lower pH environment is selected, as the presence of several uranyl-phosphate minerals indicate lower pH groundwater in localized areas.

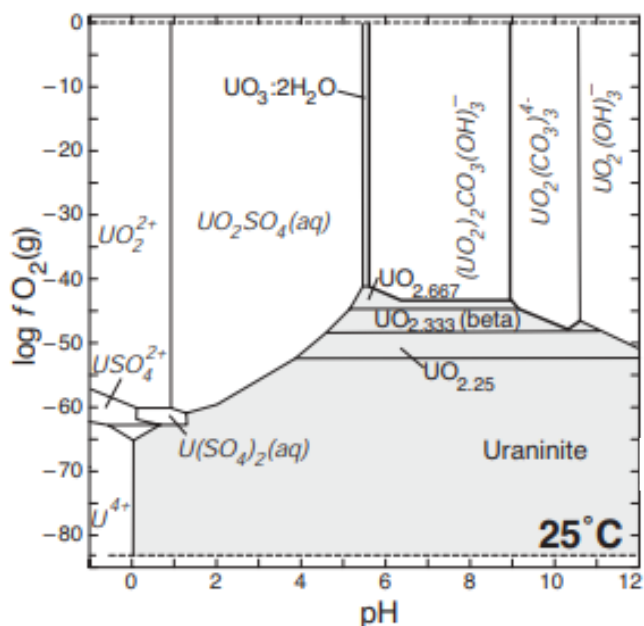
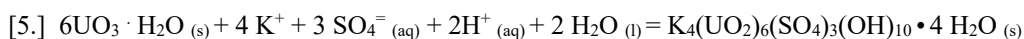
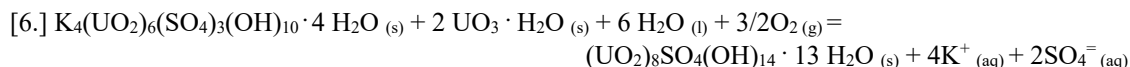


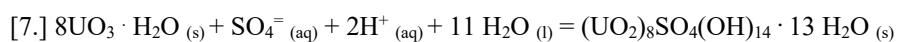
Figure 41: Eh/pH diagram displaying the stability of aqueous uranyl-sulfate and uranyl-carbonate under conditions at 25°C and 1 atmosphere of pressure, with uranium species as 10^{-5}M , sulfur species at 10^{-2}M , and carbonate species at 10^{-3}M . (Brugger et al., 2003).

Jachymovite is the second most abundant uranyl-sulfate mineral observed in this study, frequently occurring with zippeite; jachymovite can be produced at the expense of zippeite and meta-schoepite when reacted with water and oxygen. The destruction of

zippeite liberates sulfate and potassium into groundwater, allowing other sulfate minerals to precipitate.

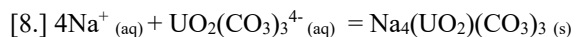


Jachymovite is observed in several samples as the only uranyl-sulfate apparently having been produced from meta-schoepite, sulfate, protons and water, as suggested in Reaction 7. The presence of jachymovite as the dominant uranium phase in areas also devoid of other uranium minerals suggests that the components to produce these complex uranium phases are not evenly distributed throughout individual deposits.



Carbonates

Uranyl-carbonates are the most volumetrically minor minerals observed in this study. Notably, the mine area from which sample STA9 was collected is characterized by ubiquitous sulfate and phosphate; nonetheless, because XRD analysis identifies the presence of cejkaite [$Na_4(UO_2)(CO_3)_3$] and calcite ($CaCO_3$), it is concluded that oxidizing solutions contained geochemically-significant carbonate in meteoric waters, representing a localized alkaline environment. Uranyl-carbonate is the preferred method of transport for uranium (Breger, 1974), while Na^+ increases the solubility of uranyl-carbonate (Gruner, 1956), meaning cejkaite is comparatively soluble. As with most of the post-mining mineralization collected in this study, it is likely that evaporation (loss of solute) is the cause for precipitation of cejkaite from very soluble uranyl-carbonate and Na^+ ions as indicated in Reaction 8.



The transportation of uranium as a carbonate is also consistent in the observation of andersonite [$Na_2Ca(UO_2)(CO_3)_3 \cdot 6H_2O$] from the Section 31 mine. This sample further illustrates the geochemical complexity of sandstone-hosted uranium; close scrutiny of the sample shows andersonite precipitating on the surface of a reduced mineralization sample, with gypsum precipitating only with and on the andersonite (Fig. 24). Figures 41 and 42 illustrate the large stability field of uranyl-sulfate (UO_2SO_4) and the alkaline-pH stability of uranyl-carbonate ($UO_2(CO_3)_3^{4-}$). Reaction 9 produces andersonite from uranyl-carbonate, sodium, calcium, and water.

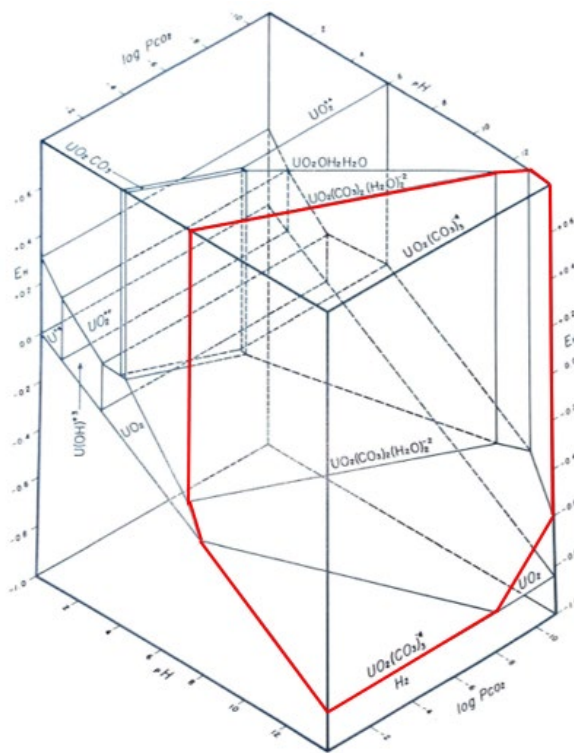
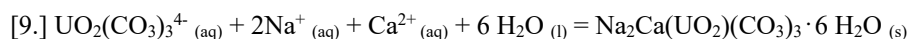


Figure 42: Phase diagram showing stability of uranyl-carbonate under certain Eh, pH, and CO₂ partial pressure conditions, at 25°C and 1 atmosphere of pressure, with total dissolved uranium species at 10⁻⁶ M. (Garrels and Christ, 1990). Red outlines the stability field for aqueous uranyl-carbonate. Note how the carbonate complex is stable under weakly acidic to very alkaline conditions.

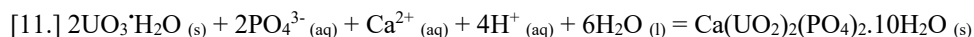
It is observed that the gypsum in sample KM1 is precipitating only on the surface of the andersonite, with gypsum likely scavenging Ca²⁺ liberated from the andersonite. Dissolution of calcite by weakly acidic waters may also provide the calcium needed in both minerals. This reaction may occur from a drop in pH below the stability for uranyl-carbonates (Fig. 42).



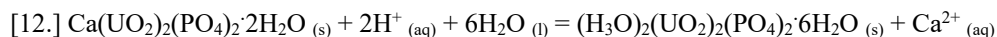
Phosphates

Uranyl-phosphates are a common oxidized mineral phase identified in the Grants region, exemplified in the St. Anthony mine sample suite. Autunite and its dehydrated counterpart, meta-autunite, are the most common and abundant phosphate species at St.

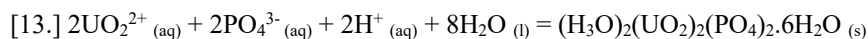
Anthony, with lesser phurcalite and trace meta-ankoleite. Reaction 11 displays how autunite can be produced when meta-schoepite reacts with phosphate, Ca^{2+} , H^+ , and water.



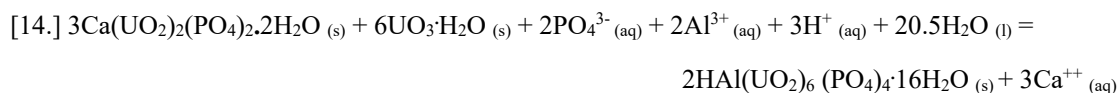
Chernikovite is much more scant than meta-autunite in sample STA21 and is produced in Reaction 12 from meta-autunite by acidic groundwaters. Hydrogen replaces the calcium in the structure of meta-autunite, and the low-pH replacement of calcium is only possible in this sample because of its proximity to organic matter, and by extension, pyrite. In contrast to STA11 discussed below, sample STA21 was collected from a reduced mineralization horizon. Figure 1 from Munasinge, et al. (2015) displays the stability fields of uranium phosphorus species, with chernikovite stable in neutral to low pH conditions. The precipitation of chernikovite is likely caused by evaporation of groundwater, concentrating protons and decreasing the pH to chernikovite stability, replacing the Ca^{2+} in autunite with hydronium.



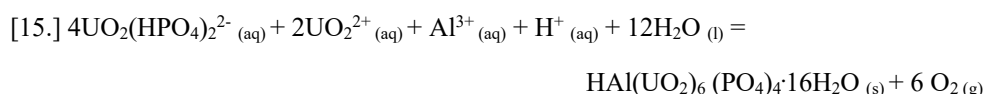
Rather than reacting with autunite, aqueous UO_2^{2+} may be supplying the uranium for chernikovite in this moderately low pH environment, shown in Reaction 13. Jerden and Sinha (2002) discuss the stability field for several uranium species, and aqueous UO_2^{2+} is stable at pH less than 4.



Also of note is the presence of sabugalite -an autunite-group mineral- with meta-autunite in sample STA11. Sabugalite is volumetrically minor compared to meta-autunite (see diffractogram, Fig. 35); in the presence of meta-schoepite and low pH solutions, sabugalite is produced, as suggested in Reaction 14. Lowering the pH of oxidizing solutions pushes meta-autunite out of its stability field and into sabugalite stability, discussed in Jerden and Sinha, (2002). The presence of sabugalite and chernikovite indicates conditions in which weakly acidic meteoric waters evaporate, the pH lowers as protons are concentrated, and these low-pH stable minerals reach their respective stability fields.



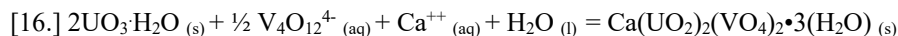
An important consideration in this study is the transportation mechanism for uranium. Mineralogy determined in this study, and observed from other studies, indicates that post-mine groundwaters are weakly acidic, with sample mineralogy characterized by uranyl-phosphate and -sulfate. This would indicate that phosphate was available for uranium transport in the St. Anthony Mine area. Biphosphate and aqueous UO_2^{2+} are the likely methods of transport of uranium, as indicated in Reaction 15; a pH of 4 or less is necessary for UO_2^{2+} to remain in solution (Garrels and Christ, 1991, Fig. 42). Uranyl-biphosphate, aqueous UO_2^{2+} , Al^{3+} , H^+ and water produce sabugalite and oxygen. This reaction is very oxidizing, and would continue to mobilize uranium from carbonaceous matter, making the element available for transport.



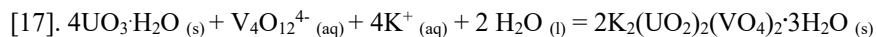
Vanadates

Uranyl-vanadates are abundant in the Grants Mineral Belt, particularly in the limestone deposits of the Todilto Formation (Hilpert, 1969; McLemore, 2002). Carnotite and (meta-) tyuyamunite are among the most volumetrically abundant, though meta-tyuyamunite was not previously described at the Piedra Triste mine (McLemore, 2002). The Todilto Formation provided calcium for the development of meta-tyuyamunite observed in these limestone deposits.

The limestone of the Todilto Formation buffered groundwaters, creating alkaline conditions (Hilpert, 1969); as such, under these alkaline pH conditions (Fig. 43) meta-vanadate is stable and will produce meta-tyuyamunite from meta-schoepite in an oxidizing reaction as shown in Reaction 16. Uraninite is observed at Piedra Triste (McLemore, 2002), therefore its hydrated product meta-schoepite is the source of the uranium in reaction 16.

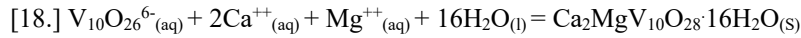


Carnotite will also precipitate under the alkaline conditions characterizing the limestone host-rock of the Todilto Formation. Meta-schoepite, meta-vanadate, potassium and water will produce carnotite in Reaction 17. Meta-schoepite is again used as the source of uranium, as uraninite is observed in the Todilto Limestones (McLemore, 2002).

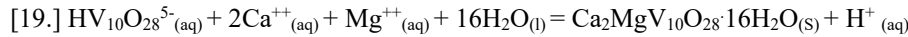


The carnotite and meta-tyuyamunite identified in this study represent precipitation under weakly acidic or weakly alkaline conditions; however, pascoite-group minerals - calcium vanadates- will only precipitate under acidic conditions (Fig. 44). The dominant mineral in sample STA1 is magnesiopascoite, which has stability pH of approximately 6

(Fig. 44). This pH places the pascoite minerals in the poly-vanadate and bi-polyvanadate stability fields. In order to produce magnesiopascoite, poly-vanadate is combined with Ca^{2+} and Mg^{2+} ions and water in reaction 18.



Production of magnesiopascoite from bi-polyvanadate, Ca^{2+} , Mg^{2+} and water also produces one mole of magnesiopascoite and releases hydrogen in Reaction 19. This will keep the pH of the system weakly acidic, driving precipitation of magnesiopascoite.



The magnesiopascoite observed from sample STA1 (Figs. 30 and 31) is an excellent example of the change in meteoric water conditions that may occur in these sandstone-hosted deposits. The reduced mineralization of the sandstone is replaced by the oxides studtite, schoepite, and the uranyl-carbonate oswaldpeetersite. The presence of a carbonate mineral indicates alkaline meteoric water conditions. The abundance of magnesiopascoite adjacent to the uranyl-oxide and -carbonate minerals indicate there was a drop in pH, permitting the precipitation of the magnesiopascoite. This sample is also of interest in regard to the abundance of vanadium, with vanadium available in the upper portions of the St. Anthony deposit that was not observed at the current pit level. The presence of vanadium increases uranium stability while decreasing solubility (Gruner, 1956), and should be considered during ISR testing.

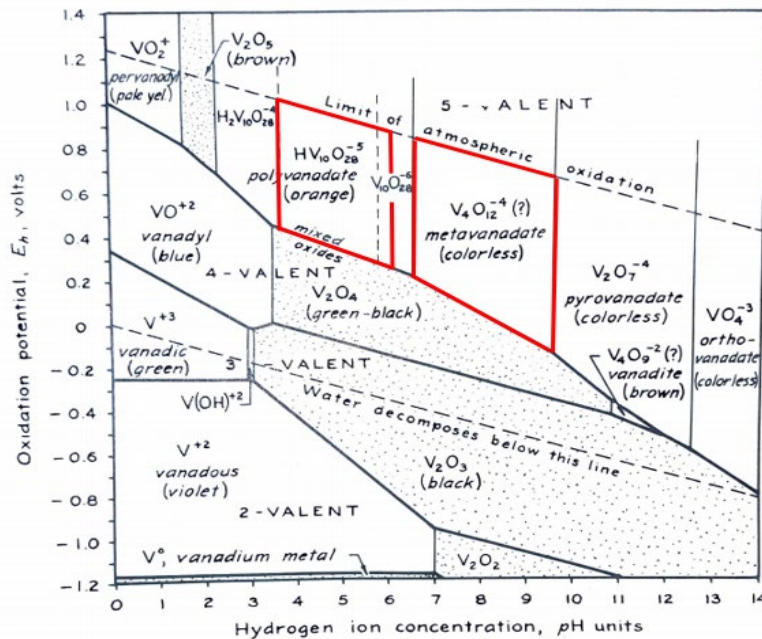


Figure 43: Eh /pH diagram of aqueous vanadium species at 25°C and 1 atmosphere of pressure, with vanadium species at 10^{-3} M (Garrels and Christ, 1990). Carnotite, tyuyamunite, and pascoite stability fields highlighted in red to show the multiple conditions that will produce these minerals.

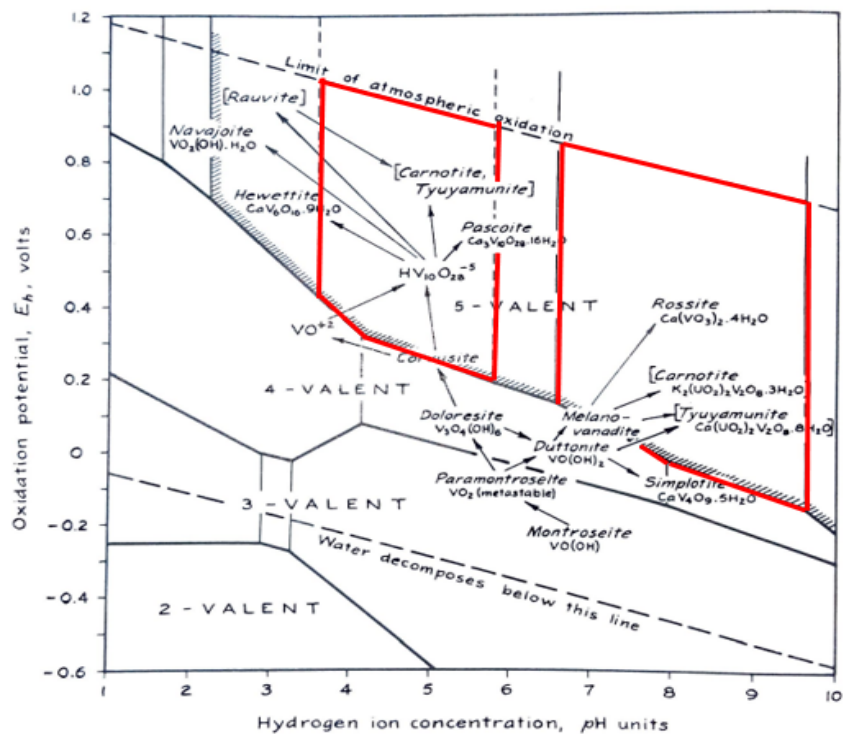


Figure 44: Eh/pH diagram of uranyl-vanadate ions at 25°C and 1 atmosphere of pressure, with vanadium species at 10^{-3} M (Garrels and Christ, 1990). Stability fields for carnotite and tyuyamunite of Figure 44 outlined in red. The pascoite phase rests in the bi-polyvanadate ($HV_{10}O_{28}^{5-}$) and poly-vanadate ($V_{10}O_{28}^{6-}$) fields, with a pH limit of approximately 6.

CHAPTER 7

CONCLUSIONS AND IMPLICATIONS

The goals for this study were to identify the mineralogy of the St. Anthony, Jackpile-Paguate, Mt. Taylor, Section 31, and Piedra Triste mines. These minerals were then used to produce possible reactions to explain their presence and to discuss the overall geochemistry of these mines. This study aims to provide preliminary geochemical data for leach testing of the mineralization for this region.

1. Uranium mineralogy determined in this study comprising the following:

Coffinite: The coffinite identified in this study is weakly-crystallized where intimately mixed with organic matter, and is well-crystallized in high-grade ore zones, as previously reported by Kelley et al. (1967). This is evident from ores in the Jackpile-Paguate and St. Anthony mines; high-grade Jackpile core samples JP2 and JP3 presented well-defined coffinite peaks in their respective diffractograms (Fig. 6; Appx. 2, Figs. 71 and 73). Weakly- and well-crystallized coffinite with minor uraninite in high-grade zones are described in the Jackpile Member of the Morrison Formation by Moench and Schlee (1967) and is corroborated in this study at the St. Anthony mine (sample STA18, Fig. 16). Reduced uranium minerals previously not identified at the Mt. Taylor mine include weakly-crystallized coffinite within the carbonaceous matter filling pore spaces, identified via XRD (Fig. 8; Appx. 2, Fig. 79); although not identified in this study, previous studies documented organo-uranium complexes in ore material from Mt. Taylor. In regard to leach tests, this profile on reduced uranium mineralization verifies the presence of coffinite and uraninite, intimately associated with organo-uranium complexes, suggesting that strongly oxidizing solutions would be required to liberate uranium from these strongly reduced ores.

2. Electron Microprobe analyses demonstrate the presence of uranium co-occurring with molybdenum, selenium, and vanadium in geochemically reduced rock volumes. Core from the Mt. Taylor mine contains extremely fine-grained coffinite associated with organic matter, identified by a 1:1 ratio of uranium to silicon in an initial microprobe analysis. Hand sample MT3 is characterized by molybdenum in the form of the molybdate “ilsemanite” in addition to coffinite. Minor vanadium and selenium were observed in sample MT3, and were not identified in the other Mt. Taylor samples. It is not possible to provide a comprehensive element profile with the small sample size of the Mt. Taylor suite, although the limited observation of co-occurring elements in the study does provide implications for future work in preparation for ISR. The variability of associated metals in this small sample size means large-scale mapping of elements in a deposit will be necessary for optimal recovery, avoidance of geochemical interference from competing elements, and environmental considerations.

3. X-ray diffraction analysis of oxide uranium minerals identifies a series of uranyl-sulfates, -phosphates, -carbonates, and -vanadates not previously described in the Grants Mineral Belt (i.e., jachymovite, meta-ankoleite, phurcalite, cejkaite, oswaldpeetersite, and magnesiopascoite). This variation in uranium minerals is especially evident in the St. Anthony mine, where uranyl-sulfates, -phosphates, -carbonates, and trace -vanadates were identified as post-mining precipitates (excluding sample STA1). This variety of uranium phases is due to the availability of these oxyanions in post-deposition environments.

4. The variety of oxidized uranium minerals identified in this study represents the various post-deposition conditions that affected Grants District Ores on a local scale, including post-mine weathering effects. Although researchers have documented oxidized uranyl-phosphate and uranyl-vanadate minerals at the Jackpile mine (Kelley et al., 1967), no uranyl-sulfate or -carbonate species have been described from this orebody. This mineralogy differs from that of the St. Anthony mine, located less than two miles northeast of the Jackpile mine, in which the oxidized portions of the St. Anthony deposit are characterized by abundant uranyl-sulfate and uranyl-phosphate minerals, and contain only sparse uranyl-carbonate and trace uranyl-vanadate minerals at the current pit level. The sulfate minerals observed at the St. Anthony deposit are post-mining and are the result of oxidizing, sulfate-bearing meteoric waters reacting with the sandstone-hosted uranium minerals.

Uranyl-vanadates described in this study from the St. Anthony mine occur in trace quantities at the current pit level. Magnesiopascoite is the dominant oxidized phase in sample STA1, indicating that there were greater quantities of vanadium available in reduced mineralization and in groundwaters within stratigraphically higher sandstone units. The magnesiopascoite is paragenetically later than the uranyl-carbonate and uranyl-oxides. The abrupt change in mineralogy from uranyl-oxide minerals to magnesiopascoite establishes that post-mine groundwaters may dramatically change original pre-mining uranium oxidation state and mineralogy on a local scale.

5. The mineral diversity indicated by this study also speaks to variable meteoric water that characterize local conditions necessary to produce these complex mineral associations.

For example, uranyl-phosphates precipitate under pH conditions that are distinct from those that form uranyl-carbonates (i.e., phosphates from pH neutral to acidic, whereas carbonates from pH near neutral to alkaline; see Fig. 42 and Jerden and Sinha, (2002)). Notably, uranyl-sulfates precipitate from very alkaline to very acidic oxygenated groundwaters (Fig. 41). The occurrence of phosphate within St. Anthony mine, probably derived from decomposing apatite, illustrates change from alkaline to moderately acidic meteoric waters at this deposit; sample STA9 is characterized by cejkaite with calcite which indicates alkaline meteoric water composition(-s) during their precipitation. These alkaline conditions are also indicated from sample STA19, as oswaldpeetersite was identified from a seep on the western North Pit highwall during 2017 collection (see Fig. 42 for uranyl-carbonate stability). These minerals indicate that the water seeping out of the highwall in that area is weakly acidic to alkaline. Meteoric water characteristics in other areas of the pit are characterized by acidic conditions, favorable to the precipitation of uranyl-phosphate minerals. This is indicated by the uranyl-phosphates collected from an in-pit talus pile close to STA9.

The mineral diversity shown in this study reflects the local changes in groundwater geochemistry, and illustrates the continued oxidation, transportation, and re-precipitation of uranium phases. Geochemical processes and mineralogic changes in the St. Anthony mine are especially evident as post-mining oxidized uranium species continue to precipitate, developing within sample channel cuts made during the 2010 Westwater Resources sampling campaign.

6. Consideration for future ISR recovery methods for the ores described herein must focus on metals commonly associated with sandstone-hosted uranium, and on the associated gangue minerals. Pyrite and calcite are both observed in abundance in the Grants Mineral Belt. The production of acid from pyrite decomposition may depress the pH of solutions if present in abundance, destabilizing any carbonate complexes used to transport uranium. Calcite will also have a detrimental effect in ISR. In barren sandstones adjacent to ore facies and throughout the Grants Mineral Belt, calcite occurs in abundance as cement and will act as a barrier, preventing alkaline solutions from contact with uranium mineralization. Mapping of both pyrite and calcite will be necessary for the future of ISR operations. While each deposit will possess varying concentrations of metals, it is recommended an oxidizing, carbonate-bearing, alkaline solution be used to recover uranium for sandstone-hosted deposits.

REFERENCES

- Adams, S. S., Curtis, H. S., and Hut'en, P. 1974. "Alteration of Detrital Magnetite-Ilmenite in Continental Sandstones of the Morrison Formation, New Mexico." Formation of Uranium Ore Deposits: Vienna, International Atomic Energy Agency. Symposium, p. 219-253.
- Adams, S. S., Curtis, H. S., Hafen, P. L., Salek-Nejad, H. 1978. "Interpretation of Post-Depositional Processes Related to the Formation and Destruction of the Jackpile-Paguate Uranium Deposit, Northwest New Mexico." Society of Economic Geologists. *Economic Geology*. Vol. 73. p. 1635-1654.
- Adler, H. H. 1974. "Concepts of Uranium-Ore Formation in Reducing Environments in Sandstones and Other Sediments." US Atomic Energy Commission. Review Paper. p. 141-156.
- Alief, M. H., Kern, R. A. 1989. "Geology of the Mt. Taylor Uranium mine, Grants, New Mexico." American Association of Petroleum Geologists. *AAPG Bulletin*. AAPG Rocky Mountain Section meeting. V. 73, p 1146.
- Arey, J. S., Seaman, J. C., Bertsch, P. M. 1999. "Immobilization of Uranium in Contaminated Sediments by Hydroxyapatite Addition." *Environmental Science Technology*. V. 33. p. 337-342.
- Austin, S. R. 1980. "Dissolution and Authigenesis of Feldspars." New Mexico Bureau of Mines and Mineral Resources. Memoir 38: *Geology and Mineral Technology of the Grants Uranium Region 1979*. p. 107-115.
- Boudette, E. L., Weis, P.L. 1956. "Geology of the Midnite Mine Area, Spokane Indian Reservation, Stevens County, Washington." United States Department of the Interior Geological Survey. *Trace Element Investigations Report 634*.
- Berglof, W. R., McLemore, V.T. 2003. "Economic Geology of the Todilto Formation." New Mexico Geological Society 54th Annual Fall Field Conference Guidebook. *Geology of the Zuni Plateau*. p. 179-189.

- Breger, I. A. 1974. "The Role of Organic Matter in the Accumulation of Uranium: The Organic Geochemistry of the Coal-Uranium Association." United States Department of the Interior Geological Survey and the International Atomic Energy Agency. IAEA-SM-183/29.
- Brugger, J., Burns, P. C., Meisser, N. 2003. "Contribution to the Mineralogy of Acid Drainage of Uranium Minerals: Marecottite and the Zippeite-group." *American Mineralogist*, V. 88, p. 676–685.
- Catalano, J. G., Giammar, D. E., Wang, Z. 2016. "Dominant Mechanisms of Uranium-Phosphate Reactions in Subsurface Sediments." Technical Report. Washington University, St. Louis. DOE Final Report.
- Clark, D. S. 1980. "Uranium Ore Rolls in Westwater Canyon Sandstone, San Juan Basin, New Mexico." New Mexico Bureau of Mines and Mineral Resources. Memoir 38: *Geology and Mineral Technology of the Grants Uranium Region 1979*. p. 195-201.
- Crook, W. W. 1979. "The Mineralogy and Geochemistry of the Monument Project, McKinley County, New Mexico." United States Energy Minerals Division.
- Dahlkamp, F. J. 2010. "Uranium Deposits of the World: USA and Latin America." Texas Coastal Plain Uranium Region. Springer, Berlin, Heidelberg. p. 311-355.
- Dam, W. L. 1995. "Geochemistry of Groundwater in the Gallup, Dakota, and Morrison Aquifers, San Juan Basin, New Mexico." United States Department of the Interior Geological Survey. Water Resources Investigation Report, 94-4253.
- Environmental Protection Agency. 2018. "Jackpile-Paguate Uranium Mine, Laguna Pueblo, NM." Background. United States Environmental Protection Agency.
- Falkowski, S. K. 1980. "Geology and Ore Deposits of Johnny M Mine, Ambrosia Lake District." New Mexico Bureau of Mines and Mineral Resources. Memoir 38: *Geology and Mineral Technology of the Grants Uranium Region 1979*. p. 230-239.
- Finch, R. J., Hawthorne, F. C., Ewing, R. C. 1998. "Structural Relations Among Schoepite, Meta-Schoepite, and Dehydrated Schoepite." *The Canadian Mineralogist*. Vol. 36, p. 831-845.
- Fischer, R. P. 1968. "The Uranium and Vanadium Deposits of the Colorado Plateau Region." United States Department of the Interior Geological Survey. *Ore Deposits of the United States: 1933-1967*. Ch. 35. p.736-746.
- Fronzel, J. S., Fleischer, M. 1955. "Glossary of Uranium- and Thorium-bearing Minerals." United States Department of the Interior Geological Survey. *Geological Survey Bulletin*. V. 8.
- Garrels, R. M., Christ, C. L. 1990. "Solutions, Minerals, and Equilibria." Uranyl-Carbonate, Sulfate, and Vanadate Activity Diagrams. Jones and Bartlett Publishers, Inc. ISBN 0-86720-148-7. p. 214, 254, 389.

- Granger, H. C., Warren, C. G. 1969. "Unstable Sulfur Compounds and the Origin of Roll-type Uranium Deposits." Society of Economic Geologists. *Economic Geology*. Vol. 64. p. 160-171.
- Gruner, J. W. 1956. "Concentration of Uranium in Sediments by Multiple Migration-Accretion." Society of Economic Geologists. *Economic Geology Bulletin*, Vol. 51, No. 6.
- Harshman, E. N. 1974. "Distribution of Elements in Some Roll-Type Uranium Deposits." United States Department of the Interior Geological Survey. Conference Paper.
- Hazen, R. M., Ewing, R.C., Sverjensky, D. A. 2009. "Evolution of Uranium and Thorium Minerals." *American Mineralogist* V. 94. p. 1293-1311.
- Hilpert, L. S. 1969. "Uranium Resources of Northwestern New Mexico." United States Department of the Interior Geological Survey. Professional Paper 603.
- Hostetler, P. B., and Garrels, R. M. 1962. "Transportation and Precipitation of Uranium and Vanadium at Low Temperatures, with Special Reference to Sandstone-Type Uranium Deposits." Society of Economic Geologists. *Economic Geology Bulletin*, Vol. 57. No. 2.
- Jennings, J. K., and Leventhal, J. S. 1978. "A Literature Review of Interaction of Oxidized Uranium Species and Uranium Complexes with Soluble Organic Matter." United States Department of the Interior Geological Survey. Open File Report 78-179.
- Jerden, J. L., Sinha, A. K. 2002. "Phosphate Based Immobilization of Uranium in an Oxidizing Bedrock Aquifer." Elsevier. *Applied Geochemistry*. p. 823-843.
- Kelley, V. C., Kittel, D. F., Melancon, P. E. 1967. "Uranium Deposits of the Grants Region." New Mexico Geological Society 18th Annual Field Conference Guidebook: *Defiance, Zuni, Mt. Taylor Region*. p. 173-183.
- Krauskopf, K. B., Bird, D. K. 1995. "Introduction to Geochemistry." 3rd Ed. McGraw-Hill, Inc. ISBN 0-07-035820-6.
- Larson, E. S., Gottfried, D. 1960. "Uranium and Thorium in Selected Suites of Igneous Rocks." American Journal of Science. *Bradley Volume*. V. 258-A. p.151-169.
- Lide, D. R. 1994: Uranium. In: LIDE, D.R.: Handbook of Chemistry and Physics. 74th ed., Boca Raton (USA): CRC Press, p.31-32.
- McLaughlin, E.D. 1963. "Uranium Deposits in the Todilto Limestone of the Grants District." New Mexico Bureau of Mines and Mineral Resources. Memoir 15. *Geology and Mineral Technology of the Grants Uranium Region 1963*. p. 136-149.
- McLemore, V. T. 1982. "Uranium in the Albuquerque Area." New Mexico Geological Society 33rd Annual Fall Field Conference Guidebook. p. 305-311.
- McLemore, V. T., Chenoweth, W. L. 1991. "Uranium Mines and Deposits in the Grants district, Cibola and McKinley Counties, New Mexico." New Mexico Bureau of Mines and Mineral Resources. Open-file Report 353.

- McLemore, V. T., Donahue, K., Krueger, C. B., Rowe, A., Ulbricht, L., Jackson, M. J., Breese, M. R., Jones, G., Wilks, M. 2002. "Database of the Uranium Mines, Prospects, Occurrences, and Mills in New Mexico: Uranium Mines." New Mexico Bureau of Geology and Mineral Resources. Open File Report-461.
- McLemore, V. T. 2010. "The Grants Uranium District, New Mexico: Update on Source, Deposition, and Exploration." New Mexico Bureau of Geology and Mineral Resources.
- McLemore, V. T., Hill, B., Khalsa, N., Lucas-Kamat, S. A. 2013. "Uranium Resources in the Grants Uranium District, New Mexico: An Update." New Mexico Geological Society 64th Field Conference, Geology of Route 66 Region: Flagstaff to Grants. p. 117-126.
- Moench, R. H., Schlee, J. S. 1967. "Geology and Uranium Deposits of the Laguna District, New Mexico." United States Department of the Interior Geological Survey. Professional Paper 519.
- Munasinge, P. S., Elwood Madden, M. E., Brooks, S. C., Elwood Madden, A. S. 2015. "Dynamic Interplay Between Uranyl Phosphate Precipitation, Sorption, and Phase Evolution." *Applied Geochemistry*. V. 58. p.147-160.
- Nash, J. T., Lehrman, N. J. 1975. "Geology of the Midnite Uranium Mine, Stevens County, Washington-A Preliminary Report." United States Department of the Interior Geological Survey. Open file report 75-402.
- Ono, S. 2001. "Detrital Uraninite and the Early Earth's Atmosphere: Sims Analyses of Uraninite in the Elliot Lake District and the Dissolution Kinetics of Natural Uraninite." Ph. D. Dissertation. Pennsylvania State University, College of Earth and Mineral Sciences.
- Owen, D. E., Walters Jr., L. S., Beck, R. G. 1984. "The Jackpile Sandstone Member of the Morrison Formation in West-Central New Mexico—A Formal Definition." New Mexico Bureau of Geology and Mineral Resources. *New Mexico Geology*. V. 6. No. 3. P. 45-52.
- Riese, A. C., Popp, C.J. 1980. "Application of Solution-Mineral Equilibrium Chemistry to Solution Mining of Uranium Ores." New Mexico Bureau of Mines and Mineral Resources. Memoir 38: *Geology and Mineral Technology of the Grants Uranium Region 1979*. p. 344-353.
- Ridgley, J. L. 1980. "Geology and Characteristics of Uranium Mineralization in Morrison Formation at Dennison-Bunn Claim, Sandoval County." New Mexico Bureau of Mines and Mineral Resources. Memoir 38: *Geology and Mineral Technology of the Grants Uranium Region 1979*. p. 299-303.
- Runnells, D. D., Lindberg, R., Lueck, S. L., Markos, G. 1980. "Applications of Computer Modeling to the genesis, Exploration, and In-Situ Mining of Uranium and Vanadium Deposits." New Mexico Bureau of Mines and Mineral Resources. Memoir 38: *Geology and Mineral Technology of the Grants Uranium Region 1979*. p. 355-367.

Saucier, A. E. 1980. "Tertiary Oxidation in Westwater Canyon Member of Morrison Formation." New Mexico Bureau of Mines and Mineral Resources. Memoir 38: *Geology and Mineral Technology of the Grants Uranium Region 1979*. p. 116-121.

Sachdev, S. C. 1980. "Mineralogical Variations Across Mariano Lake Roll-Type Uranium Deposit, McKinley County." New Mexico Bureau of Mines and Mineral Resources. Memoir 38: *Geology and Mineral Technology of the Grants Uranium Region 1979*. p. 162-171.

Singh, A. 2010. "Geochemical Conditions Affecting Uranium(VI) Fate and Transport in Soil and Groundwater in the Presence of Phosphate" Ph. D. Dissertation. Washington University of St. Louis.

Squyres, J. B. 1980. "Origin and Significance of Organic Matter in Uranium Deposits of Morrison Formation, San Juan Basin, New Mexico." New Mexico Bureau of Mines and Mineral Resources. Memoir 38: *Geology and Mineral Technology of the Grants Uranium Region 1979*. p. 86-97.

St. Anthony Mine. 2018. "North Pit." 35°09'48.02" N, 107°18'18.83 W. Google Earth Image. Image date 1 Oct. 2014.

St. Anthony Mine. 2018. "South Pit." 35°09'25.35" N, 107°17'38.11 W. Google Earth Image. Image date 1 Oct. 2014.

Tessendorf, T. N. 1980. "Redistributed Ore Bodies of Poison Canyon, Sec. 18 and 19, T. 13N., R. 9 W., McKinley County." New Mexico Bureau of Mines and Mineral Resources. Memoir 38: *Geology and Mineral Technology of the Grants Uranium Region 1979*. p. 226-229.

Turner-Peterson, C. E., Santos, E. S., Fishman, N. S. (editors), 1986. "A Basin Analysis Case Study: The Morrison Formation, Grants uranium Region, New Mexico." Energy Minerals Division, American Association of Petroleum Geologists AAPG Studies in Geology #22, 391 pages, 2 plates.

Wilton, T. 2017. "Uranium Deposits at the Cebolleta Project, Laguna Mining District, Cibola County, New Mexico." *New Mexico Geology*. V. 39, No. 1.

Wilton, T. 2018. "Stratigraphic Column of the Cebolleta Project, Laguna-Paguate Area." New Mexico.

APPENDIX 1

PHOTOS AND DESCRIPTIONS OF SAMPLES

1. Sample Photos

Jackpile Mine

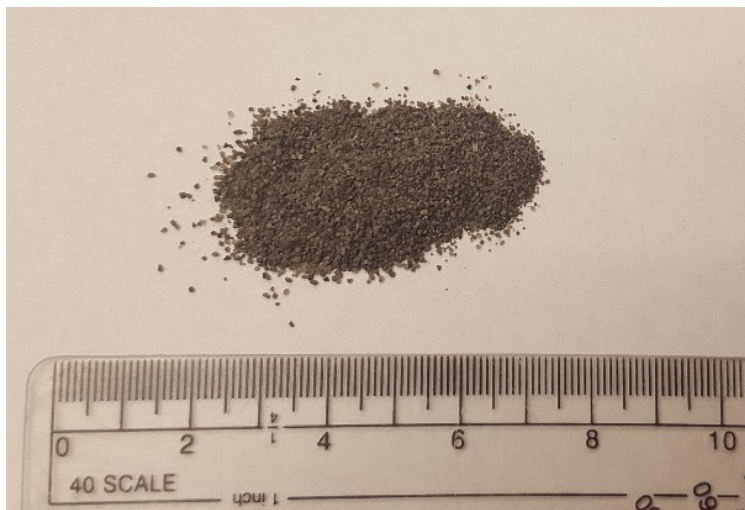


Figure 45: Sample JP3 provided by Alexandra Pearce. Sample was crushed and sorted by grain size (75-600 micron) prior to collection by author. XRD analysis identifies coffinite with lesser pyrite coating the sand grains. Sample JP2 has a grade of 4.41% U_3O_8 . Sample JP2 is visibly identical to JP3; the grade is higher, at 5.76% U_3O_8 .

Piedra Triste Mine

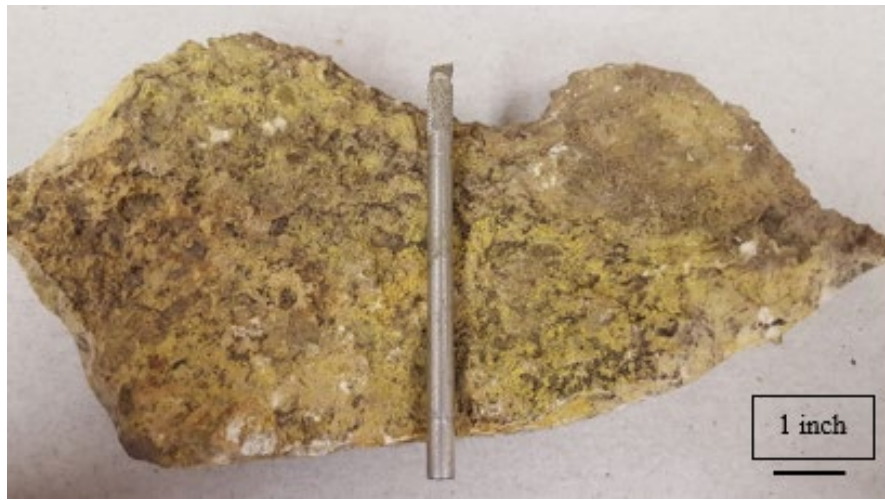


Figure 46: Sample PT2 is the back side of sample PT1 (Figure 19). The color difference on either side of sample appeared to consist of differing uranium phases. Both analyses concluded the presence of the uranyl-vanadate meta-tyuyamunite.



Figure 47: Sample PT3 consists of crystallized meta-tyuyamunite on a sparitic limestone, differing from the dominantly micritic limestone of the Todilto Formation.

Midnite Mine, Washington State



Figure 48: MD1 and MD2 are both hosted in a phyllite schist, and coarse-grained. Samples were analyzed to determine the diffractogram of pitchblende (amorphous UO_2). Arrows point to sample collection. Uraninite was identified with the distinct “amorphous hump” on the diffractogram (Appendix 2). This hump was used to determine the presence of pitchblende in the reduced mineralization analyses of this study.

St. Anthony Mine



Figure 49: Sample STA2 is a thin yellow-orange precipitate on a reduced mineralization horizon (circle). Trace meta-ankoleite was identified precipitating on the Host-rock (black arrow). The very friable sandstone disintegrated during collection and transport.



Figure 50: Sample STA 4 is a thin coating of natrozippeite $[\text{Na}_4(\text{UO}_2)_6(\text{SO}_4)_3(\text{OH})_{10} \cdot 4(\text{H}_2\text{O})]$. This mineral is precipitating on the surface of a small pod of reduced mineralization (arrow).



Figure 51: Collection area for samples STA5, 6, 21. This 5-inch horizon of reduced mineralization contains thin coatings of the phosphate minerals meta-autunite $[\text{Ca}(\text{UO}_2)_2(\text{PO}_4)_2 \cdot 2-6(\text{H}_2\text{O})]$, trace chernikovite $[(\text{H}_3\text{O})_2(\text{UO}_2)_2(\text{PO}_4)_2 \cdot 6(\text{H}_2\text{O})]$ and phurcalite $[\text{Ca}_2(\text{UO}_2)_3\text{O}_2(\text{PO}_4)_2 \cdot 7(\text{H}_2\text{O})]$. A polished probe mount was made from the reduced mineralization, and coffinite $[\text{U}(\text{SiO}_4)_{1-x}(\text{OH})_{4x}]$ was identified through optical petrography. Top and bottom of horizon outlined in red. Sample area just above hammer.

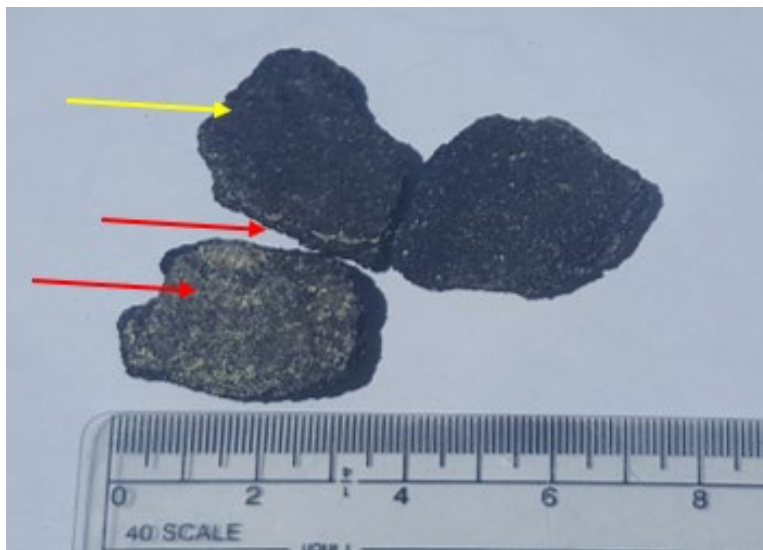


Figure 52: Sample STA5. Red arrows point to collection for XRD analysis. Trace quantities of the mineral meta-autunite were identified and occur as flecks and thin seams. A polished section was made of STA5 (yellow arrow) in order to determine the content of the reduced mineralization. Optical petrography analysis indicates coffinite present. Sample STA6 manifests similarly to STA5 as patches and flecks on the rock. Trace phurcalite $[\text{Ca}_2(\text{UO}_2)_3\text{O}_2(\text{PO}_4)_2 \cdot 7(\text{H}_2\text{O})]$ and carnotite $[\text{K}_2(\text{UO}_2)_2\text{V}_2\text{O}_8 \cdot 3(\text{H}_2\text{O})]$ were identified in STA6.



Figure 53: Sample STA8. The uranyl-sulfates jachymovite $[(\text{UO}_2)_8(\text{SO}_4)(\text{OH})_{14} \cdot 13(\text{H}_2\text{O})]$, zippeite $[\text{K}_4(\text{UO}_2)_6(\text{SO}_4)_3(\text{OH})_{10} \cdot 4(\text{H}_2\text{O})]$, and Natro-jarosite $[\text{NaFe}^{3+}_3(\text{SO}_4)_2(\text{OH})_6]$ were identified via XRD with lesser gypsum. Sample was collected from a reduced mineral horizon similar to samples STA 5,6, and 21. Sample STA7 is similar in appearance to STA8, and consists of schoepite $[(\text{UO}_2)_8\text{O}_2(\text{OH})_{12} \cdot 12(\text{H}_2\text{O})]$, hydronium-jarosite $[(\text{H}_3\text{O})\text{Fe}^{3+}_3(\text{SO}_4)_2(\text{OH})_6]$, and pyrite (FeS_2) in fossil trash.

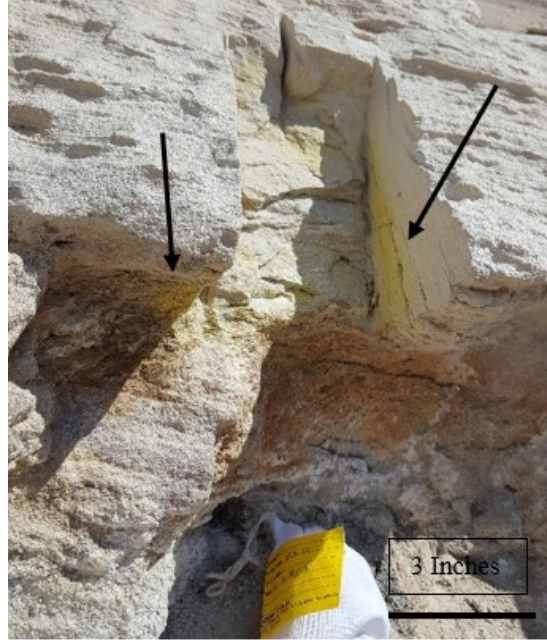


Figure 54: Sample location of STA10. Natrozippeite $[\text{Na}_4(\text{UO}_2)_6(\text{SO}_4)_3(\text{OH})_{10} \cdot 4(\text{H}_2\text{O})]$ and gypsum $[\text{Ca}(\text{SO}_4) \cdot 2\text{H}_2\text{O}]$ are precipitating only on the surface of the sandstone (Jackpile Member, Morrison Formation). This sandstone is not friable, differing from many of the other samples collected this study.

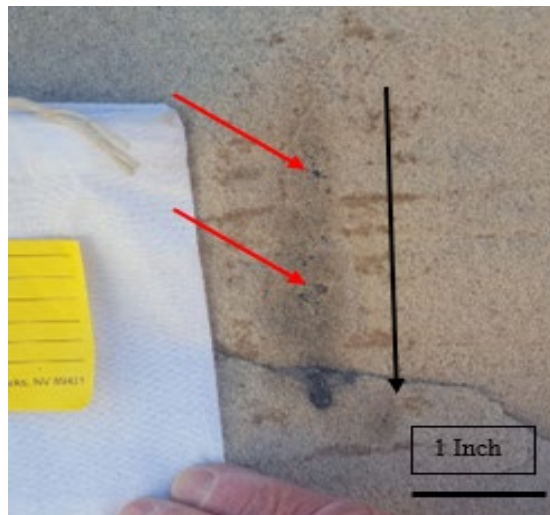


Figure 55: Sample STA12, identified via XRD as trace coffinite. This small area of reduced mineralization was collected from a friable quartz-arenite host (Jackpile Member, Morrison Formation). The mineralization moves downward, leaving behind a darker oxidized trail (black arrow). Small flecks of fossil trash (red arrows) may have served to reduce this mineralization.



Figure 56: Collection area for samples STA13A (black horizon) and STA13B (red horizon). These horizons are separated by approximately 6 inches of barren sandstone.

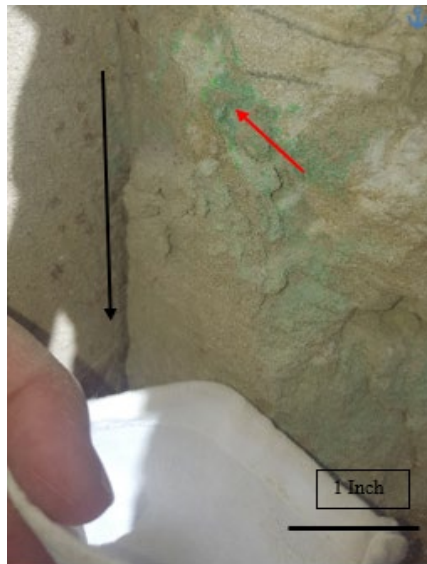


Figure 57: Sample STA14. During the sampling campaign of 2010, Westwater Resources Inc. made a series of cuts (black arrow) into the highwall, painting the area for later ease of finding cuts. Samples STA16 and 20 were also collected from similar cuts along the highwall. During sampling in 10/2017, there appeared to be a precipitate behind the paint (red arrow). However, scintillometer counts are identical to the barren sandstone collected for host-rock characterization.



Figure 58: Sample STA15. Black arrow points to sample collected. A yellow mineral identified as zippeite $[K_4(UO_2)_6(SO_4)_3(OH)_{10} \cdot 4(H_2O)]$ + gypsum $[CaSO_4 \cdot 2(H_2O)]$ was precipitating beneath a pod of reduced mineralization that pinches out toward the right side of the photo (red).

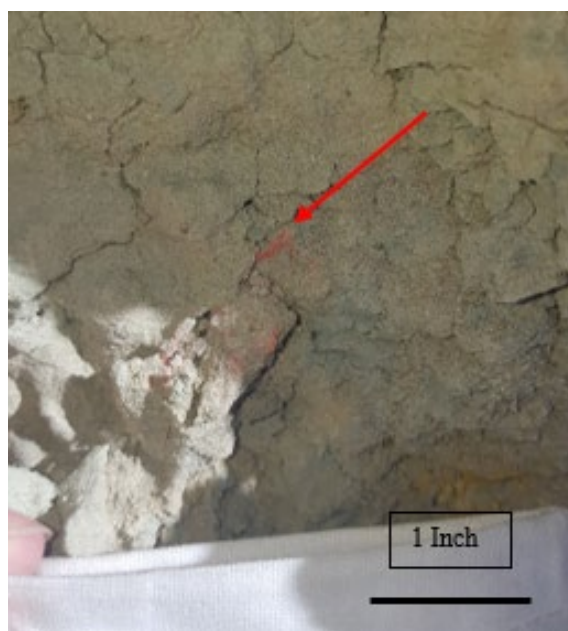


Figure 59: Sample STA17 (red arrow) was found in the talus material eroding from the highwall. The orange-red mineral was identified via XRD as trace carnotite $[K_2(UO_2)_2V_2O_8 \cdot 3(H_2O)]$.

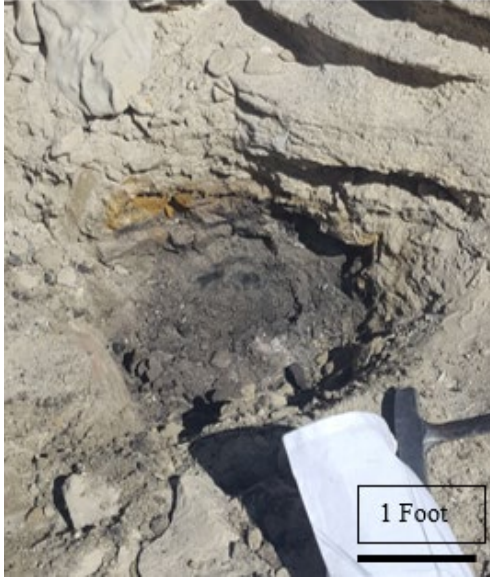


Figure 60: Sample STA18 was collected from this small pod, discovered through the use of a portable scintillometer. The mineralization is very hard and was expected to consist of the mineraloid pitchblende. XRD and optical petrographic analyses conclude the dominant mineral is coffinite, with lesser uraninite.

2. Optical Microscopy

Mt. Taylor Mine

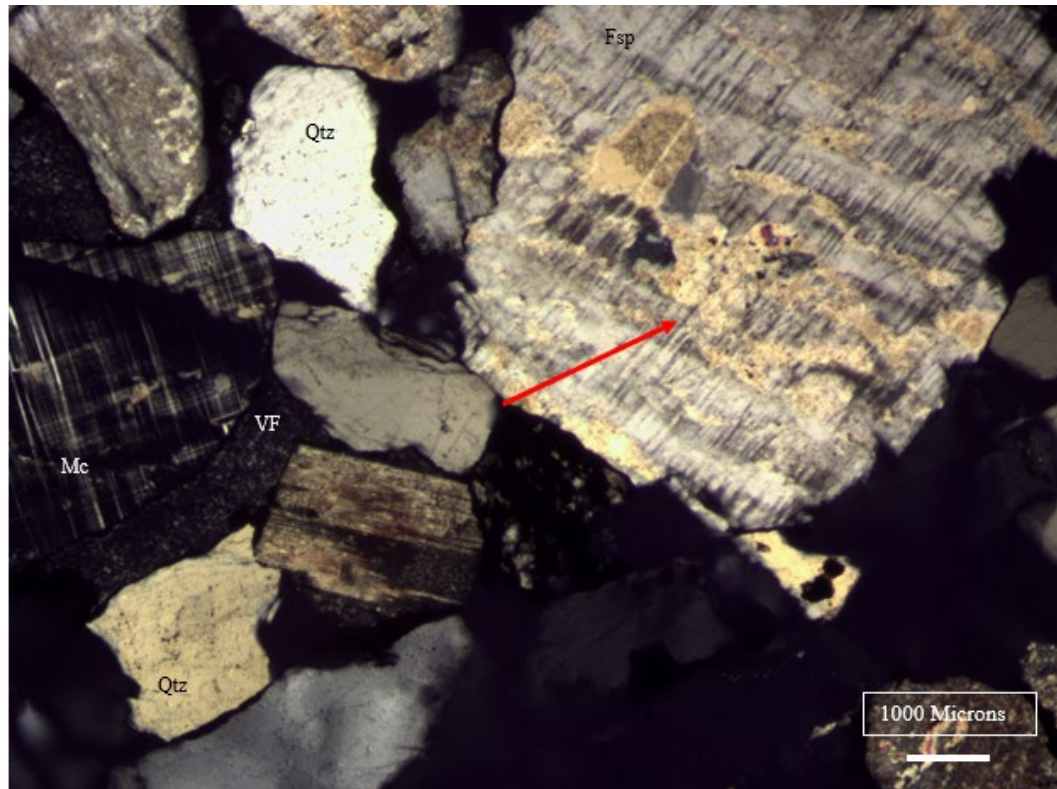


Figure 61: Sample MT1, analyzed to determine the uranium minerals present within the carbonaceous matter. Much of the organic material was removed during thin section preparation. Sample consists of quartz, microcline, lesser plagioclase and volcanic fragments. Of note is the feldspar in the upper right-hand corner. White phyllosilicate is preferentially altering the plagioclase from the center. Photo at 4x magnification.

St. Anthony Mine

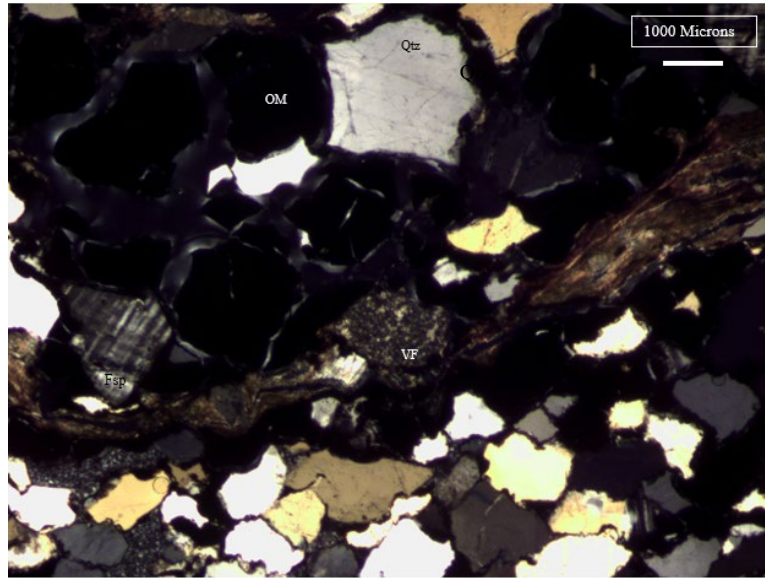


Figure 62: Sample STA3 contains dominantly quartz with lesser volcanic fragments and feldspar. The organic matter was preserved during thin section preparation, and contains weakly crystalline coffinite, identified via XRD. 4x magnification.

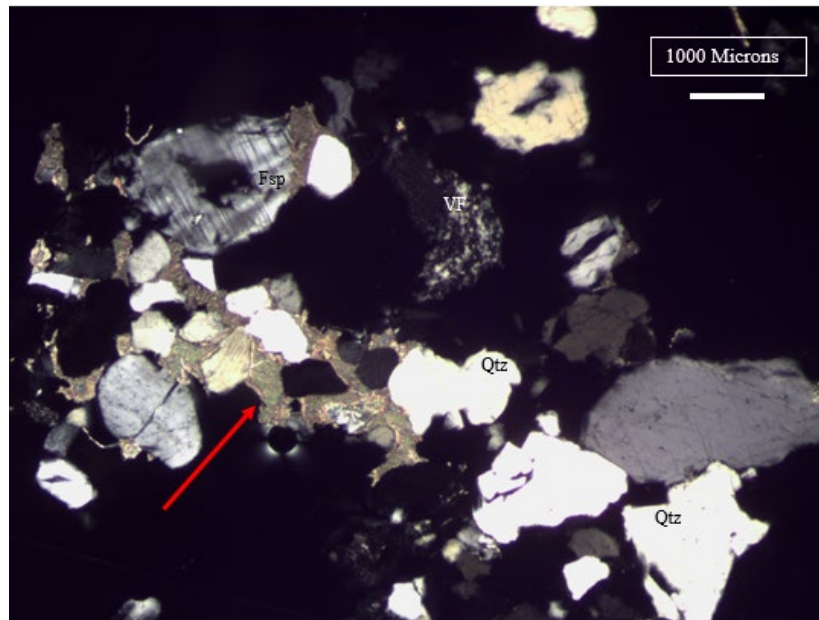
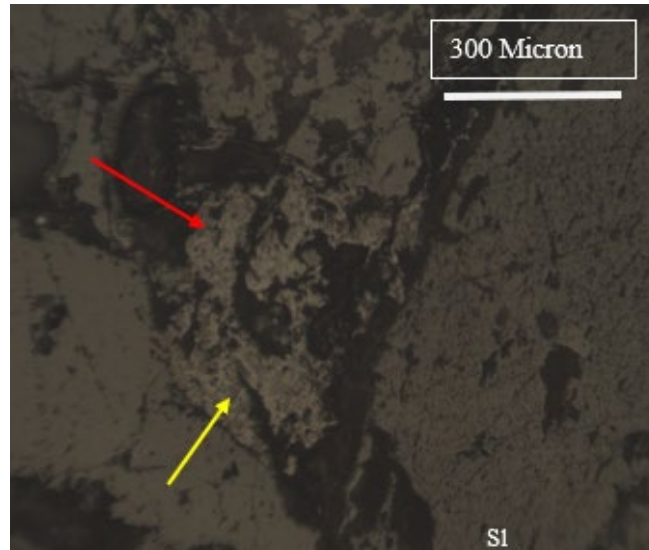


Figure 63: Sample STA18A, one of two barren host-rock samples were collected from the North of the St. Anthony Mine. Sample STA18A is a small channel scour that eroded and re-filled with an angular, coarse arkosic-arenite. Most of the carbonate cement (red arrow) was removed during preparation. XRD analysis identifies calcite as the cement. 4x magnification.

3. Optical Petrography

Mt. Taylor Mine



Figures 64: Polished probe mount of sample MT1. Weakly crystalline coffinite with darker uraninite (yellow arrow) overgrowths are present in pore space with organic matter. 10x magnification.

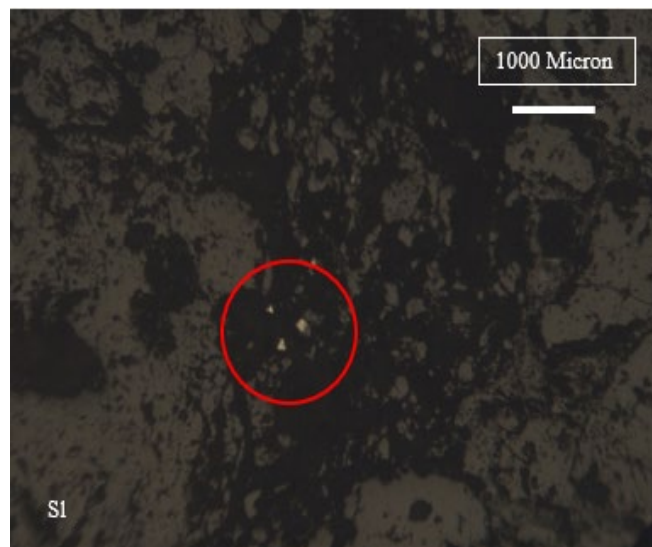


Figure 65: Sample MT1 also contains fine-grained, euhedral pyrite (red circle) occurring in the pore space with the organic matter. 4x magnification.

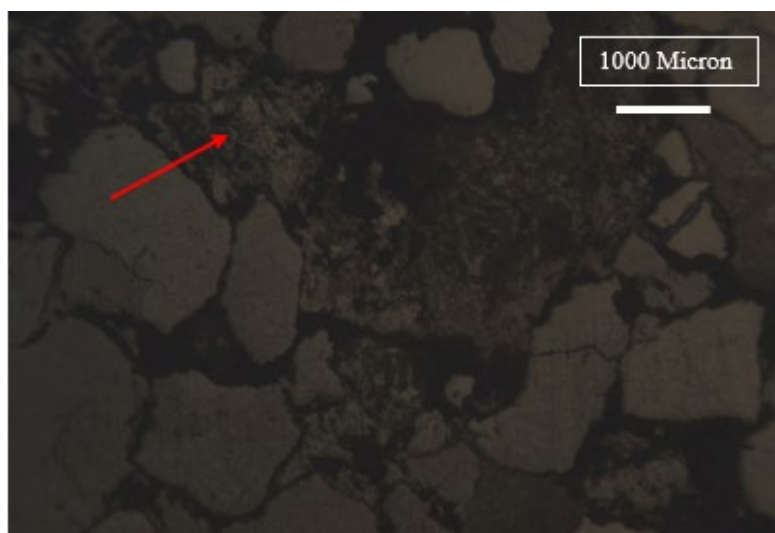


Figure 66: Sample MT3 contains very fine-grained, weakly crystallized coffinite (red arrow) in the organic matter. MT3 also contains significant Mo in the form of ilsemanite occurring in the organic matter as well and washed out of the sample during polished probe mount preparation. 4x magnification.

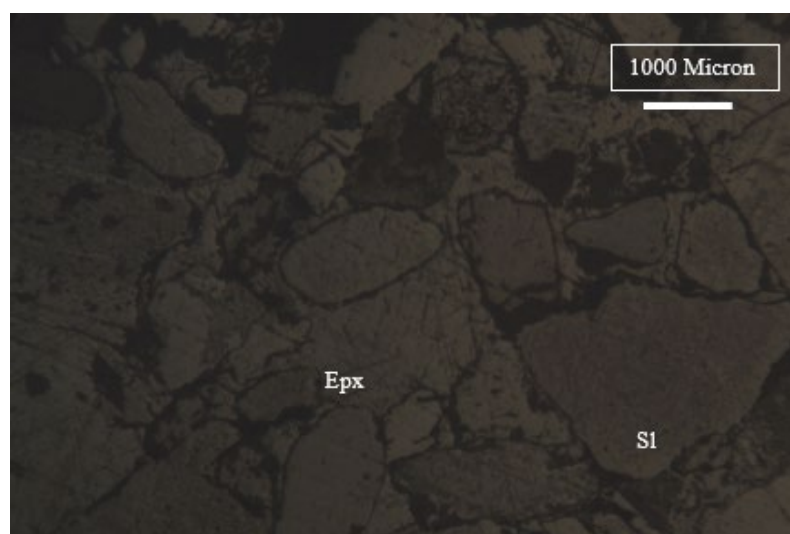


Figure 67: Sample MT5 was analyzed by XRD and microprobe to determine the uranium phases present. The sample is characterized by rare uranium, confirmed with low scintillometer counts. Similar to MT3, the Mo content is much higher than U. Sample is very porous, which was filled by epoxy during preparation. 4x magnification.

Section 31 Mine

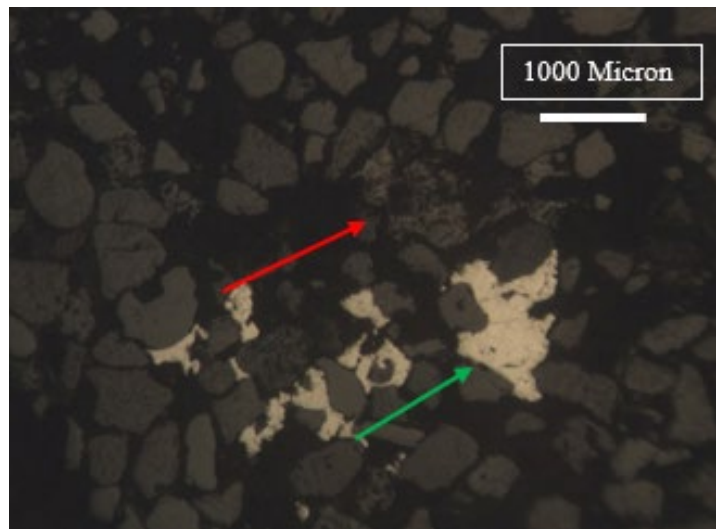


Figure 68: Optical petrography and microprobe analysis identify dominant, poorly crystalline coffinite with lesser uraninite (red arrow) for sample KM2. There is abundant well-crystallized, coarse pyrite throughout the sample (green arrow). The pyrite is so abundant within the sample, it extends into the clay galls (shown in Appendix 3). 4x Magnification.

St. Anthony Mine

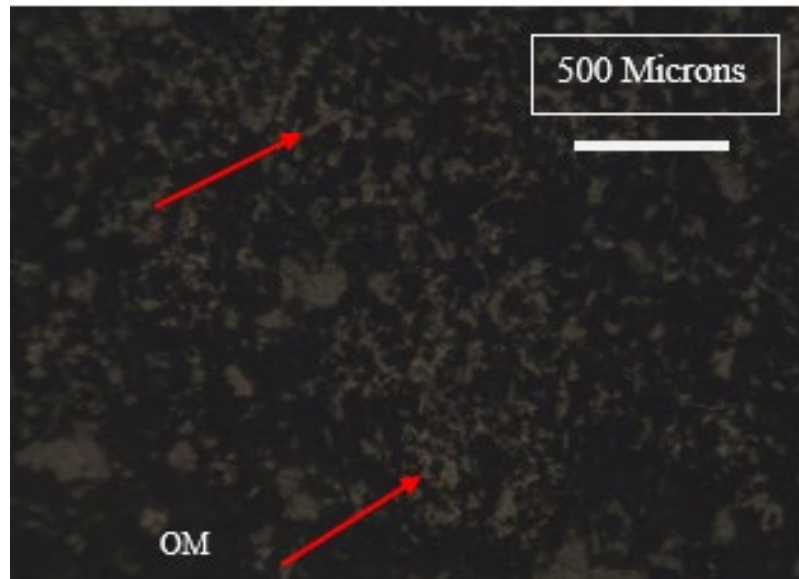


Figure 69: Sample STA3 was collected from a thin horizon along a sandstone-mudstone contact (Section IV, main writing). The sample is characterized by very fine-grained coffinite (red arrows) identified by XRD and optical petrography and is finely mixed with the organic matter. 10x magnification.



Figure 70: Sample STA7 consists of quartz-arenite and fossil trash (red arrow). Schoepite $[(\text{UO}_2)_8\text{O}_2(\text{OH})_{12} \cdot 12(\text{H}_2\text{O})]$ is present as a thin grain coating identified via XRD. Microprobe analysis identifies abundant very fine-grained pyrite in the fossil trash. 4x magnification.

APPENDIX 2

REFERENCE DIFFRACTOGRAMS, PATTERN AND PEAK LISTS

X-ray diffraction was utilized as the primary means of mineral identification for this study. Samples were powdered to a very fine grain size and flattened on a pure silicon crystal base for analysis. All samples were scanned for 40 minutes, excluding samples STA 18A and B; scanned for 5 minutes. Scan parameters are presented in Table 5 below.

Table 6: Scan parameters for X-ray diffraction analyses.

Parameter	Description
Scan Axis	Gonio
Start Position [$^{\circ}2\theta$]	6.0044
End Position [$^{\circ}2\theta$]	69.9754
Step Size [$^{\circ}2\theta$]	0.0170
Scan Step Time [s]	77.4700
Scan Type	Continuous
PSD Mode	Scanning
PSD Length [$^{\circ}2\theta$]	2.12
Offset [$^{\circ}2\theta$]	0.0000
Divergence Slit Type	Fixed
Divergence Slit Size [$^{\circ}$]	0.2500
Specimen Length [mm]	10.00
Measurement Temperature [$^{\circ}\text{C}$]	25.00
Anode Material	Cu
K-Alpha1 [\AA]	1.54060
Generator Settings	40 mA, 45 kV
Diffractionmeter Type	0000000011071336
Diffractionmeter Number	0
Goniometer Radius [mm]	240.00
Dist. Focus-Diverg. Slit [mm]	100.00
Incident Beam Monochromator	No
Spinning	Yes

Jackpile Mine

Figure 71: Reference diffractogram for Sample JP1. Arrows point out most intense peaks for coffinite. Silicates removed from diffractogram to highlight coffinite and pyrite peaks.

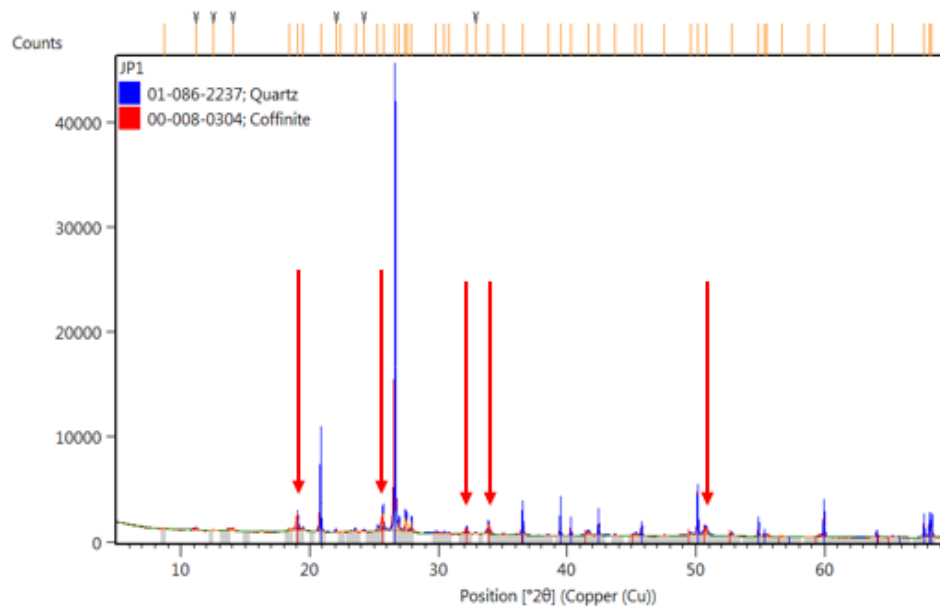


Figure 72: Reference pattern list for Sample JP1.

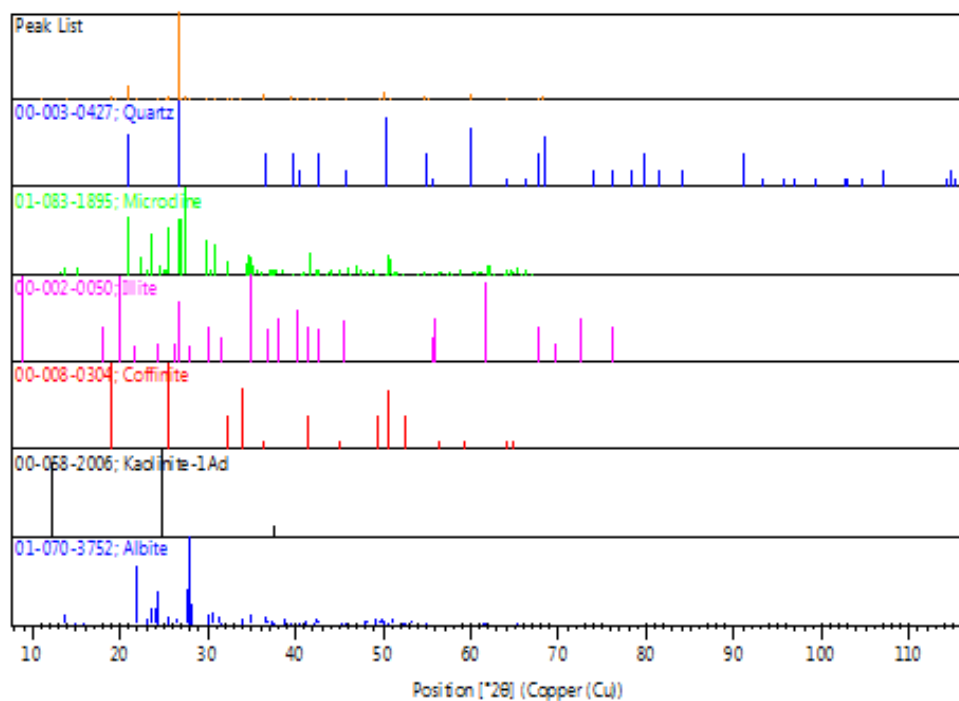


Table 7: Peak list for sample JP1.

Pos. [$^{\circ}2\theta$]	Height [cts]	FWHM Left [$^{\circ}2\theta$]	d-spacing [\AA]	Rel. Int. [%]
8.6739	35.83	0.1889	10.18626	0.11
11.1246	248.55	0.1102	7.94709	0.78
12.4445	53.62	0.4408	7.10702	0.17
14.0190	222.56	0.1102	6.31216	0.70
18.3647	155.52	0.1574	4.82713	0.49
19.0030	1746.41	0.0630	4.66640	5.50
19.4200	301.53	0.1260	4.56714	0.95
20.8075	5391.79	0.0672	4.26561	16.98
21.9809	175.46	0.1152	4.04049	0.55
22.3753	41.91	0.3072	3.97015	0.13
23.4998	213.81	0.1728	3.78265	0.67
24.1968	123.95	0.1920	3.67524	0.39
25.2199	389.00	0.0768	3.52843	1.22
25.6515	1702.98	0.0960	3.47002	5.36
26.5897	31755.60	0.0576	3.34968	100.00
26.9110	851.47	0.0384	3.31041	2.68
27.3877	1360.07	0.0576	3.25386	4.28
27.4704	1183.31	0.0576	3.24426	3.73
27.8668	1045.36	0.0576	3.19900	3.29
29.7746	139.16	0.2304	2.99822	0.44
30.4016	144.78	0.0576	2.93780	0.46
30.7683	107.81	0.2304	2.90362	0.34
32.1510	514.72	0.0960	2.78183	1.62
32.8379	101.77	0.1536	2.72519	0.32
33.8236	867.78	0.1344	2.64799	2.73
34.9742	27.95	0.4608	2.56347	0.09
36.4926	2192.79	0.0864	2.46021	6.91
38.4574	99.25	0.1920	2.33892	0.31
39.4149	1520.48	0.0672	2.28428	4.79
40.2443	786.20	0.0576	2.23909	2.48
41.6045	318.19	0.2688	2.16898	1.00
42.3951	1203.05	0.0864	2.13034	3.79
43.6775	83.81	0.0768	2.07072	0.26
45.2689	191.60	0.3072	2.00155	0.60
45.7427	900.93	0.0864	1.98192	2.84
47.5100	62.93	0.2304	1.91224	0.20
49.5223	152.50	0.2304	1.83914	0.48
50.0893	3355.33	0.0768	1.81964	10.57
50.7224	546.66	0.3456	1.79841	1.72
52.7484	210.03	0.1920	1.73400	0.66
54.8338	1004.91	0.0768	1.67288	3.16
55.2625	330.37	0.0576	1.66092	1.04
55.4220	190.88	0.0768	1.65651	0.60
56.6440	71.11	0.3072	1.62364	0.22
58.6904	39.40	0.3072	1.57181	0.12
59.9115	1971.71	0.1056	1.54266	6.21
64.0004	388.77	0.0768	1.45361	1.22
65.2196	53.40	0.3840	1.42935	0.17
67.6925	1149.91	0.0864	1.38303	3.62
68.0996	1431.82	0.0864	1.37575	4.51
68.2754	1512.28	0.0960	1.37263	4.76

Figure 73: Reference diffractogram for Sample JP2. Red arrows point to most intense coffinite peaks, black to pyrite. Silicates removed from diffractogram to highlight coffinite and pyrite peaks.

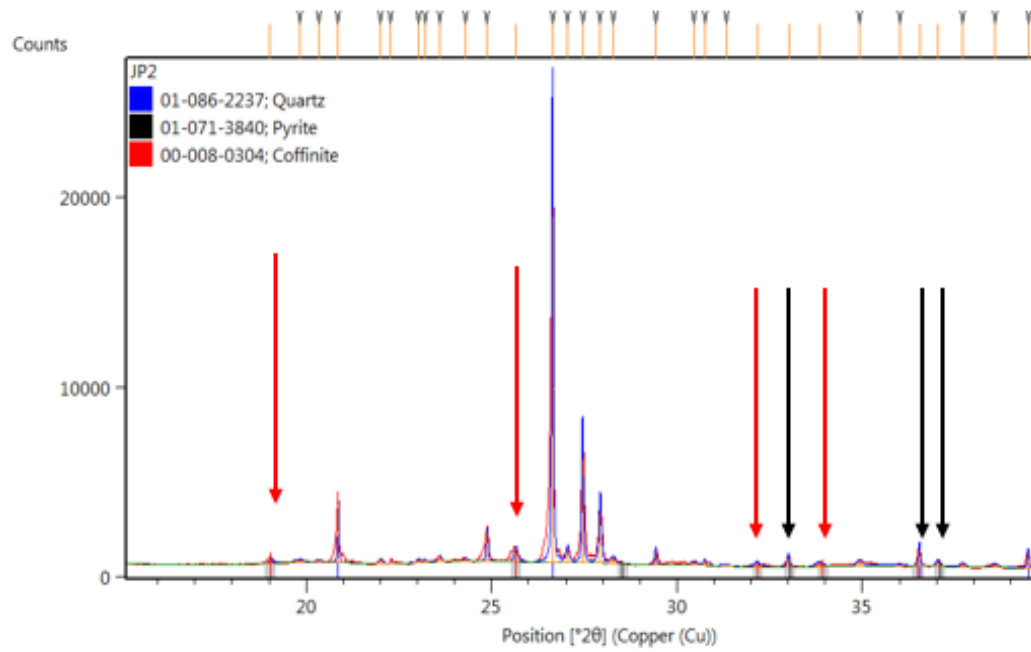


Figure 74: Reference pattern list for Sample JP2.

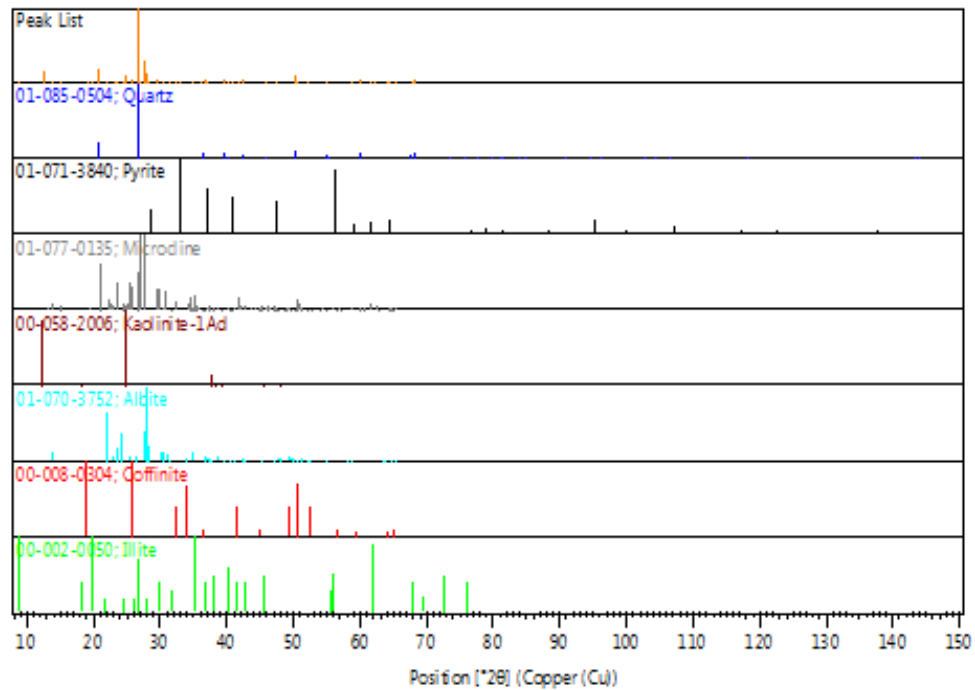


Table 8: Reference peak list for sample JP2.

Pos. [$^{\circ}2\theta$]	Height [cts]	FWHM Left [$^{\circ}2\theta$]	d-spacing [Å]	Rel. Int. [%]
8.8603	149.83	0.0945	9.97234	0.81
12.4138	2888.33	0.0630	7.12453	15.52
13.6768	366.73	0.0394	6.46935	1.97
13.9080	359.84	0.0630	6.36232	1.93
14.9975	41.88	0.3779	5.90245	0.23
19.0660	347.85	0.0630	4.65112	1.87
19.8665	157.55	0.2834	4.46549	0.85
20.3784	136.96	0.1260	4.35446	0.74
20.8900	3156.18	0.0394	4.24896	16.96
22.0495	211.66	0.1102	4.02807	1.14
22.3268	188.09	0.0472	3.97866	1.01
23.0648	160.00	0.1102	3.85299	0.86
23.2387	124.73	0.0945	3.82456	0.67
23.6399	254.15	0.0945	3.76054	1.37
24.3307	140.85	0.1417	3.65532	0.76
24.9062	1629.06	0.0551	3.57215	8.75
25.6905	740.83	0.1102	3.46484	3.98
26.6894	18610.64	0.0480	3.33739	100.00
27.0997	581.98	0.0960	3.28778	3.13
27.5002	5521.06	0.0480	3.24081	29.67
27.9719	2583.88	0.0768	3.18721	13.88
28.3330	246.56	0.1536	3.14741	1.32
29.4733	690.17	0.0480	3.02818	3.71
30.5096	141.45	0.1536	2.92765	0.76
30.7946	210.23	0.0960	2.90120	1.13
31.3812	39.07	0.3072	2.84829	0.21
32.2057	179.71	0.1536	2.77723	0.97
33.0540	477.99	0.0768	2.70787	2.57
33.8780	171.57	0.2304	2.64387	0.92
34.9758	214.31	0.1536	2.56335	1.15
36.0463	53.50	0.2304	2.48965	0.29
36.5866	899.03	0.0480	2.45411	4.83
37.0885	242.32	0.1152	2.42204	1.30
37.7505	146.34	0.1536	2.38108	0.79
38.6139	150.99	0.1920	2.32980	0.81
39.5139	707.93	0.0576	2.27878	3.80
40.3307	455.33	0.0672	2.23450	2.45
40.7834	148.20	0.0576	2.21073	0.80
41.8383	355.50	0.0576	2.15740	1.91
42.4870	775.59	0.0576	2.12595	4.17
45.8407	462.81	0.0384	1.97791	2.49
45.9535	259.94	0.0576	1.97332	1.40
47.4848	117.38	0.2304	1.91319	0.63
48.9914	38.91	0.4608	1.85782	0.21
50.1876	1831.74	0.0576	1.81631	9.84
50.5726	428.37	0.0672	1.80338	2.30
50.7012	402.21	0.0576	1.79911	2.16
52.0233	35.10	0.2304	1.75645	0.19
52.8100	56.92	0.3840	1.73213	0.31
54.9088	513.66	0.0480	1.67078	2.76

Table 8 Continued

56.2924	211.23	0.0768	1.63295	1.14
58.7243	65.31	0.1536	1.57099	0.35
59.9974	843.81	0.0864	1.54066	4.53
61.6393	55.27	0.6144	1.50350	0.30
62.3397	48.40	0.2304	1.48828	0.26
64.0574	247.59	0.0768	1.45245	1.33
64.2492	169.56	0.1152	1.44858	0.91
65.2438	53.93	0.3840	1.42888	0.29
67.7828	490.61	0.0672	1.38140	2.64
68.1820	726.32	0.0576	1.37428	3.90
68.3475	638.41	0.0864	1.37136	3.43

Figure 75: Reference pattern list for Sample JP3.

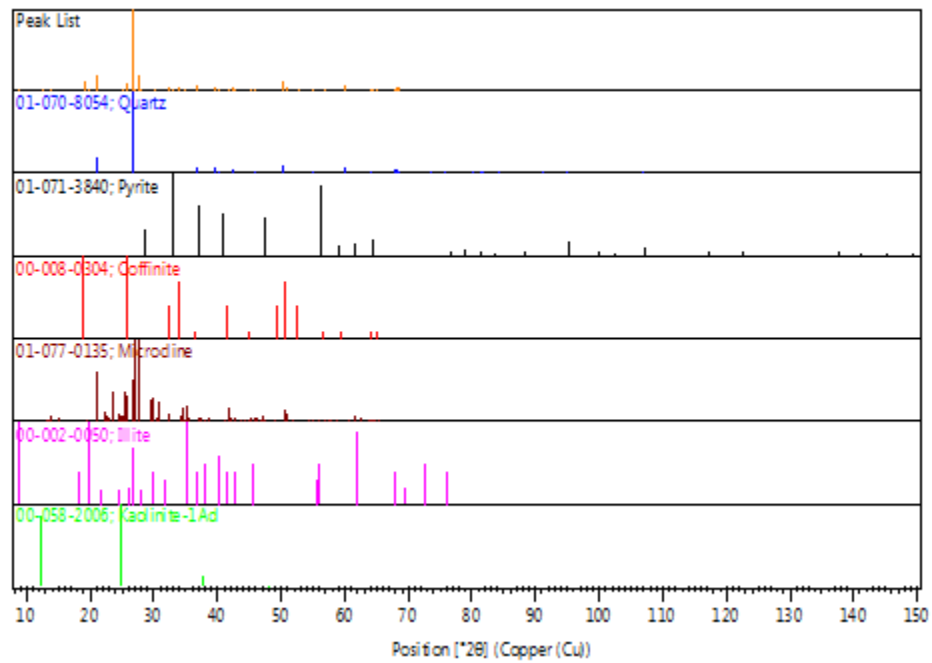


Table 9: Reference peak list for sample JP3.

Pos. [°2θ]	Height [cts]	FWHM Left [°2θ]	d-spacing [Å]	Rel. Int. [%]
8.8919	272.02	0.0945	9.94519	1.09
12.4278	593.38	0.0787	7.12242	2.39
13.7079	357.37	0.0630	6.46008	1.44
19.0882	2732.12	0.0472	4.64962	11.00
19.7677	576.07	0.2204	4.49128	2.32
20.9220	4461.95	0.0551	4.24603	17.96

Table 9 Continued

23.2541	100.99	0.1889	3.82522	0.41
24.0691	97.17	0.0945	3.69751	0.39
24.9535	260.35	0.1260	3.56844	1.05
25.7175	2683.26	0.0708	3.46414	10.80
26.7023	24842.46	0.0576	3.33581	100.00
26.7772	11090.88	0.0384	3.33491	44.64
27.1365	485.13	0.1152	3.28341	1.95
27.5158	4624.12	0.0480	3.23900	18.61
27.5905	3032.64	0.0480	3.23843	12.21
27.9812	608.93	0.0288	3.18618	2.45
28.5325	79.64	0.2304	3.12585	0.32
29.5327	186.50	0.1152	3.02222	0.75
30.1461	484.74	0.0576	2.96211	1.95
30.7977	164.95	0.2688	2.90091	0.66
32.1993	767.43	0.2496	2.77776	3.09
33.0172	317.78	0.1344	2.71080	1.28
33.9239	1415.01	0.1728	2.64039	5.70
34.9805	256.02	0.6144	2.56302	1.03
36.6008	1498.63	0.0672	2.45319	6.03
37.0912	248.34	0.1920	2.42187	1.00
38.6914	99.96	0.3072	2.32531	0.40
39.5368	1127.95	0.0672	2.27752	4.54
39.6315	518.47	0.0576	2.27794	2.09
40.3532	625.45	0.0672	2.23330	2.52
40.7717	77.03	0.1536	2.21134	0.31
41.6785	483.83	0.3456	2.16530	1.95
42.5060	980.79	0.0480	2.12504	3.95
42.6319	441.11	0.0576	2.12432	1.78
45.2417	339.94	0.2688	2.00270	1.37
45.8400	670.88	0.0672	1.97794	2.70
45.9696	354.24	0.0768	1.97756	1.43
47.3823	115.94	0.2304	1.91709	0.47
49.6361	277.14	0.1536	1.83519	1.12
50.1988	2496.61	0.0576	1.81593	10.05
50.3365	1229.91	0.0576	1.81579	4.95
50.7616	872.34	0.1728	1.79711	3.51
52.8415	299.13	0.1536	1.73117	1.20
54.9147	721.00	0.0672	1.67061	2.90
55.0679	335.49	0.0672	1.67047	1.35
55.3782	207.32	0.0768	1.65772	0.83
56.2423	135.40	0.1920	1.63428	0.55
56.7330	74.56	0.3072	1.62131	0.30
58.7710	66.64	0.2304	1.56985	0.27
60.0101	1551.80	0.0960	1.54036	6.25
60.1835	781.46	0.0576	1.54016	3.15
61.6484	169.06	0.3840	1.50330	0.68
64.0827	389.25	0.0960	1.45194	1.57
64.2653	266.35	0.1344	1.44825	1.07
65.2049	100.14	0.3840	1.42964	0.40
67.7753	924.06	0.0384	1.38154	3.72
67.9732	526.94	0.0960	1.37800	2.12
68.1996	995.62	0.0576	1.37397	4.01
68.3699	1144.86	0.0960	1.37097	4.61
68.5595	349.85	0.0768	1.37103	1.41

Mt. Taylor Mine

Figure 76: Reference pattern list for Sample MT1.

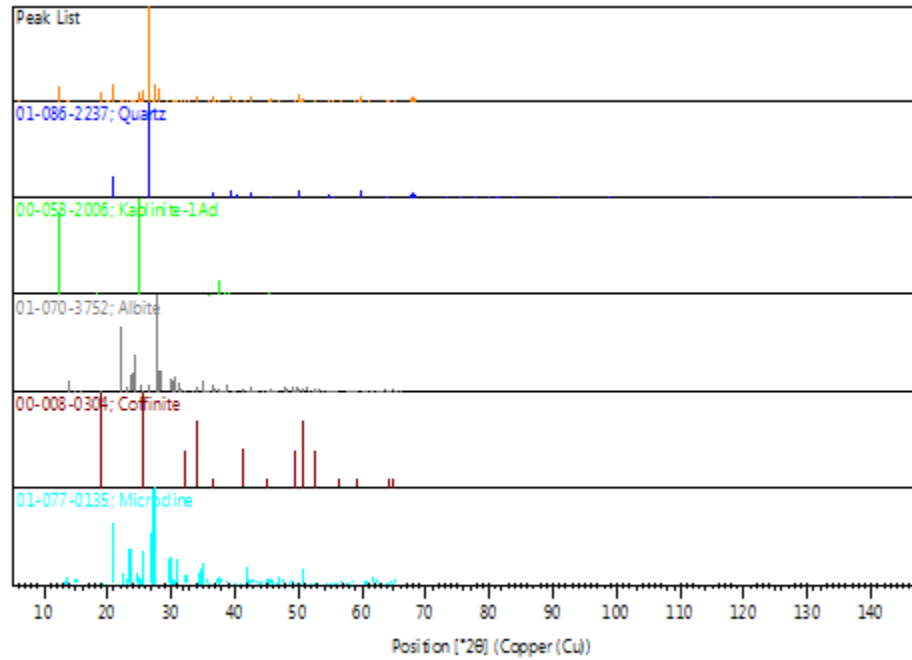


Table 10: Reference peak list for sample MT1.

Pos. [°2θ]	Height [cts]	FWHM Left [°2θ]	d-spacing [Å]	Rel. Int. [%]
6.1669	89.12	0.5038	14.32036	0.39
12.3665	3776.39	0.0630	7.15168	16.66
12.5119	1230.83	0.0472	7.06892	5.43
13.6316	288.86	0.0630	6.49067	1.27
13.8568	438.45	0.0630	6.38571	1.93
19.0665	2078.27	0.0945	4.65101	9.17
19.8376	82.63	0.0945	4.47193	0.36
20.3721	80.02	0.1260	4.35579	0.35
20.8492	4302.36	0.0472	4.25717	18.99
22.0061	396.66	0.1102	4.03591	1.75
22.3017	104.93	0.0945	3.98307	0.46
22.9977	130.78	0.1260	3.86408	0.58
23.1849	194.80	0.0472	3.83332	0.86
23.5985	312.78	0.1260	3.76706	1.38
23.9747	213.12	0.0945	3.70879	0.94
24.2950	226.98	0.1102	3.66062	1.00
24.8529	1921.75	0.0551	3.57969	8.48

Table 10 Continued

25.1603	739.25	0.0630	3.53665	3.26
25.6415	2529.52	0.0551	3.47135	11.16
26.6425	22660.75	0.0480	3.34315	100.00
27.0615	359.91	0.0768	3.29234	1.59
27.4566	4119.22	0.0672	3.24585	18.18
27.9244	3212.56	0.0672	3.19253	14.18
29.4520	112.67	0.1152	3.03033	0.50
30.4528	251.45	0.0960	2.93297	1.11
30.7368	153.08	0.1536	2.90652	0.68
30.9539	235.79	0.0576	2.88663	1.04
31.3898	38.63	0.2688	2.84753	0.17
32.2012	708.24	0.1056	2.77761	3.13
32.9808	79.14	0.1536	2.71371	0.35
33.9309	1321.37	0.0576	2.63987	5.83
35.0087	108.00	0.2304	2.56102	0.48
35.8804	275.92	0.3456	2.50077	1.22
36.5445	1447.26	0.0576	2.45684	6.39
36.9836	97.49	0.1152	2.42867	0.43
37.6834	170.98	0.1920	2.38516	0.75
38.4967	142.67	0.3072	2.33662	0.63
39.4700	1212.33	0.0480	2.28122	5.35
40.2928	613.94	0.0672	2.23651	2.71
41.5896	409.32	0.1536	2.16972	1.81
42.4582	1109.85	0.0768	2.12732	4.90
45.3134	324.94	0.0960	1.99969	1.43
45.7879	607.54	0.0672	1.98007	2.68
47.1133	34.67	0.4608	1.92741	0.15
48.8667	57.18	0.3072	1.86227	0.25
49.5235	265.35	0.1152	1.83910	1.17
50.1450	1795.99	0.0768	1.81775	7.93
50.5287	307.37	0.0576	1.80484	1.36
50.7550	826.26	0.0672	1.79733	3.65
52.7143	279.11	0.1920	1.73504	1.23
54.8618	603.50	0.0672	1.67210	2.66
55.3220	255.92	0.0768	1.65927	1.13
56.0933	34.87	0.3072	1.63827	0.15
56.5972	102.83	0.1920	1.62488	0.45
58.7006	42.47	0.3072	1.57156	0.19
59.6125	275.31	0.1728	1.54968	1.21
59.9586	1373.78	0.0768	1.54156	6.06
61.2259	69.32	0.3072	1.51266	0.31
62.3366	25.75	0.2304	1.48835	0.11
64.0245	319.69	0.0672	1.45312	1.41
64.2144	321.41	0.0768	1.44928	1.42
65.3198	169.46	0.0768	1.42740	0.75
66.0619	39.88	0.4608	1.41315	0.18
67.7417	725.02	0.1056	1.38214	3.20
68.1390	1002.21	0.0576	1.37505	4.42
68.3023	1037.67	0.0768	1.37216	4.58

Figure 77: Reference diffractogram of schoepite and jachymovite in Sample MT2. Black arrows point to most intense Jachymovite peaks, green to schoepite. Silicates removed from diffractogram to highlight uranyl-sulfates.

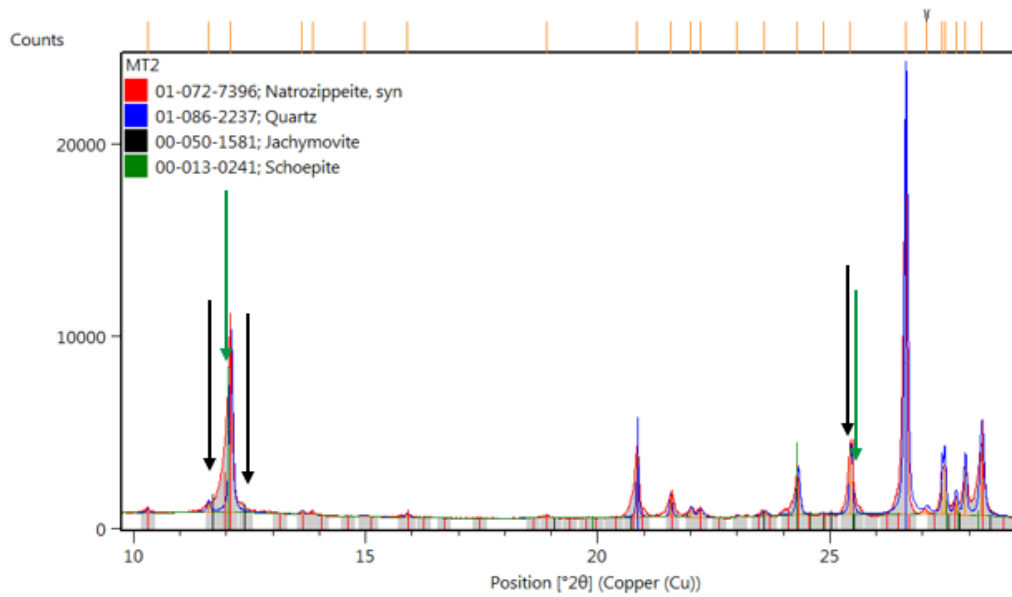


Figure 78: Reference pattern list of schoepite and jachymovite in Sample MT2.

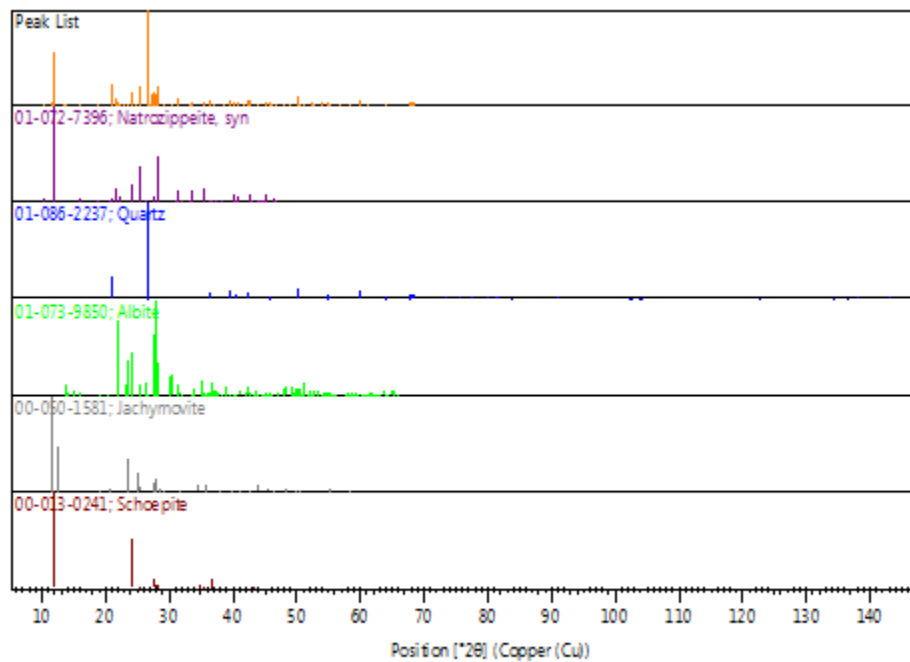


Table 11: Reference peak list for sample MT2

Pos. [$^{\circ}2\theta$]	Height [cts]	FWHM Left [$^{\circ}2\theta$]	d-spacing [Å]	Rel. Int. [%]
10.3001	239.77	0.0630	8.58133	1.49
11.6068	526.60	0.0787	7.61802	3.27
12.0931	8779.88	0.0866	7.31277	54.59
13.6305	158.52	0.0945	6.49120	0.99
13.8505	180.71	0.0472	6.38857	1.12
14.9615	59.19	0.1889	5.91659	0.37
15.8933	217.16	0.0787	5.57173	1.35
18.8958	128.39	0.0945	4.69263	0.80
20.8395	3377.69	0.0472	4.25914	21.00
21.5623	1131.76	0.0630	4.11796	7.04
21.9963	495.48	0.0945	4.03768	3.08
22.2063	413.82	0.1260	3.99998	2.57
22.9870	77.88	0.1260	3.86587	0.48
23.5857	248.73	0.1102	3.76907	1.55
24.3003	2296.71	0.0866	3.65982	14.28
24.8530	26.10	0.1260	3.57967	0.16
25.4397	3375.31	0.0787	3.49843	20.99
26.6423	16084.33	0.0864	3.34318	100.00
27.0970	218.52	0.1344	3.28810	1.36
27.4220	1738.79	0.0384	3.24987	10.81
27.4809	2310.33	0.0672	3.24303	14.36
27.7232	820.93	0.0768	3.21524	5.10
27.9243	2154.04	0.0672	3.19254	13.39
28.2810	3355.67	0.1056	3.15308	20.86
29.1252	96.88	0.1536	3.06358	0.60
29.4410	95.94	0.1152	3.03143	0.60
30.4603	261.49	0.0576	2.93227	1.63
30.7771	116.95	0.2304	2.90281	0.73
31.2770	1150.95	0.1056	2.85754	7.16
32.3569	79.54	0.3840	2.76459	0.49
33.1869	139.77	0.1920	2.69732	0.87
33.6324	561.32	0.1344	2.66261	3.49
35.5226	678.11	0.1536	2.52514	4.22
36.5416	922.07	0.0576	2.45703	5.73
36.8751	122.62	0.1536	2.43557	0.76
37.6693	49.69	0.2304	2.38602	0.31
38.5034	21.06	0.3840	2.33623	0.13
39.4664	767.81	0.0480	2.28142	4.77
40.0286	320.96	0.0960	2.25066	2.00
40.2814	561.18	0.0768	2.23712	3.49
40.8033	433.51	0.0960	2.20970	2.70
41.7663	130.91	0.1920	2.16095	0.81
42.4535	889.20	0.0768	2.12755	5.53
42.5831	807.35	0.0768	2.12137	5.02
42.7055	757.79	0.0960	2.11557	4.71
43.6303	67.85	0.1920	2.07285	0.42
44.0604	68.01	0.1536	2.05361	0.42
45.3046	421.25	0.2304	2.00006	2.62
45.7883	538.12	0.0768	1.98005	3.35
46.2514	237.78	0.1152	1.96130	1.48

Table 11 Continued

46.6249	125.89	0.1152	1.94645	0.78
48.0535	186.11	0.1920	1.89187	1.16
49.0579	69.56	0.2688	1.85546	0.43
50.1304	1602.28	0.0672	1.81825	9.96
50.5268	191.70	0.2688	1.80491	1.19
51.2416	59.47	0.2304	1.78140	0.37
52.2792	577.93	0.1152	1.74846	3.59
52.8139	97.50	0.3072	1.73201	0.61
53.8558	546.74	0.1536	1.70093	3.40
54.8701	508.85	0.0576	1.67186	3.16
55.3124	137.95	0.0960	1.65954	0.86
56.9207	98.20	0.3072	1.61641	0.61
58.4513	307.89	0.1536	1.57767	1.91
59.9469	1045.02	0.0864	1.54184	6.50
61.0947	28.40	0.4608	1.51559	0.18
61.8219	40.83	0.4608	1.49950	0.25
64.0250	237.05	0.0576	1.45311	1.47
65.3058	97.41	0.2304	1.42767	0.61
66.7581	87.25	0.2304	1.40010	0.54
67.7245	603.38	0.0768	1.38245	3.75
68.1587	661.93	0.0384	1.37470	4.12
68.3308	712.14	0.0960	1.37165	4.43

Figure 79: Reference graphic XRD scan for Sample MT3.

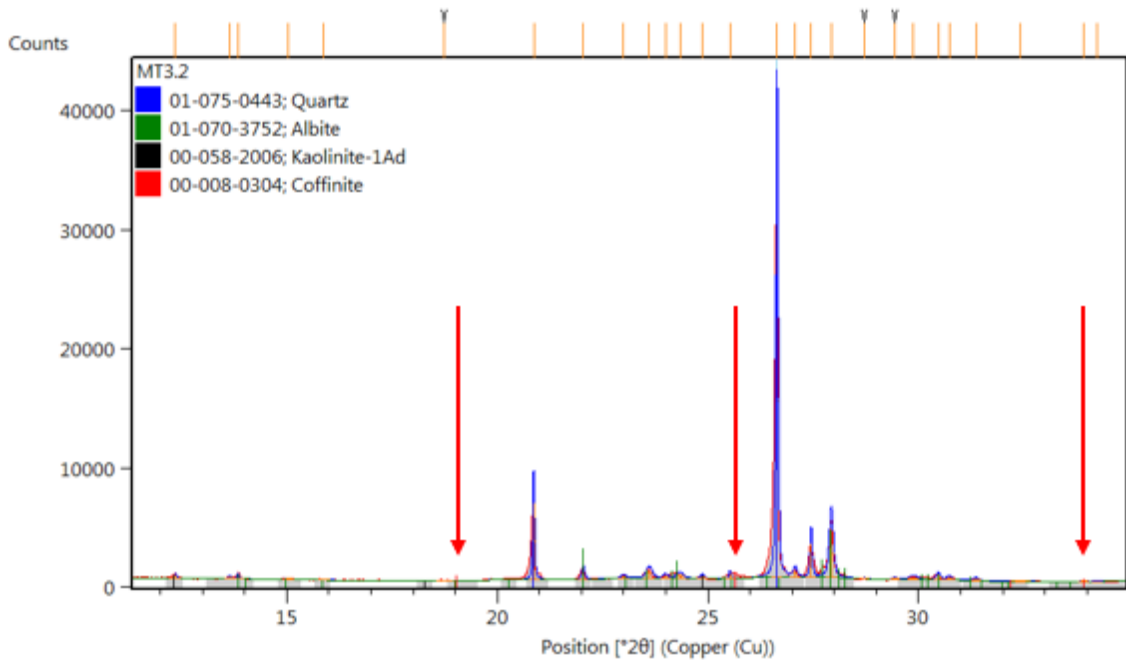


Figure 80: Reference pattern list for sample MT3.

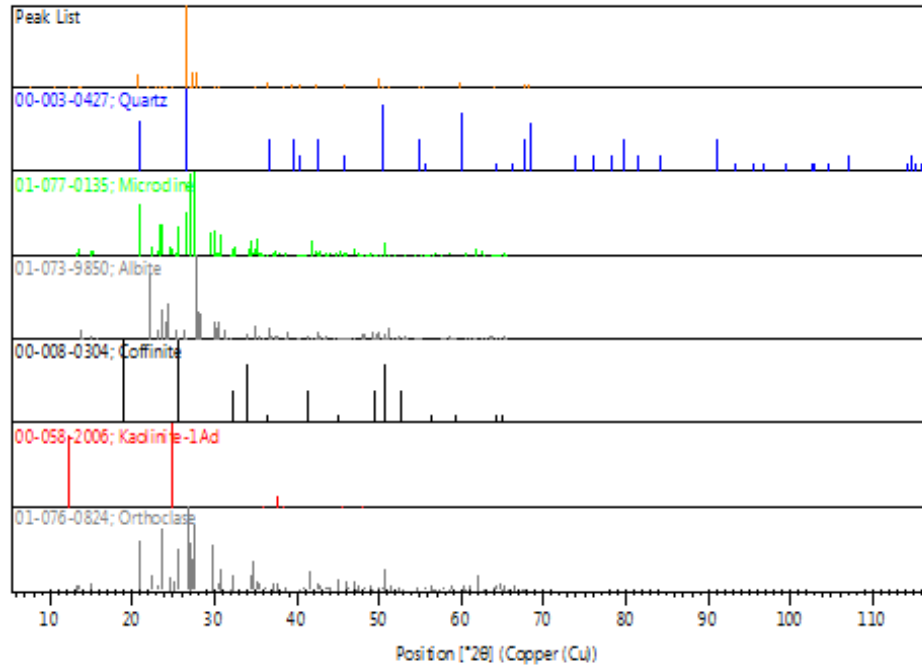


Table 12: Reference peak list for sample MT3.

Pos. [°2θ]	Height [cts]	FWHM Left [°2θ]	d-spacing [Å]	Rel. Int. [%]
6.4372	75.11	0.3779	13.71967	0.16
7.5317	137.99	0.1889	11.72828	0.29
8.7716	84.74	0.0945	10.07298	0.18
10.6770	304.41	0.0630	8.27928	0.65
11.5710	75.57	0.0945	7.64150	0.16
12.3183	929.12	0.0551	7.17953	1.97
13.5681	600.13	0.0394	6.52089	1.27
13.8011	994.60	0.0551	6.41134	2.11
14.9256	91.55	0.3779	5.93074	0.19
19.6973	129.89	0.1574	4.50347	0.28
20.7947	7943.48	0.0551	4.26822	16.85
21.9651	767.94	0.0945	4.04334	1.63
22.2444	152.24	0.0945	3.99321	0.32
22.9612	245.35	0.0945	3.87014	0.52
23.4699	705.96	0.0551	3.78740	1.50
23.9538	482.00	0.0472	3.71197	1.02
24.2306	668.38	0.1102	3.67019	1.42
24.8101	557.06	0.0945	3.58577	1.18

Table 12 Continued

25.5776	462.95	0.0945	3.47989	0.98
26.5943	47139.65	0.0576	3.34911	100.00
27.0492	714.91	0.1536	3.29381	1.52
27.4099	8550.57	0.0768	3.25128	18.14
27.8791	8961.75	0.0672	3.19761	19.01
28.2265	489.90	0.1536	3.15904	1.04
29.3772	115.13	0.0768	3.03787	0.24
30.1427	285.04	0.1152	2.96244	0.60
30.4006	560.97	0.0960	2.93789	1.19
30.7158	348.04	0.1536	2.90846	0.74
31.2685	134.83	0.1920	2.85830	0.29
32.0914	58.76	0.3072	2.78686	0.12
33.8561	48.62	0.1920	2.64552	0.10
34.1732	69.53	0.1536	2.62170	0.15
35.0835	235.32	0.1920	2.55573	0.50
36.4982	3017.06	0.0768	2.45985	6.40
36.9510	56.48	0.1536	2.43074	0.12
37.5986	101.42	0.3072	2.39035	0.22
38.5227	183.99	0.1920	2.33511	0.39
39.4073	2410.80	0.0768	2.28470	5.11
40.2481	1476.63	0.0768	2.23889	3.13
41.1117	43.03	0.3072	2.19383	0.09
41.7764	379.52	0.0672	2.16045	0.81
42.4053	1974.31	0.0768	2.12985	4.19
45.7487	1646.13	0.0864	1.98167	3.49
47.0557	55.99	0.2304	1.92963	0.12
48.2327	70.66	0.1920	1.88526	0.15
48.8052	50.18	0.2304	1.86447	0.11
49.0642	50.95	0.3072	1.85524	0.11
50.0938	4879.91	0.0960	1.81949	10.35
50.5244	362.57	0.2688	1.80499	0.77
51.0946	183.13	0.0768	1.78618	0.39
52.1689	29.05	0.3072	1.75189	0.06
53.2256	48.66	0.2688	1.71958	0.10
54.8269	1663.38	0.0672	1.67308	3.53
55.2855	465.89	0.0864	1.66028	0.99
56.6724	25.43	0.2304	1.62290	0.05
57.1781	83.64	0.0576	1.60974	0.18
57.7785	34.81	0.7680	1.59443	0.07
58.5972	106.49	0.1536	1.57409	0.23
59.9270	3221.17	0.0864	1.54230	6.83
63.0426		0.1152	1.47337	0.17
63.9905	745.77	0.0768	1.45381	1.58
65.1656	33.02	0.3840	1.43041	0.07
65.7308	28.37	0.0960	1.41947	0.06
67.6925	2030.95	0.0864	1.38303	4.31
68.1037	2207.16	0.0768	1.37567	4.68
68.2802	2179.12	0.1056	1.37255	4.62

Figure 81: Reference pattern list for Sample MT5.

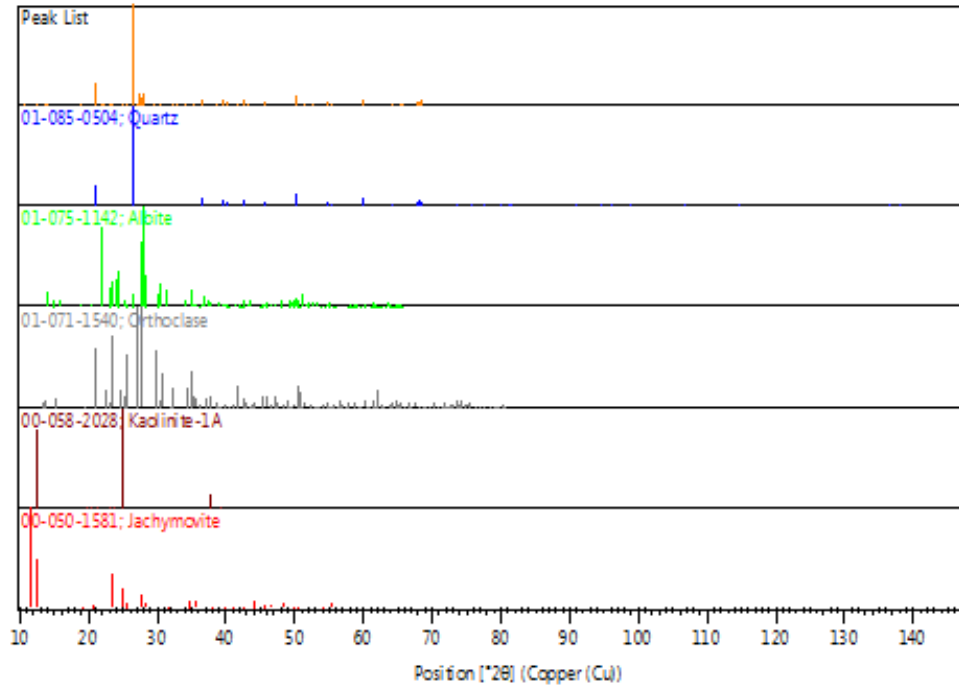


Table 13: Reference peak list for sample MT5.

Pos. [°2θ]	Height [cts]	FWHM Left [°2θ]	d-spacing [Å]	Rel. Int. [%]
10.7443	61.29	0.2519	8.22755	0.31
11.6306	89.53	0.1889	7.60249	0.46
12.3675	440.96	0.0315	7.15112	2.24
13.6138	119.13	0.0787	6.49914	0.61
13.8520	207.79	0.0630	6.38792	1.06
18.9848	44.06	0.2519	4.67083	0.22
19.7723	44.87	0.1889	4.48654	0.23
20.8614	4414.99	0.0480	4.25472	22.47
22.0254	393.09	0.1152	4.03242	2.00
22.3099	135.04	0.0768	3.98163	0.69
23.0217	144.11	0.0960	3.86012	0.73
23.5974	410.98	0.0672	3.76723	2.09
24.0040	145.14	0.1152	3.70433	0.74
24.3399	156.97	0.1536	3.65395	0.80
24.8828	313.32	0.0672	3.57545	1.59
25.5366	352.13	0.0960	3.48538	1.79

Table 13 Continued

25.6752	458.39	0.0576	3.46688	2.33
26.6448	19647.49	0.0576	3.34288	100.00
27.0819	313.94	0.1344	3.28991	1.60
27.4447	2160.01	0.0480	3.24723	10.99
27.5240	1569.79	0.0576	3.23806	7.99
27.7183	534.70	0.0576	3.21580	2.72
27.9183	2326.67	0.0480	3.19322	11.84
29.4672	356.21	0.0480	3.02879	1.81
30.4680	244.22	0.1344	2.93155	1.24
30.8057	143.76	0.2688	2.90018	0.73
31.3667	59.35	0.2304	2.84957	0.30
32.4027	67.77	0.4608	2.76079	0.34
32.9982	45.37	0.1152	2.71231	0.23
34.2230	51.09	0.1536	2.61800	0.26
35.1583	99.03	0.1920	2.55047	0.50
36.5424	1126.45	0.0672	2.45698	5.73
37.7263	61.10	0.2688	2.38255	0.31
38.5484	77.88	0.1536	2.33361	0.40
39.4670	1116.31	0.0576	2.28138	5.68
40.2870	653.43	0.0480	2.23682	3.33
41.8122	214.73	0.1152	2.15868	1.09
42.4534	1073.37	0.0480	2.12755	5.46
43.2731	43.97	0.3072	2.08913	0.22
45.7917	631.77	0.0576	1.97991	3.22
47.0611	39.38	0.3072	1.92942	0.20
48.3004	39.73	0.2304	1.88277	0.20
50.1394	1875.96	0.0864	1.81794	9.55
50.5411	161.54	0.2688	1.80443	0.82
51.2329	53.74	0.2304	1.78168	0.27
52.7154	66.55	0.1152	1.73501	0.34
54.8848	519.32	0.0672	1.67145	2.64
55.3146	176.35	0.0768	1.65948	0.90
56.7388	2.30	0.3072	1.62116	0.01
57.4944	9.72	0.4608	1.60163	0.05
58.7143	39.34	0.2304	1.57123	0.20
59.9535	1218.60	0.0960	1.54168	6.20
64.0452	250.84	0.0768	1.45270	1.28
65.3003	27.91	0.3840	1.42778	0.14
65.7683	40.75	0.1152	1.41875	0.21
67.7307	731.41	0.0960	1.38234	3.72
68.1444	859.49	0.0960	1.37495	4.37
68.3205	958.20	0.1056	1.37184	4.88

Section 31

Figure 82: Reference pattern list for sample KM1.

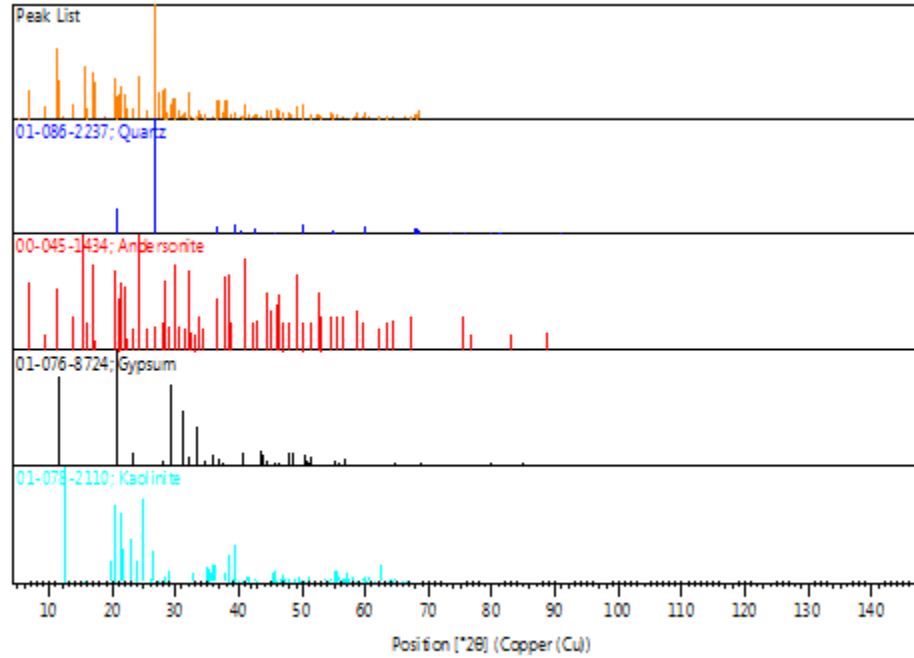


Table 14: Reference peak list for sample KM1.

Pos. [°2θ]	Height [cts]	FWHM Left [°2θ]	d-spacing [Å]	Rel. Int. [%]
5.2861	47.63	0.5038	16.70431	1.12
6.8086	1038.59	0.0551	12.97203	24.47
9.3655	448.71	0.0551	9.43554	10.57
11.1509	2582.44	0.0472	7.92843	60.86
11.6312	1389.16	0.0472	7.60207	32.74
12.3454	112.77	0.0945	7.16384	2.66
13.6121	530.62	0.0630	6.49995	12.50
15.5495	1969.73	0.0630	5.69414	46.42
15.9423	413.17	0.0630	5.55474	9.74
16.8347	1732.29	0.0630	5.26222	40.82
17.1308	1366.35	0.0708	5.17193	32.20
18.7712	93.68	0.0945	4.72350	2.21
20.4688	1504.73	0.0551	4.33541	35.46
20.6722	595.28	0.0787	4.29323	14.03
20.8314	870.12	0.0472	4.26077	20.50
20.9567	887.36	0.0787	4.23557	20.91
21.2559	1171.60	0.0551	4.17663	27.61
21.8846	917.69	0.0315	4.05804	21.63
22.3942	402.67	0.0315	3.96683	9.49

Table 14 Continued

23.1950	420.36	0.0551	3.83166	9.91
23.3645	316.44	0.0472	3.80425	7.46
24.0771	1588.93	0.0480	3.69324	37.44
24.8997	55.42	0.1152	3.57306	1.31
25.5420	349.55	0.1152	3.48465	8.24
26.6443	4243.48	0.0576	3.34294	100.00
26.8358	362.69	0.0960	3.31951	8.55
27.4615	987.67	0.0480	3.24528	23.27
27.9362	1055.95	0.0960	3.19121	24.88
28.1311	184.70	0.3072	3.16954	4.35
28.3379	1142.48	0.0672	3.14687	26.92
28.6514	252.93	0.0768	3.11315	5.96
29.1116	520.58	0.0576	3.06498	12.27
29.4400	501.13	0.0480	3.03153	11.81
29.6932	790.93	0.1344	3.00626	18.64
29.9049	773.53	0.0672	2.98546	18.23
30.3756	325.52	0.0960	2.94025	7.67
30.7205	77.35	0.1152	2.90802	1.82
31.1118	165.11	0.1536	2.87234	3.89
31.3604	277.76	0.1536	2.85013	6.55
32.0222	1026.75	0.0576	2.79272	24.20
32.5501	100.62	0.1152	2.74863	2.37
33.0157	82.96	0.1536	2.71092	1.95
33.3232	85.69	0.1344	2.68660	2.02
33.7661	308.50	0.0960	2.65237	7.27
34.0796	179.25	0.0576	2.62868	4.22
34.6670	175.95	0.0768	2.58548	4.15
35.9632	116.57	0.0960	2.49521	2.75
36.5369	714.20	0.0480	2.45733	16.83
36.7149	645.86	0.0480	2.44582	15.22
37.3765	223.40	0.0768	2.40404	5.26
37.6917	673.31	0.0672	2.38465	15.87
38.2129	677.26	0.0384	2.35332	15.96
38.7924	216.60	0.0768	2.31949	5.10
39.4746	264.71	0.0864	2.28096	6.24
40.2801	122.59	0.0576	2.23719	2.89
40.6164	139.40	0.1152	2.21944	3.29
40.8792	504.86	0.0960	2.20577	11.90
41.6657	189.15	0.0576	2.16593	4.46
42.1122	138.52	0.1920	2.14399	3.26
42.4422	158.90	0.0864	2.12809	3.74
42.6758	193.04	0.0768	2.11698	4.55
43.6032	83.43	0.1920	2.07407	1.97
44.5257	348.80	0.0768	2.03322	8.22
45.1107	323.30	0.0864	2.00820	7.62
45.8197	406.99	0.0864	1.97877	9.59
46.2955	285.84	0.0960	1.95953	6.74
46.4389	277.35	0.0768	1.95382	6.54
46.9733	252.10	0.0960	1.93282	5.94
47.9167	270.22	0.0768	1.89695	6.37
48.2907	160.79	0.0576	1.88313	3.79
49.1674	349.00	0.0576	1.85158	8.22
49.2908	432.04	0.0960	1.84724	10.18
50.1323	572.75	0.0672	1.81818	13.50

Table 14 Continued

51.3833	196.84	0.1152	1.77681	4.64
52.1384	164.72	0.1344	1.75285	3.88
52.3017	217.60	0.0960	1.74776	5.13
52.5322	209.55	0.1152	1.74063	4.94
53.0011	120.36	0.2688	1.72633	2.84
53.5891	44.89	0.1536	1.70877	1.06
54.4565	236.21	0.0960	1.68358	5.57
54.8717	180.43	0.0576	1.67182	4.25
55.6049	122.85	0.1152	1.65150	2.90
56.4818	95.35	0.1152	1.62792	2.25
57.6727	75.84	0.1920	1.59710	1.79
58.3250	117.20	0.0768	1.58079	2.76
58.6706	232.11	0.0960	1.57230	5.47
59.6800	122.18	0.0960	1.54809	2.88
59.9439	258.42	0.0768	1.54190	6.09
60.6749	86.53	0.1536	1.52507	2.04
62.1663	122.28	0.1152	1.49201	2.88
63.3743	144.87	0.0768	1.46645	3.41
64.5187	112.41	0.1152	1.44318	2.65
66.2123	88.42	0.0768	1.41031	2.08
67.2115	122.51	0.1920	1.39175	2.89
67.7317	171.12	0.0960	1.38232	4.03
68.1405	192.21	0.0672	1.37502	4.53
68.3112	299.33	0.0672	1.37200	7.05
69.6708	51.42	0.1152	1.34851	1.21

Figure 83: Reference pattern list for sample KM2.

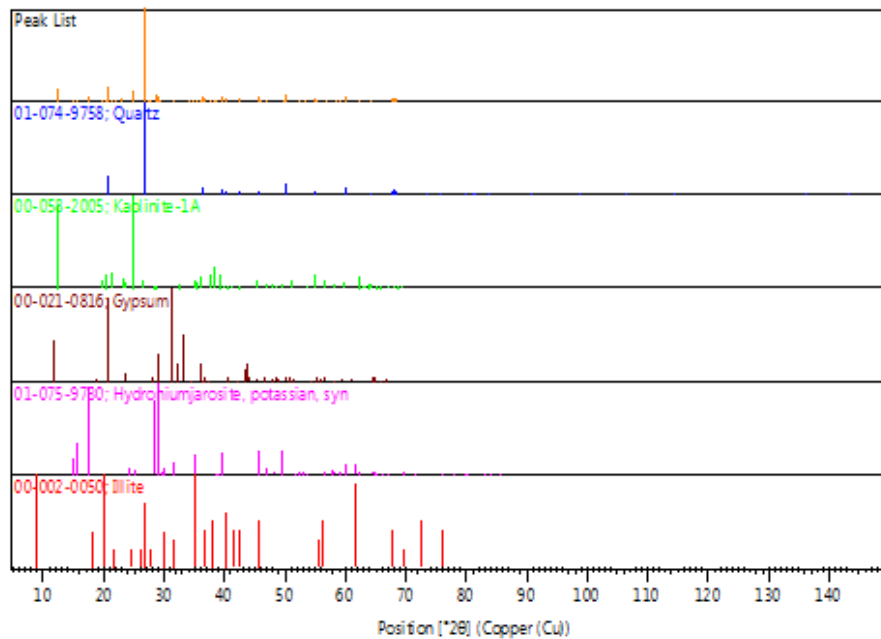


Table 15: Reference peak list for sample KM2.

Pos. [$^{\circ}2\theta$]	Height [cts]	FWHM Left [$^{\circ}2\theta$]	d-spacing [\AA]	Rel. Int. [%]
5.6945	50.49	0.7557	15.52000	0.16
8.8534	210.57	0.0630	9.98840	0.68
11.6239	244.69	0.0630	7.61316	0.79
12.3644	4176.49	0.0708	7.15881	13.55
14.8814	492.21	0.0787	5.95319	1.60
15.5932	557.29	0.1102	5.68301	1.81
17.3894	2037.08	0.0787	5.09982	6.61
19.8286	419.41	0.0945	4.47764	1.36
20.3309	599.15	0.0945	4.36813	1.94
20.8523	4983.73	0.0472	4.26008	16.17
21.2281	400.09	0.0945	4.18549	1.30
21.8771	71.75	0.1889	4.06278	0.23
23.0665	1078.08	0.0630	3.85592	3.50
24.2708	235.14	0.1260	3.66724	0.76
24.8805	3327.51	0.0551	3.57875	10.80
25.8338	210.70	0.1260	3.44880	0.68
26.6351	30822.24	0.0576	3.34408	100.00
26.7067	14136.24	0.0384	3.34355	45.86
27.4416	592.77	0.0288	3.24759	1.92
27.6751	283.24	0.0768	3.22072	0.92
28.5728	2284.15	0.1056	3.12154	7.41
28.9568	1980.30	0.0576	3.08101	6.42
29.4129	165.69	0.1152	3.03426	0.54
30.0223	266.75	0.1920	2.97405	0.87
31.4212	235.43	0.1920	2.84476	0.76
34.1674	52.04	0.2304	2.62213	0.17
34.9438	303.19	0.1152	2.56563	0.98
35.3833	435.23	0.1536	2.53476	1.41
35.9419	320.93	0.2688	2.49664	1.04
36.5317	1694.43	0.0672	2.45767	5.50
36.6338	783.33	0.0480	2.45714	2.54
37.6959	321.11	0.0768	2.38440	1.04
38.3334	289.42	0.1536	2.34620	0.94
38.4763	388.02	0.1152	2.33781	1.26
39.4601	1449.96	0.0576	2.28177	4.70
39.5651	783.85	0.0480	2.28161	2.54
40.2852	763.45	0.0480	2.23692	2.48
42.4342	1108.90	0.0672	2.12847	3.60
42.5522	526.34	0.0672	2.12812	1.71
45.7797	1326.83	0.0672	1.98040	4.30
45.9055	656.25	0.0576	1.98017	2.13
47.0567	117.30	0.3840	1.92959	0.38
47.9143	61.73	0.2304	1.89704	0.20
49.6902	515.15	0.2688	1.83332	1.67
50.1290	2732.40	0.0576	1.81830	8.87
50.2625	1371.09	0.0576	1.81828	4.45
51.0864	74.64	0.3072	1.78644	0.24
52.4427	52.80	0.3072	1.74339	0.17

Table 15 Continued

53.1466	96.88	0.2688	1.72195	0.31
54.8690	956.77	0.0864	1.67189	3.10
55.0105	616.04	0.0768	1.67207	2.00
55.3076	361.08	0.0768	1.65967	1.17
56.7659	143.99	0.2304	1.62044	0.47
58.3627	56.80	0.6144	1.57986	0.18
59.1577	64.46	0.3072	1.56051	0.21
59.9497	1916.88	0.0864	1.54177	6.22
60.1203	1114.00	0.0768	1.54162	3.61
62.3185	253.66	0.3840	1.48873	0.82
64.0175	306.40	0.0576	1.45326	0.99
64.2078	206.07	0.0768	1.44941	0.67
64.8514	81.12	0.3840	1.43657	0.26
67.7288	982.18	0.0672	1.38237	3.19
67.9250	537.99	0.0384	1.38228	1.75
68.1359	1275.35	0.0672	1.37510	4.14
68.3047	1150.29	0.0960	1.37212	3.73
68.4906	349.83	0.0768	1.37224	1.13

Figure 84: Reference diffractogram for sample KM3. Red arrows point to most intense gypsum peaks, black to pyrite. Silicates removed for clarity.

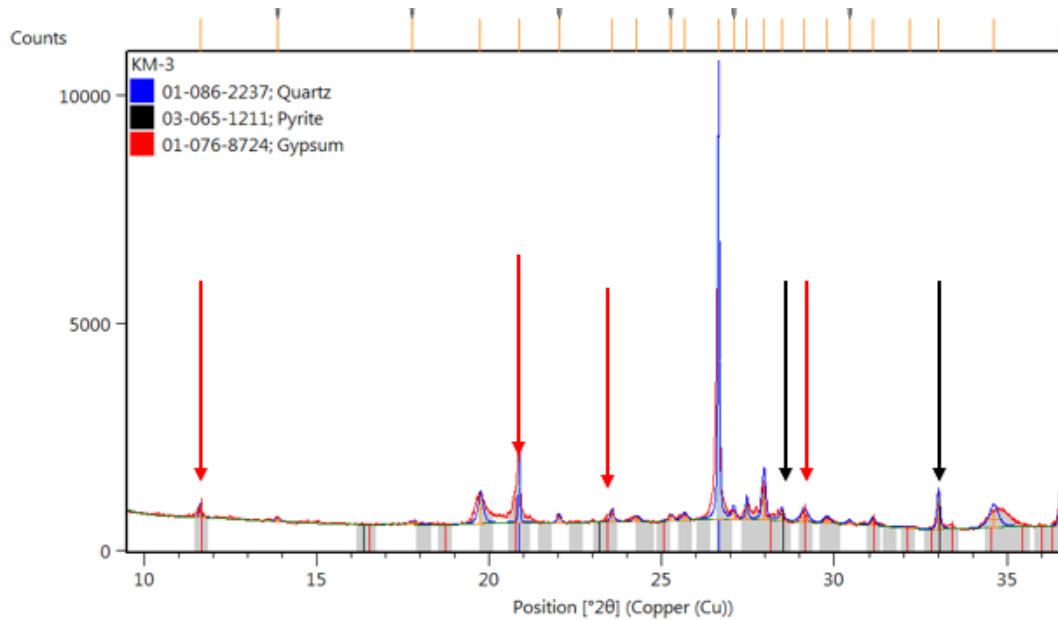


Figure 85: Reference pattern list for sample KM3.

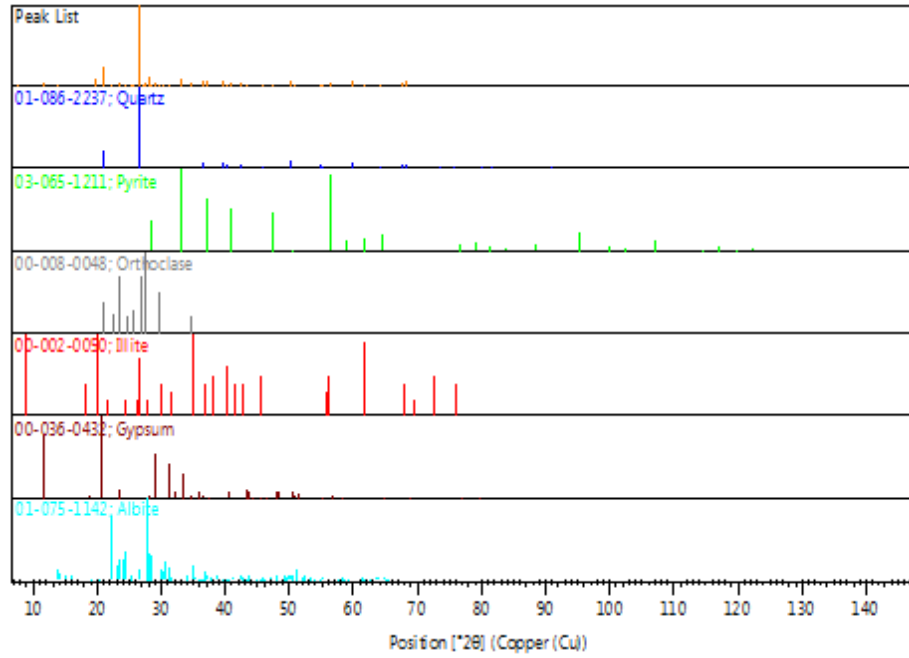


Table 16: Reference peak list for sample KM3.

Pos. [°2θ]	Height [cts]	FWHM Left [°2θ]	d-spacing [Å]	Rel. Int. [%]
7.6634	108.73	0.8817	11.52694	1.52
8.8129	62.01	0.1889	10.02583	0.87
11.6129	287.68	0.0630	7.61407	4.03
13.8598	63.22	0.1889	6.38430	0.89
17.7698	55.01	0.3779	4.98738	0.77
19.7266	651.16	0.1732	4.49683	9.13
20.8439	1639.38	0.0394	4.25824	22.99
22.0035	184.53	0.1102	4.03639	2.59
23.5353	246.65	0.1102	3.77702	3.46
24.2520	114.88	0.1889	3.66701	1.61
25.2394	126.46	0.1260	3.52574	1.77
25.6342	143.44	0.1889	3.47232	2.01
26.6407	7129.86	0.0576	3.34338	100.00
27.0786	186.29	0.1152	3.29030	2.61
27.4564	353.77	0.0768	3.24587	4.96
27.9574	772.08	0.1152	3.18884	10.83
28.4737	195.06	0.1152	3.13218	2.74
29.1247	212.64	0.2304	3.06363	2.98
29.7774	106.30	0.1920	2.99795	1.49
30.4288	61.25	0.1536	2.93523	0.86
31.1150	126.73	0.1536	2.87205	1.78

Table 16 Continued

32.1735	35.34	0.4608	2.77994	0.50
33.0151	610.60	0.0960	2.71097	8.56
34.6158	340.98	0.3072	2.58918	4.78
36.5348	574.82	0.0672	2.45747	8.06
37.0461	425.99	0.0960	2.42472	5.97
37.6950	77.65	0.3840	2.38445	1.09
39.4636	396.62	0.0768	2.28157	5.56
40.2891	224.04	0.0768	2.23671	3.14
40.7304	272.29	0.0960	2.21349	3.82
41.7229	49.01	0.3072	2.16310	0.69
42.4393	326.61	0.0960	2.12822	4.58
43.4917	40.79	0.4608	2.07913	0.57
45.7794	210.52	0.0768	1.98042	2.95
47.3986	199.18	0.0768	1.91647	2.79
47.9632	53.81	0.2304	1.89522	0.75
50.1273	569.07	0.0576	1.81835	7.98
50.6218	126.32	0.1152	1.80174	1.77
53.9443	38.80	0.6144	1.69835	0.54
54.8687	225.13	0.0768	1.67190	3.16
55.3140	96.22	0.1152	1.65949	1.35
56.2512	380.30	0.1536	1.63404	5.33
58.9168	29.05	0.4608	1.56631	0.41
59.9391	407.03	0.0672	1.54202	5.71
61.5742	229.32	0.1920	1.50493	3.22
64.2296	102.70	0.1152	1.44897	1.44
67.7423	213.86	0.0960	1.38213	3.00
68.1346	393.09	0.0288	1.37513	5.51
68.3282	413.79	0.0768	1.37170	5.80

Midnite Mine, WA State

Figure 86: Reference diffractogram for sample MD1.

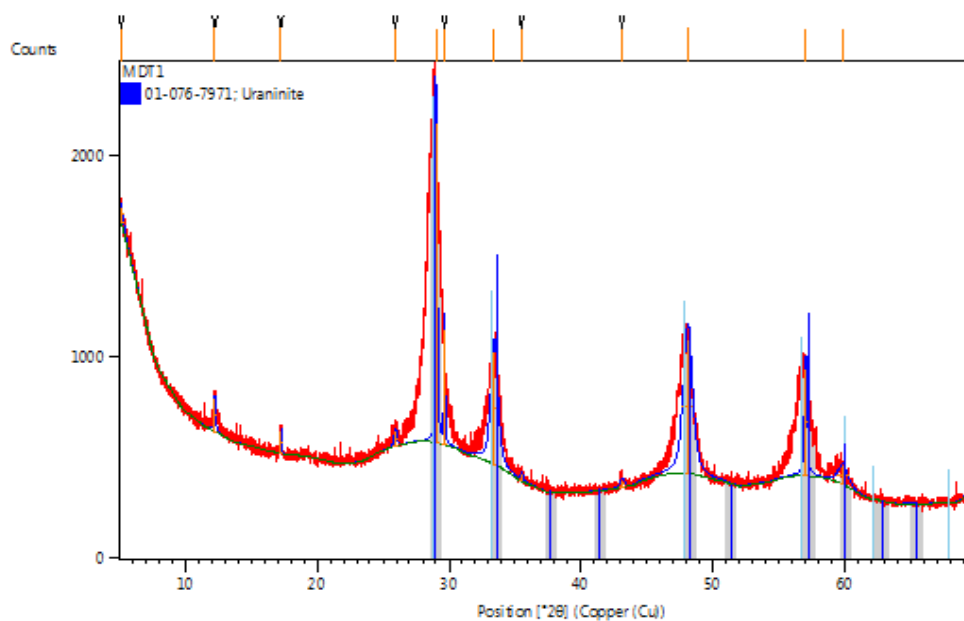


Figure 87: Reference pattern list for sample MD1.

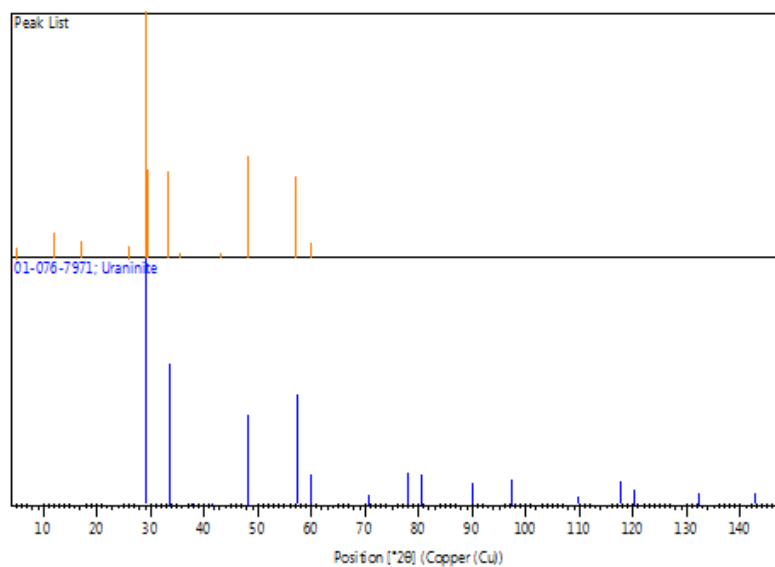


Table 17: Reference peak list for sample MD1.

Pos. [$^{\circ}2\theta$]	Height [cts]	FWHM Left [$^{\circ}2\theta$]	d-spacing [\AA]	Rel. Int. [%]
5.1236	71.83	0.5038	17.23380	4.53
12.2314	163.57	0.1574	7.23036	10.32
17.2518	109.46	0.0945	5.13592	6.90
25.9200	78.17	0.2519	3.43469	4.93
29.0218	1585.65	0.1574	3.07425	100.00
29.6410	575.24	0.0945	3.01143	36.28
33.4278	560.16	0.6298	2.67843	35.33
35.4878	37.96	0.1889	2.52754	2.39
43.1072	36.87	0.3779	2.09678	2.33
48.0897	664.52	0.8187	1.89053	41.91
57.0189	530.97	0.2519	1.61385	33.49
59.8436	92.57	0.8817	1.54425	5.84

Figure 88: Reference diffractogram for sample MD2.

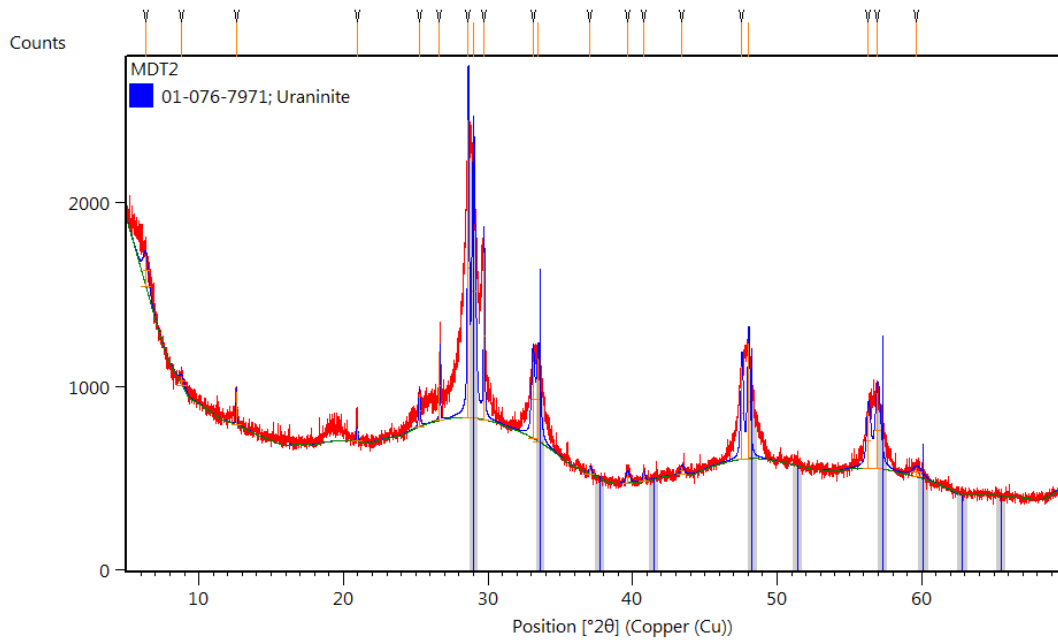


Figure 89: Reference pattern list for sample MD2.

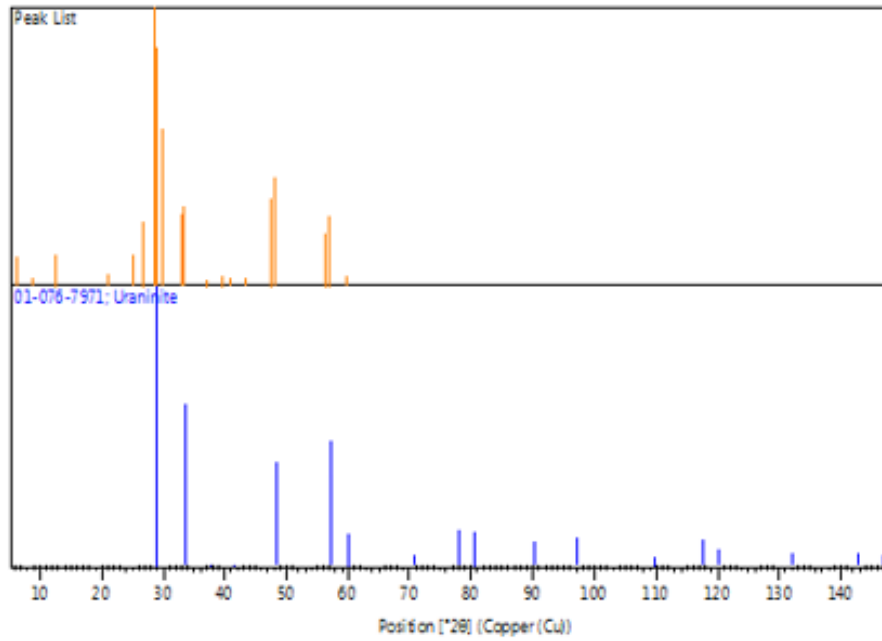


Table 18: Reference peak list for sample MD2.

Pos. [$^{\circ}2\theta$]	Height [cts]	FWHM Left [$^{\circ}2\theta$]	d-spacing [\AA]	Rel. Int. [%]
6.3419	173.55	0.4408	13.92558	10.46
8.8234	50.33	0.3779	10.01392	3.03
12.5853	186.82	0.0630	7.02786	11.26
20.9414	71.44	0.1260	4.23864	4.31
25.2390	186.77	0.1260	3.52579	11.26
26.6493	384.55	0.0630	3.34232	23.18
28.6172	1659.03	0.1260	3.11679	100.00
28.9923	1408.58	0.2834	3.07732	84.90
29.7094	931.33	0.0945	3.00466	56.14
33.0965	428.87	0.2519	2.70449	25.85
33.4764	467.09	0.3149	2.67466	28.15
37.0571	41.47	0.1889	2.42402	2.50
39.6410	58.29	0.3149	2.27177	3.51
40.7639	48.46	0.1889	2.21174	2.92
43.4312	48.01	0.2519	2.08189	2.89
47.5407	516.68	0.2204	1.91107	31.14
48.0058	644.03	0.2204	1.89364	38.82
56.2932	313.38	0.3149	1.63293	18.89
56.9336	420.54	0.4408	1.61607	25.35
59.6541	55.69	0.7557	1.54870	3.36

Piedra Triste Mine

Figure 90: Reference diffractogram for sample PT1. Red arrows point to most intense meta-tyuyamunite peaks.

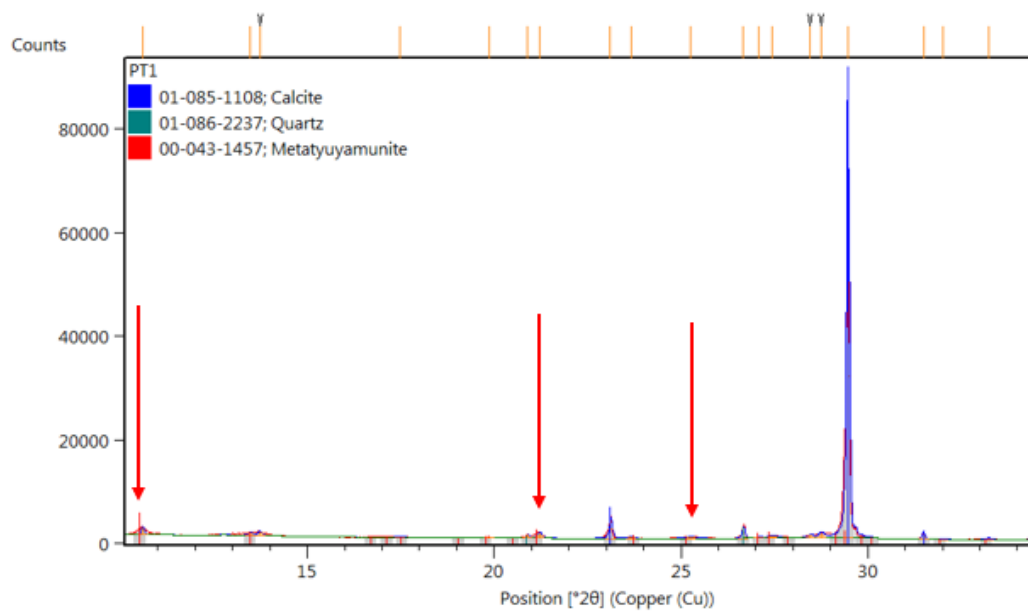


Figure 91: Reference pattern list for sample PT1.

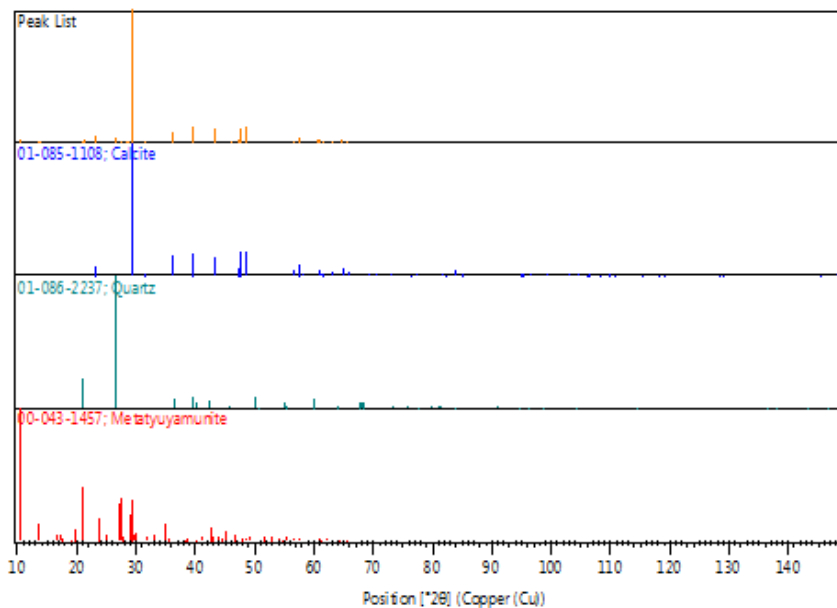


Table 19: Reference peak list for sample PT1.

Pos. [$^{\circ}2\theta$]	Height [cts]	FWHM Left [$^{\circ}2\theta$]	d-spacing [Å]	Rel. Int. [%]
10.5934	1556.43	0.0836	8.34441	2.44
13.4757	637.26	0.1004	6.56539	1.00
13.7261	715.66	0.1338	6.44618	1.12
17.4921	201.95	0.2007	5.06592	0.32
19.8728	123.32	0.1004	4.46407	0.19
20.8980	643.59	0.0669	4.24734	1.01
21.2035	1076.51	0.1506	4.18683	1.69
23.1070	3739.89	0.1004	3.84605	5.87
23.6556	233.91	0.1673	3.75810	0.37
25.2492	289.82	0.2342	3.52440	0.45
26.6630	2140.78	0.0836	3.34063	3.36
27.0893	268.98	0.1338	3.28902	0.42
27.4496	434.32	0.2342	3.24666	0.68
28.4589	553.37	0.1338	3.13377	0.87
28.7385	755.20	0.1673	3.10392	1.19
29.4668	63706.79	0.0816	3.02884	100.00
31.4950	974.73	0.0816	2.83826	1.53
32.0203	85.73	0.2448	2.79289	0.13
33.2359	179.22	0.2040	2.69346	0.28
34.8405	198.31	0.4080	2.57300	0.31
36.0364	5053.91	0.0816	2.49031	7.93
36.6196	268.88	0.1224	2.45197	0.42
39.4742	7613.43	0.0816	2.28098	11.95
41.1619	33.01	0.3264	2.19127	0.05
42.5356	142.19	0.1632	2.12363	0.22
43.2275	6991.33	0.0816	2.09123	10.97
45.8917	93.36	0.2448	1.97583	0.15
47.1727	1953.21	0.0816	1.92512	3.07
47.5609	7268.36	0.0816	1.91031	11.41
48.5659	7714.21	0.0816	1.87310	12.11
50.1751	139.17	0.1224	1.81673	0.22
51.7287	11.04	0.6528	1.76576	0.02
54.9565	112.92	0.3264	1.66944	0.18
56.6271	1035.84	0.0816	1.62409	1.63
57.4640	3039.77	0.1020	1.60241	4.77
58.1210	294.24	0.0816	1.58585	0.46
60.0051	174.23	0.0816	1.54048	0.27
60.7283	1791.78	0.1020	1.52385	2.81
61.0606	1163.35	0.0816	1.51636	1.83
61.4286	887.00	0.1020	1.50815	1.39
63.1174	656.20	0.0816	1.47180	1.03
64.7217	1766.10	0.1020	1.43914	2.77
65.6550	913.33	0.1020	1.42092	1.43
67.7858	180.80	0.0816	1.38135	0.28
68.2959	60.43	0.2448	1.37227	0.09
69.2540	359.33	0.1020	1.35561	0.56

Figure 92: Reference diffractogram for sample PT2. Red arrows point to most intense meta-tyuyamunite.

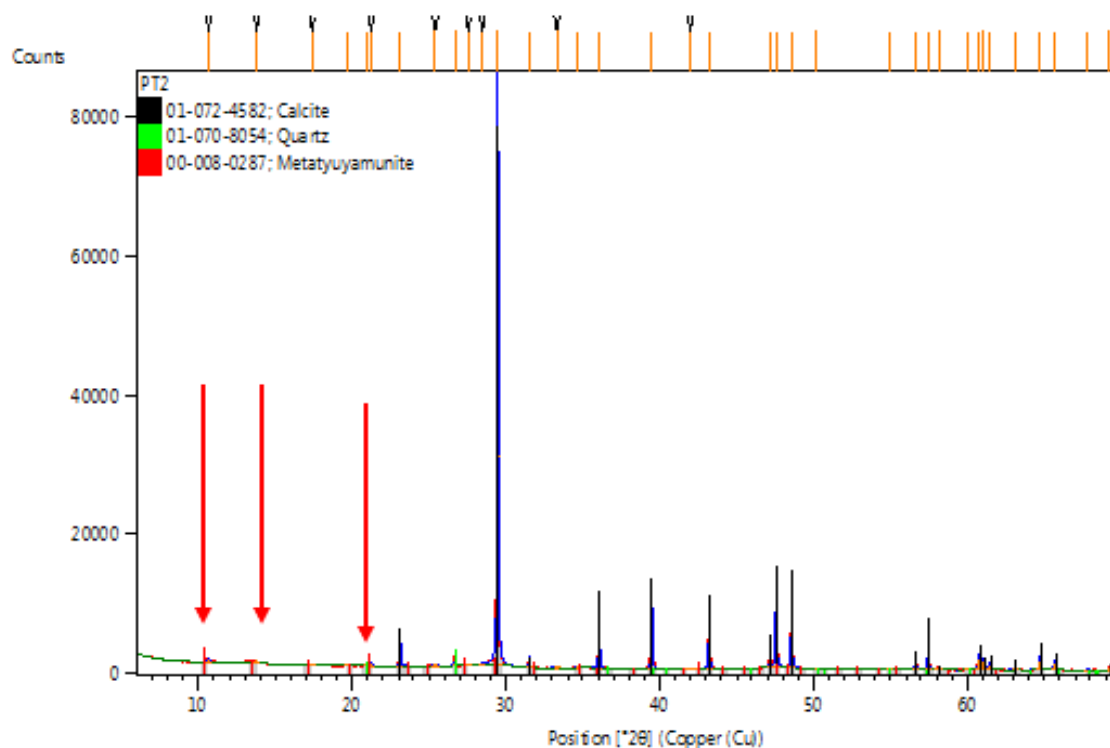


Figure 93: Reference pattern list for sample PT2.

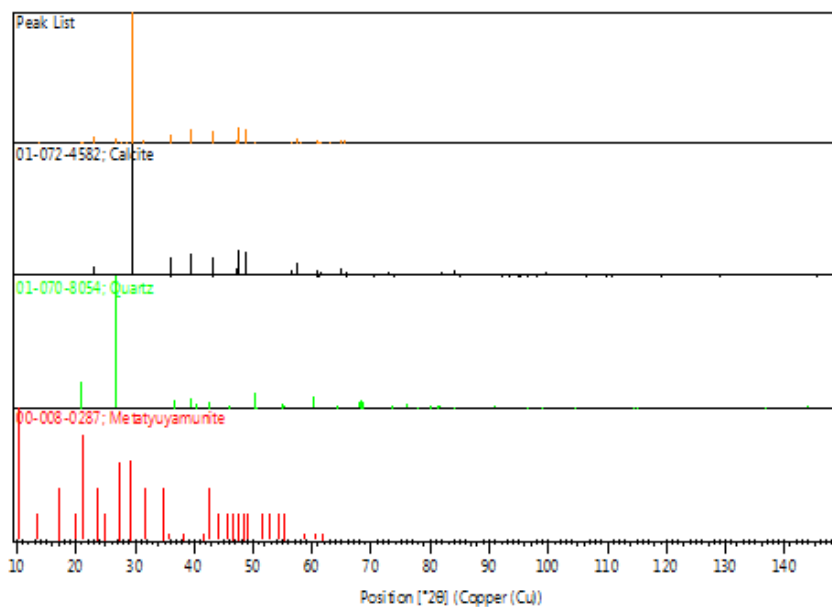


Table 20: Reference peak list for sample PT2.

Pos. [$^{\circ}2\theta$]	Height [cts]	FWHM Left [$^{\circ}2\theta$]	d-spacing [Å]	Rel. Int. [%]
10.6391	541.19	0.1171	8.30869	0.91
13.7776	356.22	0.1673	6.42224	0.60
17.4020	78.61	0.4015	5.09193	0.13
19.7204	75.93	0.4015	4.49823	0.13
20.9098	470.52	0.0669	4.24496	0.79
21.2319	420.47	0.1673	4.18129	0.70
23.1107	3096.68	0.1171	3.84545	5.19
25.3931	147.44	0.3346	3.50474	0.25
26.6873	1852.97	0.0836	3.33764	3.10
27.5581	141.88	0.2676	3.23412	0.24
28.4899	352.49	0.2007	3.13044	0.59
29.4740	59710.21	0.1020	3.02812	100.00
31.5083	1043.99	0.0816	2.83709	1.75
33.2955	76.09	0.4896	2.68877	0.13
34.6917	109.85	0.3264	2.58369	0.18
36.0457	3972.79	0.1020	2.48969	6.65
39.4806	6350.86	0.0816	2.28063	10.64
41.9977	43.92	0.8160	2.14958	0.07
43.2313	5474.12	0.0816	2.09106	9.17
47.1833	1675.42	0.0816	1.92471	2.81
47.5726	6993.99	0.1020	1.90987	11.71
48.5727	6246.26	0.1020	1.87285	10.46
50.2025	177.14	0.1020	1.81581	0.30
54.9470	80.93	0.2448	1.66970	0.14
56.6329	839.56	0.1020	1.62393	1.41
57.4656	2210.15	0.1020	1.60237	3.70
58.1441	260.96	0.0816	1.58527	0.44
59.9914	134.89	0.1224	1.54080	0.23
60.7360	1498.92	0.1020	1.52368	2.51
61.0616	1101.85	0.0816	1.51633	1.85
61.4447	696.40	0.1224	1.50779	1.17
63.1240	435.77	0.1224	1.47166	0.73
64.7327	1309.67	0.1020	1.43892	2.19
65.6610	961.12	0.1020	1.42081	1.61
67.8069	44.10	0.2448	1.38097	0.07
69.2503	296.97	0.0816	1.35567	0.50

Figure 94: Reference pattern list for sample PT3.

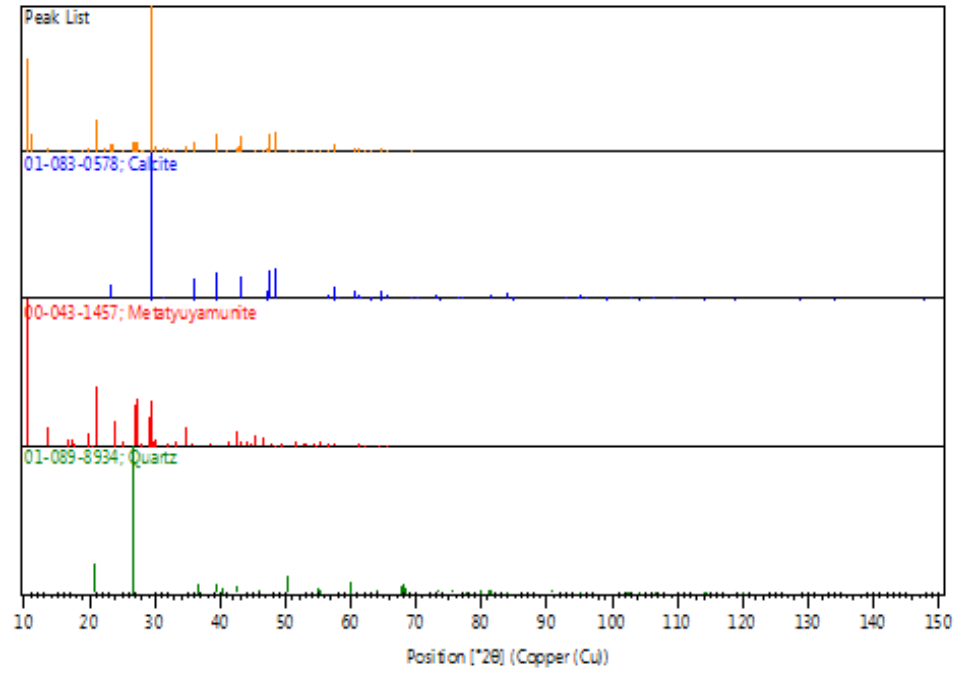


Table 21: Reference peak list for sample PT3.

Pos. [°2θ]	Height [cts]	FWHM Left [°2θ]	d-spacing [Å]	Rel. Int. [%]
10.5387	14767.82	0.1171	8.38762	63.24
11.1767	2956.10	0.0836	7.91022	12.66
13.4325	580.51	0.0836	6.58644	2.49
16.7312	242.90	0.1004	5.29456	1.04
17.0825	356.77	0.1673	5.18645	1.53
18.9667	59.34	0.2007	4.67525	0.25
19.7957	551.24	0.1338	4.48130	2.36
21.0926	5003.67	0.1673	4.20860	21.43
22.4105	454.78	0.1673	3.96398	1.95
23.0598	1148.11	0.1004	3.85383	4.92
23.5934	1092.34	0.1171	3.76786	4.68
25.0885	331.08	0.1673	3.54660	1.42
26.6299	1680.10	0.0669	3.34471	7.19
27.0386	1418.70	0.1506	3.29508	6.08
27.3501	1492.80	0.1338	3.25825	6.39
27.7259	343.96	0.1338	3.21493	1.47
28.3587	122.78	0.2007	3.14462	0.53
29.4112	23351.41	0.1224	3.03444	100.00
30.0126	747.23	0.2040	2.97499	3.20
31.4483	423.16	0.1020	2.84237	1.81

Table 21 Continued

31.8752	697.37	0.2448	2.80526	2.99
32.9837	195.07	0.1224	2.71348	0.84
34.7689	888.41	0.1632	2.57813	3.80
35.9787	1585.30	0.0816	2.49417	6.79
38.5186	108.25	0.3264	2.33534	0.46
39.4205	2928.60	0.0816	2.28396	12.54
41.0580	175.93	0.2040	2.19658	0.75
42.5292	763.39	0.2040	2.12393	3.27
42.9173	807.63	0.1224	2.10562	3.46
43.1698	2510.71	0.0612	2.09389	10.75
44.0764	168.69	0.4080	2.05290	0.72
45.4093	307.17	0.2448	1.99569	1.32
46.5929	337.26	0.1224	1.94772	1.44
47.1285	694.41	0.0816	1.92682	2.97
47.5123	2875.43	0.0816	1.91215	12.31
48.5145	3000.10	0.0816	1.87496	12.85
49.3107	119.10	0.4080	1.84654	0.51
50.1771	45.72	0.2448	1.81666	0.20
50.7324	57.71	0.3264	1.79807	0.25
51.6280	255.13	0.4896	1.76897	1.09
52.9787	163.30	0.3264	1.72701	0.70
54.4796	174.01	0.5712	1.68292	0.75
55.3786	191.36	0.1632	1.65771	0.82
56.5721	440.55	0.0816	1.62554	1.89
57.4027	1308.23	0.0816	1.60397	5.60
58.0806	98.00	0.1224	1.58686	0.42
59.0440	125.25	0.4080	1.56324	0.54
59.9575	96.60	0.1224	1.54159	0.41
60.6842	633.62	0.1020	1.52485	2.71
61.0044	568.83	0.0816	1.51762	2.44
61.3877	326.02	0.1020	1.50906	1.40
62.0218	156.25	0.4080	1.49514	0.67
63.0393	208.05	0.0816	1.47344	0.89
64.6708	656.26	0.1020	1.44015	2.81
65.6233	418.88	0.1020	1.42153	1.79
66.7087	39.15	0.4896	1.40101	0.17
68.2565	74.96	0.2448	1.37297	0.32
69.2013	172.34	0.1428	1.35651	0.74

Westwater Canyon Member

Figure 95: Reference pattern list for sample WWCM.

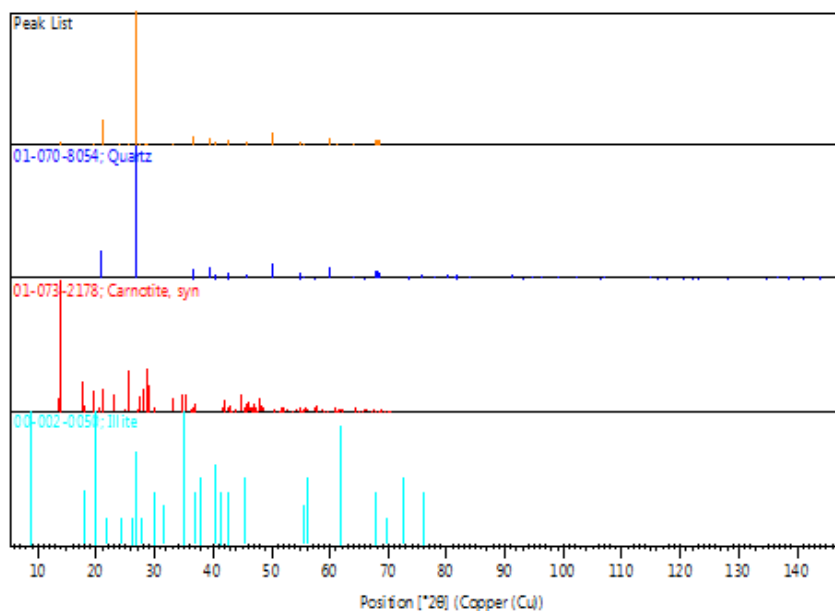


Table 22: Reference peak list for sample WWCM.

Pos. [$^\circ 2\theta$]	Height [cts]	FWHM Left [$^\circ 2\theta$]	d-spacing [\AA]	Rel. Int. [%]
6.3322	65.21	0.2519	13.94702	0.13
8.8498	189.04	0.6298	9.98410	0.38
11.6780	30.46	0.3779	7.57171	0.06
13.7749	1501.46	0.3149	6.42349	3.01
17.5111	153.69	0.2519	5.06045	0.31
18.8011	33.61	0.2519	4.71605	0.07
19.6314	227.36	0.2204	4.51843	0.46
20.9185	9132.11	0.0576	4.24323	18.32
21.2183	352.37	0.1536	4.18395	0.71
24.0759	93.23	0.1152	3.69342	0.19
25.3761	288.05	0.2688	3.50705	0.58
25.8020	107.14	0.1152	3.45012	0.21
26.6994	49860.42	0.0576	3.33616	100.00
27.5239	453.13	0.0384	3.23806	0.91
28.4882	382.71	0.1536	3.13062	0.77
28.7724	539.08	0.1920	3.10034	1.08

Table 22 Continued

32.5757	69.82	0.3072	2.74652	0.14
33.2583	128.65	0.1536	2.69170	0.26
34.6647	174.75	0.5376	2.58564	0.35
35.1952	189.22	0.3840	2.54787	0.38
36.5952	3406.97	0.0576	2.45355	6.83
39.5237	2421.01	0.0672	2.27824	4.86
40.3452	1278.65	0.0768	2.23373	2.56
41.9432	85.89	0.3840	2.15225	0.17
42.4930	1954.60	0.0672	2.12566	3.92
44.7914	73.64	0.3072	2.02178	0.15
45.8436	1309.38	0.0672	1.97779	2.63
46.9346	56.63	0.4608	1.93433	0.11
50.1907	4555.64	0.0768	1.81620	9.14
54.9217	1504.01	0.0672	1.67041	3.02
55.3843	461.14	0.0672	1.65755	0.92
57.2563	85.23	0.1152	1.60773	0.17
60.0062	2937.55	0.0864	1.54045	5.89
61.2980	41.90	0.9216	1.51105	0.08
64.0924	425.71	0.0960	1.45174	0.85
65.8264	139.14	0.0768	1.41764	0.28
67.7729	1801.45	0.0960	1.38158	3.61
68.1865	2222.10	0.0768	1.37421	4.46
68.3775	1989.03	0.0960	1.37083	3.99

St. Anthony Mine

Figure 96: Reference diffractogram for sample STA1 (meta-schoepite and magnesiopascoite). Red arrows point to most intense meta-schoepite.

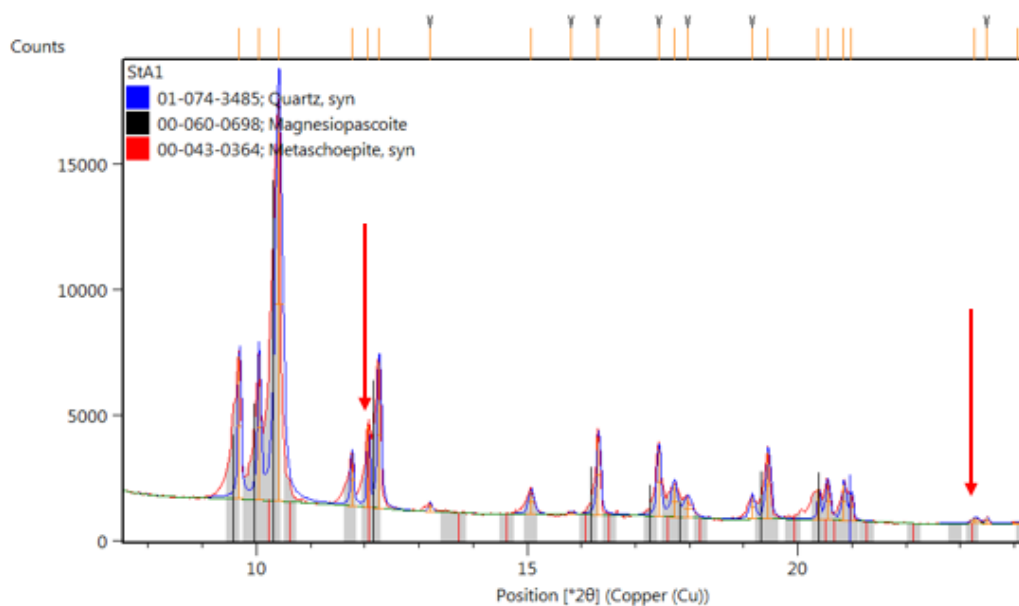


Figure 97: Reference diffractogram for sample STA1 (studtite and magnesiopascoite). Red arrows point to most intense studtite.

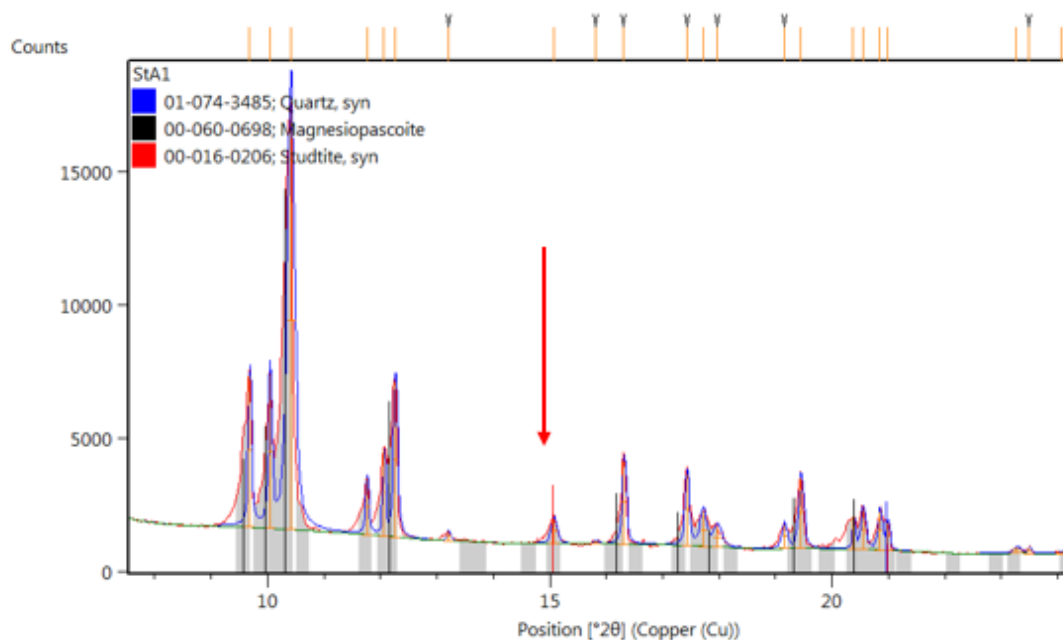


Figure 98: Reference diffractogram for sample STA1 (oswaldpeetersite and magnesiopascoite). Red arrows point to most intense oswaldpeetersite peaks.

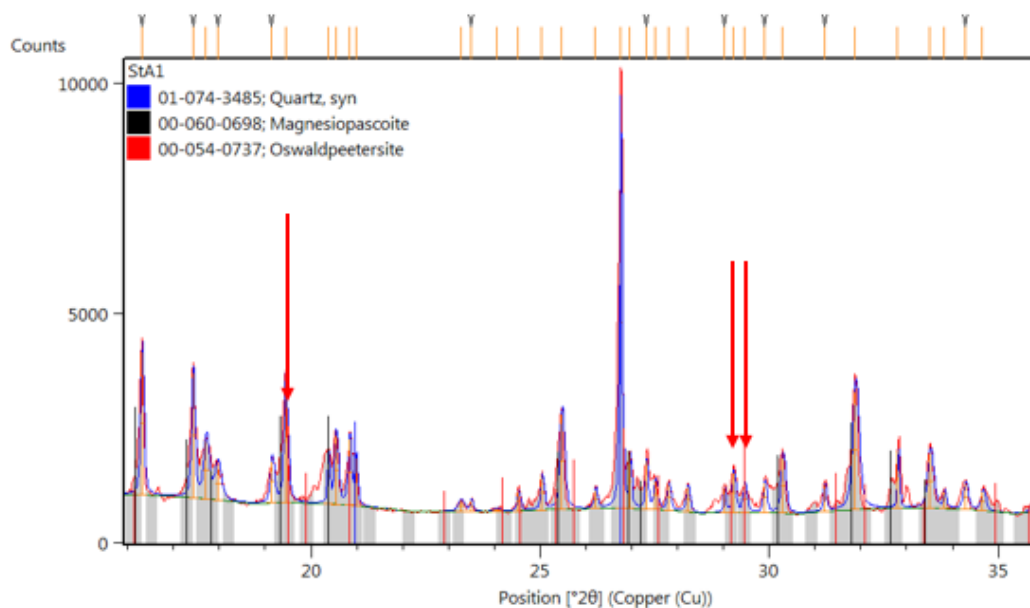


Figure 99: Reference pattern list for sample STA1.

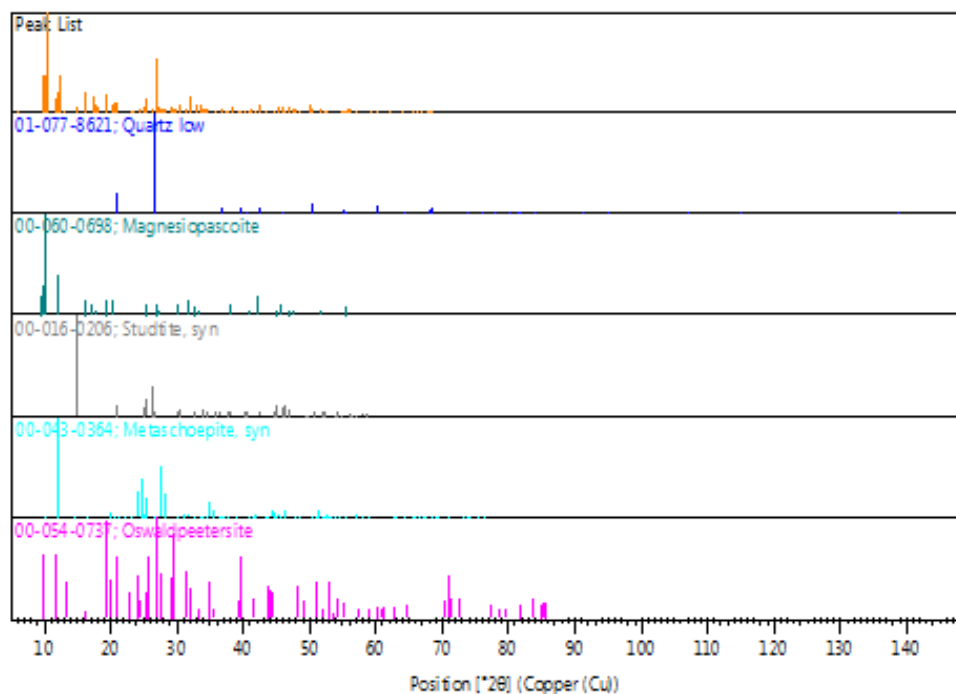


Table 23: Reference peak list for sample STA1.

Pos. [$^{\circ}2\theta$]	Height [cts]	FWHM Left [$^{\circ}2\theta$]	d-spacing [\AA]	Rel. Int. [%]
6.1173	214.95	0.4015	14.44840	0.90
9.7020	8764.50	0.0669	9.11654	36.68
10.0631	8804.65	0.0669	8.79021	36.85
10.4264	23895.86	0.1506	8.48471	100.00
11.7816	3217.98	0.0669	7.51160	13.47
12.0823	4966.96	0.0502	7.32530	20.79
12.2804	8893.05	0.0836	7.20759	37.22
13.2273	537.55	0.0669	6.69371	2.25
15.0932	1412.01	0.1171	5.87013	5.91
15.8364	139.28	0.1004	5.59626	0.58
16.3345	4762.78	0.0836	5.42672	19.93
17.4469	4150.97	0.0836	5.08316	17.37
17.7341	1942.79	0.1338	5.00146	8.13
17.9868	1156.10	0.1673	4.93177	4.84
19.1724	1395.67	0.1004	4.62938	5.84
19.4698	4059.76	0.1004	4.55934	16.99
20.3999	1865.51	0.0502	4.35352	7.81
20.5716	2290.01	0.1004	4.31756	9.58
20.8656	2224.86	0.0836	4.25738	9.31
21.0052	1597.25	0.0669	4.22941	6.68
23.2986	342.99	0.1673	3.81802	1.44
23.5212	366.56	0.0669	3.78239	1.53
24.0804	101.43	0.2007	3.69580	0.42
24.5533	652.09	0.0836	3.62569	2.73
25.0681	1130.56	0.0836	3.55238	4.73
25.5023	3154.89	0.1171	3.49287	13.20
26.2338	620.53	0.0836	3.39711	2.60
26.7797	12365.87	0.0669	3.32909	51.75
26.9891	1798.10	0.0502	3.30374	7.52
27.3436	1624.46	0.0669	3.26170	6.80
27.5451	958.54	0.1004	3.23831	4.01
27.8340	852.28	0.0836	3.20535	3.57
28.2507	844.05	0.1004	3.15901	3.53
29.0458	821.50	0.0502	3.07432	3.44
29.2473	1345.13	0.0836	3.05359	5.63
29.4916	899.75	0.1004	3.02885	3.77
29.9282	1000.78	0.0836	2.98566	4.19
30.3266	1843.73	0.1171	2.94733	7.72
31.2369	883.79	0.0669	2.86349	3.70
31.9086	3927.28	0.1673	2.80473	16.43
32.8389	1896.26	0.0502	2.72736	7.94
33.5441	1830.24	0.1506	2.67163	7.66
33.8508	592.52	0.0669	2.64812	2.48
34.3105	868.05	0.1171	2.61369	3.63
34.6927	648.47	0.1171	2.58576	2.71
35.8120	313.82	0.1673	2.50747	1.31
36.6696	633.30	0.0669	2.45077	2.65
37.2704	269.80	0.1004	2.41264	1.13
37.6752	460.71	0.1338	2.38764	1.93
38.3125	1239.42	0.1004	2.34937	5.19

Table 23 Continued

39.3593	441.23	0.0836	2.28927	1.85
39.6945	649.84	0.0502	2.27071	2.72
40.1705	157.81	0.1004	2.24490	0.66
40.8279	473.30	0.1338	2.21026	1.98
41.1319	959.98	0.0669	2.19462	4.02
41.8659	234.67	0.1673	2.15782	0.98
42.3467	1784.84	0.0816	2.13266	7.47
42.4659	1982.47	0.0612	2.12696	8.30
43.5347	105.35	0.2007	2.07890	0.44
44.6415	265.00	0.1004	2.02990	1.11
45.2094	947.17	0.1171	2.00571	3.96
45.9386	1416.43	0.1004	1.97556	5.93
46.3879	465.11	0.1673	1.95747	1.95
47.0373	964.57	0.1506	1.93194	4.04
47.6354	697.40	0.1224	1.90749	2.92
47.7758	764.72	0.0816	1.90694	3.20
48.6286	132.16	0.2040	1.87083	0.55
50.2620	1732.75	0.0816	1.81379	7.25
50.3962	957.33	0.0612	1.81377	4.01
51.6643	575.16	0.1224	1.76781	2.41
52.3891	144.44	0.1224	1.74505	0.60
52.7194	124.36	0.2448	1.73489	0.52
53.3106	129.48	0.2448	1.71703	0.54
54.9994	407.07	0.0816	1.66824	1.70
55.1411	221.47	0.0612	1.66842	0.93
55.5146	372.00	0.2040	1.65397	1.56
55.8148	683.92	0.1224	1.64578	2.86
55.9389	740.67	0.1020	1.64243	3.10
56.9595	223.55	0.2448	1.61540	0.94
58.3570	60.34	0.2448	1.58000	0.25
59.2904	377.17	0.1224	1.55733	1.58
60.0756	553.85	0.0816	1.53884	2.32
60.2342	235.21	0.0816	1.53898	0.98
61.9453	225.18	0.2856	1.49681	0.94
64.1336	241.97	0.1224	1.45091	1.01
64.3619	192.36	0.1224	1.44631	0.80
65.7399	148.92	0.4896	1.41929	0.62
66.3797	347.81	0.2040	1.40716	1.46
66.9587	213.80	0.3264	1.39639	0.89
67.8567	508.90	0.0816	1.38008	2.13
68.2325	462.58	0.0816	1.37339	1.94
68.4328	585.45	0.0816	1.36986	2.45

Figure 100: Diffractogram, pattern and peak lists for sample STA2. Red arrows point to most intense meta-ankoleite peaks.

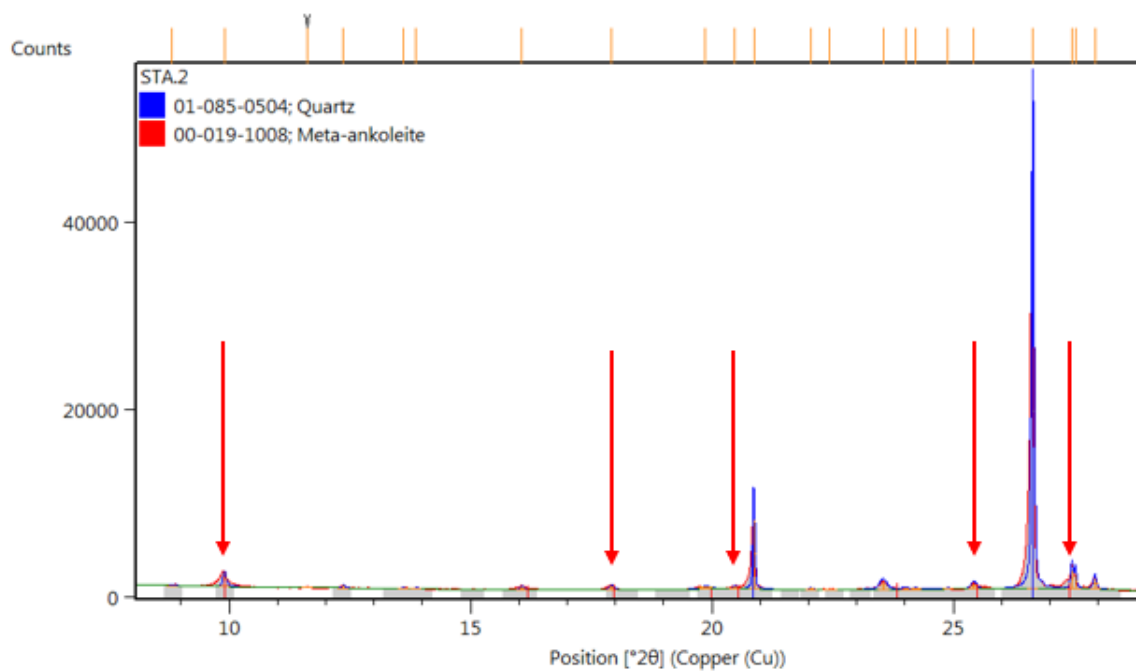


Figure 101: Reference pattern list for sample STA2.

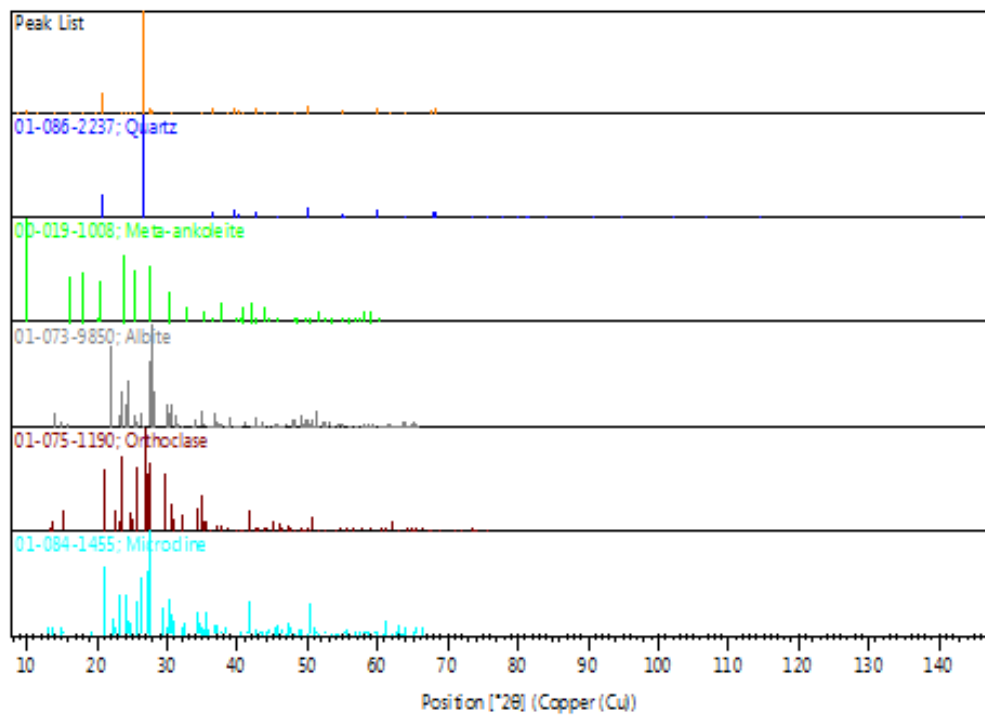


Table 24: Reference peak list for sample STA2.

Pos. [$^{\circ}2\theta$]	Height [cts]	FWHM Left [$^{\circ}2\theta$]	d-spacing [Å]	Rel. Int. [%]
8.8109	86.61	0.1889	10.02810	0.22
9.9010	1509.03	0.0866	8.92632	3.90
11.6146	70.79	0.0945	7.61294	0.18
12.3697	300.32	0.0630	7.14984	0.78
13.5980	91.63	0.0945	6.50662	0.24
13.8709	140.15	0.0630	6.37923	0.36
16.0573	400.27	0.0787	5.51521	1.04
17.9109	479.28	0.1102	4.94840	1.24
19.8643	269.17	0.2834	4.46598	0.70
20.4612	298.18	0.0945	4.33701	0.77
20.8704	7636.19	0.0480	4.25289	19.75
22.0602	142.83	0.1152	4.02614	0.37
22.4283	41.23	0.3072	3.96089	0.11
23.5491	758.79	0.1728	3.77485	1.96
24.0112	157.95	0.1152	3.70324	0.41
24.2221	94.94	0.1920	3.67147	0.25
24.8917	82.24	0.1536	3.57420	0.21
25.4294	555.63	0.1344	3.49982	1.44
26.6496	38666.03	0.0576	3.34228	100.00
27.4605	2022.83	0.0480	3.24540	5.23
27.5315	1579.98	0.0576	3.23719	4.09
27.9371	1126.33	0.0768	3.19111	2.91
29.0462	24.38	0.3072	3.07173	0.06
30.2584	293.59	0.1536	2.95138	0.76
30.7730	107.00	0.2304	2.90318	0.28
32.5398	122.41	0.6144	2.74948	0.32
35.0448	194.25	0.4608	2.55846	0.50
35.5438	129.95	0.0960	2.52368	0.34
36.5443	2351.00	0.0576	2.45685	6.08
37.7175	154.93	0.2688	2.38308	0.40
38.5979	66.30	0.1536	2.33073	0.17
39.4724	1810.41	0.0672	2.28108	4.68
40.3015	1293.14	0.0672	2.23605	3.34
40.7207	145.52	0.2688	2.21399	0.38
41.7541	129.92	0.1536	2.16155	0.34
42.4577	1853.11	0.0576	2.12734	4.79
43.7085	68.49	0.3072	2.06932	0.18
45.8099	1194.85	0.0672	1.97917	3.09
48.0682	46.20	0.4608	1.89132	0.12
50.1472	3396.91	0.0672	1.81768	8.79
50.6304	173.99	0.1920	1.80146	0.45
51.2562	58.94	0.2304	1.78092	0.15
52.2500	27.91	0.3840	1.74936	0.07
53.2937	41.64	0.3072	1.71754	0.11
54.8802	1068.95	0.0672	1.67158	2.76
55.3256	316.77	0.0768	1.65917	0.82
56.6671	16.35	0.4608	1.62304	0.04
58.8352	28.10	0.6144	1.56829	0.07
59.9685	2430.68	0.0864	1.54133	6.29
61.6561	54.52	0.4608	1.50313	0.14

Table 24 Continued

64.0422	492.11	0.0768	1.45276	1.27
65.7856	84.95	0.1152	1.41842	0.22
67.7489	1520.40	0.0864	1.38201	3.93
68.1489	1867.34	0.0864	1.37487	4.83
68.3245	1817.91	0.0960	1.37177	4.70

Figure 102: Reference diffractogram for sample STA3. Red arrows point to most intense coffinite peaks.

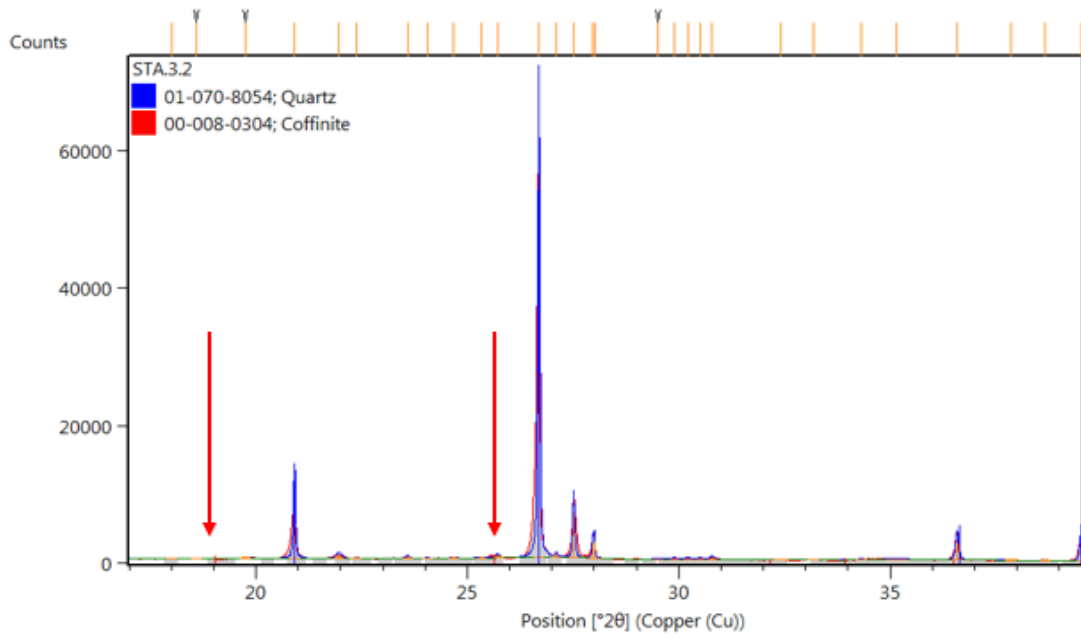


Figure 103: Reference pattern list for sample STA3.

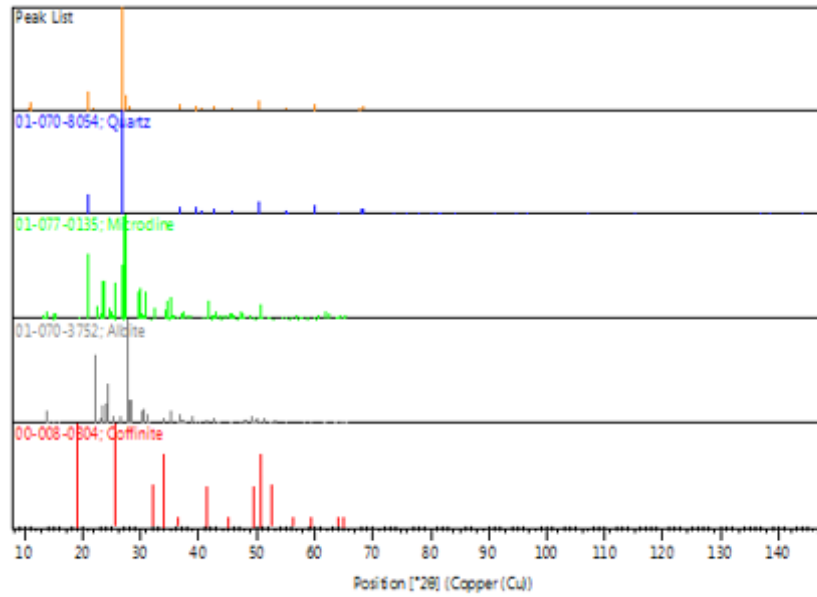


Table 25: Reference peak list for sample STA3.

Pos. [°2θ]	Height [cts]	FWHM Left [°2θ]	d-spacing [Å]	Rel. Int. [%]
8.8817	124.07	0.0945	9.94833	0.25
10.5329	946.20	0.0787	8.39217	1.89
10.9469	3811.88	0.0787	8.07571	7.59
13.6931	543.01	0.0630	6.46164	1.08
13.9234	306.32	0.0787	6.35532	0.61
15.0309	32.15	0.3779	5.88942	0.06
16.5474	139.68	0.1260	5.35296	0.28
18.0102	80.99	0.0945	4.92134	0.16
18.5962	61.42	0.1889	4.76755	0.12
19.7668	205.38	0.2204	4.48777	0.41
20.9180	9633.85	0.0576	4.24333	19.19
21.9780	598.27	0.1536	4.04100	1.19
22.3936	146.68	0.0768	3.96694	0.29
23.5957	285.73	0.0960	3.76750	0.57
24.0630	69.97	0.1152	3.69538	0.14
24.6896	137.39	0.1344	3.60299	0.27
25.3390	87.53	0.1152	3.51210	0.17
25.7166	353.78	0.1536	3.46138	0.70
26.6975	50191.41	0.0576	3.33639	100.00
27.1123	556.23	0.0576	3.28628	1.11
27.5267	6848.21	0.0576	3.23775	13.64
27.9686	2190.78	0.0384	3.18759	4.36
28.0110	2602.99	0.0384	3.18285	5.19
29.5079	71.08	0.1536	3.02471	0.14
29.9049	125.53	0.1920	2.98545	0.25

Table 25 Continued

30.2268	134.43	0.1536	2.95439	0.27
30.5184	131.77	0.1344	2.92682	0.26
30.7991	309.21	0.1152	2.90078	0.62
32.4324	56.22	0.3072	2.75833	0.11
33.1828	43.11	0.2304	2.69765	0.09
34.3347	117.22	0.1536	2.60974	0.23
35.1619	154.96	0.5376	2.55021	0.31
36.5968	3001.22	0.0864	2.45345	5.98
37.8551	36.70	0.3072	2.37474	0.07
38.6629	72.11	0.1536	2.32696	0.14
39.5161	2583.49	0.0576	2.27866	5.15
40.3400	1392.79	0.0672	2.23400	2.77
40.9544	38.73	0.2304	2.20190	0.08
41.8408	362.79	0.0768	2.15727	0.72
42.4988	2047.01	0.0672	2.12538	4.08
43.3881	39.96	0.3840	2.08386	0.08
45.8502	1346.04	0.0768	1.97752	2.68
47.1282	46.25	0.3072	1.92683	0.09
49.0737	92.77	0.2304	1.85490	0.18
50.1919	4706.61	0.0768	1.81616	9.38
50.6940	259.73	0.2304	1.79935	0.52
52.2084	78.37	0.0768	1.75066	0.16
54.9235	1315.54	0.0864	1.67036	2.62
55.3662	514.00	0.0576	1.65805	1.02
57.3085	16.21	0.2304	1.60639	0.03
58.7459	51.65	0.3072	1.57046	0.10
60.0023	2898.01	0.0960	1.54055	5.77
61.9158	49.85	0.6144	1.49745	0.10
64.0793	597.63	0.0960	1.45201	1.19
65.8308	83.66	0.1344	1.41755	0.17
67.7787	1684.42	0.1056	1.38148	3.36
68.1798	2338.19	0.0672	1.37432	4.66
68.3605	2133.99	0.0960	1.37113	4.25

Figure 104: Reference diffractogram for sample STA4.

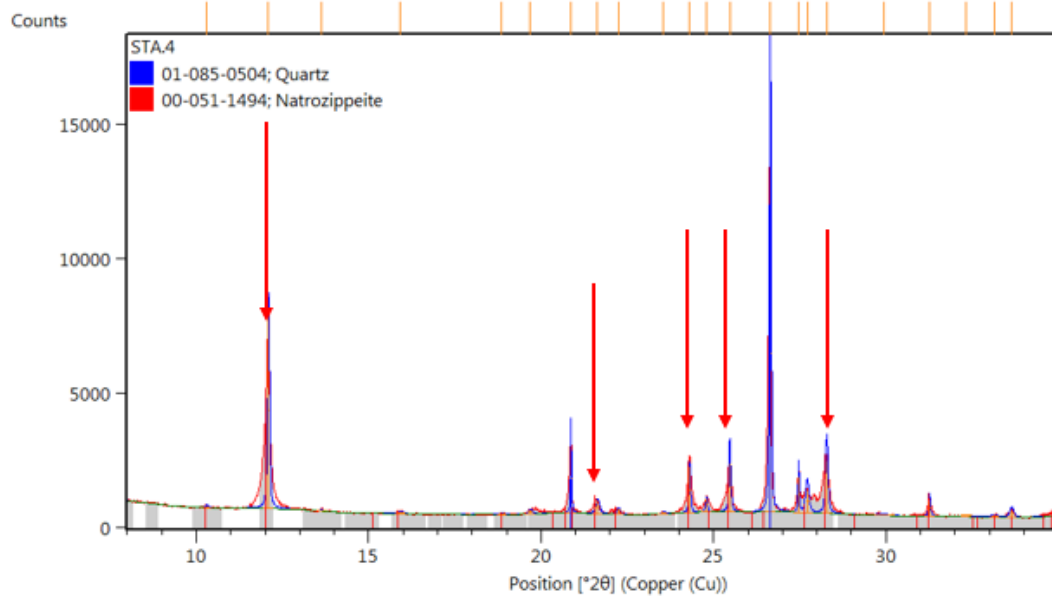


Figure 105: Reference diffractogram of sample STA4 (meta-schoepite and schoepite). Red arrows point to most intense schoepite peaks. Green arrows point to the most intense meta-schoepite peaks.

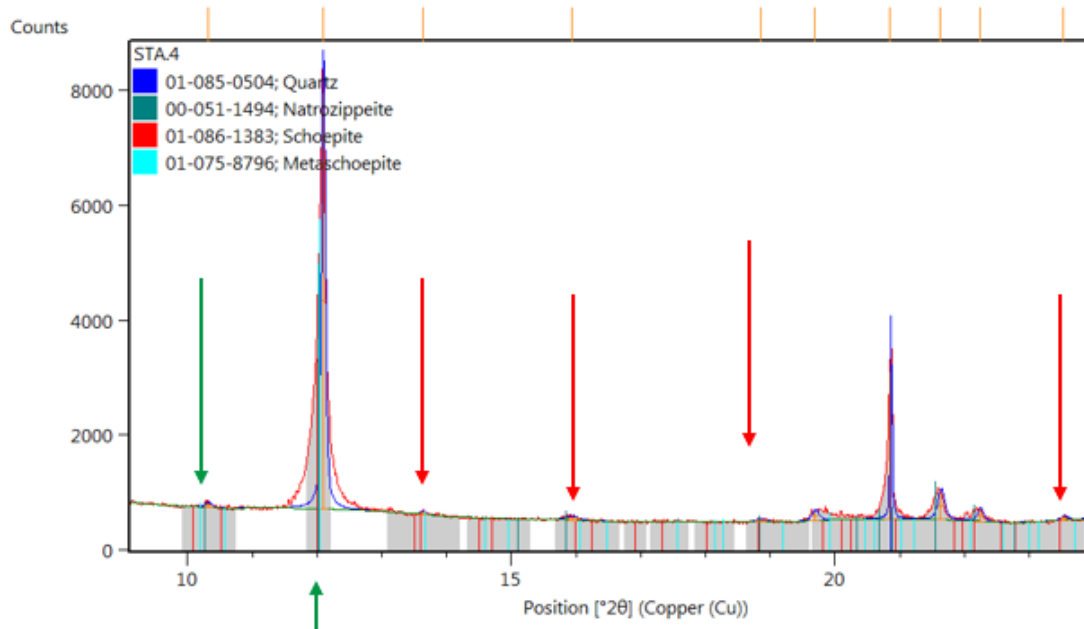


Figure 106: Reference pattern list for sample STA4.

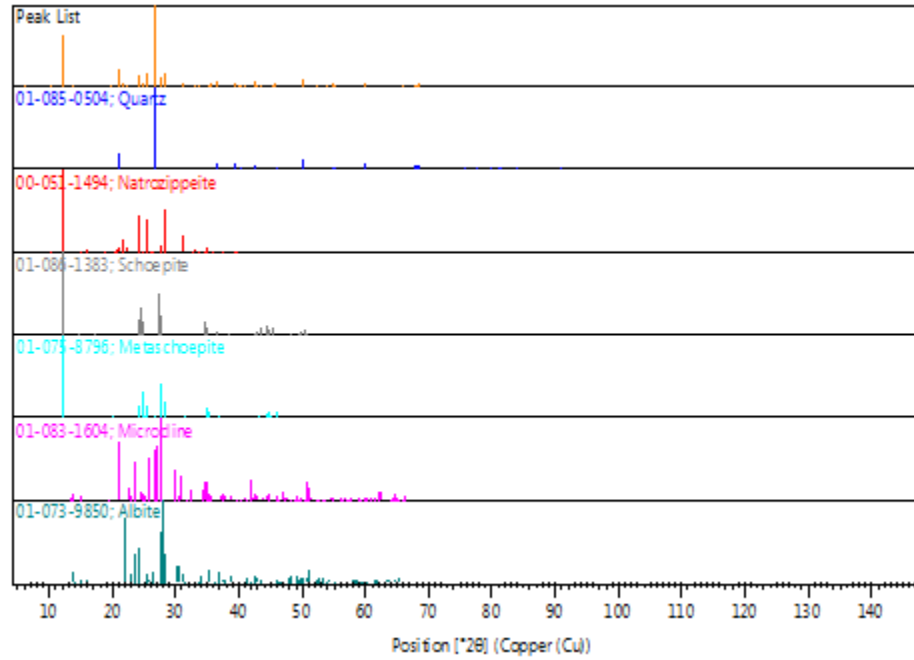


Table 26: Reference peak list for sample STA4.

Pos. [°2θ]	Height [cts]	FWHM Left [°2θ]	d-spacing [Å]	Rel. Int. [%]
5.9910	70.97	0.7557	14.74047	0.59
10.3149	87.46	0.1260	8.56904	0.73
12.0897	7404.41	0.0708	7.31482	61.48
13.6280	59.03	0.0945	6.49237	0.49
15.9268	62.71	0.2519	5.56011	0.52
18.8509	47.96	0.1889	4.70371	0.40
19.6853	167.88	0.1260	4.50617	1.39
20.8531	2617.76	0.0394	4.25638	21.74
21.6278	490.16	0.1260	4.10565	4.07
22.2336	212.13	0.1102	3.99513	1.76
23.5359	65.73	0.1260	3.77693	0.55
24.2875	1771.64	0.0551	3.66173	14.71
24.7802	513.23	0.0630	3.59003	4.26
25.4775	1873.99	0.0672	3.49333	15.56
26.6468	12042.90	0.0576	3.34263	100.00
27.4679	1367.18	0.0384	3.24454	11.35
27.7201	841.99	0.1152	3.21560	6.99
28.2842	1990.69	0.0864	3.15273	16.53
29.9352	28.11	0.6144	2.98250	0.23
31.2663	569.83	0.0576	2.85850	4.73
32.3224	44.35	0.3072	2.76747	0.37
33.1473	51.69	0.2304	2.70046	0.43
33.6509	247.93	0.1344	2.66119	2.06

Table 26 Continued

35.0699	253.65	0.1536	2.55669	2.11
35.4791	463.95	0.1536	2.52814	3.85
36.5477	949.13	0.0576	2.45663	7.88
36.8318	136.42	0.2304	2.43833	1.13
39.4716	631.45	0.0576	2.28113	5.24
40.0116	159.62	0.1920	2.25158	1.33

Figure 107: Diffractogram, pattern and peak lists for sample STA5. Red arrows point to most intense meta-autunite peaks.

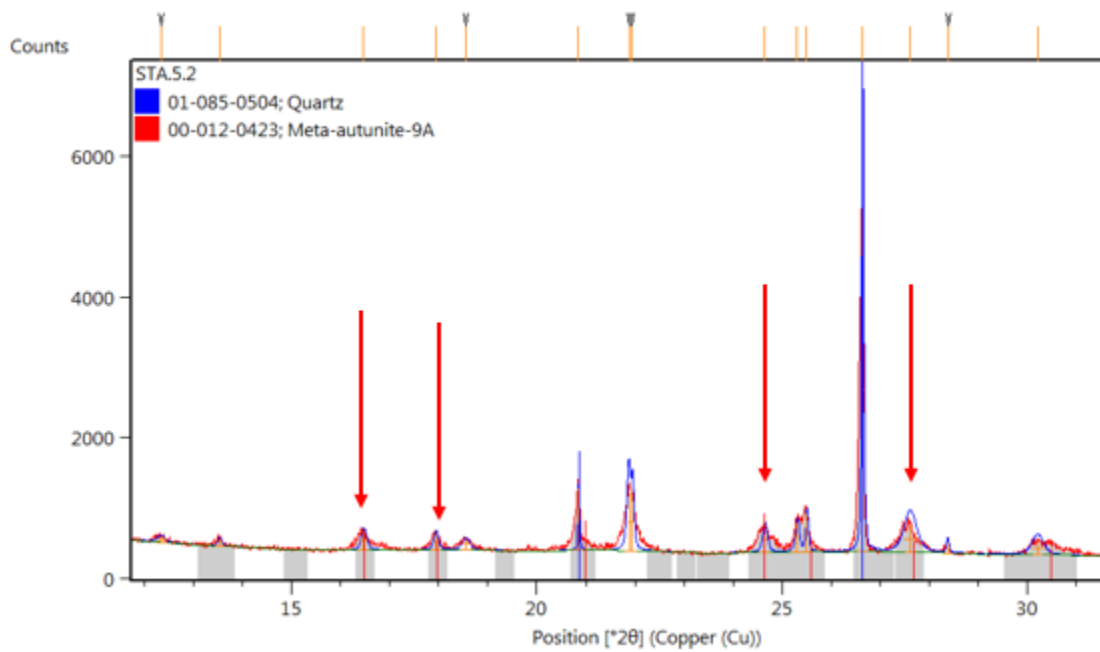


Figure 108: Reference pattern list for sample STA5.

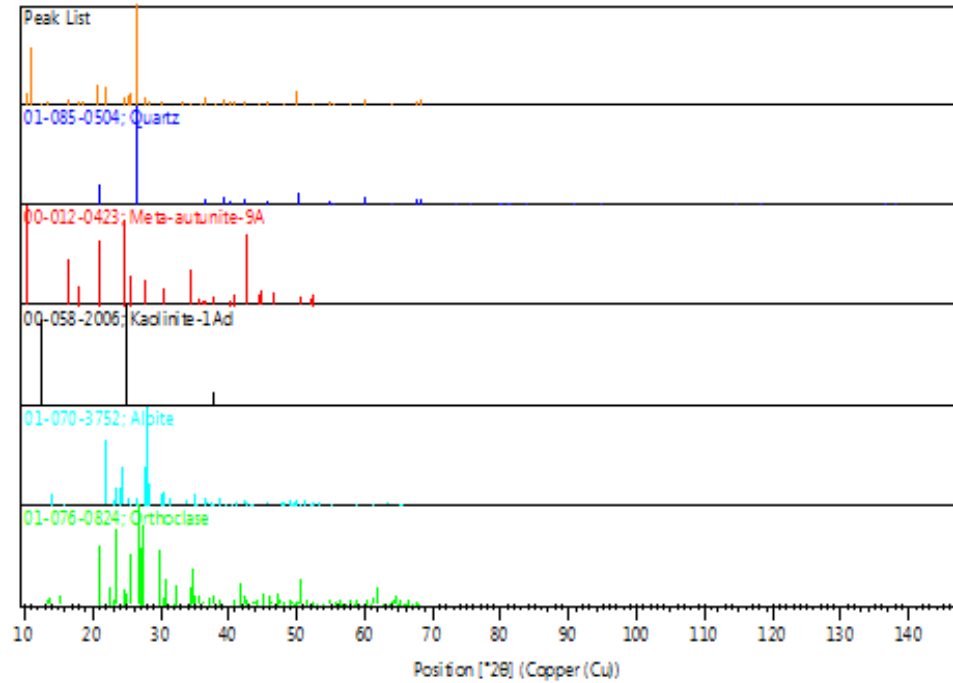


Table 27: Reference peak list for sample STA5.

Pos. [°2θ]	Height [cts]	FWHM Left [°2θ]	d-spacing [Å]	Rel. Int. [%]
10.4951	576.48	0.1102	8.42232	12.29
10.9144	2725.76	0.0787	8.09967	58.11
12.3361	93.40	0.1889	7.16924	1.99
13.5297	123.00	0.0945	6.53935	2.62
16.4680	282.22	0.1260	5.37859	6.02
17.9312	242.79	0.1102	4.94284	5.18
18.5462	158.85	0.1889	4.78029	3.39
20.8398	905.80	0.0394	4.25906	19.31
21.8761	842.97	0.0960	4.05960	17.97
21.9414	835.43	0.0630	4.04767	17.81
24.6304	377.47	0.1102	3.61152	8.05
25.2931	432.56	0.0945	3.51837	9.22
25.4901	561.74	0.0630	3.49163	11.98
26.6445	4690.80	0.0480	3.34291	100.00
27.6137	401.10	0.3072	3.22774	8.55
28.3764	141.57	0.0576	3.14270	3.02
30.2087	193.26	0.2688	2.95612	4.12
33.1018	137.82	0.2304	2.70407	2.94

Table 27 Continued

34.3581	80.90	0.3072	2.60801	1.72
35.7980	50.04	0.3072	2.50634	1.07
36.5446	389.98	0.0480	2.45683	8.31
38.0067	52.17	0.3072	2.36561	1.11
39.4714	257.85	0.0576	2.28114	5.50
40.3028	121.90	0.0576	2.23598	2.60
40.8945	123.45	0.2304	2.20498	2.63
42.4323	209.37	0.0768	2.12856	4.46
43.2239	31.41	0.4608	2.09139	0.67
44.5517	89.67	0.3840	2.03210	1.91
45.7856	152.84	0.0576	1.98016	3.26
46.8522	13.37	0.4608	1.93754	0.28
48.0526	31.50	0.6144	1.89190	0.67
50.1378	582.34	0.0576	1.81800	12.41
52.4056	51.87	0.2304	1.74454	1.11
53.5926	32.76	0.3840	1.70866	0.70
54.8693	154.54	0.0768	1.67189	3.29
55.3185	69.17	0.1152	1.65937	1.47
57.8026	37.22	0.6144	1.59383	0.79
59.9696	305.82	0.0960	1.54131	6.52
64.0374	85.01	0.0768	1.45286	1.81
67.7284	201.86	0.0960	1.38238	4.30
68.1399	250.36	0.0672	1.37503	5.34
68.3411	209.23	0.0768	1.37147	4.46

Figure 109: Reference diffractogram for sample STA6. Red arrows point to most intense phurcalite peaks, and black arrows point to most intense carnotite peaks. Silicates remove for clarity.

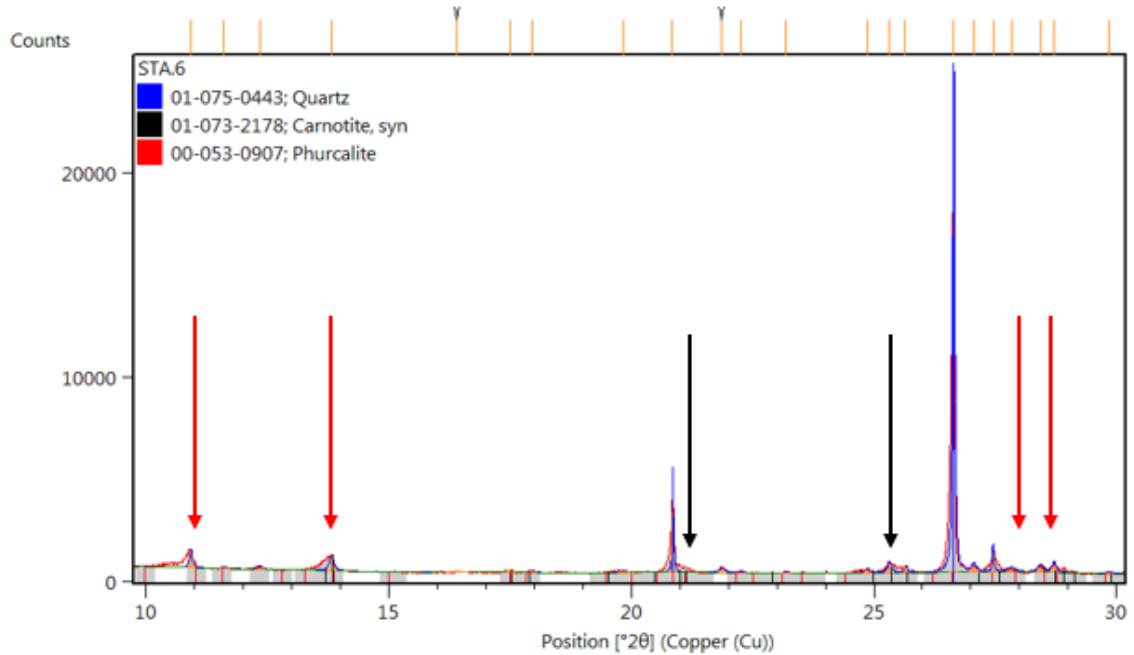


Figure 110: Reference pattern list for sample STA6.

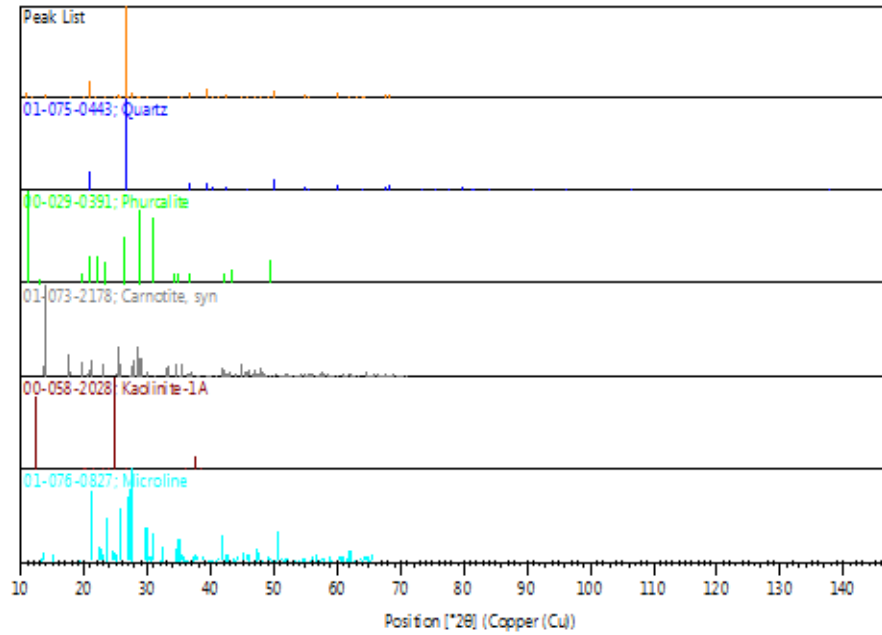


Table 28: Reference peak list for sample STA6.

Pos. [°2θ]	Height [cts]	FWHM Left [°2θ]	d-spacing [Å]	Rel. Int. [%]
10.9178	801.00	0.0787	8.09719	4.66
11.5897	59.50	0.1260	7.62923	0.35
12.3340	130.74	0.1260	7.17048	0.76
13.8119	697.97	0.1102	6.40634	4.06
16.4055	15.28	0.5038	5.39892	0.09
17.5103	55.34	0.1732	5.06068	0.32
17.9421	70.33	0.1574	4.93985	0.41
19.8187	74.99	0.2519	4.47615	0.44
20.8436	3078.10	0.0472	4.25830	17.89
21.8519	212.41	0.1260	4.06404	1.23
22.2574	71.31	0.1260	3.99091	0.41
23.1793	66.47	0.0945	3.83422	0.39
24.8567	170.10	0.1260	3.57915	0.99
25.3040	475.84	0.1102	3.51689	2.77
25.6436	308.31	0.0787	3.47107	1.79
26.6471	17206.02	0.0576	3.34259	100.00
27.0632	267.46	0.1152	3.29214	1.55
27.4624	937.16	0.0480	3.24517	5.45
27.8500	139.70	0.1920	3.20089	0.81
28.4473	257.08	0.1536	3.13502	1.49
28.7156	357.34	0.0960	3.10634	2.08
29.8504	67.51	0.1536	2.99078	0.39
30.8754	57.28	0.2304	2.89379	0.33

Table 28 Continued

33.1569	106.51	0.3840	2.69970	0.62
34.5104	112.97	0.3072	2.59685	0.66
35.2496	159.35	0.2304	2.54407	0.93
36.5525	828.26	0.0480	2.45632	4.81
39.4835	1549.50	0.0576	2.28047	9.01
40.2975	450.78	0.0576	2.23626	2.62
41.0173	28.73	0.4608	2.19866	0.17
41.8337	76.12	0.2688	2.15762	0.44
42.4471	685.86	0.0768	2.12785	3.99
44.0848	13.78	0.2304	2.05253	0.08
44.7679	59.44	0.3072	2.02278	0.35
45.8040	349.18	0.0768	1.97941	2.03
46.8558	47.94	0.4608	1.93740	0.28
47.7696	36.82	0.2304	1.90245	0.21
49.0059	21.97	0.4608	1.85730	0.13
50.1367	1227.05	0.0768	1.81803	7.13
50.6426	47.91	0.2304	1.80105	0.28
52.2094	7.48	0.9216	1.75063	0.04
54.8643	758.05	0.0672	1.67203	4.41
55.3257	131.35	0.0768	1.65917	0.76
57.2765	22.33	0.2304	1.60721	0.13
58.7425	18.92	0.3072	1.57054	0.11
59.9700	874.55	0.0960	1.54130	5.08
61.7017	32.58	0.4608	1.50213	0.19
63.1541	26.63	0.4608	1.47103	0.15
64.0372	152.63	0.0576	1.45286	0.89
64.2131	96.35	0.0768	1.44930	0.56
65.8102	24.76	0.2304	1.41795	0.14
67.7380	538.11	0.0768	1.38221	3.13
68.1491	656.87	0.1056	1.37487	3.82
68.3425	597.32	0.0960	1.37145	3.47

Figure 111: Reference diffractogram for sample STA7. Red arrows point to most intense schoepite peaks, and black arrows point to most intense hydronium-jarosite peaks. Silicates remove for clarity.

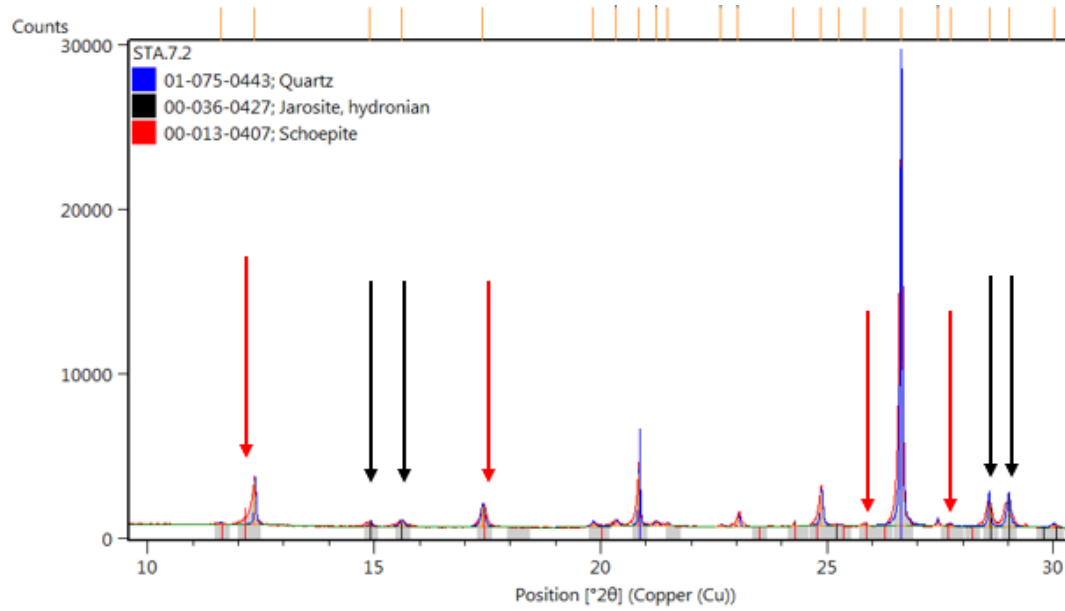


Figure 112: Reference pattern list for sample STA 7.

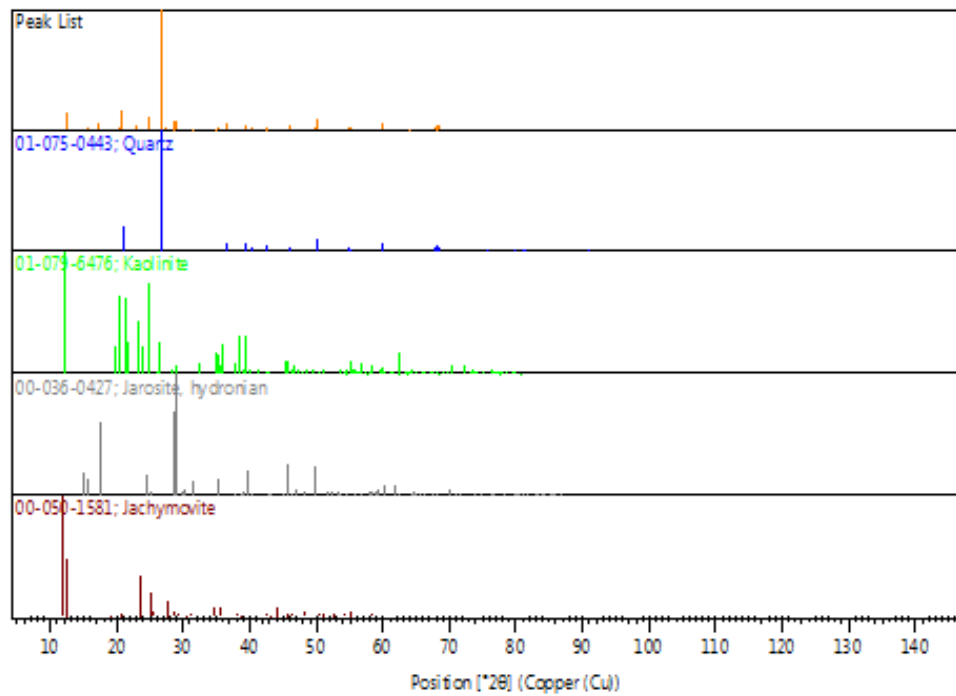


Table 29: Reference peak list for sample STA7.

Pos. [$^{\circ}2\theta$]	Height [cts]	FWHM Left [$^{\circ}2\theta$]	d-spacing [Å]	Rel. Int. [%]
5.2590	36.30	0.7557	16.79031	0.18
8.8676	111.61	0.0630	9.96412	0.55
11.6090	146.64	0.0630	7.61660	0.73
12.3643	2778.16	0.0472	7.15297	13.81
14.9061	321.43	0.0630	5.93846	1.60
15.6020	394.52	0.1102	5.67512	1.96
17.3850	1309.69	0.1023	5.09688	6.51
19.8217	284.96	0.0945	4.47547	1.42
20.3382	361.97	0.1102	4.36297	1.80
20.8431	3329.80	0.0472	4.25840	16.55
21.2191	273.51	0.0945	4.18379	1.36
21.4792	143.29	0.0945	4.13371	0.71
22.6563	87.76	0.0945	3.92154	0.44
23.0374	748.09	0.0394	3.85752	3.72
24.2510	143.63	0.0630	3.66715	0.71
24.8650	2102.57	0.0708	3.57797	10.45
25.2533	74.39	0.1260	3.52383	0.37
25.8264	134.43	0.0945	3.44691	0.67
26.6424	20115.61	0.0576	3.34316	100.00
27.4506	351.84	0.0480	3.24655	1.75
27.7262	136.96	0.0960	3.21490	0.68
28.5850	1490.84	0.0576	3.12023	7.41
29.0141	1404.78	0.0960	3.07506	6.98
30.0212	175.24	0.1536	2.97415	0.87
31.4366	149.39	0.1920	2.84340	0.74
33.1033	17.59	0.4608	2.70394	0.09
34.1822	21.22	0.2304	2.62103	0.11
34.9174	150.35	0.1344	2.56751	0.75
35.3901	266.01	0.1152	2.53429	1.32
35.9372	198.22	0.2304	2.49695	0.99
36.5472	1092.23	0.0672	2.45666	5.43
37.6962	210.36	0.0768	2.38438	1.05
38.4825	254.29	0.3072	2.33745	1.26
39.4685	926.99	0.0576	2.28130	4.61
40.2967	522.88	0.0672	2.23630	2.60
42.4525	694.71	0.0672	2.12759	3.45
45.7983	840.60	0.0768	1.97964	4.18
47.1700	53.57	0.5376	1.92522	0.27
49.6855	343.48	0.0960	1.83348	1.71
50.1382	1784.95	0.0576	1.81798	8.87
51.0210	71.46	0.1152	1.78858	0.36
52.4940	75.05	0.2304	1.74180	0.37
53.1269	78.49	0.2688	1.72254	0.39
54.8730	605.90	0.0768	1.67178	3.01
55.3201	250.97	0.0576	1.65932	1.25
56.7397	87.53	0.3072	1.62113	0.44
58.3864	35.84	0.6912	1.57927	0.18
59.1889	46.09	0.3072	1.55976	0.23
59.9560	1246.52	0.0672	1.54162	6.20
62.2533	186.45	0.1152	1.49014	0.93

Table 29 Continued

64.0307	194.26	0.0576	1.45299	0.97
64.2051	91.33	0.1152	1.44947	0.45
64.9478	41.33	0.4608	1.43468	0.21
65.7771	52.22	0.2304	1.41858	0.26
67.7485	605.32	0.0768	1.38202	3.01
68.1486	802.13	0.0768	1.37488	3.99
68.3146	821.46	0.0864	1.37194	4.08

Figure 113: Reference diffractogram for sample STA8. Red arrows point to most intense jachymovite peaks, and black arrows point to most intense zippeite peaks. Silicates remove for clarity.

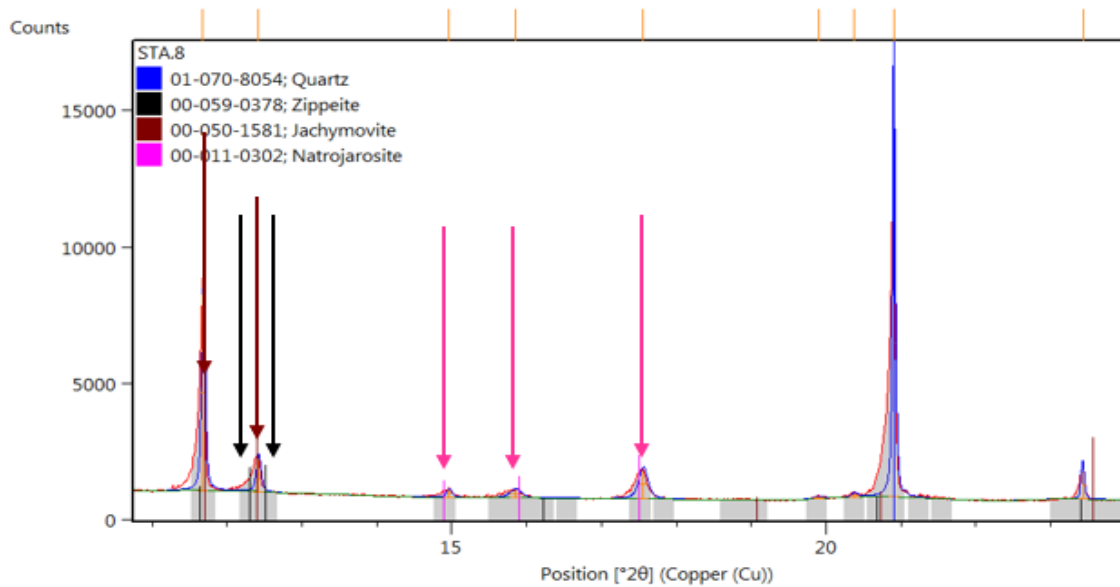


Figure 114: Reference pattern list for sample STA8.

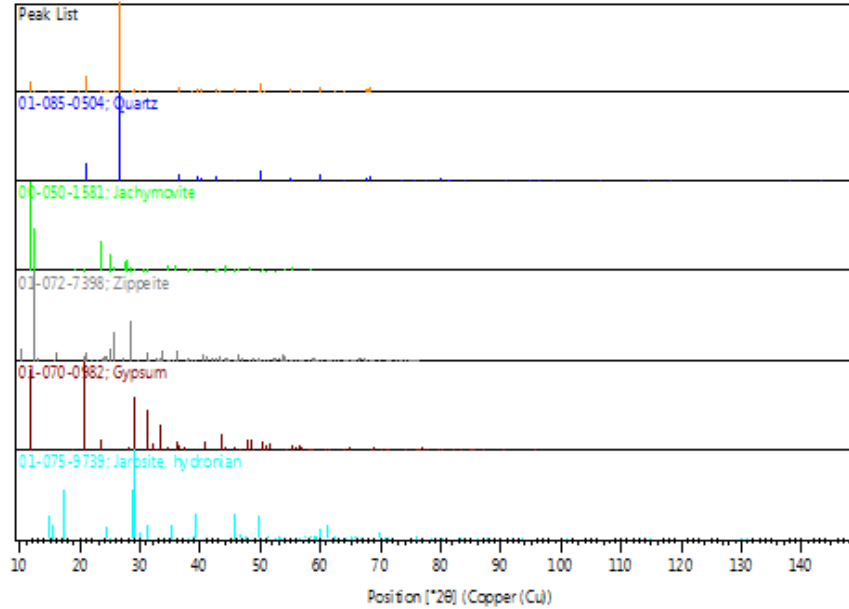


Table 30: Reference peak list for sample STA8.

Pos. [°2θ]	Height [cts]	FWHM Left [°2θ]	d-spacing [Å]	Rel. Int. [%]
11.6290	7364.30	0.0551	7.60354	10.82
12.3658	1279.27	0.0708	7.15208	1.88
14.9112	307.18	0.0787	5.93645	0.45
15.7970	300.86	0.1889	5.60548	0.44
17.4986	1055.37	0.1417	5.06405	1.55
19.8501	79.39	0.1260	4.46913	0.12
20.3240	157.64	0.0945	4.36599	0.23
20.8608	11517.68	0.0480	4.25482	16.92
23.3843	1011.90	0.0480	3.80108	1.49
24.0292	127.92	0.0960	3.70050	0.19
24.3063	108.28	0.1152	3.65893	0.16
24.8884	801.79	0.0480	3.57465	1.18
25.7574	106.19	0.1152	3.45600	0.16
26.6445	68065.88	0.0576	3.34291	100.00
27.4452	241.57	0.0576	3.24718	0.35
28.6106	1143.05	0.0576	3.11750	1.68
29.1113	1826.29	0.0672	3.06501	2.68
30.0834	115.24	0.1536	2.96814	0.17
31.1149	151.34	0.1920	2.87206	0.22
32.0377	90.61	0.2304	2.79141	0.13
33.3391	189.51	0.0768	2.68536	0.28
35.4287	149.12	0.2304	2.53162	0.22
36.0066	22.02	0.1920	2.49230	0.03
36.5457	3682.03	0.0672	2.45676	5.41
37.7190	30.50	0.2304	2.38299	0.04
38.4860	75.97	0.3072	2.33725	0.11

39.4673	3042.65	0.0480	2.28137	4.47
40.2969	2015.06	0.0672	2.23629	2.96
42.4492	2616.12	0.0576	2.12775	3.84
43.3299	93.02	0.1920	2.08652	0.14
45.7932	2335.35	0.0576	1.97985	3.43
47.8194	167.64	0.2688	1.90058	0.25
49.7742	311.20	0.1536	1.83042	0.46
50.1418	6446.85	0.0768	1.81786	9.47
50.6204	105.07	0.0768	1.80179	0.15
51.2465	25.54	0.3840	1.78124	0.04
52.5575	65.17	0.2304	1.73985	0.10
54.8733	2396.65	0.0576	1.67177	3.52
55.3246	585.52	0.0768	1.65920	0.86
56.7147	95.13	0.1536	1.62179	0.14
58.4812	51.66	0.2304	1.57694	0.08
59.3324	7.57	0.2304	1.55633	0.01
59.9568	4205.99	0.0768	1.54161	6.18
62.5163	83.79	0.4608	1.48450	0.12
64.0425	623.83	0.0672	1.45275	0.92
65.0876	16.68	0.3072	1.43193	0.02
65.7799	185.57	0.0768	1.41853	0.27
67.7421	2575.18	0.0768	1.38213	3.78
68.1442	2652.55	0.0768	1.37495	3.90
68.3231	3207.46	0.0864	1.37179	4.71

Figure 115: Reference pattern list for sample STA9.

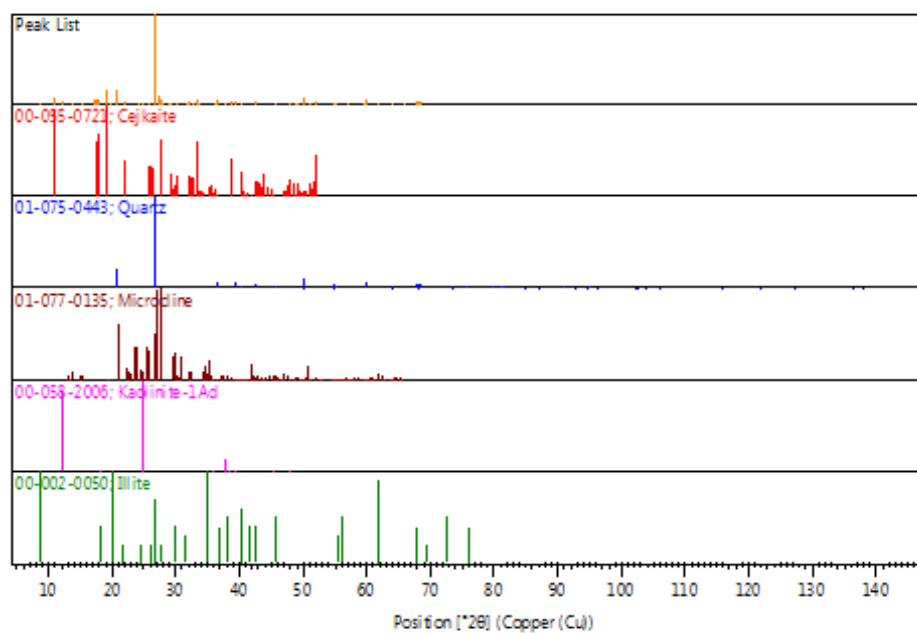


Table 31: Reference peak list for sample STA9.

Pos. [°2 θ]	Height [cts]	FWHM Left [°2 θ]	d-spacing [Å]	Rel. Int. [%]
5.2889	30.14	0.7557	16.69555	0.08
8.8343	47.07	0.3779	10.00161	0.12
10.9903	3354.06	0.0551	8.04396	8.35
12.3652	1400.49	0.0787	7.15242	3.49
13.6481	162.48	0.0630	6.48288	0.40
15.4717	63.51	0.2519	5.72262	0.16
17.3854	2066.35	0.0708	5.09676	5.14
17.6096	2748.50	0.0472	5.03237	6.84
17.8094	2229.58	0.0551	4.97637	5.55
19.0943	6364.59	0.0864	4.64430	15.85
19.8549	93.56	0.1536	4.46807	0.23
20.3543	146.79	0.1152	4.35955	0.37
20.8653	6220.81	0.0480	4.25393	15.49
22.0776	1214.28	0.0480	4.02300	3.02
23.1682	254.23	0.0672	3.83603	0.63
24.0365	77.47	0.0768	3.69938	0.19
24.8975	912.98	0.0672	3.57337	2.27
25.6684	459.70	0.0288	3.46777	1.14
25.8294	648.42	0.0768	3.44652	1.61
26.6490	40164.12	0.0480	3.34235	100.00
27.0719	209.13	0.0960	3.29109	0.52
27.4618	3812.71	0.0480	3.24525	9.49
27.6414	2022.52	0.0768	3.22457	5.04
28.0533	639.45	0.0480	3.17816	1.59
29.3449	772.85	0.0480	3.04114	1.92
30.0673	256.47	0.1536	2.96970	0.64
30.8252	65.63	0.2304	2.89839	0.16
31.7046	83.13	0.0960	2.81997	0.21
32.1429	1643.96	0.0576	2.78251	4.09
32.7845	577.18	0.1536	2.72951	1.44
33.3826	2063.52	0.0672	2.68196	5.14
33.8636	791.85	0.0480	2.64495	1.97
34.9337	124.73	0.1536	2.56635	0.31
36.0951	196.05	0.2688	2.48639	0.49
36.5516	1918.07	0.0576	2.45638	4.78
37.7299	65.77	0.1920	2.38233	0.16
38.7318	1496.47	0.0672	2.32298	3.73
39.4763	1419.94	0.0576	2.28086	3.54
40.2980	1224.99	0.0576	2.23623	3.05
40.3948	1150.69	0.0576	2.23110	2.86
41.1262	32.48	0.3840	2.19309	0.08
41.7977	101.33	0.0768	2.15940	0.25
42.4526	1758.20	0.0576	2.12759	4.38
43.1031	342.95	0.2688	2.09697	0.85
43.8113	177.36	0.2304	2.06471	0.44
44.3810	22.60	0.2304	2.03951	0.06
45.8074	827.84	0.0672	1.97927	2.06
47.0167	42.26	0.2304	1.93114	0.11
47.5710	67.26	0.3072	1.90992	0.17
47.9962	45.28	0.2304	1.89399	0.11

Table 31 Continued

48.8004	425.56	0.0672	1.86465	1.06
49.3150	184.66	0.0576	1.84638	0.46
50.1495	3399.62	0.0672	1.81760	8.46
50.6616	67.02	0.1152	1.80042	0.17
51.2008	192.61	0.3456	1.78272	0.48
52.0286	1306.63	0.0672	1.75629	3.25
54.5705	173.37	0.0768	1.68033	0.43
54.8850	1194.98	0.0768	1.67144	2.98
55.3273	307.23	0.0672	1.65913	0.76
57.2237	146.06	0.4608	1.60857	0.36
59.4859	233.99	0.0576	1.55268	0.58
59.6515	278.29	0.0576	1.54876	0.69
59.9675	1957.36	0.0768	1.54135	4.87
60.5333	84.60	0.2304	1.52829	0.21
61.9094	52.19	0.1152	1.49759	0.13
62.3897	93.60	0.3072	1.48721	0.23
64.0404	348.95	0.0480	1.45280	0.87
65.2235	40.79	0.1152	1.42928	0.10
65.7768	104.20	0.0960	1.41859	0.26
67.7523	1115.48	0.0864	1.38195	2.78
68.1455	1271.97	0.0864	1.37493	3.17
68.3280	1523.27	0.0864	1.37170	3.79

Figure 116: Reference diffractogram for sample STA10. Red arrows point to most intense natrozippeite peaks, and black arrows point to most intense gypsum peaks. Silicates remove for clarity.

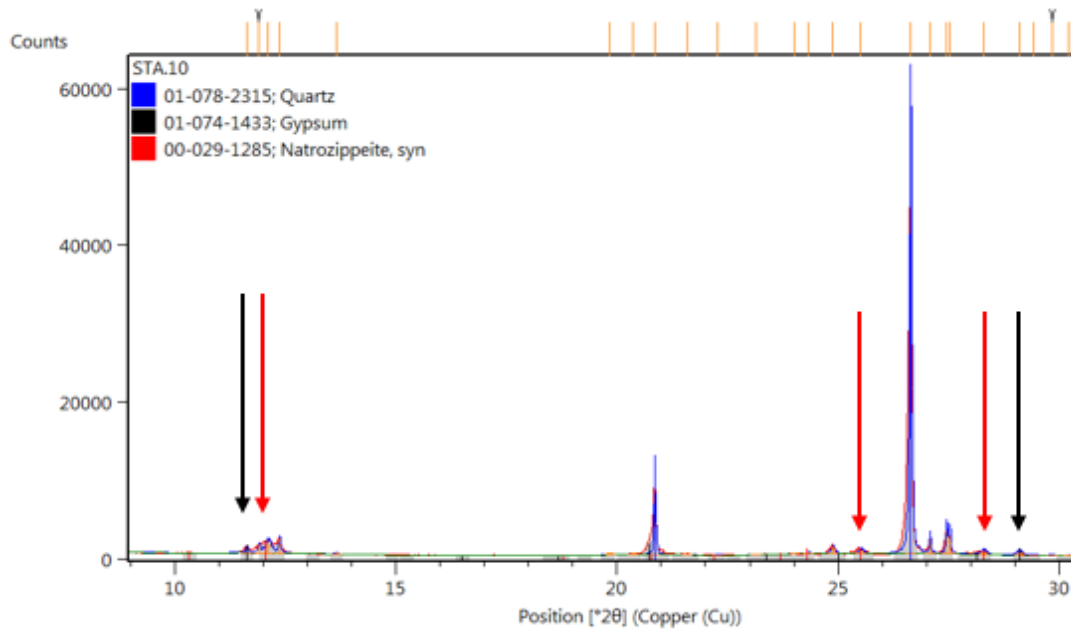


Figure 117: Reference pattern list for sample STA10.

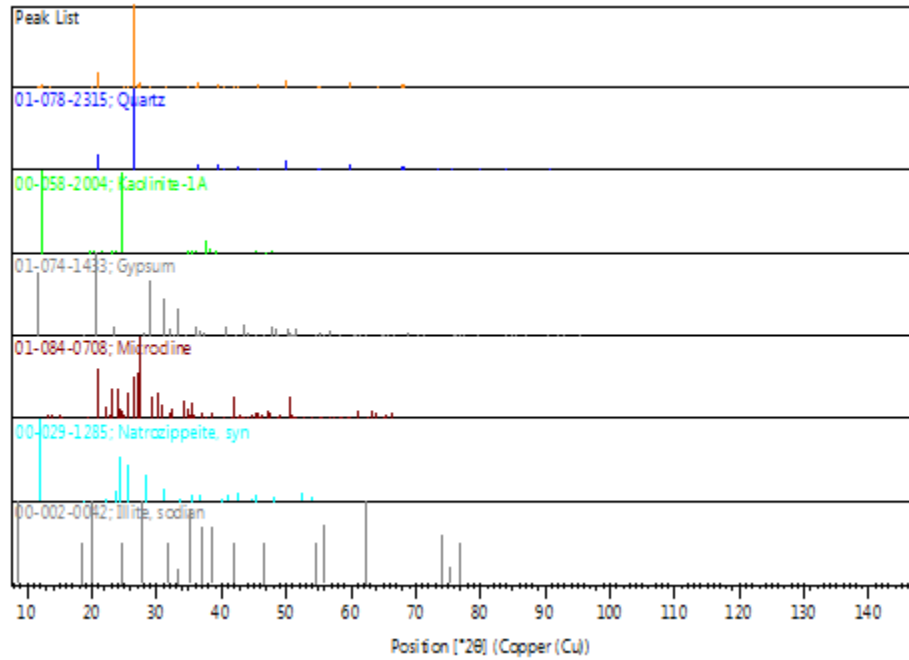


Table 32: Reference peak list for sample STA10.

Pos. [°2θ]	Height [cts]	FWHM Left [°2θ]	d-spacing [Å]	Rel. Int. [%]
8.7339	43.92	0.3779	10.11633	0.10
11.6279	899.78	0.0551	7.60423	2.09
11.9026	1084.76	0.0630	7.42935	2.52
12.1126	1661.75	0.1574	7.30102	3.86
12.3661	2009.18	0.0551	7.15194	4.67
13.6465	180.91	0.0787	6.48360	0.42
19.8425	145.58	0.1574	4.47083	0.34
20.3459	180.28	0.0945	4.36134	0.42
20.8478	7863.75	0.0551	4.25746	18.28
21.6063	119.34	0.1260	4.10967	0.28
22.2770	105.15	0.1102	3.98744	0.24
23.1459	67.32	0.0945	3.83967	0.16
23.9990	58.08	0.0787	3.70509	0.13
24.3299	124.05	0.0787	3.65544	0.29
24.8732	1010.62	0.0945	3.57681	2.35
25.5100	650.14	0.1102	3.48895	1.51
26.6468	43026.03	0.0576	3.34263	100.00
27.0897	1961.17	0.0384	3.28897	4.56
27.4627	2944.28	0.0480	3.24514	6.84
27.5342	2427.07	0.0480	3.23689	5.64
28.3066	467.83	0.1536	3.15029	1.09

Table 32 Continued

29.1131	468.37	0.1536	3.06482	1.09
29.4365	93.94	0.1536	3.03188	0.22
29.8496	88.83	0.1536	2.99086	0.21
30.2214	74.99	0.1920	2.95490	0.17
30.7945	227.48	0.1344	2.90121	0.53
31.0896	289.07	0.0960	2.87434	0.67
31.3126	185.57	0.1536	2.85437	0.43
32.0894	70.43	0.2304	2.78703	0.16
32.4263	65.78	0.2304	2.75883	0.15
33.3628	186.97	0.0960	2.68351	0.43
34.9477	188.57	0.1536	2.56535	0.44
35.5285	89.70	0.2304	2.52473	0.21
35.9636	123.96	0.1152	2.49518	0.29
36.5521	2523.29	0.0576	2.45634	5.86
37.7153	80.52	0.1920	2.38322	0.19
38.4476	155.02	0.2304	2.33949	0.36
39.4707	1949.62	0.0768	2.28118	4.53
40.2950	1133.55	0.0576	2.23639	2.63
40.7712	38.16	0.3072	2.21137	0.09
41.7981	193.21	0.0960	2.15938	0.45
42.4548	1563.74	0.0768	2.12749	3.63
43.3436	81.36	0.1536	2.08590	0.19
45.8079	1290.32	0.0960	1.97925	3.00
47.9159	41.01	0.3072	1.89698	0.10
50.1476	4116.05	0.0864	1.81766	9.57
50.5960	164.93	0.2304	1.80260	0.38
52.3283	78.88	0.3840	1.74693	0.18
53.8852	82.87	0.2304	1.70007	0.19
55.3324	408.82	0.0960	1.65899	0.95
56.7738	72.51	0.3072	1.62024	0.17
58.6486	40.43	0.3072	1.57283	0.09
59.9682	2534.50	0.0864	1.54134	5.89
61.2091	24.94	0.2304	1.51303	0.06
62.2492	70.61	0.1536	1.49023	0.16
64.0347	528.42	0.0576	1.45291	1.23
65.3353	71.96	0.3072	1.42710	0.17
65.7673	93.46	0.1152	1.41877	0.22
67.7637	1284.28	0.0768	1.38175	2.98
68.1491	1483.50	0.0864	1.37487	3.45
68.3090	1778.54	0.0768	1.37204	4.13

Figure 118: Reference diffractogram for sample STA11 (hexahydrite and minasragrite). Red arrows point to most intense hexahydrite peaks, and black arrows point to most intense minasragrite. Silicates remove for clarity.

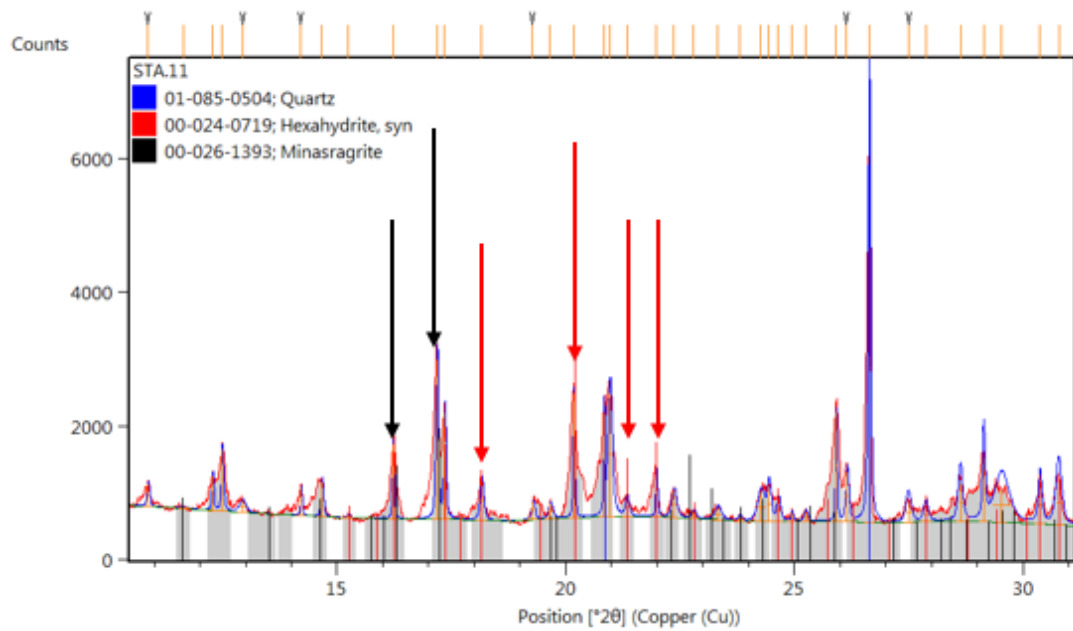


Figure 119: Reference diffractogram for sample STA11 (zippeite). Red arrows point to most intense zippeite peaks. Silicates remove for clarity.

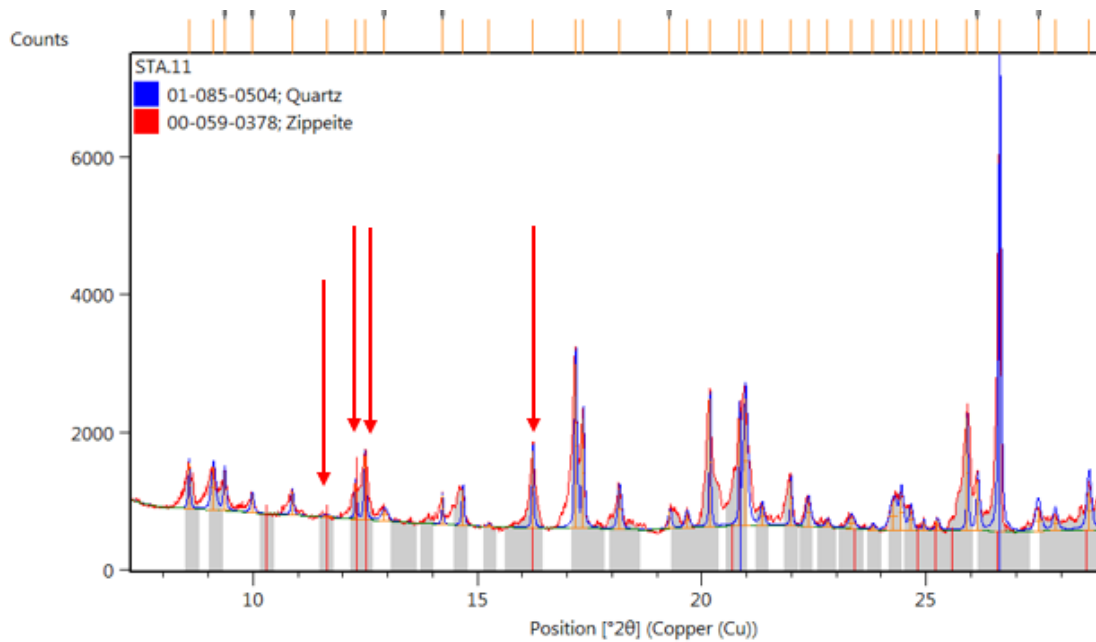


Figure 120: Reference pattern list for sample STA11.

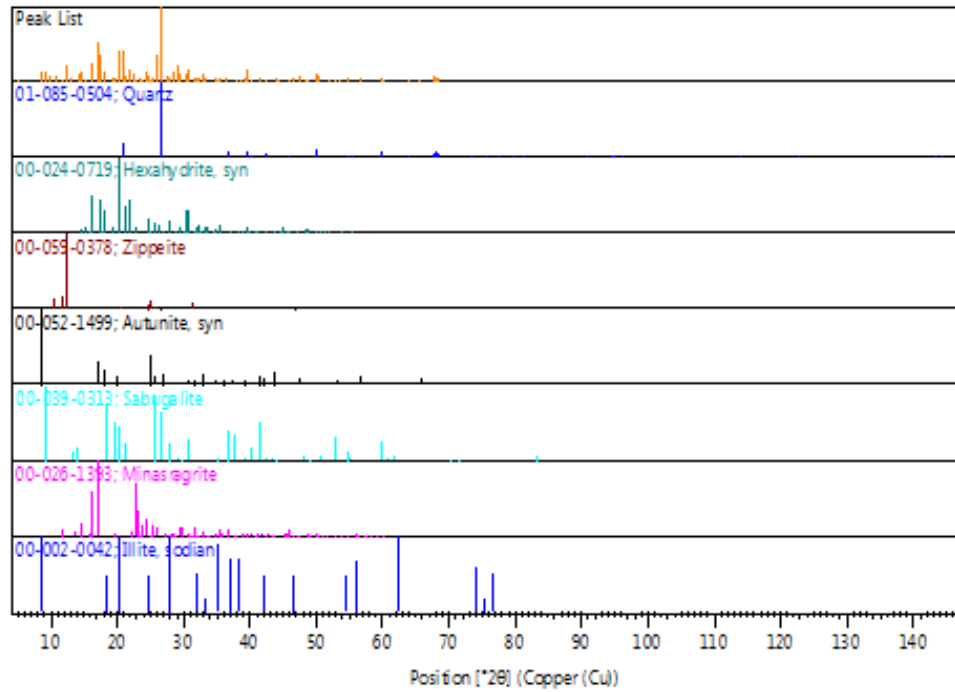


Table 33: Reference peak list for sample STA11.

Pos. [°2θ]	Height [cts]	FWHM Left [°2θ]	d-spacing [Å]	Rel. Int. [%]
5.1548	72.82	0.6298	17.12963	1.56
8.5713	680.72	0.0472	10.30788	14.56
9.1129	650.61	0.1102	9.69644	13.92
9.3651	599.41	0.0630	9.43594	12.82
9.9773	278.10	0.0787	8.85822	5.95
10.8722	359.46	0.0630	8.13106	7.69
11.6414	32.03	0.2204	7.59548	0.69
12.2803	542.03	0.0472	7.20172	11.59
12.4890	947.08	0.0551	7.08180	20.26
12.9294	174.29	0.1574	6.84157	3.73
14.2111	439.61	0.0394	6.22726	9.40
14.6708	541.69	0.0630	6.03318	11.59
15.2496	53.13	0.0945	5.80546	1.14
16.2276	1148.82	0.0472	5.45772	24.57
17.1812	2434.86	0.0630	5.15689	52.08
17.3533	1630.27	0.0551	5.10613	34.87
18.1570	609.64	0.0945	4.88189	13.04
19.2790	266.88	0.0787	4.60022	5.71
19.6591	234.01	0.1102	4.51213	5.01
20.1690	1905.67	0.0394	4.39919	40.76
20.8257	1594.66	0.0315	4.26193	34.11

Table 33 Continued

20.9590	1902.00	0.1102	4.23512	40.68
21.3335	298.27	0.0945	4.16161	6.38
21.9766	682.24	0.0472	4.04127	14.59
22.3612	412.35	0.1260	3.97262	8.82
22.7930	117.71	0.0945	3.89833	2.52
23.3217	191.03	0.1574	3.81113	4.09
23.7998	77.35	0.0945	3.73565	1.65
24.2591	443.46	0.1889	3.66595	9.49
24.4332	528.60	0.0945	3.64022	11.31
24.6430	321.88	0.0945	3.60971	6.88
24.9320	132.94	0.0472	3.56850	2.84
25.2344	157.86	0.0945	3.52643	3.38
25.8978	1674.06	0.0394	3.43758	35.81
26.1377	767.88	0.0787	3.40657	16.42
26.6434	4675.19	0.0672	3.34304	100.00
27.4977	317.25	0.1344	3.24109	6.79
27.8803	223.77	0.1152	3.19748	4.79
28.6327	580.00	0.1152	3.11515	12.41
29.1462	985.10	0.0672	3.06142	21.07
29.5367	509.21	0.3840	3.02182	10.89
30.3715	543.56	0.0960	2.94065	11.63
30.7811	684.78	0.1536	2.90244	14.65
31.6865	207.34	0.3072	2.82154	4.43
32.0300	222.99	0.1152	2.79206	4.77
32.2885	167.12	0.1152	2.77030	3.57
32.8382	286.94	0.1152	2.72517	6.14
33.0371	416.81	0.1152	2.70921	8.92
33.3144	259.88	0.1920	2.68729	5.56
35.1461	141.29	0.1536	2.55132	3.02
35.5188	171.70	0.1344	2.52540	3.67
36.5242	265.84	0.0768	2.45816	5.69
37.9629	104.89	0.3072	2.36824	2.24
38.5829	143.84	0.2688	2.33160	3.08
39.1347	179.37	0.2688	2.29999	3.84
39.4696	668.82	0.0576	2.28124	14.31
40.2961	119.88	0.0960	2.23634	2.56
41.2873	169.47	0.2688	2.18491	3.62
42.4462	192.98	0.0672	2.12789	4.13
43.8627	198.41	0.1536	2.06241	4.24
44.3162	103.52	0.1920	2.04235	2.21
45.7809	141.94	0.0960	1.98035	3.04
46.7090	179.40	0.1920	1.94314	3.84
47.5304	371.78	0.1920	1.91146	7.95
48.3633	98.08	0.3072	1.88047	2.10
48.8280	89.78	0.2304	1.86366	1.92
50.1137	460.38	0.0576	1.81881	9.85
50.2668	265.39	0.0960	1.81363	5.68
51.8283	70.88	0.4608	1.76260	1.52
52.9420	96.21	0.1152	1.72812	2.06
53.4383	81.55	0.2304	1.71323	1.74
54.8690	202.21	0.0768	1.67189	4.33
56.7070	174.02	0.1536	1.62199	3.72
58.2511	25.10	0.4608	1.58262	0.54
59.9380	246.62	0.0672	1.54204	5.28

Table 33 Continued

60.1036	131.54	0.0960	1.53819	2.81
64.0428	94.23	0.1344	1.45275	2.02
65.6643	43.56	0.6144	1.42075	0.93
67.7390	336.24	0.0480	1.38219	7.19
67.9288	213.80	0.0768	1.37879	4.57
68.1234	225.13	0.0960	1.37532	4.82
68.3211	217.04	0.0960	1.37183	4.64

Figure 121: Reference diffractogram for sample STA12. Observe the extremely low intensity of coffinite (red arrow).

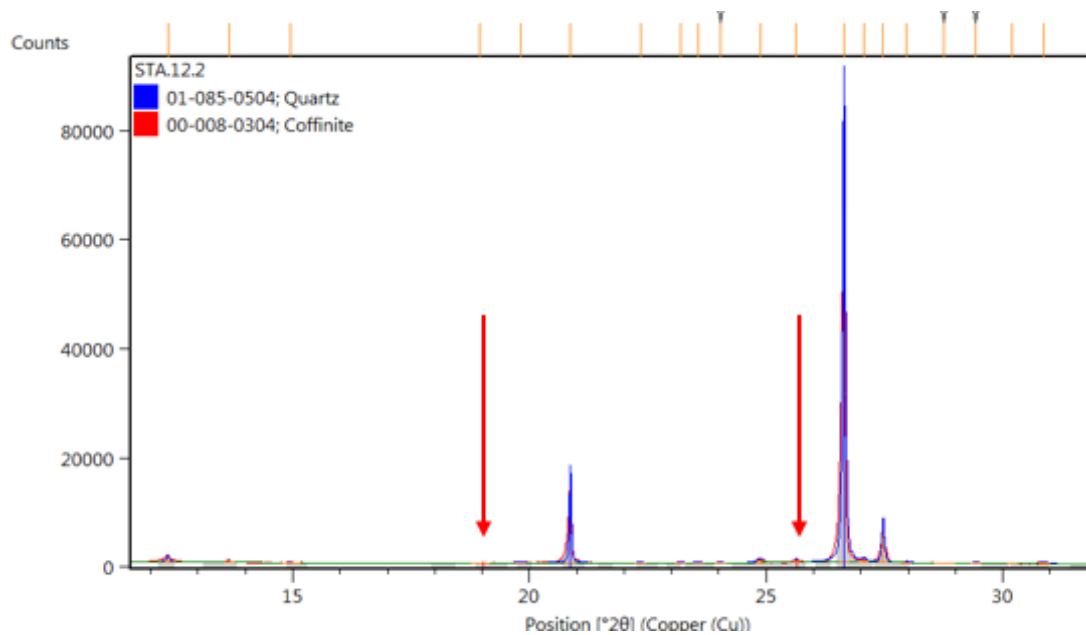


Figure 122: Pattern list for sample STA12.

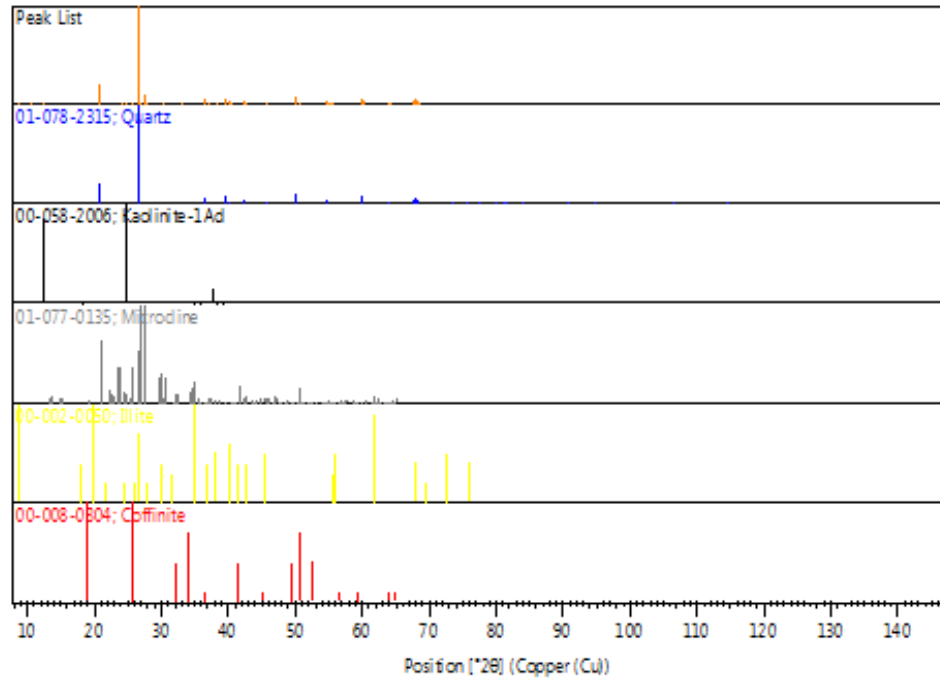


Table 34: Reference peak list for sample STA 12.

Pos. [°2θ]	Height [cts]	FWHM Left [°2θ]	d-spacing [Å]	Rel. Int. [%]
8.8374	142.42	0.1260	9.99815	0.23
10.4886	77.04	0.1574	8.42758	0.12
10.9187	156.47	0.1260	8.09652	0.25
12.3592	1241.64	0.0708	7.15591	1.96
13.6530	408.74	0.0472	6.48054	0.65
14.9456	44.07	0.3779	5.92284	0.07
18.9576	12.02	0.3779	4.67747	0.02
19.8096	72.85	0.1889	4.47817	0.12
20.8676	12603.58	0.0480	4.25345	19.94
22.3415	101.66	0.1536	3.97608	0.16
23.2025	68.58	0.1152	3.83044	0.11
23.5589	52.99	0.1536	3.77330	0.08
24.0406	134.68	0.0672	3.69878	0.21
24.8763	548.34	0.1536	3.57638	0.87
25.6322	434.81	0.0768	3.47259	0.69
26.6473	63221.15	0.0672	3.34257	100.00
27.0743	441.05	0.0768	3.29082	0.70
27.4749	5599.67	0.0672	3.24373	8.86
27.9714	153.12	0.1344	3.18727	0.24
28.7442	35.45	0.4608	3.10331	0.06

Table 34 Continued

29.4230	186.90	0.1152	3.03324	0.30
30.2023	89.05	0.1152	2.95673	0.14
30.8616	203.44	0.2688	2.89505	0.32
32.3808	63.79	0.3840	2.76261	0.10
33.0440	124.02	0.1536	2.70866	0.20
34.9363	139.95	0.2304	2.56616	0.22
35.9514	17.19	0.2304	2.49600	0.03
36.5482	3628.57	0.0576	2.45660	5.74
37.0809	86.10	0.1536	2.42252	0.14
37.7104	78.68	0.1920	2.38352	0.12
38.4991	75.12	0.3840	2.33648	0.12
39.4701	2905.45	0.0576	2.28121	4.60
40.2909	1684.46	0.0576	2.23661	2.66
41.7875	320.64	0.1920	2.15990	0.51
42.4535	2931.06	0.0672	2.12755	4.64
45.7943	1608.53	0.0672	1.97981	2.54
47.4718	45.77	0.2304	1.91369	0.07
49.0568	66.90	0.3072	1.85550	0.11
50.1447	5302.49	0.0768	1.81776	8.39
50.6378	179.64	0.1920	1.80121	0.28
54.8807	1806.58	0.0768	1.67156	2.86
55.3277	570.17	0.0672	1.65912	0.90
56.2438	71.21	0.1152	1.63424	0.11
57.2562	47.32	0.3072	1.60773	0.07
59.9613	3626.07	0.0864	1.54150	5.74
64.0448	626.99	0.0672	1.45271	0.99
65.7835	176.45	0.0960	1.41846	0.28
67.7498	2070.12	0.0960	1.38200	3.27
68.1431	2691.41	0.0672	1.37498	4.26
68.3326	2494.57	0.0864	1.37162	3.95

Figure 123: Pattern and peak lists for sample STA13A. Red arrows point to most intense coffinite peaks. Silicates remove for clarity.

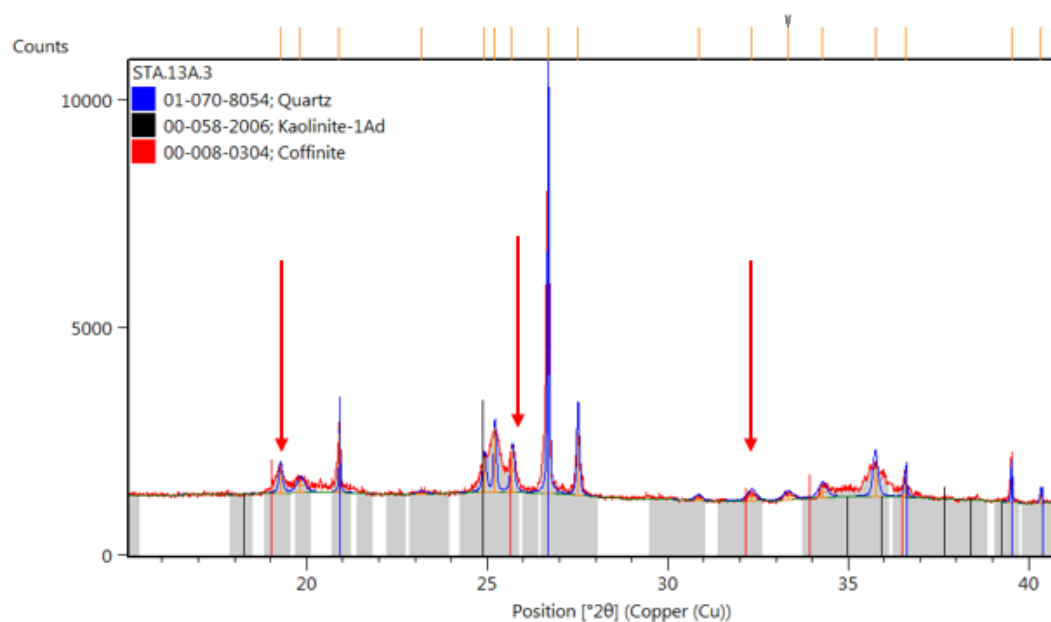


Figure 124: Reference pattern list for sample STA13A.

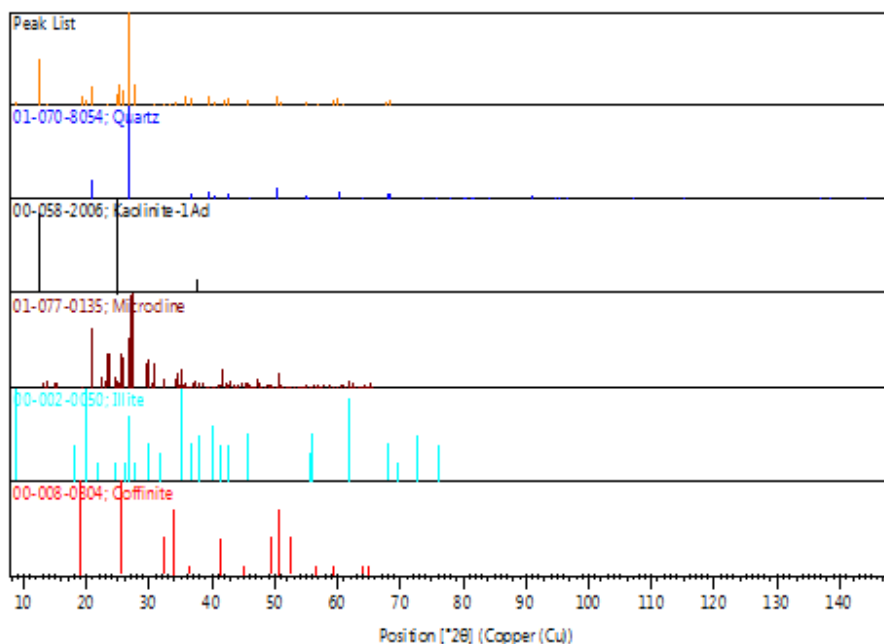


Table 35: Reference peak list for sample STA13A.

Pos. [$^{\circ}2\theta$]	Height [cts]	FWHM Left [$^{\circ}2\theta$]	d-spacing [\AA]	Rel. Int. [%]
8.8419	190.55	0.2519	9.99306	2.98
12.3978	3165.42	0.1260	7.13373	49.57
12.5553	2824.09	0.1102	7.04458	44.22
13.6857	107.45	0.1260	6.46513	1.68
19.2587	626.89	0.1102	4.60501	9.82
19.8157	316.26	0.2519	4.47682	4.95
20.8830	1336.81	0.0472	4.25036	20.93
23.1529	56.69	0.3779	3.83854	0.89
24.8965	794.37	0.1260	3.57351	12.44
25.1930	1464.29	0.0787	3.53213	22.93
25.6781	973.85	0.1260	3.46649	15.25
26.6892	6385.82	0.0576	3.33741	100.00
27.5089	1395.73	0.0864	3.23979	21.86
30.8484	83.96	0.2304	2.89626	1.31
32.3241	175.17	0.2688	2.76733	2.74
33.3349	128.60	0.3072	2.68569	2.01
34.2867	225.15	0.2688	2.61328	3.53
35.7481	690.70	0.1536	2.50972	10.82
36.5829	462.48	0.0768	2.45435	7.24
39.5232	635.68	0.0480	2.27827	9.95
40.3301	234.56	0.0576	2.23453	3.67
41.8376	305.19	0.1920	2.15743	4.78
42.4849	422.73	0.0576	2.12604	6.62
45.8263	259.55	0.0576	1.97850	4.06
50.1838	648.86	0.0768	1.81644	10.16
51.0886	194.38	0.2304	1.78637	3.04
54.9106	210.83	0.0768	1.67072	3.30
56.7978	66.49	0.3072	1.61961	1.04
59.4998	254.00	0.4608	1.55235	3.98
59.9943	583.53	0.0672	1.54073	9.14
61.0323	65.59	0.6144	1.51699	1.03
62.4327	45.13	0.6144	1.48629	0.71
65.8556	42.38	0.7680	1.41708	0.66
67.7699	288.37	0.0768	1.38163	4.52
68.1758	300.14	0.0768	1.37439	4.70
68.3415	387.40	0.0576	1.37147	6.07

Figure 125: Reference diffractogram for sample STA13B. Red arrows point to most intense hematite peaks, and black arrows point to most intense calcite peaks. Silicates remove for clarity.

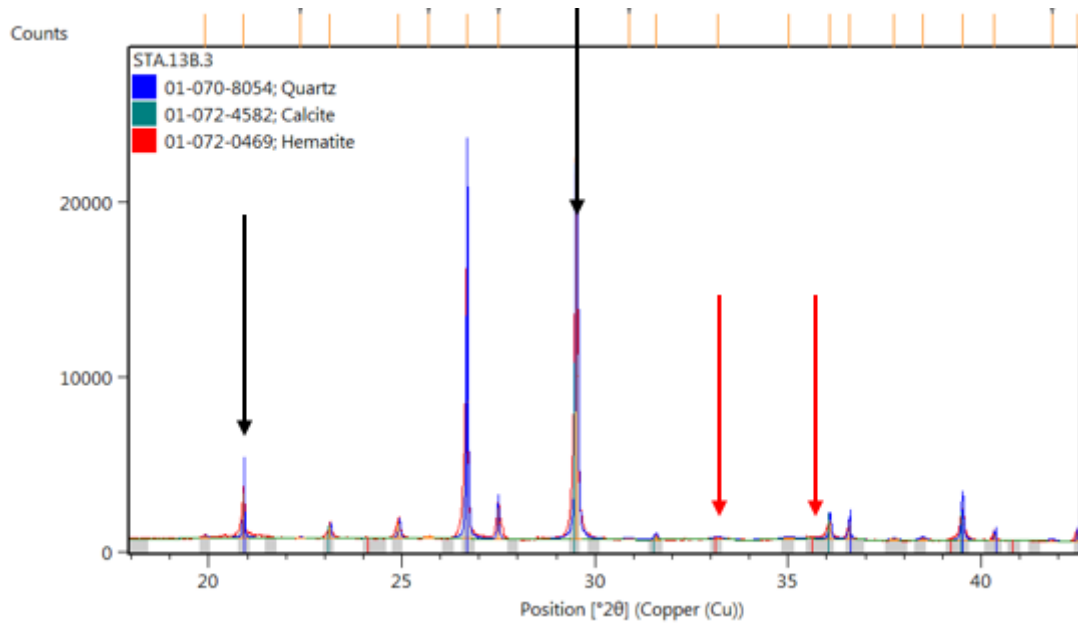


Figure 126: Reference pattern list for sample STA13B.

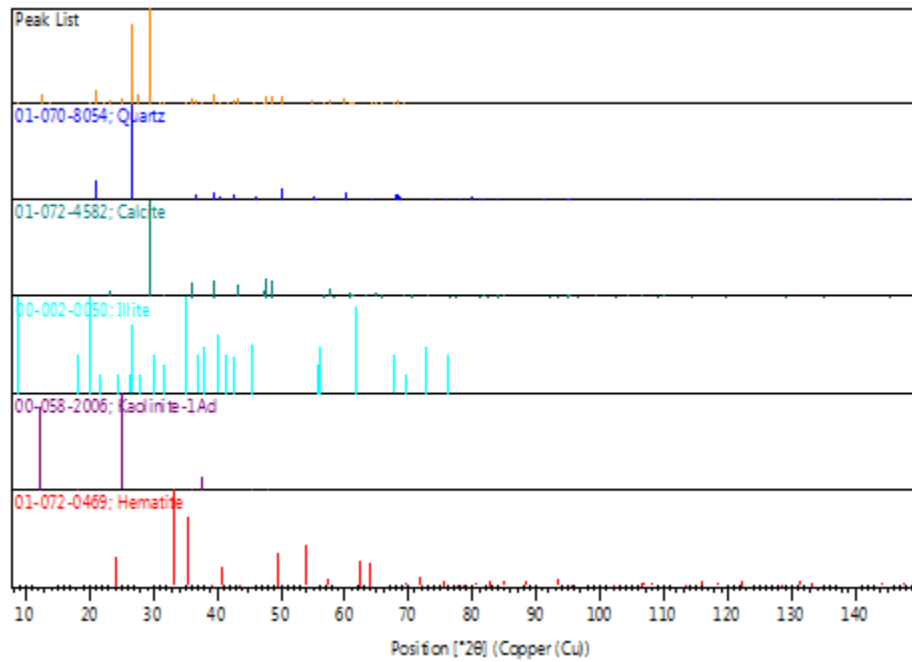


Table 36: Reference peak list for sample STA13B.

Pos. [$^{\circ}2\theta$]	Height [cts]	FWHM Left [$^{\circ}2\theta$]	d-spacing [Å]	Rel. Int. [%]
8.8345	57.67	0.2519	10.00140	0.30
12.4179	1810.15	0.0787	7.12220	9.49
13.6776	120.49	0.0945	6.46895	0.63
19.9025	144.87	0.0945	4.45749	0.76
20.8950	2614.96	0.0472	4.24795	13.71
22.3828	51.37	0.1889	3.96884	0.27
23.1399	851.36	0.0472	3.84067	4.46
24.9196	1042.19	0.0630	3.57026	5.46
25.7017	93.34	0.2204	3.46335	0.49
26.6953	15911.66	0.0480	3.33667	83.40
27.5023	1798.88	0.0480	3.24056	9.43
29.5320	19078.23	0.0672	3.02230	100.00
30.8804	73.82	0.2688	2.89333	0.39
31.5812	240.64	0.1152	2.83071	1.26
33.1897	114.57	0.3072	2.69710	0.60
35.0260	82.35	0.3072	2.55979	0.43
36.0892	1050.89	0.0672	2.48678	5.51
36.5901	876.86	0.0672	2.45388	4.60
37.7475	76.66	0.2304	2.38126	0.40
38.4893	121.74	0.1920	2.33705	0.64
39.5249	1894.10	0.0768	2.27818	9.93
40.3444	414.81	0.0384	2.23377	2.17
41.8372	65.79	0.2304	2.15745	0.34
42.5070	547.22	0.0384	2.12499	2.87
43.2875	1191.04	0.0480	2.08847	6.24
45.8476	368.91	0.0672	1.97763	1.93
47.2482	351.41	0.0960	1.92222	1.84
47.6743	1572.51	0.0864	1.90603	8.24
48.6658	1470.93	0.0864	1.86949	7.71
50.1895	1326.07	0.0576	1.81624	6.95
54.0948	47.17	0.4608	1.69398	0.25
54.9275	469.58	0.0768	1.67025	2.46
55.3715	159.46	0.0768	1.65791	0.84
56.7135	203.20	0.0768	1.62182	1.07
57.5532	470.05	0.0960	1.60014	2.46
58.3391	50.04	0.2304	1.58044	0.26
60.0044	916.70	0.0672	1.54050	4.80
60.8244	249.27	0.0960	1.52168	1.31
61.1970	260.49	0.1152	1.51330	1.37
61.5794	174.42	0.1152	1.50482	0.91
62.3717	56.27	0.3840	1.48759	0.29
63.2274	80.44	0.1920	1.46950	0.42
64.0898	191.38	0.0672	1.45180	1.00
64.8229	243.85	0.0960	1.43714	1.28
65.8549	249.18	0.1536	1.41709	1.31
67.7745	446.59	0.0768	1.38155	2.34
68.1953	603.65	0.0672	1.37405	3.16
68.3740	575.76	0.0864	1.37089	3.02
69.3826	65.00	0.2304	1.35341	0.34

Figure 127: Reference diffractogram for sample STA14. Red arrows point to most intense kaolinite peaks, and black arrows point to most intense calcite peaks.

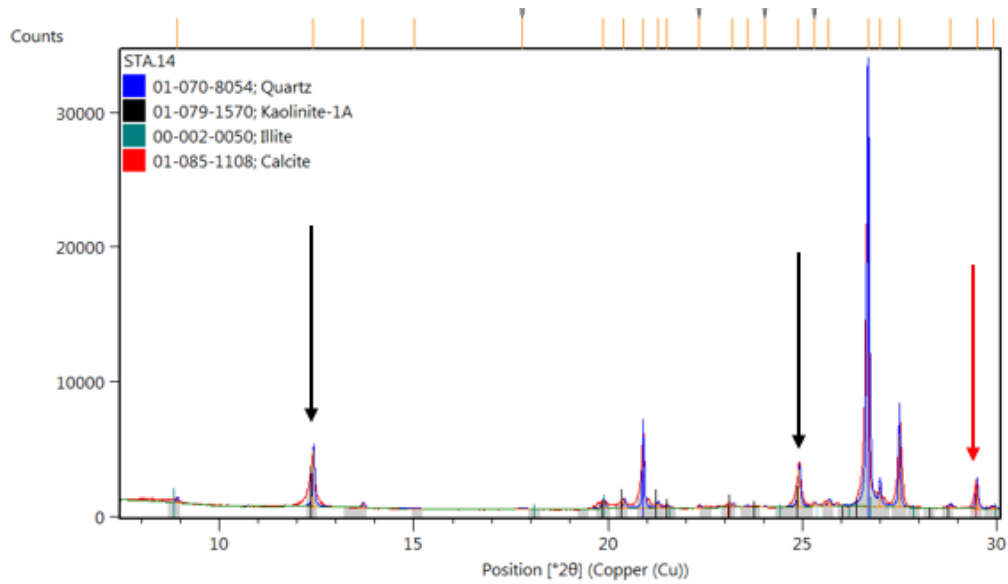


Figure 128: Reference pattern list for sample STA14.

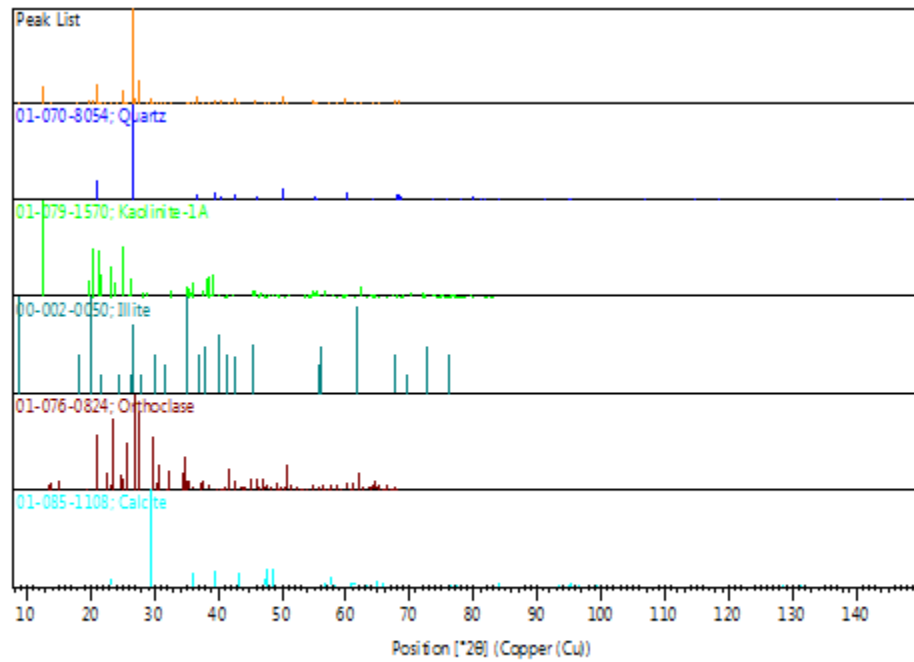


Table 37: Reference peak list for sample STA14.

Pos. [°2 θ]	Height [cts]	FWHM Left [°2 θ]	d-spacing [Å]	Rel. Int. [%]
8.9110	364.76	0.0630	9.91566	1.60
12.4120	4277.81	0.0630	7.12556	18.73
13.6915	352.23	0.0630	6.46240	1.54
15.0165	27.19	0.3779	5.89506	0.12
17.7911	61.03	0.3779	4.98143	0.27
19.8715	623.96	0.0945	4.46436	2.73
20.4073	646.38	0.0787	4.34835	2.83
20.8981	4869.65	0.0551	4.24732	21.33
21.2767	421.02	0.0945	4.17259	1.84
21.5176	211.16	0.0945	4.12642	0.92
22.3444	176.52	0.0630	3.97556	0.77
23.2067	316.45	0.0630	3.82976	1.39
23.5785	105.88	0.1260	3.77021	0.46
24.0256	47.46	0.0945	3.70105	0.21
24.9067	2937.95	0.0708	3.57208	12.87
25.3243	278.81	0.0630	3.51411	1.22
25.6821	486.64	0.1102	3.46596	2.13
26.6928	22834.23	0.0768	3.33697	100.00
27.0038	1300.28	0.0576	3.29925	5.69
27.5025	5481.86	0.0480	3.24054	24.01
28.8175	229.05	0.1344	3.09559	1.00
29.5011	1569.96	0.0672	3.02540	6.88
29.9256	149.88	0.1536	2.98344	0.66
30.2537	206.48	0.0768	2.95182	0.90
30.9020	360.65	0.0672	2.89136	1.58
31.5827	78.36	0.2304	2.83058	0.34
32.4811	52.66	0.4608	2.75430	0.23
32.9245	57.34	0.2304	2.71822	0.25
34.9709	481.77	0.1728	2.56370	2.11
35.4576	195.58	0.1920	2.52962	0.86
36.0311	365.27	0.1344	2.49066	1.60
36.5958	1595.73	0.0672	2.45351	6.99
37.0759	72.87	0.1536	2.42283	0.32
37.7351	271.51	0.0768	2.38201	1.19
38.5593	406.85	0.1152	2.33297	1.78
39.5169	1041.48	0.0768	2.27862	4.56
40.3339	593.85	0.0576	2.23433	2.60
41.8365	270.93	0.0768	2.15749	1.19
42.5032	1159.22	0.0768	2.12517	5.08
43.2527	203.56	0.0768	2.09007	0.89
44.1375	30.02	0.2304	2.05020	0.13
45.4443	173.25	0.2304	1.99424	0.76
45.8192	702.04	0.0672	1.97879	3.07
47.1656	109.84	0.1152	1.92539	0.48
47.6108	146.82	0.1920	1.90842	0.64
48.0349	41.08	0.1536	1.89256	0.18
48.5861	101.49	0.1152	1.87237	0.44
49.0288	102.72	0.2304	1.85649	0.45
50.1891	1774.19	0.0768	1.81626	7.77
50.5798	201.77	0.1536	1.80314	0.88

Table 37 Continued

51.0637	137.82	0.1152	1.78718	0.60
54.9204	719.65	0.0576	1.67045	3.15
55.0634	512.70	0.0768	1.66645	2.25
55.3542	301.10	0.0768	1.65838	1.32
56.8304	83.11	0.1536	1.61876	0.36
57.4762	46.35	0.1152	1.60210	0.20
58.1983	22.92	0.2304	1.58393	0.10
58.7613	35.24	0.3072	1.57009	0.15
60.0086	1293.84	0.0768	1.54040	5.67
61.6220	40.53	0.6144	1.50388	0.18
62.2971	161.19	0.1152	1.48920	0.71
62.4759	134.44	0.1152	1.48536	0.59
64.0713	303.23	0.0960	1.45217	1.33
65.2532	66.48	0.2304	1.42870	0.29
65.7968	64.65	0.1152	1.41820	0.28
66.4007	23.81	0.3072	1.40676	0.10
67.7830	840.40	0.0576	1.38140	3.68
68.1812	869.95	0.0384	1.37430	3.81
68.3637	972.68	0.0768	1.37107	4.26

Figure 129: Reference diffractogram for sample STA15. Red arrows point to most intense zippeite peaks, and black arrows point to most intense gypsum peaks. Feldspars remove for clarity.

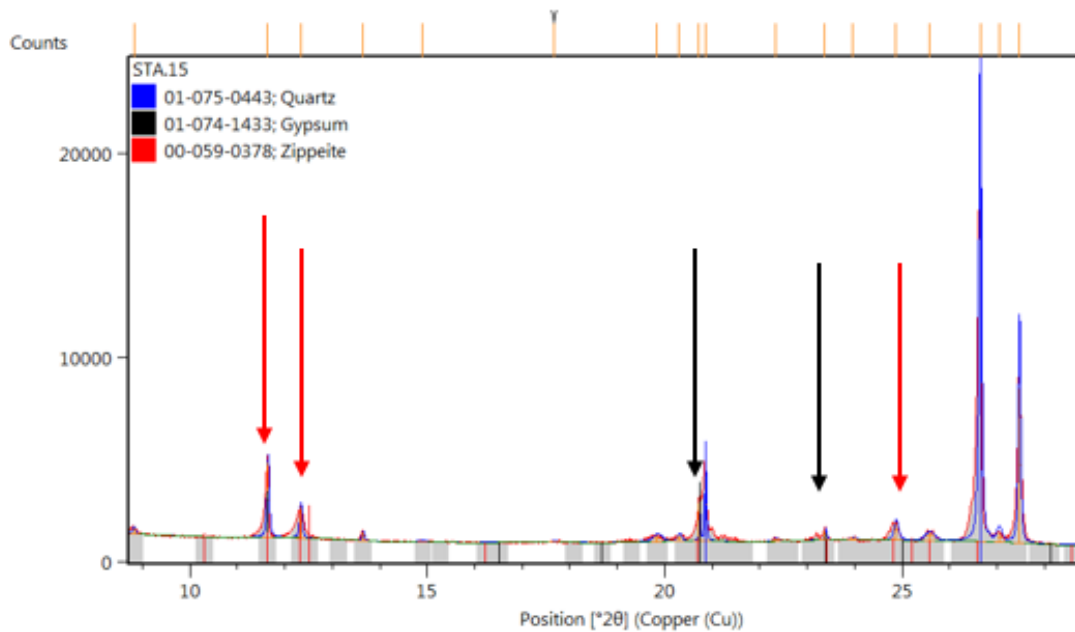


Figure 133: Reference pattern list for sample STA15.

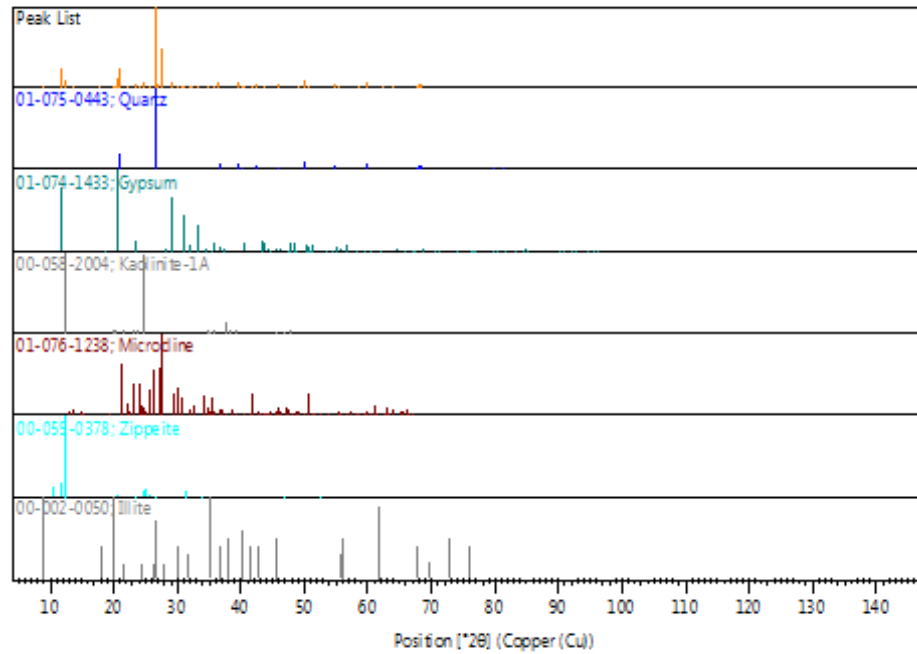


Table 38: Reference peak list for sample STA15.

Pos. [°2θ]	Height [cts]	FWHM Left [°2θ]	d-spacing [Å]	Rel. Int. [%]
5.1561	72.51	0.7557	17.12521	0.46
8.8239	332.88	0.0630	10.01342	2.10
11.6407	3777.21	0.0630	7.59590	23.81
12.3316	1623.00	0.0630	7.17187	10.23
13.6447	449.29	0.0551	6.48450	2.83
14.8966	74.70	0.1889	5.94221	0.47
17.6784	59.80	0.1889	5.01295	0.38
19.8356	333.73	0.2204	4.47237	2.10
20.3004	331.91	0.1102	4.37101	2.09
20.7214	1957.37	0.0315	4.28313	12.34
20.8478	3579.77	0.0394	4.25745	22.57
22.3217	148.20	0.1260	3.97955	0.93
23.3741	532.42	0.0472	3.80270	3.36
23.9551	106.72	0.1260	3.71178	0.67
24.8573	907.23	0.1102	3.57906	5.72
25.5703	431.35	0.2204	3.48086	2.72
26.6431	15863.98	0.0672	3.34308	100.00
27.0462	479.67	0.1152	3.29417	3.02
27.4688	7706.70	0.0576	3.24443	48.58
29.1182	994.41	0.0864	3.06430	6.27
29.4551	178.01	0.1152	3.03001	1.12
30.1918	216.85	0.0960	2.95773	1.37
30.7759	282.13	0.1344	2.90292	1.78

Table 38 Continued

31.1164	299.09	0.0768	2.87193	1.89
32.1314	99.64	0.3072	2.78348	0.63
32.4153	98.97	0.2304	2.75975	0.62
33.3606	185.11	0.1920	2.68368	1.17
34.2221	120.56	0.2304	2.61806	0.76
34.9548	294.21	0.1920	2.56484	1.85
35.4292	111.45	0.1536	2.53158	0.70
35.9439	114.13	0.1920	2.49650	0.72
36.5421	976.14	0.0960	2.45699	6.15
37.6720	73.19	0.3072	2.38585	0.46
38.5726	138.21	0.1920	2.33220	0.87
39.4735	895.91	0.0576	2.28102	5.65
40.2911	438.88	0.0672	2.23660	2.77
40.6403	133.69	0.1536	2.21818	0.84
41.7972	295.69	0.1344	2.15942	1.86
42.4489	645.26	0.0960	2.12776	4.07
43.6194	118.90	0.4608	2.07334	0.75
45.7861	502.02	0.0384	1.98014	3.16
47.8377	99.88	0.1920	1.89990	0.63
48.9212	61.05	0.3072	1.86032	0.38
50.1413	1556.32	0.0768	1.81788	9.81
50.5256	247.69	0.1152	1.80495	1.56
52.7619	15.43	0.4608	1.73359	0.10
54.8709	463.69	0.0768	1.67184	2.92
55.3200	215.63	0.0960	1.65933	1.36
56.7286	125.02	0.1920	1.62142	0.79
58.7025	108.12	0.3072	1.57152	0.68
59.9634	940.81	0.0768	1.54145	5.93
61.2938	30.43	0.6144	1.51114	0.19
62.2803	79.29	0.4608	1.48956	0.50
64.0285	235.19	0.0960	1.45304	1.48
65.2226	41.01	0.2304	1.42929	0.26
67.7301	570.60	0.0672	1.38235	3.60
68.1429	643.05	0.0864	1.37498	4.05
68.3027	670.34	0.0672	1.37215	4.23

Figure 131: Reference diffractogram for sample STA16. Kaolinite peak illustrated by green arrow.

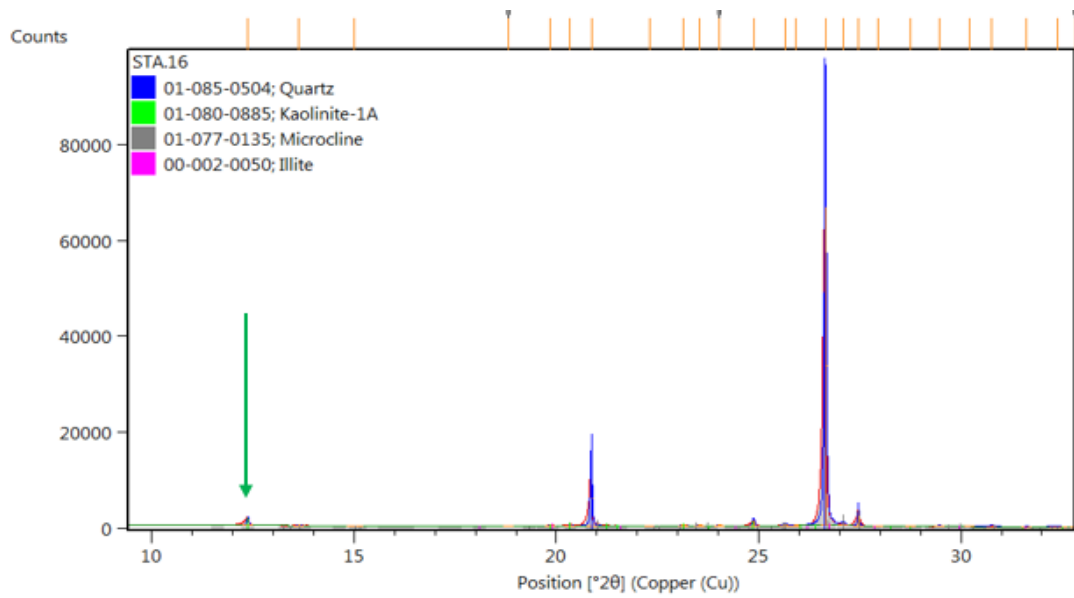


Figure 132: Reference pattern list for sample STA16.

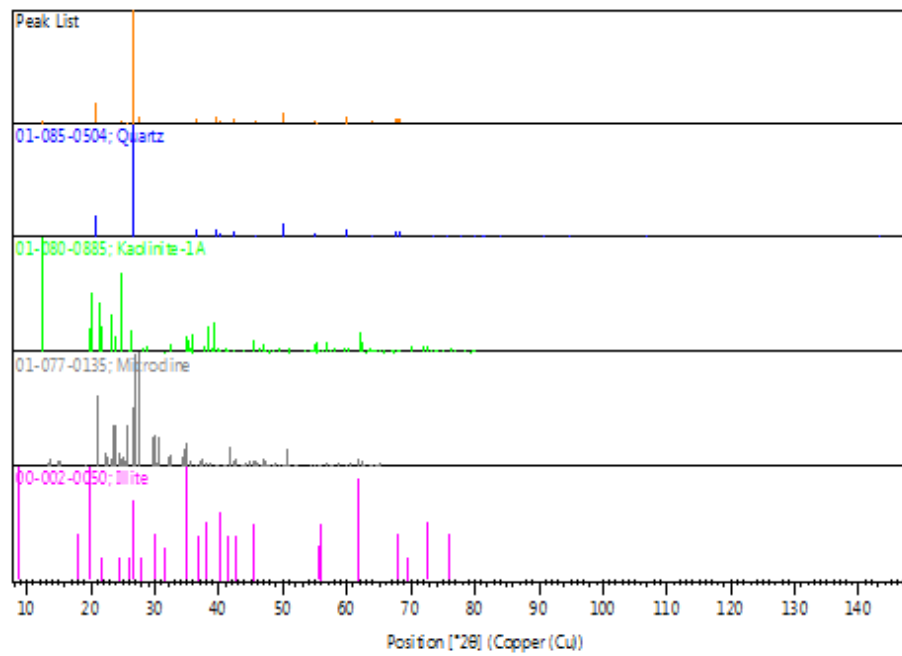


Table 39: Reference peak list for sample STA16.

Pos. [$^{\circ}2\theta$]	Height [cts]	FWHM Left [$^{\circ}2\theta$]	d-spacing [Å]	Rel. Int. [%]
8.8296	60.39	0.1889	10.00692	0.09
12.3676	1672.33	0.0551	7.15107	2.47
13.6375	168.25	0.0630	6.48789	0.25
15.0030	22.12	0.3779	5.90030	0.03
18.8197	41.95	0.1260	4.71143	0.06
19.8328	203.66	0.0787	4.47299	0.30
20.3377	280.61	0.0630	4.36308	0.42
20.8644	11402.87	0.0480	4.25410	16.87
22.3088	43.12	0.1920	3.98184	0.06
23.1446	86.62	0.1920	3.83989	0.13
23.5361	81.95	0.1152	3.77690	0.12
24.0334	128.09	0.1344	3.69985	0.19
24.8763	1196.98	0.0672	3.57638	1.77
25.6657	281.79	0.1344	3.46814	0.42
25.9021	143.42	0.1152	3.43701	0.21
26.6464	67598.64	0.0576	3.34268	100.00
27.0831	396.11	0.0960	3.28976	0.59
27.4646	3446.83	0.0384	3.24492	5.10
27.9548	67.14	0.1536	3.18913	0.10
28.7515	118.14	0.1536	3.10254	0.17
29.4594	203.87	0.0960	3.02958	0.30
30.2102	80.86	0.1152	2.95598	0.12
30.7681	189.48	0.2304	2.90364	0.28
31.6270	37.03	0.1920	2.82671	0.05
32.3845	42.54	0.4608	2.76230	0.06
32.8205	38.10	0.2304	2.72659	0.06
34.1947	39.04	0.1152	2.62010	0.06
34.9573	153.08	0.1536	2.56467	0.23
35.1167	144.19	0.1536	2.55339	0.21
35.4101	74.92	0.1152	2.53290	0.11
35.9742	118.50	0.1344	2.49447	0.18
36.5470	3601.44	0.0672	2.45668	5.33
37.7257	85.45	0.1920	2.38258	0.13
38.4902	211.50	0.4224	2.33700	0.31
39.4772	3609.95	0.0672	2.28082	5.34
40.2914	1649.38	0.0768	2.23659	2.44
41.8025	238.20	0.0576	2.15916	0.35
42.4510	2615.85	0.0672	2.12767	3.87
44.1226	12.36	0.2304	2.05086	0.02
45.7970	1928.48	0.0768	1.97970	2.85
47.1308	99.87	0.1536	1.92673	0.15
49.0262	46.84	0.2304	1.85659	0.07
50.1454	6394.77	0.0768	1.81774	9.46
50.6269	246.37	0.0576	1.80157	0.36
54.8811	1920.46	0.0768	1.67155	2.84
55.3257	650.67	0.0864	1.65917	0.96
56.8125	36.59	0.3072	1.61923	0.05
57.2271	72.78	0.0768	1.60848	0.11
58.6869	17.89	0.3072	1.57190	0.03
59.9651	3891.00	0.0960	1.54141	5.76

Table 39 Continued

62.2627	104.67	0.1536	1.48993	0.15
64.0448	744.93	0.0768	1.45271	1.10
65.1971	14.88	0.3072	1.42979	0.02
65.7810	139.92	0.0960	1.41851	0.21
66.4138	14.71	0.2304	1.40652	0.02
67.7480	2470.19	0.0864	1.38203	3.65
68.1506	2850.77	0.0768	1.37484	4.22
68.3368	2567.79	0.1152	1.37155	3.80

Figure 133: Reference diffractogram for sample STA17. Trace carnotite peaks highlighted by red arrows.

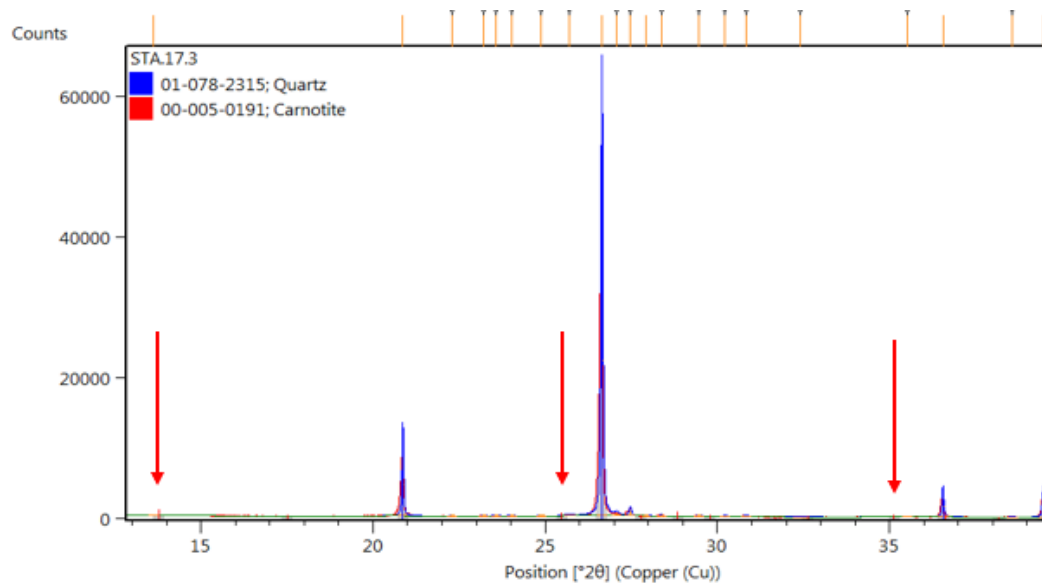


Figure 134: Reference pattern list for sample STA17.

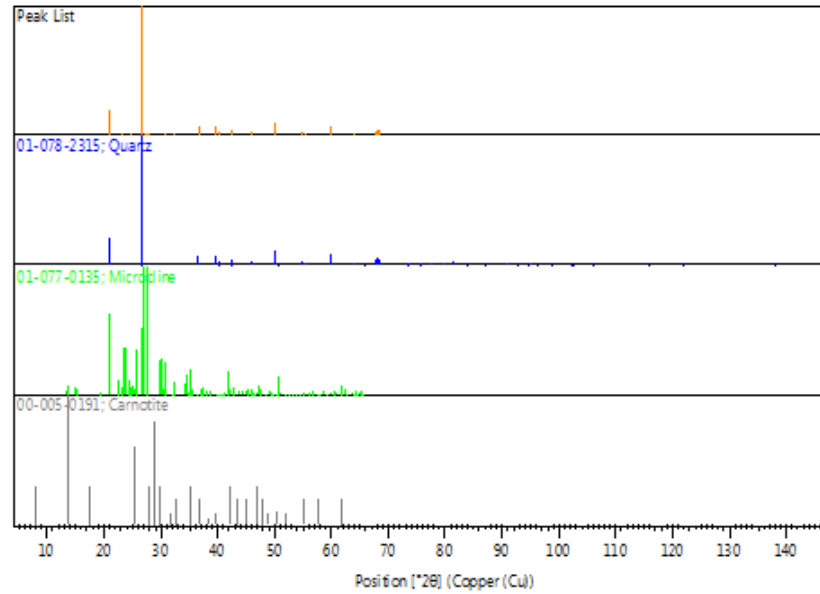


Table 40: Reference peak list for sample STA17.

Pos. [°2θ]	Height [cts]	FWHM Left [°2θ]	d-spacing [Å]	Rel. Int. [%]
5.1760	61.78	0.5038	17.05951	0.14
12.3889	108.63	0.1260	7.13882	0.24
13.6738	46.62	0.0945	6.47075	0.10
20.9165	8815.77	0.0576	4.24362	19.65
22.3271	54.29	0.1152	3.97860	0.12
23.2682	41.29	0.1152	3.81977	0.09
23.6205	46.29	0.1536	3.76360	0.10
24.0809	106.91	0.1152	3.69267	0.24
24.9135	50.75	0.1920	3.57112	0.11
25.7345	151.20	0.3072	3.45902	0.34
26.6967	44871.46	0.0672	3.33649	100.00
27.1319	326.58	0.1152	3.28396	0.73
27.5154	873.05	0.0864	3.23905	1.95
27.9834	44.57	0.1152	3.18593	0.10
28.4176	171.79	0.0288	3.13823	0.38
29.5155	125.38	0.1536	3.02395	0.28
30.2736	82.75	0.1920	2.94993	0.18
30.8749	120.41	0.1920	2.89383	0.27
32.4681	47.84	0.4608	2.75538	0.11
35.5561	35.49	0.2304	2.52284	0.08
36.6007	2946.70	0.0672	2.45319	6.57
38.6011	31.17	0.3072	2.33054	0.07
39.5209	2614.63	0.0768	2.27839	5.83
40.3414	1317.21	0.0576	2.23393	2.94
41.8437	122.74	0.1152	2.15713	0.27
42.5057	1882.03	0.0768	2.12505	4.19
45.8482	1366.79	0.0672	1.97760	3.05

Table 40 Continued

47.2035	27.43	0.2304	1.92393	0.06
48.8291	74.49	0.1152	1.86362	0.17
50.1900	4473.05	0.1056	1.81623	9.97
50.6609	145.83	0.1920	1.80044	0.33
53.4536	25.37	0.2304	1.71278	0.06
54.9226	1208.64	0.0864	1.67039	2.69
55.3778	489.71	0.1056	1.65773	1.09
57.2760	78.27	0.0768	1.60722	0.17
60.0130	2652.70	0.1056	1.54030	5.91
64.0891	476.82	0.0960	1.45181	1.06
65.8360	106.28	0.1344	1.41745	0.24
67.7980	1581.99	0.1056	1.38113	3.53
68.1888	2004.51	0.0960	1.37417	4.47
68.3632	2007.36	0.0960	1.37108	4.47

Figure 135: Reference pattern list for sample STA18.

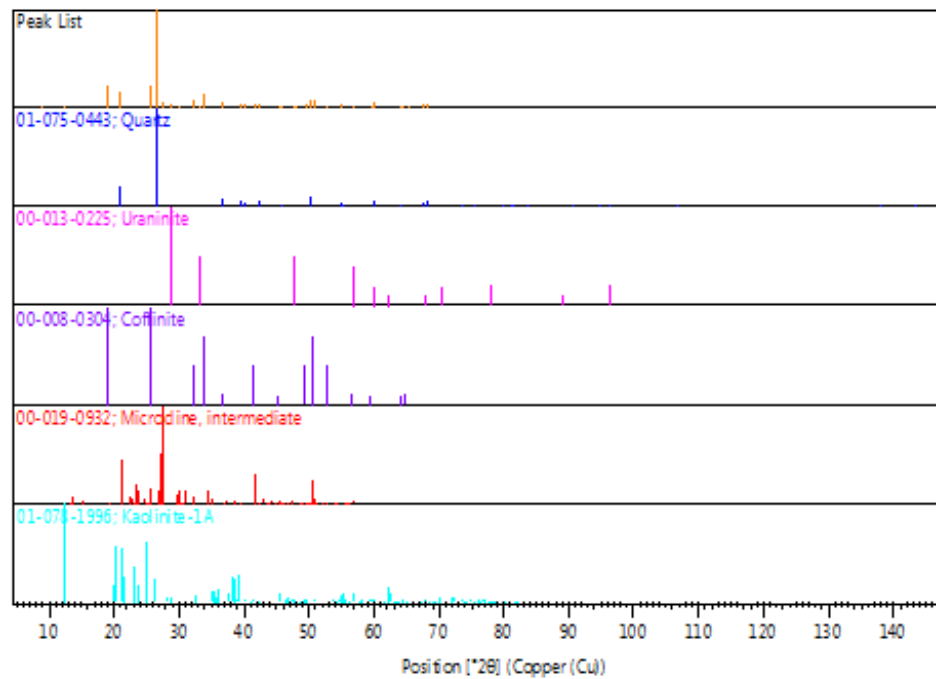


Table 41: reference peak list for sample STA18.

Pos. [$^{\circ}2\theta$]	Height [cts]	FWHM Left [$^{\circ}2\theta$]	d-spacing [Å]	Rel. Int. [%]
5.4690	74.30	0.8817	16.14628	0.44
8.7244	62.58	0.3779	10.12735	0.37
12.3224	217.53	0.2204	7.17716	1.28
13.6370	116.47	0.0945	6.48811	0.68
19.1200	3572.40	0.0945	4.63810	20.96
20.8561	2726.27	0.0480	4.25578	15.99
25.7065	3851.87	0.1248	3.46273	22.60
26.6421	17046.27	0.0480	3.34321	100.00
27.4572	1166.56	0.0480	3.24578	6.84
27.5334	1083.43	0.0576	3.23697	6.36
28.8222	691.83	0.9216	3.09509	4.06
30.1314	177.89	0.1152	2.96352	1.04
32.2422	1216.07	0.1152	2.77417	7.13
33.2976	212.66	0.6144	2.68861	1.25
34.0002	2139.98	0.0576	2.63464	12.55
36.5293	917.78	0.0480	2.45782	5.38
36.6263	900.03	0.0480	2.45154	5.28
39.4686	745.95	0.0672	2.28129	4.38
40.2937	421.87	0.0288	2.23646	2.47
41.7048	711.56	0.0864	2.16400	4.17
42.4187	460.24	0.0768	2.12921	2.70
43.0888	59.54	0.1920	2.09764	0.35
45.4812	405.88	0.1536	1.99270	2.38
45.7914	360.12	0.0384	1.97993	2.11
47.6725	177.42	0.6144	1.90609	1.04
48.0135	164.02	0.3840	1.89335	0.96
49.5692	448.28	0.0960	1.83751	2.63
50.1383	1187.23	0.0672	1.81798	6.96
50.8774	1274.22	0.1536	1.79329	7.48
52.8204	463.37	0.1152	1.73181	2.72
54.8717	536.14	0.0672	1.67182	3.15
55.3211	141.17	0.0576	1.65930	0.83
56.7167	314.37	0.3840	1.62173	1.84
59.6296	295.59	0.1536	1.54928	1.73
59.9493	817.36	0.0864	1.54178	4.79
64.0191	220.18	0.0576	1.45323	1.29
64.3181	225.02	0.3072	1.44719	1.32
65.4951	111.15	0.3840	1.42401	0.65
67.7141	462.12	0.0768	1.38264	2.71
68.1358	504.78	0.0864	1.37510	2.96
68.2991	546.44	0.1056	1.37221	3.21
69.4456	146.16	0.1536	1.35234	0.86

Figure 136: Reference diffractogram for sample STA18A (Host-rock). Red arrows point to most intense calcite peaks.

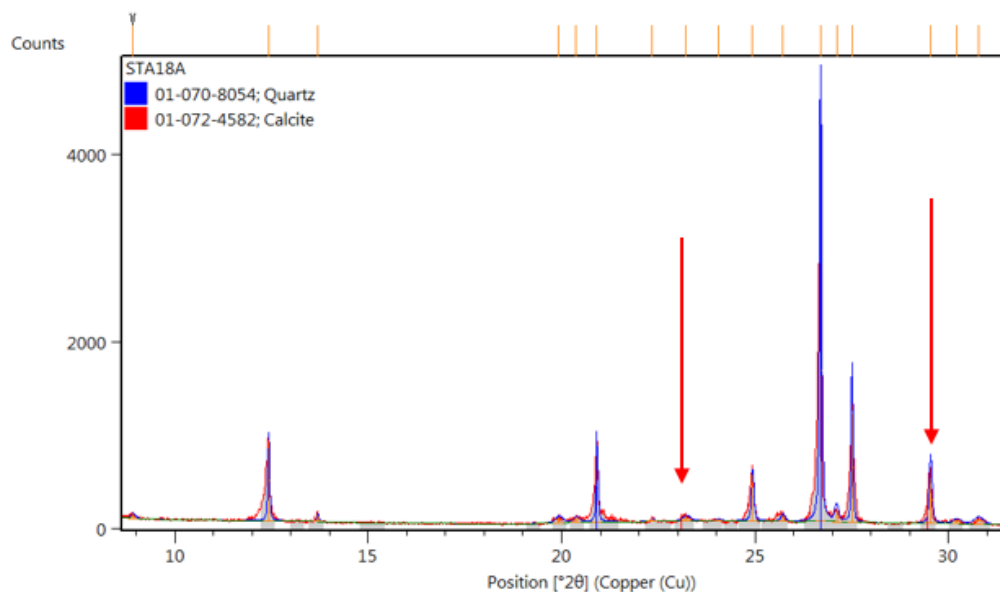


Figure 137: Reference pattern list for sample STA18A (Host-rock).

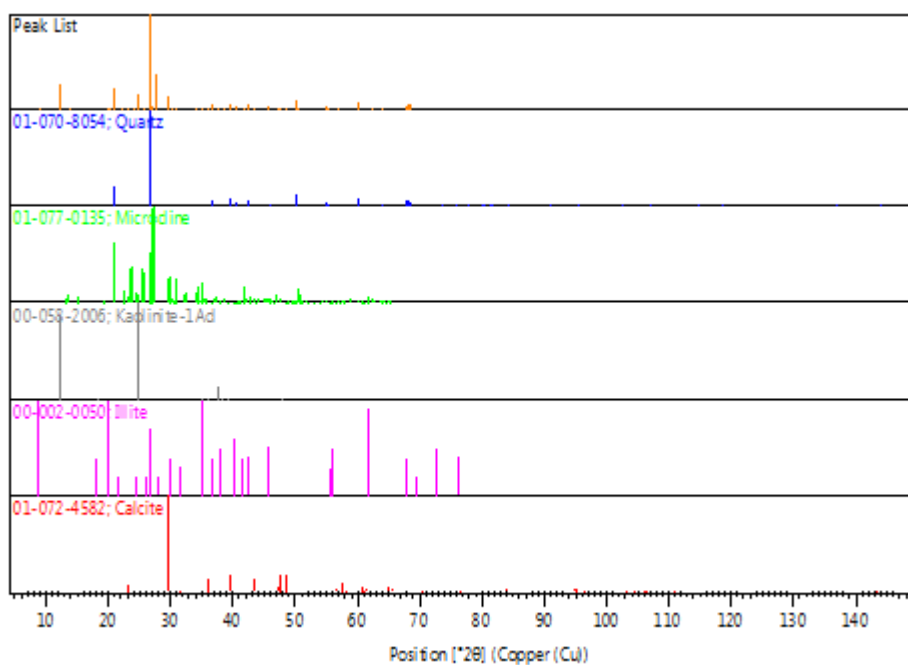


Table 42: reference peak list for sample STA18A (Host-rock).

Pos. [$^{\circ}2\theta$]	Height [cts]	FWHM Left [$^{\circ}2\theta$]	d-spacing [\AA]	Rel. Int. [%]
5.2275	20.75	0.8817	16.89163	0.63
8.9180	52.57	0.1260	9.90789	1.59
12.4200	875.47	0.0551	7.12099	26.47
13.6904	78.48	0.0630	6.46294	2.37
19.9183	66.53	0.2204	4.45400	2.01
20.3779	55.54	0.1889	4.35456	1.68
20.9040	739.15	0.0630	4.24613	22.35
22.3431	28.45	0.0945	3.97580	0.86
23.2214	54.77	0.2204	3.82736	1.66
24.0497	19.00	0.0945	3.69739	0.57
24.9231	507.32	0.0787	3.56976	15.34
25.7079	77.59	0.1260	3.46254	2.35
26.6983	3307.17	0.0672	3.33629	100.00
27.1133	120.11	0.1152	3.28617	3.63
27.5126	1183.09	0.0480	3.23937	35.77
29.5457	502.02	0.0864	3.02093	15.18
30.2234	36.35	0.2304	2.95471	1.10
30.7885	52.04	0.2688	2.90176	1.57
32.5041	20.35	0.2304	2.75241	0.62
34.2756	14.66	0.2304	2.61410	0.44
34.9945	59.59	0.2688	2.56203	1.80
36.5993	205.57	0.0768	2.45329	6.22
37.7522	39.20	0.2304	2.38097	1.19
38.5990	64.15	0.3072	2.33067	1.94
39.5089	196.75	0.0960	2.27906	5.95
40.3377	94.99	0.0768	2.23412	2.87
41.8687	76.77	0.0960	2.15590	2.32
42.4938	164.96	0.0768	2.12562	4.99
43.3040	27.51	0.1920	2.08771	0.83
45.8446	115.23	0.0768	1.97775	3.48
47.2310	23.58	0.2304	1.92288	0.71
47.6948	45.46	0.1536	1.90526	1.37
48.6592	45.80	0.1152	1.86972	1.38
50.1924	339.88	0.0480	1.81615	10.28
50.5794	58.76	0.1920	1.80315	1.78
54.9158	106.60	0.0960	1.67058	3.22
55.3837	52.44	0.0960	1.65757	1.59
56.8293	22.57	0.3072	1.61879	0.68
57.5650	12.11	0.2304	1.59984	0.37
60.0011	237.20	0.0768	1.54057	7.17
62.3660	29.99	0.3840	1.48772	0.91
64.0684	59.09	0.0960	1.45223	1.79
65.2286	6.88	0.6144	1.42918	0.21
67.7967	129.58	0.1152	1.38115	3.92
68.1839	175.22	0.0672	1.37425	5.30
68.3742	184.85	0.0576	1.37089	5.59

Figure 138: Reference diffractogram for sample STA18B (Host-rock). Calcite highlighted by red arrows.

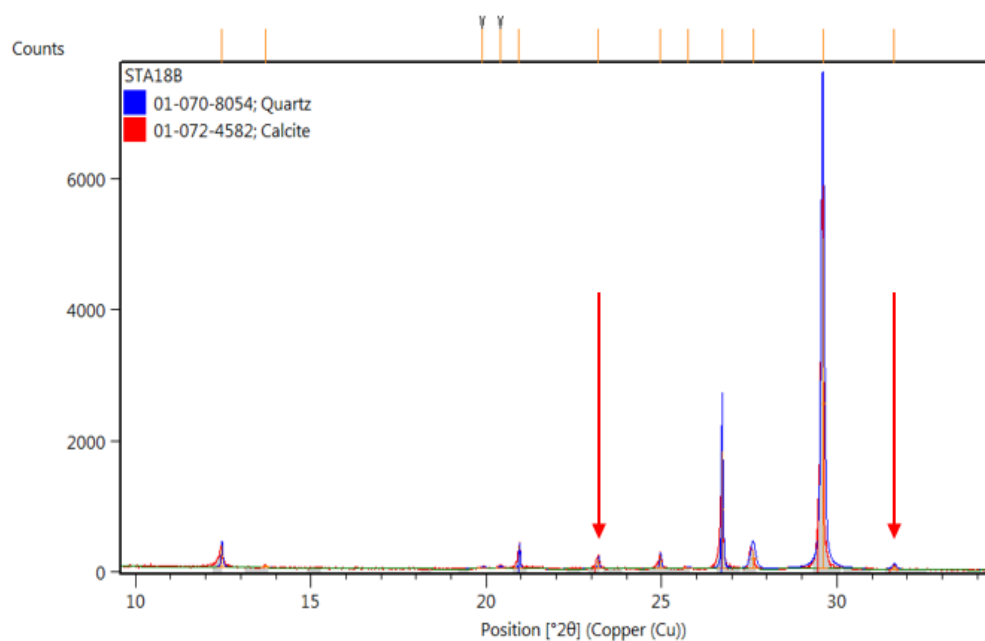


Figure 139: Reference pattern list of sample STA18B (Host-rock).

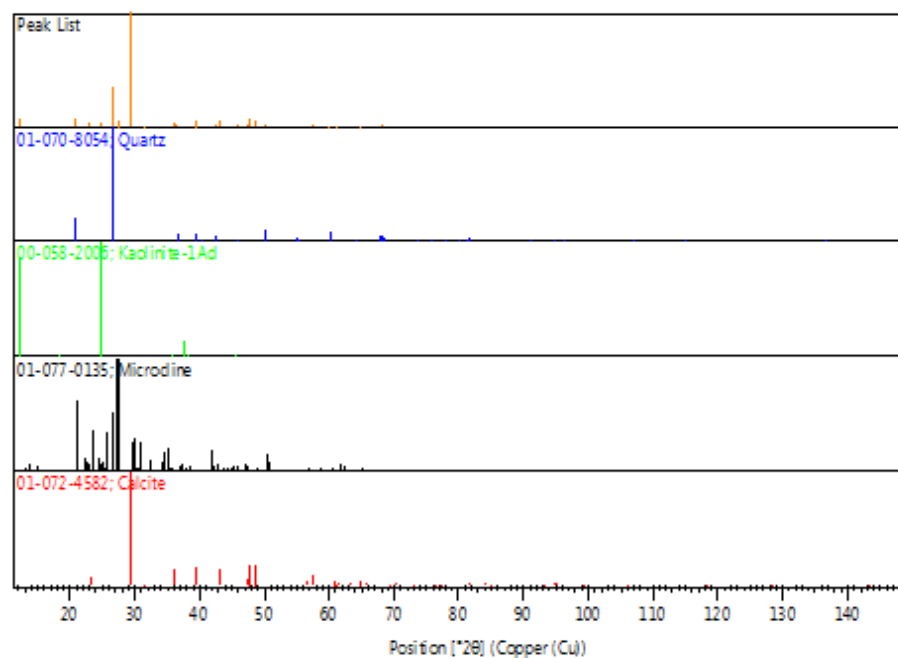


Table 43: Reference peak list of sample STA18B (host-rock).

Pos. [$^{\circ}2\theta$]	Height [cts]	FWHM Left [$^{\circ}2\theta$]	d-spacing [\AA]	Rel. Int. [%]
12.3307	353.81	0.0551	7.17240	6.88
13.5832	22.96	0.0945	6.51368	0.45
19.7671	21.61	0.1889	4.48771	0.42
20.2796	27.98	0.1260	4.37544	0.54
20.8099	342.68	0.0394	4.26512	6.67
23.0586	172.95	0.0472	3.85402	3.37
24.8261	215.06	0.0630	3.58349	4.18
25.6366	16.61	0.1889	3.47200	0.32
26.6065	1835.07	0.0480	3.34760	35.71
27.4802	283.49	0.1728	3.24312	5.52
29.4682	5139.32	0.1056	3.02869	100.00
31.5103	59.24	0.1152	2.83692	1.15
34.9735	17.05	0.3072	2.56351	0.33
36.0083	180.88	0.0864	2.49218	3.52
36.5058	111.06	0.0480	2.45935	2.16
37.7020	14.60	0.2304	2.38403	0.28
38.4020	26.32	0.3072	2.34217	0.51
39.4426	327.83	0.0576	2.28274	6.38
41.7474	15.85	0.3072	2.16188	0.31
42.4156	82.40	0.0576	2.12936	1.60
43.2353	285.79	0.1152	2.09087	5.56
45.7641	55.23	0.0768	1.98104	1.07
47.2156	75.09	0.0768	1.92347	1.46
47.6330	362.96	0.0672	1.90759	7.06
48.6338	297.77	0.0576	1.87064	5.79
50.1044	168.49	0.0480	1.81913	3.28
54.8428	48.31	0.0768	1.67263	0.94
56.6622	32.21	0.1536	1.62317	0.63
57.4994	91.90	0.0960	1.60150	1.79
58.3000	14.03	0.3072	1.58140	0.27
59.9095	107.56	0.0576	1.54271	2.09
60.7875	67.23	0.0768	1.52251	1.31
61.1766	66.95	0.1152	1.51376	1.30
62.4113	10.08	0.4608	1.48674	0.20
63.2047	17.00	0.3072	1.46998	0.33
64.0006	18.25	0.1152	1.45360	0.36
64.7890	55.52	0.1152	1.43781	1.08
65.8720	70.74	0.0768	1.41677	1.38
67.7111	63.48	0.0768	1.38269	1.24
68.1157	77.76	0.0768	1.37546	1.51
68.2912	76.68	0.0960	1.37235	1.49

Figure 140: Reference Diffractogram for sample STA19.

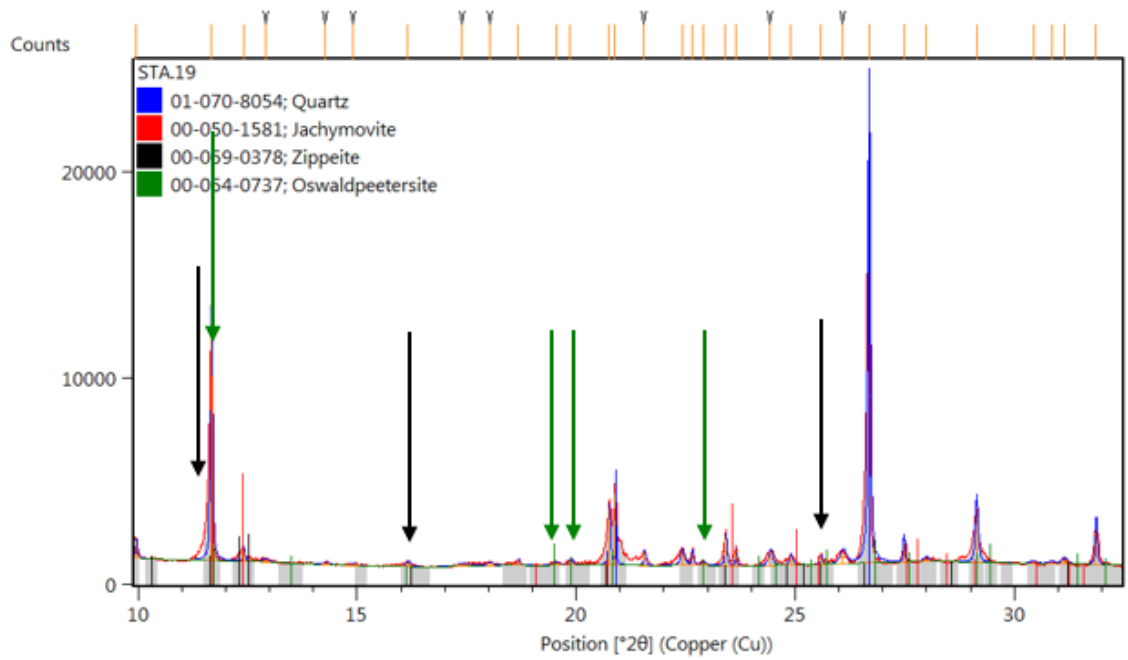


Figure 141: Reference pattern list for sample STA19.

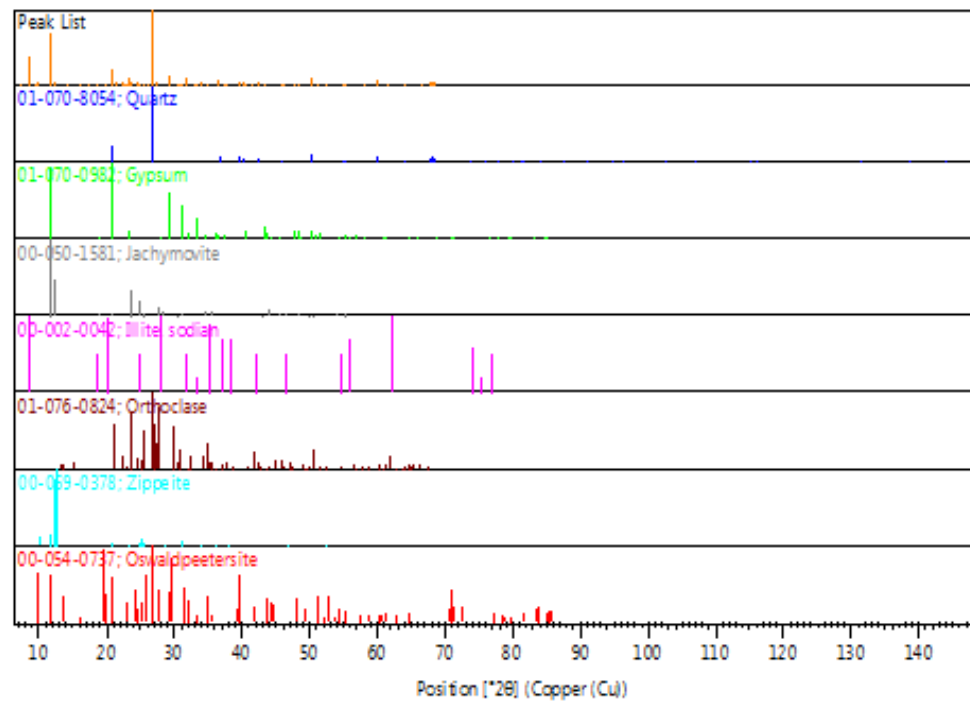


Table 44: Reference peak list for sample STA19.

Pos. [$^{\circ}2\theta$]	Height [cts]	FWHM Left [$^{\circ}2\theta$]	d-spacing [\AA]	Rel. Int. [%]
7.3834	129.06	0.0945	11.96341	0.78
8.6737	6096.17	0.1181	10.18639	36.92
9.3887	228.92	0.0630	9.41225	1.39
9.9624	828.53	0.0630	8.87150	5.02
11.6739	11396.16	0.0630	7.57440	69.02
12.4156	643.76	0.0472	7.12349	3.90
12.9026	144.69	0.1889	6.85572	0.88
14.2832	82.92	0.1889	6.19599	0.50
14.9002	68.54	0.3149	5.94079	0.42
16.1649	235.49	0.1260	5.47875	1.43
17.4091	112.18	0.3779	5.08989	0.68
18.0254	149.92	0.1574	4.91722	0.91
18.6797	274.52	0.0630	4.74643	1.66
19.5423	146.90	0.1260	4.53882	0.89
19.8704	262.15	0.0945	4.46461	1.59
20.7508	2827.89	0.0472	4.27713	17.13
20.8861	3509.57	0.0315	4.24974	21.25
21.5493	680.59	0.0551	4.12042	4.12
22.6451	649.05	0.0551	3.92345	3.93
22.8909	185.03	0.0945	3.88187	1.12
23.4047	1446.59	0.0551	3.79781	8.76
23.6347	834.49	0.0315	3.76136	5.05
24.4223	716.61	0.1102	3.64182	4.34
24.8884	472.68	0.0945	3.57465	2.86
25.5833	411.54	0.0394	3.47912	2.49
26.0777	615.52	0.1732	3.41428	3.73
26.6900	16511.90	0.0672	3.33731	100.00
27.4900	917.66	0.0480	3.24198	5.56
27.9936	157.03	0.1536	3.18480	0.95
29.1480	2237.44	0.0768	3.06124	13.55
30.4392	72.92	0.1536	2.93425	0.44
30.8580	82.09	0.1536	2.89538	0.50
31.1516	194.51	0.1536	2.86876	1.18
31.8724	1583.26	0.0576	2.80551	9.59
32.9171	269.86	0.2688	2.71882	1.63
33.3879	285.79	0.2304	2.68154	1.73
34.0527	990.34	0.0672	2.63070	6.00
35.0455	141.76	0.2304	2.55841	0.86
36.5867	1311.13	0.0672	2.45410	7.94
37.3300	83.71	0.2304	2.40693	0.51
37.8702	432.32	0.0576	2.37382	2.62
38.6145	97.13	0.2304	2.32976	0.59
39.5189	715.64	0.0768	2.27850	4.33
40.3409	542.48	0.0576	2.23395	3.29
40.6400	146.53	0.1536	2.21820	0.89
41.3477	49.46	0.2304	2.18185	0.30
42.4862	698.19	0.0480	2.12598	4.23
43.3626	130.21	0.1536	2.08502	0.79
44.3126	136.12	0.2304	2.04250	0.82
45.8424	603.66	0.0672	1.97784	3.66

Table 44 Continued

46.2351	301.56	0.0672	1.96195	1.83
47.8567	170.01	0.1536	1.89919	1.03
48.3365	192.14	0.0768	1.88145	1.16
50.1790	1551.11	0.0864	1.81660	9.39
51.3188	184.04	0.3072	1.77890	1.11
52.5369	235.01	0.0576	1.74048	1.42
54.9248	508.48	0.0480	1.67033	3.08
55.3576	186.86	0.0768	1.65829	1.13
56.7732	160.14	0.1536	1.62025	0.97
58.2078	266.08	0.0768	1.58369	1.61
59.0689	143.78	0.0960	1.56264	0.87
60.0018	1088.13	0.0864	1.54056	6.59
61.6071	29.76	0.7680	1.50421	0.18
64.0694	282.89	0.0960	1.45221	1.71
65.8630	30.61	0.4608	1.41694	0.19
66.6561	132.20	0.0576	1.40199	0.80
67.7732	665.63	0.0480	1.38158	4.03
67.9646	351.72	0.0768	1.37815	2.13
68.1824	792.66	0.0768	1.37428	4.80
68.3429	833.39	0.0768	1.37144	5.05

Figure 142: Reference diffractogram for sample STA20. Observe the dominance of quartz in this diffractogram.

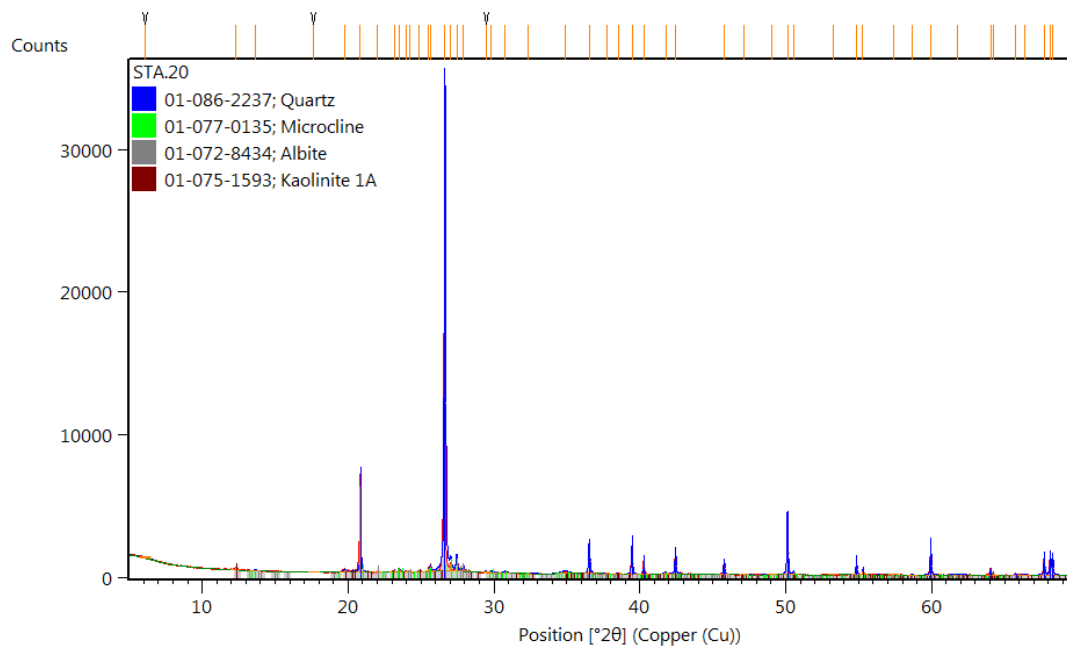


Figure143: Reference pattern list of sample STA20.

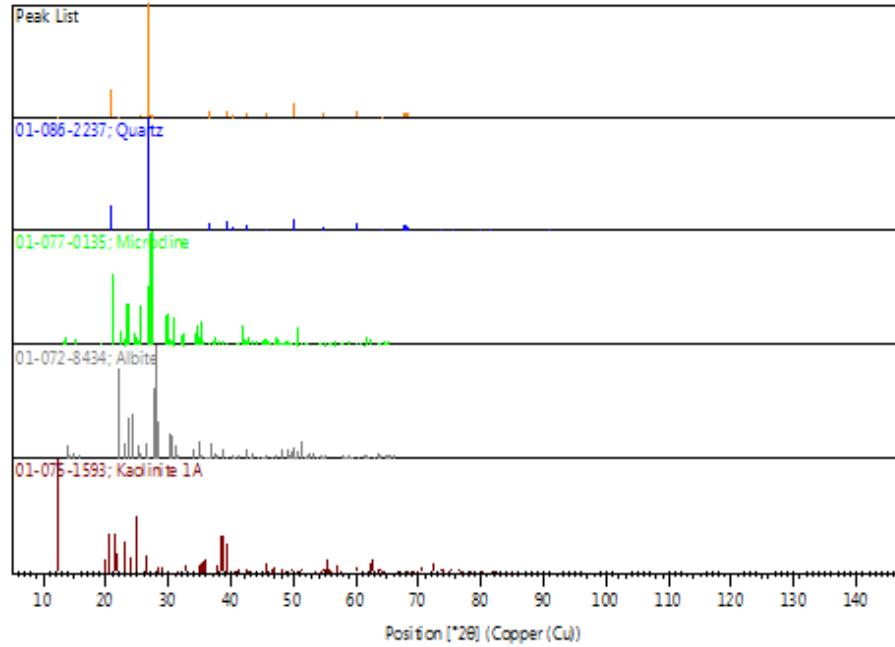


Table 45: Reference peak list for sample STA20.

Pos. [2θ]	Height [cts]	FWHM Left [2θ]	d-spacing [Å]	Rel. Int. [%]
6.0981	64.70	0.7557	14.48180	0.27
12.3330	134.13	0.1102	7.17107	0.56
13.6426	51.94	0.1260	6.48546	0.22
17.6331	25.66	0.7557	5.02571	0.11
19.7675	172.94	0.1889	4.48763	0.72
20.8424	6084.73	0.0708	4.25854	25.33
22.0043	112.58	0.1102	4.03623	0.47
23.1779	99.43	0.0472	3.83445	0.41
23.5123	143.06	0.1260	3.78067	0.60
23.9735	63.92	0.0945	3.70896	0.27
24.2609	52.76	0.0945	3.66568	0.22
24.8663	71.30	0.1574	3.57779	0.30
25.4946	198.43	0.0472	3.49102	0.83
25.6290	390.66	0.0945	3.47302	1.63
26.6457	24017.95	0.1056	3.34276	100.00
27.0390	473.72	0.1344	3.29503	1.97
27.4547	749.03	0.1152	3.24608	3.12
27.9173	231.52	0.1344	3.19332	0.96
29.4391	63.69	0.1152	3.03163	0.27
29.8212	55.36	0.1920	2.99364	0.23
30.7581	78.38	0.3072	2.90456	0.33
32.3709	37.17	0.2304	2.76343	0.15
34.8501	115.79	0.6144	2.57231	0.48

Table 45 Continued

36.5421	1643.45	0.1056	2.45700	6.84
37.7451	32.55	0.2688	2.38140	0.14
38.5332	38.48	0.3072	2.33449	0.16
39.4640	1398.01	0.0960	2.28155	5.82
40.2920	743.00	0.0480	2.23655	3.09
41.7826	77.17	0.2688	2.16014	0.32
42.4468	1258.19	0.0864	2.12787	5.24
45.7932	719.28	0.0960	1.97985	2.99
47.1575	47.72	0.2688	1.92571	0.20
49.0081	26.77	0.4608	1.85723	0.11
50.1263	3020.24	0.0960	1.81839	12.57
50.5471	170.43	0.0576	1.80423	0.71
53.2649	10.62	0.3072	1.71840	0.04
54.8632	719.88	0.0768	1.67206	3.00
55.2845	253.83	0.0672	1.66031	1.06
57.4006	8.83	0.4608	1.60403	0.04
58.6874	20.90	0.2304	1.57189	0.09
59.9547	1298.27	0.1056	1.54165	5.41
61.7866	27.72	0.4608	1.50027	0.12
64.0468	300.29	0.0384	1.45267	1.25
64.2145	164.48	0.0576	1.44928	0.68
65.7769	51.73	0.0960	1.41858	0.22
66.3499	28.76	0.3840	1.40772	0.12
67.7401	980.14	0.0768	1.38217	4.08
68.1508	964.63	0.0864	1.37484	4.02
68.3057	962.21	0.0960	1.37210	4.01

Figure 144: Reference pattern list for sample STA21.

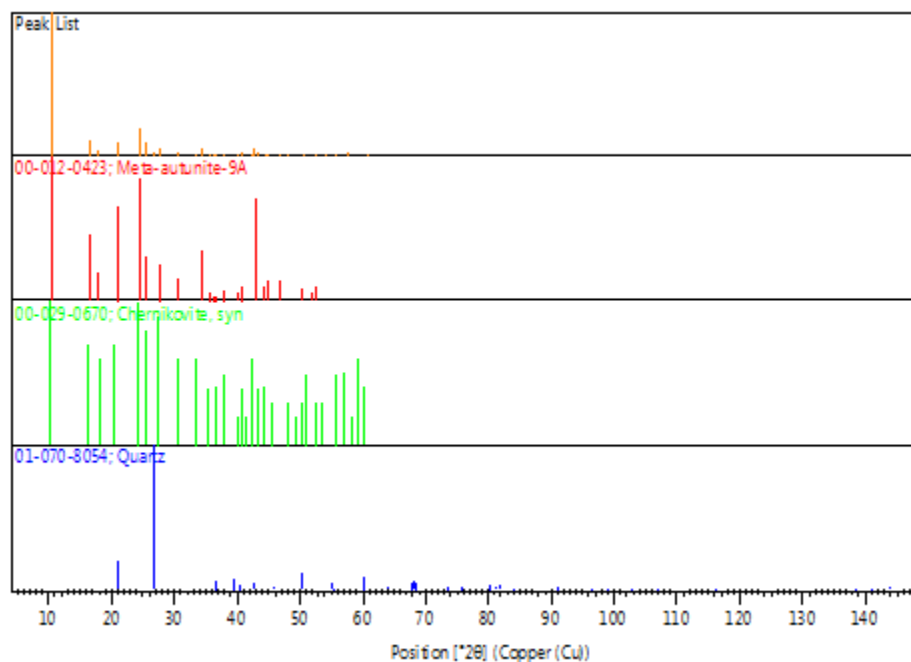


Table 46: Reference peak list for sample STA21.

Pos. [$^{\circ}2\theta$]	Height [cts]	FWHM Left [$^{\circ}2\theta$]	d-spacing [\AA]	Rel. Int. [%]
5.1822	67.46	0.8817	17.03894	0.21
10.5108	31695.61	0.0945	8.40983	100.00
16.4834	3313.22	0.0384	5.37357	10.45
16.5110	3192.04	0.0394	5.36467	10.07
17.9832	1293.53	0.1417	4.92867	4.08
20.8792	2329.84	0.0945	4.25113	7.35
21.0350	3149.20	0.0394	4.21998	9.94
23.3347	43.10	0.1889	3.80904	0.14
24.6615	5826.29	0.1260	3.60703	18.38
25.5103	2927.44	0.0708	3.48891	9.24
26.6933	959.80	0.0384	3.33691	3.03
27.6450	1901.21	0.1056	3.22416	6.00
30.5056	782.19	0.1728	2.92803	2.47
31.7830	92.59	0.2688	2.81320	0.29
33.3081	185.61	0.1920	2.68779	0.59
34.3533	1833.12	0.1920	2.60836	5.78
35.7892	449.12	0.2688	2.50694	1.42
36.4501	300.18	0.1536	2.46298	0.95
36.7280	282.57	0.2304	2.44498	0.89
38.0243	316.02	0.1728	2.36456	1.00
40.1842	249.55	0.1536	2.24230	0.79
42.3130	451.55	0.1920	2.13429	1.42
42.7925	1677.36	0.1536	2.11147	5.29
43.2988	755.23	0.2304	2.08795	2.38
44.4167	450.50	0.2688	2.03796	1.42
44.8296	515.81	0.3072	2.02014	1.63
46.7396	556.95	0.3840	1.94194	1.76
48.2335	118.61	0.3456	1.88523	0.37
50.4988	273.46	0.2688	1.80584	0.86
50.9312	176.27	0.3072	1.79152	0.56
51.8914	160.26	0.3072	1.76061	0.51
52.3883	307.15	0.1344	1.74507	0.97
53.6184	125.11	0.2304	1.70790	0.39
54.2319	225.14	0.1920	1.69002	0.71
55.3563	63.74	0.2304	1.65832	0.20
55.8894	52.96	0.3840	1.64376	0.17
57.6262	750.90	0.3072	1.59828	2.37
59.1395	121.08	0.4608	1.56094	0.38
59.9886	128.67	0.0768	1.54086	0.41
60.8240	380.74	0.2688	1.52169	1.20
62.5616	20.53	0.4608	1.48353	0.06
64.0925	62.50	0.4608	1.45174	0.20
66.3212	44.54	0.2304	1.40826	0.14
67.7792	165.17	0.1152	1.38147	0.52
40.9000	500.90	0.1536	2.20470	1.58

APPENDIX 3

MICROPROBE DATA

A 4 Wavelength Dispersive Spectrometer Cameca SX 100 electron microprobe was used for this analysis. A beam current of 15 nano-amps was used on a tungsten filament. A beam width of 5 microns was used due to the fine-grained nature of sandstone-hosted uranium. Detection limits for uranium and molybdenum for this study averages 150 and 300 parts per million (ppm). Standards and element times are tabled below.

Table 47: Standards and beam time for microprobe analysis.

Element	Standard	Beam Time (seconds)
Uranium (U)	Synthetic Uraninite (UO ₂)	40
Silicon (Si)	Orthoclase (KAlSi ₃ O ₈)	20
Iron (Fe)	Magnetite (Fe ₃ O ₄)	20
Sulfur (S)	Pyrite (FeS ₂)	20
Molybdenum (Mo)	Native Molybdenum	20
Vanadium (V)	Native Vanadium	30
Selenium (Se)	Zinc Selenide (ZnSe)	40

1. BSE Images and Element Maps

Mt. Taylor mine

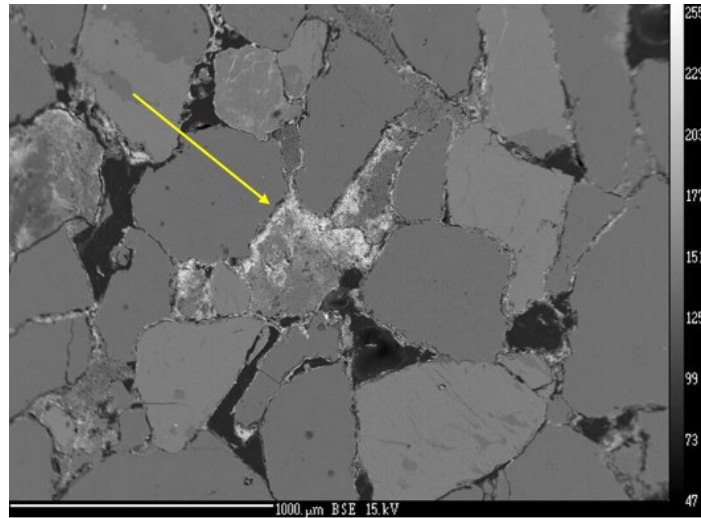


Figure 145: BSE photo of very intense Mo (yellow arrow) in sample MT3. Sample is characterized by abundant ilsemannite, with rare uranium (Figure 2). Note the differing intensities of Mo (255) compared to uranium in Figure 2.



Figure 146: Element map of displaying the Uranium intensity in sample MT3. The uranium here is much less abundant than the Mo shown in Figure 1. Observe the intensity of 5 for uranium, and 225 for molybdenum in Figure 1.

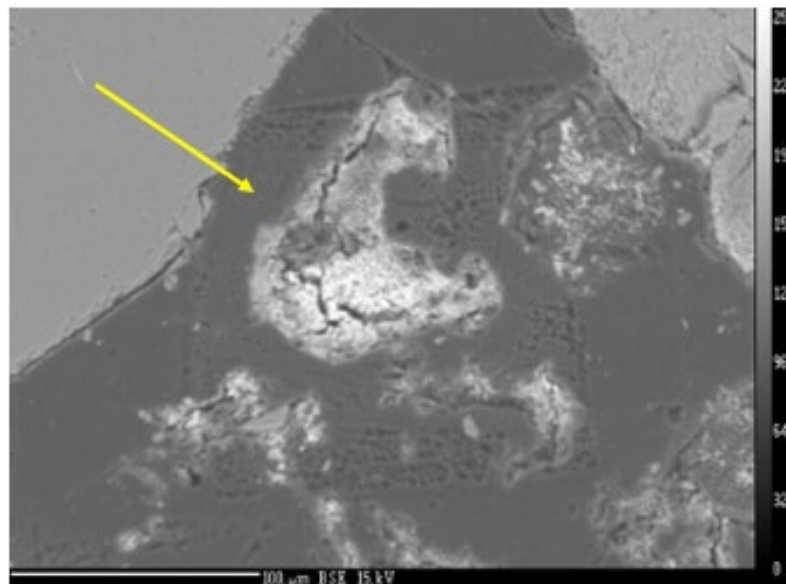


Figure 147: BSE image of the Mo (yellow arrow) in sample MT5. Similar to sample MT3, the Mo is very abundant throughout the sample, with much less intense uranium (Figure 4).

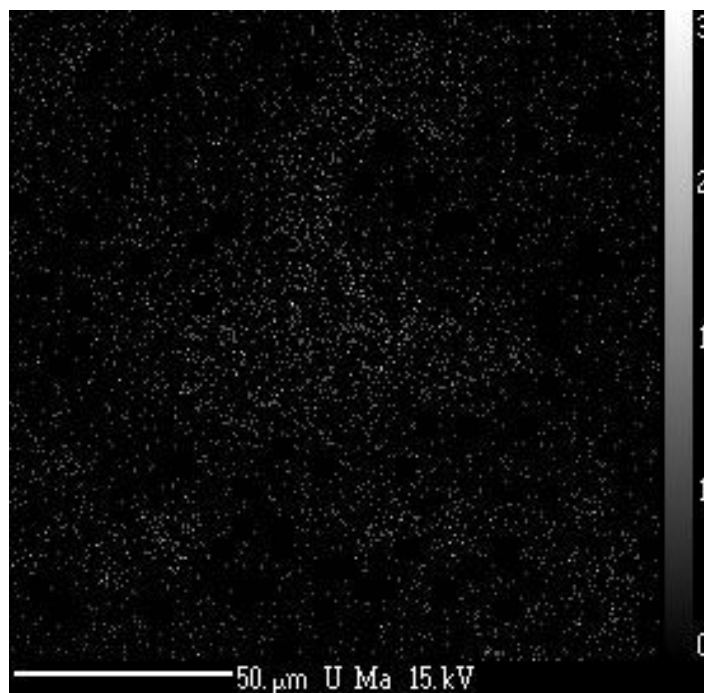


Figure 148: Element map of uranium in sample MT5 of the same area as Figure 3. There is an extreme difference in the intensity of Mo (255) compared to U (3). The uranium concentration in T5 is much less than that of MT3.

Section 31 Mine

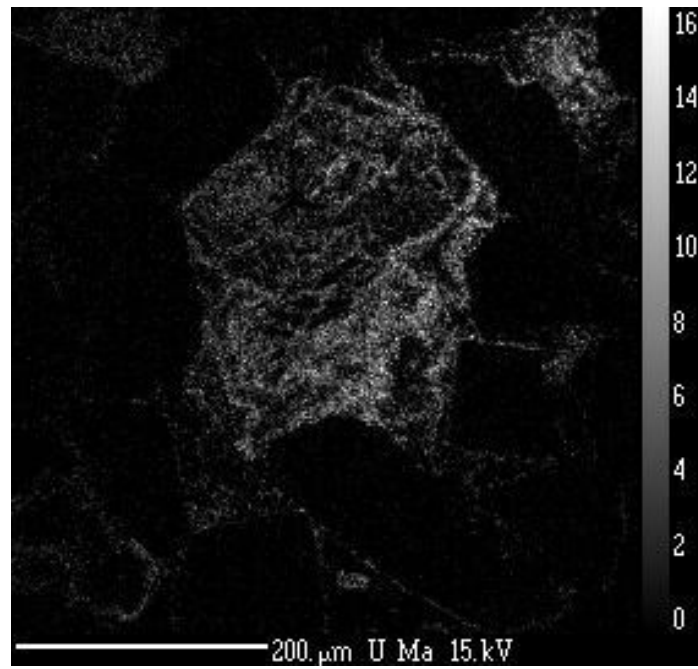


Figure 149: Element map of uranium in sample KM2. Qualitative analysis identifies a mixed phase of dominantly coffinite with much less uraninite (Table 3, Section II.).



Figure 150: BSE image of clay gall in sample KM3. Pyrite is abundant in the reduced mineralization of Section 31 and penetrates to the center of the gall (yellow arrows).

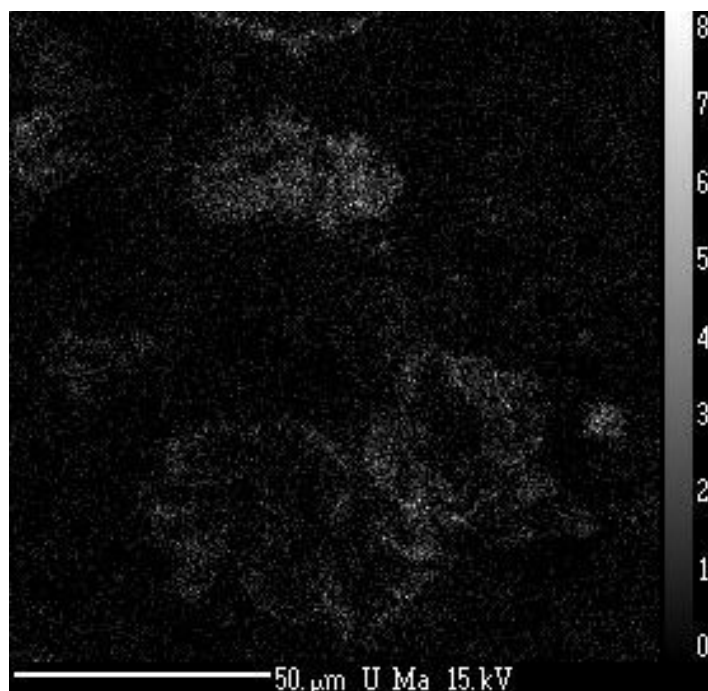


Figure 151: Element map of uranium in KM3. Photo is same location as Fig. 152. Observe the low intensity of U compared to Fe in previous photo. Qualitative analysis shows abundant Si compared to U. This indicates adsorption of U onto the clay (Table 3, Section II.).

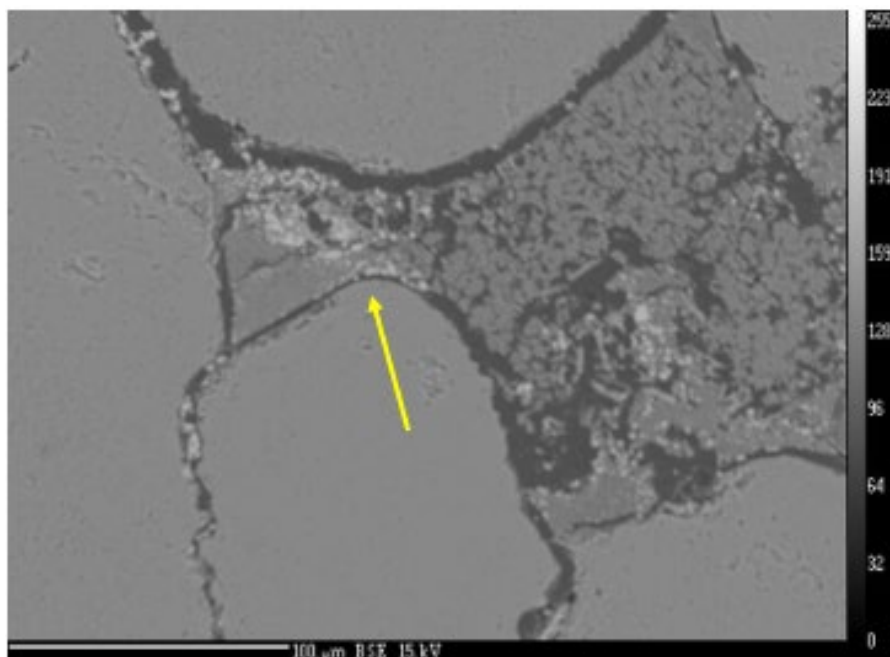


Figure 152: BSE image of Fe (yellow arrow) in sample STA7. Pyrite is abundant within the fossil trash material. Uranium is extremely low (see Table 4).

2. Qualitative Analysis of Samples Represented by Weight Percent

Table 48: Element weight percent of sample MT3. Oxygen is calculated stoichiometrically from the total element weight percent. Sample MT3 is characterized by abundant Mo in the form of ilsemannite, with significantly less U and Si.

Point Number	Si	S	Fe	V	U	Mo	Se	Total
MT3-01	3.97	2.33	7.01	1.57	0.68	37.59	2.54	55.7
MT3-02	1.71	1.76	0.62	0.14	0.19	62.41	0.3	67.12
MT3-03	1.05	1.27	8.99	2.61	2.02	35.37	1.63	52.94
MT3-04	2.02	7.6	2.35	0.92	1.49	42.06	4.07	60.52
MT3-05	3.96	0.21	9.48	2.93	0.55	4.13	2.53	23.78
MT3-06	1.3	3.49	1.82	0.18	1.12	36.5	2.66	47.08
MT3-07	1.35	1.76	17.9	2.67	1.13	26.73	0.72	52.26
MT3-08	0.49	1.33	0.81	0.28	0.3	58.54	0.22	61.97
MT3-09	0.71	1.49	1.12	0.39	0.24	58.87	0.15	62.97
MT3-010	1.1	1.1	0.76	0.37	0.73	58.75	0.33	63.14
MT3-011	0.82	1.6	21.6	4.52	3.04	13.55	0.4	45.53

Table 49: Element weight percent of sample MT5. Oxygen is stoichiometrically calculated and incorporated into chart. Similar to MT3, Mo as the mineraloid ilsemannite is dominant, with rare uranium. Vanadium and selenium were not detected during element mapping.

Point number	MoO3	SiO2	SO2	UO2	FeO	Total
MT5-01	52.62	15.98	3.11	0.09	4.77	76.56
MT5-02	7.76	33.64	1.88	0.06	28.16	71.5
MT5-03	0.76	58	0.41	0.23	2.15	61.55

Table 50: Quantitative analysis of weight percent of elements in the selected uranium phase and clay galls of sample KM2 and 3. Oxygen is stoichiometrically calculated and incorporated into chart. The weight percent of U in coffinite is 60%, and 88% U in uraninite. The weight % U in KM2 suggests there is a mixed phase of dominant coffinite with lesser uraninite. The weight percent of U in sample KM3 is very low compared to the weight % Si, indicating adsorption of U onto clay.

Point Number	MoO3	SiO2	SO2	UO2	FeO	Total
KM2-04	0.25	19.09	0.39	64.83	0.61	85.17
KM2-05	0.07	17.37	0.67	57.59	0.56	76.26
KM2-06	0.1	20.76	0.28	68.38	0.23	89.75
KM2-07	0.1	20.01	0.34	69.63	0.07	90.16
KM2-08	0.06	21.28	0.4	68.22	0.13	90.09
KM2-09	0.03	7.08	1.76	36.26	0.5	45.63
KM3-01	0.77	25.55	5.43	3.25	2.9	37.9
KM3-02	0	11.98	9.74	10.43	2.04	34.19
KM3-03	0.02	21.53	8.4	3.88	3.33	37.17

Table 51: Quantitative analysis of weight percent of elements in sample STA7. Oxygen is stoichiometrically calculated and incorporated into chart. Fe is dominant in the fossil trash as pyrite, with other sulfates. U is very low in concentration, indicating adsorption onto the fossil trash in the sample.

Point Number	MoO3	SiO2	SO2	UO2	FeO	Total
STA7-01	0.13	6.12	3.19	2.38	5.53	17.35
STA7-02	0.11	7.08	4.71	2.47	8.44	22.81
STA7-03	0.01	39.46	5.06	0	14.75	59.28
STA7-04	0.09	18.54	6.32	0.08	14.92	39.95
STA7-05	0.39	20.57	7.87	0.11	18.83	47.78

APPENDIX 4

MAPS OF IDENTIFIED MINERALS FOR THE ST. ANTHONY MINE

Figure 153: North Pit map of minerals. Observe that the North pit is weakly uranyl-sulfate dominant. Western edge of pit was not sampled. Carnotite and oswaldpeetersite are present in trace quantities.

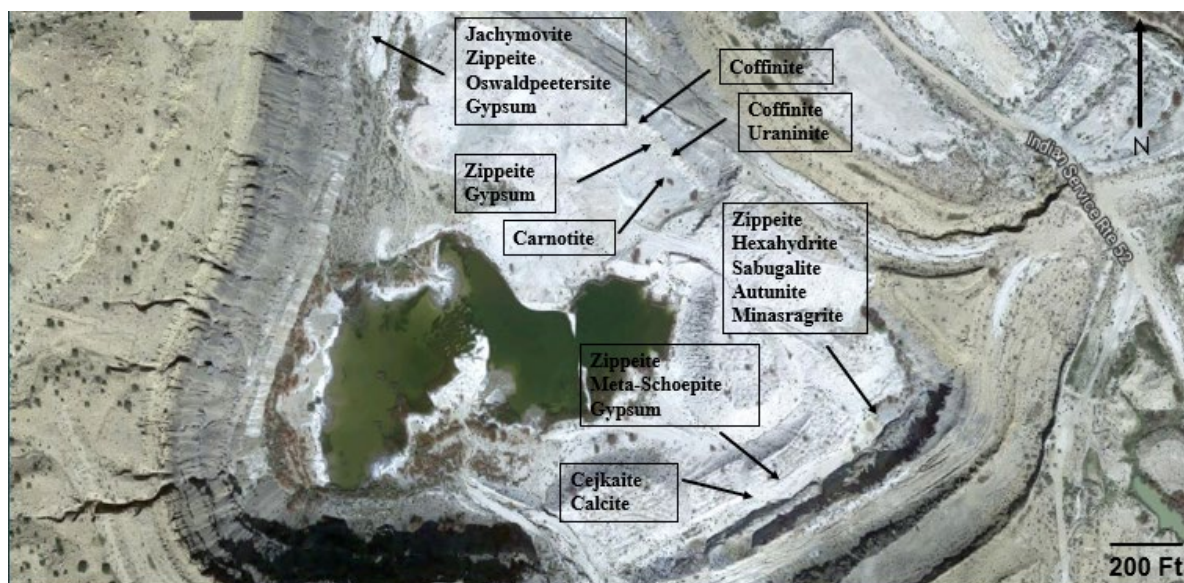


Figure 154: South Pit map of minerals. Observe the change from weakly uranyl-sulfate dominant to weakly uranyl-phosphate dominant.

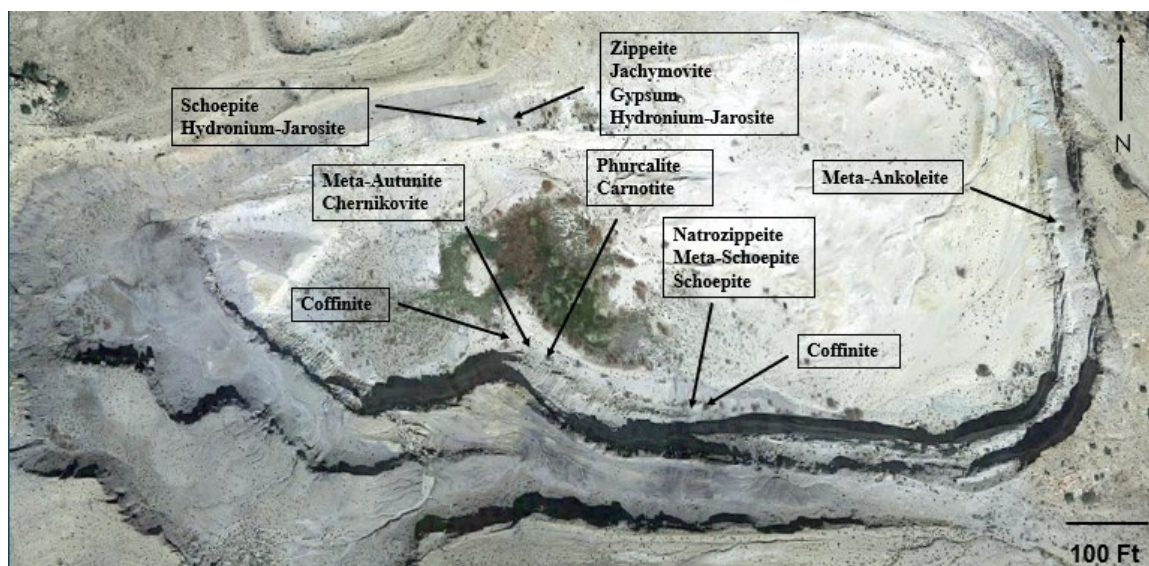


Figure 155: North Pit map of sample numbers with their respective locations.

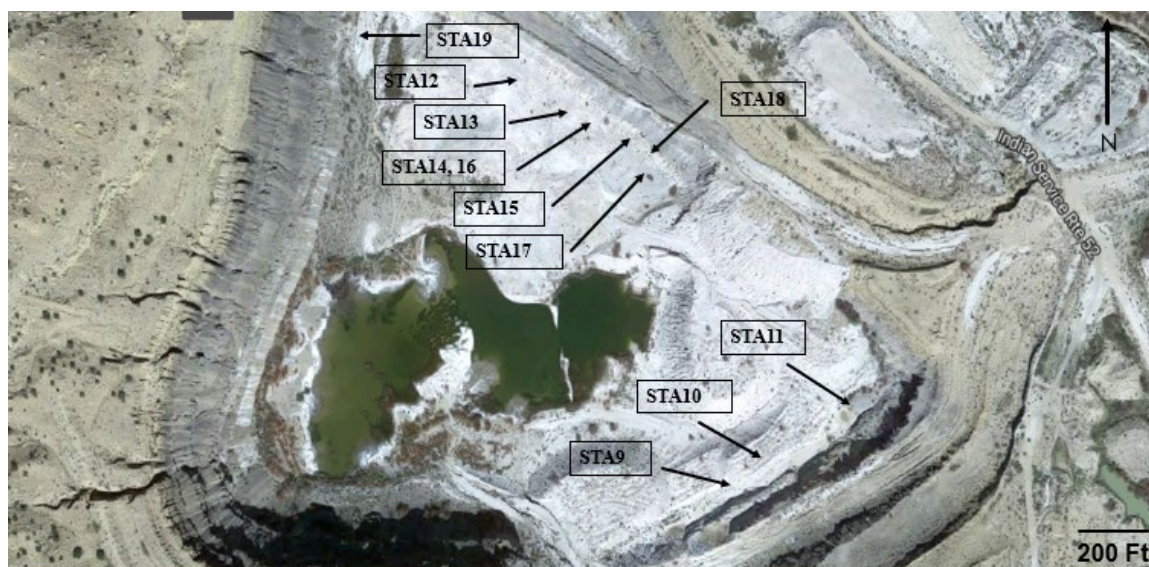
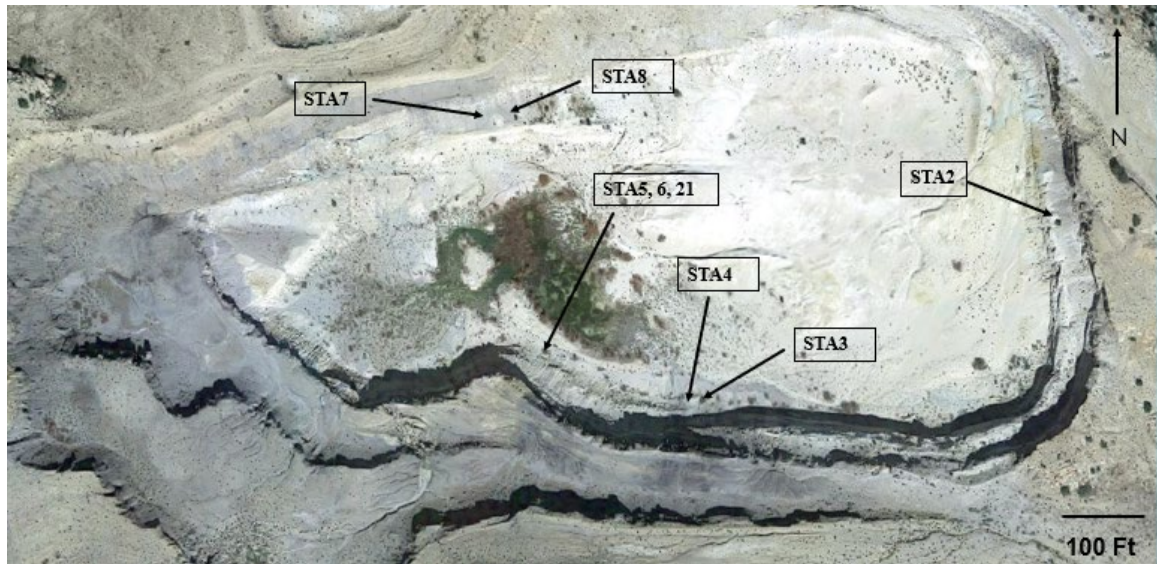


Figure 156: South Pit map of sample numbers with their respective locations.



PERMISSIONS

May 23, 2018

Ms. Samantha Caldwell
New Mexico Institute of Mining and Technology
Mineral Engineering Department
Socorro, NM 87801

Dear Ms. Caldwell-

With this letter I grant you permission to include in your Master of Science thesis any data and technical information derived from the following documents I have authored:

- Wilton, T. 2017. "Uranium Deposits at the Cebolleta Project, Laguna Mining District, Cibola County, New Mexico." *New Mexico Geology*. V. 39, No. 1. p. 1-10
- Wilton, T. 2018. "Technical Report on the Ambrosia Lake Uranium Project, McKinley County, New Mexico, USA." Technical Report Prepared for Westwater Resources Inc., 82 Pages, 8 Tables, 17 Figures; accessed through: www.westwaterresources.net/docs/default-source/technical-reports/ambrosia-lake-project-2018-technical-report.pdf?sfvrsn+6e3537_0

Should you or anyone have questions regarding this matter please feel free to contact me at the address below.

Regards,

Dean T. (Ted) Wilton; PG, CPG. MAIG



Chief geologist
Westwater Resources Inc.
3536 Desert Fox Drive,
Sparks, Nevada 89463, USA
775-276-2764 [mobile]
twilton@radiumtrail.us
twilton@westwaterresources.net

March 30, 2019

Samantha Caldwell

New Mexico Institute of Mining and Technology
Mineral Engineering Department
Socorro, NM 87801

Samantha Caldwell is permitted to include in her Master of Science thesis Figure One, Map of Uranium Districts in Northwest New Mexico, from the publication:

- McLemore, V. T. 2010. "The Grants Uranium District, New Mexico: Update on Source, Deposition, and Exploration." New Mexico Bureau of Geology and Mineral Resources.

Questions regarding the publication or Masters permissions may contact the address below.

Dr. Virginia McLemore, PhD, CPG



Principal Senior Economic Geologist and Minerals Outreach Liaison
New Mexico Bureau of Mines and Mineral Resources
Adjunct Professor
New Mexico Institute of Mining and Technology
Mineral Engineering Department
Socorro, NM 87801
Virginia.mclemore@nmt.edu



NEW MEXICO GEOLOGICAL SOCIETY, Inc.

801 Leroy Place, Socorro, NM 87801
575 835-5490, 835-6333 FAX

Re: Permission to use an unmodified figure (Fig. 2, p. 175, of NMGS Guidebook 18) in master's thesis of Samantha Caldwell

Dear Ms. Caldwell,

NMGS herein grants you permission to use an unmodified figure from our 18th Fall Field Conference Guidebook (fig. 2, p. 175) in your master's thesis. The specified figure is from the following paper authored by the deceased Vincent Kelley:

Kelley, V. C., Kittel, D. F., Melancon, P. E. 1967. "Uranium Deposits of the Grants Region." New Mexico Geological Society 18th Annual Field Conference Guidebook: Defiance, Zuni, Mt. Taylor Region. p. 173-183.

Please acknowledge in the associated caption of your guidebook that this is an unmodified figure from Kelley et al. (1967, fig. 2), and put the full citation in your list of references.

Thank you for formally requesting this permission, and we wish you the best in finishing your master's thesis.

Sincerely,

Daniel J. Koning
President of the New Mexico Geological Society



MINERALOGICAL SOCIETY OF AMERICA

3635 Concorde Pkwy Ste 500 • Chantilly VA 20151-1110 • USA
Tel: 1 (703) 652-9950 • Fax: 1 (703) 652-9951 • Internet: www.minsocam.org

7 January 2019

Samantha Caldwell
El Camino Dr. Trailer 8
Bagdad AZ 86321
United States

Email: samantha.caldwell@student.nmt.edu

Dear Ms. Caldwell:

I received your e-mail message of 2019-01-06 requesting permission to reproduce the following figure for your thesis, "Paragenesis Of Uranium Minerals In The Grants Mineral Belt, New México: Applied Geochemistry And The Development Of Oxidized Uranium Mineralization" for the New Mexico Institute of Mining and Technology:

- Figure Number(s): 1 from Brugger, J., Burns, P. C., and Meisser, N. (2003) Contribution to the Mineralogy of Acid Drainage of Uranium Minerals: Marcottite and the Zippeite-group, *American Mineralogist* v 88, 676–685.

It is with pleasure that we grant you permission to reproduce this figure without cost in this and all subsequent editions of the work, its ancillaries, advertisements and promotional materials, and other derivative works, in any form or medium, whether now known or hereafter developed, in all languages, for distribution throughout the world on the conditions that reference is given to the original publication of the Mineralogical Society of America.

Sincerely,

J. Alexander Speer
Executive Director, MSA



JONES & BARTLETT LEARNING

5 Wall Street | Burlington, MA | 01803 | 978-443-5000 | www.jblearning.com

PERMISSIONS AGREEMENT

To obtain copyright permission from Jones & Bartlett Learning, including imprints from affiliates and subsidiaries (as listed on the website www.jblearning.com), you must fill out this form completely. This agreement grants nonexclusive, one-time use to reproduce the material in the language specified by the requester. Permission is granted for the material specified, and does not extend to material that is separately copyrighted. This agreement does not include future revisions or editions of the work. Please note that it is your responsibility to ensure that the material you are requesting has not been referenced to another source. If the material has been referenced to another source, you must obtain permission from the original copyright owner. We regret that electronic files of figures cannot be provided. Please allow thirty days for processing.

Requester Information:

Name: <u>Samantha Caldwell</u>	College/Company: <u>New Mexico Institute of Mining and Technology</u>
Street: <u>Trailer B El Camino Dr.</u>	City: <u>Regid</u> State: <u>AZ</u> Zip: <u>85621-1987</u>
Phone Number: <u>(859) 690-3441</u>	Fax Number: <u>() - -</u> Email: <u>samanthacaldwell@bndt.com</u>

Billing Information (if different from above):

Name: <u>same as above</u>	College/Company: _____
Street: _____	City: _____ State: _____ Zip: _____
Phone Number: <u>() - -</u>	Fax Number: <u>() - -</u> Email: _____

I wish to borrow material from the following product published by Jones & Bartlett Learning or Jones & Bartlett Learning imprints:

Title: <u>Solutions, Minerals, and Equilibrium</u>	Edition: <u>1st</u>
ISBN #: <u>0867201487</u>	(ISBN located on the back cover)
Author(s): <u>RA Maxwell and L Christ</u>	Are you the Author of this work? Yes <input type="checkbox"/> No <input checked="" type="checkbox"/> Copyright date: <u>02-05-1990</u>
For text material, list page numbers: <u>—</u>	Total page count: <u>—</u>
For illustrations, list table/figure numbers: <u>7.32a, 11.6a, 11.6b</u>	
Found on page number(s): <u>354, 389, 390</u>	Total number of figures/tables being requested: <u>3</u>

I plan to use this material in the following way (note that multiple uses often incur multiple fees):

Print Book/Publication <input type="checkbox"/>	Ebook <input type="checkbox"/>	CD/DVD <input type="checkbox"/>
Author(s): _____	Affiliation: _____	
Title: _____	Publisher: _____	
Total number of copies to be printed (if print): _____	Estimated number of users (if ebook): _____	
Duration of use (please include dates): _____	Language(s): _____	
Course Packet: Print <input checked="" type="checkbox"/> Electronic <input type="checkbox"/>		
College/Company: <u>New Mexico Institute of Mining and Technology</u>		
Total number of copies to be printed (if print): <u>3</u>	Estimated number of users (if electronic): <u>—</u>	



JONES & BARTLETT LEARNING

5 Wall Street | Burlington, MA | 01803 | 978-443-5000 | www.jblearning.com

Duration of use (please include dates): 01/15/19 - 05/28/19

Website use ☐

If online, please list URL: http://

Name of website owner: _____ Is website password protected? Yes ☐ No ☐

Duration of use (please include dates): _____ Language(s): _____

Other use ☐ (please be very specific) _____

I AGREE TO THESE TERMS:

Samantha Caldwell Samantha Caldwell 01/15/19
Printed name Signature Date

For use of Jones & Bartlett Learning only:

Permission is: ☒ Denied
☒ Granted upon payment of the fee of \$ 18 payable to Jones & Bartlett Learning within 30 days of the agreement date. Your confirmation email will contain the agreement and invoice to be paid.

Reference No.: 199910110-1959 Date: 3/27/19 Permission granted by: Missy Sund

The following credit line must be used, unless a specific credit line is required below: Author (Editor if the work is part of an anthology), Title of work, Year of copyright: Jones & Bartlett Learning (or applicable imprint), Burlington, MA. www.jblearning.com. Reprinted with permission.

Specific credit line required (not applicable unless listed here):

The following 3rd party content must be redacted:

**Paragenesis Of Uranium Minerals In The Grants Mineral Belt, New
México: Applied Geochemistry And The Development Of Oxidized
Uranium Mineralization**

By Samantha Caldwell

Permission to make digital hard copies of all or part of this work for personal or classroom use is granted without fee provided that copies are not made or distributed for profit or commercial advantage and that copies bear this notice and the full citation on the last page. To copy otherwise, to republish, to post on servers or to redistribute to lists, requires prior specific permission and may require a fee